Heralded Atom-Atom Entanglement

Julian Hofmann

München 2013

Heralded Atom-Atom Entanglement

Julian Hofmann

Dissertation
an der Fakultät für Physik
der Ludwig–Maximilians–Universität
München

vorgelegt von
Julian Hofmann
aus Bremen

München, den 11.10.2013

Zusammenfassung

Verschränkung ist eines der ungewöhnlichsten Phänomene der Quantenmechanik. Sie beschreibt nicht-separable Quantenzustände, deren Eigenschaften der Intuition widersprechen, die man sich durch Beobachtungen klassischer Phänomene angeeignet hat. Mittlerweile ist sie ein wichtiger Bestandteil in vielen Quanteninformations- und Quantenkommunikationsprotokollen, da sie Informationsverarbeitung ermöglicht, die schneller als klassische Informationsverarbeitung ist. Besonders die Verschränkung von weit voneinander entfernten massiven Teilchen, die als Quantenspeicher genutzt werden können, erlaubt den Bau von sogenannten "Quantum Repeatern" und später von ganzen Quantennetzwerken. Außerdem kann eine solche Verschränkung für einen schlupflochfreien Test der Bellschen Ungleichung genutzt werden und somit die 80 Jahre alte Frage beantworten, mit welcher Theorie die physikalische Welt beschrieben werden muss. Diese Frage wurde als erstes von Einstein, Podolsky und Rosen gestellt, die gefordert hatten, dass die Welt von einer kompletten Theorie beschrieben werden sollte. Eine komplette Theorie ist in ihren Augen sowohl realistisch als auch lokal. Diese Anforderungen erfüllt die Quantenmechanik nur, wenn man sie um sogenannte lokale versteckte Variablen erweitert. Obwohl alle bisherigen Tests der Bellschen Ungleichung die Existenz von lokalen versteckten Variablen widerlegten, ist die Frage nach deren Existenz noch nicht endgültig beantwortet, da alle bisherigen Experimente mindestens ein Schlupfloch für diese zulassen mussten. Angekündigte Verschränkung zwischen massiven Teilchen, die weit voneinander entfernt sind, könnte einen endgültigen Test der Bellschen Ungleichung ermöglichen und somit auch eine endgültige Aussage über die Existenz lokaler versteckter Variablen.

In dieser Dissertation wird die Erzeugung und der Nachweis von angekündigter Verschränkung zweier $20\,\mathrm{m}$ voneinander entfernter Rubidiumatome besprochen. Durch den großen räumlichen Abstand der Atome kann keine direkte Wechselwirkung zwischen den Atomen genutzt werden, um die Verschränkung zu erzeugen. Deswegen werden einzelne Photonen genutzt, um die Verschränkung über eine so große Strecke erzeugen zu können. In einem ersten Schritt wird der Spin jedes Atoms mit der Polarisation eines Photons verschränkt. Danach werden beide Photonen zu einem Strahlteiler geleitet, an welchem sie interferieren. Der resultierende zwei-Photonenzustand wird auf einen maximal verschränkten Bellzustand projiziert. Dieses sogenannte "entanglement swapping" Protokoll ermöglicht die Verschränkung von beiden Atomen ohne direkte Wechselwirkung zwischen den Atomen. In einem weiteren Schritt wird die Atom-Atom Verschränkung durch Messung von Korrelationen zwischen beiden atomaren Spins nachgewiesen. Um einen hohen Grad der Verschränkung zu erreichen, müssen auch alle zugrunde liegenden Prozesse wie die Atom-Photon Verschränkung und die zwei-Photonen Quanteninterferenz genau studiert und optimiert werden. In dieser Arbeit werden Daten präsentiert, die einen hohen Grad von Atom-Photon Verschränkung in beiden Teilexperimenten, einen sehr guten zwei-Photon Interferenzkontrast und letztlich auch Atom-Atom Verschränkung sowie eine Verletzung der Bellschen Ungleichung zeigen.

Die Qualität der Atom-Atom Verschränkung ist dabei gut genug für die Demonstration weiterer Anwendungen in der Quanteninformationswissenschaft. Zukünftige Verbesserungen werden zudem einen schlupflochfreien Test der Bellschen Ungleichung ermöglichen und somit auch die Demonstration von geräteunabhängiger Sicherheit eines Quantenkryptographieprotokolls.

Abstract

Entanglement is a most extraordinary phenomenon in quantum mechanics as it describes non separable quantum states which characteristics contradict the common intuition based on observations in classical physics. It is essential in most quantum information and communication protocols because it provides a resource for faster-than-classical information processing as well as processing of even physically separated quantum systems. Especially, the entanglement of widely separated, massive particles used as quantum memories allows the construction of quantum repeaters and furthermore, of quantum networks. Such entanglement can also be utilized for a test of Bell's inequality solving the 80 year old question how the physical world needs to be described. It was first raised by Einstein, Podolsky and Rosen demanding that the world should be described by a complete theory, which is realistic, local and deterministic - restrictions that quantum mechanics could only fulfill by implementation of so called local hidden variables. Although experimental tests of Bell's inequality favored quantum mechanics over local hidden variable theories the question is still an open one as all these tests suffered from at least one major loophole. Here, heralded entanglement of massive particles over a large distance may enable a conclusive test of Bell's inequality providing a final statement about the existence of local hidden variables.

This thesis presents the generation and verification of heralded entanglement of two rubidium atoms located in two independent experimental setups at a distance of $20\,\mathrm{m}$. As the atoms are physically separated, no direct interaction between them can be established for entanglement generation. For this reason photons are used for long distance entanglement distribution. In a first step entanglement is generated between the spin state of each atom and the polarization of a single photon. The two photons are guided to a beam splitter, at which they interfere, and the resulting two photon state is projected onto a maximally entangled Bell-state. This, so called, entanglement swapping protocol entangles the two atoms, although they never interacted directly. In a second step the atom-atom entanglement is verified by correlation measurements of the two atomic spin states. In oder to achieve a high degree of entanglement, all underlying processes including atom-photon entanglement as well as two-photon quantum interference need to be studied in detail and optimized. Data are presented verifying high atom-photon entanglement visibilities in both setups, high two-photon interference visibility and finally, atom-atom entanglement as well as a test of Bell's inequality.

The atom-atom entanglement visibilities are high enough for demonstration of further applications of quantum information science. Future improvements will allow a loophole-free test of Bell's inequality and thereby, demonstration of device-independent security of quantum cryptography.

Contents

1. Introduction

Early 20th century technical advances allowed new experiments on the microscopic scale of single atoms, electrons and photons. The results of these experiments could not be explained by classical physics. A new theory was needed describing these phenomena. The answer to describe these phenomenas was the theory of *quantum mechanics*. Even though all new phenomena could be described by this theory, there still existed doubts caused by the many counter intuitive features of quantum mechanics as the superposition principle, the wave-particle dualism, the irreversible measurement collapse or the uncertainty principle. The most extraordinary of these new properties is entanglement. Entangled particles are in a common quantum state, and measurement results on the entangled particles show correlations between them which can not be explained by classical statistics. Furthermore, the theory allows arbitrary distances between the entangled particles without any change of the measurement results! This inherent non-locality of quantum mechanics, combined with its characteristic that only probabilities for measurement outcomes can be predicted (indeterminism), brought the three physicists Einstein, Podolsky and Rosen to raise the following question in 1935: "Can Quantum-Mechanical Description of Physical Reality Be Considered Complete?" [1]. In their work they discussed the possible existence of so called *"local hidden variables"* (LHV), which can not be observed, but determine every measurement result beforehand. This additional assumption would turn quantum mechanics into a theory, which they considered to be complete as it would be realistic and local.

In the following years the discussions about the existence of LHV remained purely philosophically, until Bell proposed a possibility to experimentally test their existence in 1964 [2, 3]. He introduced an experiment based on perfect correlation measurements on two entangled particles in different bases, and showed that for a set of distinct measurements quantum mechanics and LHV-theories predict different outcomes of such an experiment. In the following years more practical *"Bell inequalities"* were proposed considering also non-perfect correlations between the particles. In 1969 Clauser, Horne, Shimony and Holt presented an inequality (CHSH-inequality), which is limited to a value of 2 for all LHV-theories [4], but allows quantum mechanics to violate this limit with values up to $2\sqrt{2}$. In subsequent years many experiments were executed using the CHSH-inequality to test LHV-theories [5, 6, 7, 8]. They all violated the inequality thereby conforming quantum mechanics. But all these experiments suffered of at least one of two main *"loopholes",* which serve as a back door for LHV-theories. The analysis of the particles was not space-like independent or relied on a fair sampling assumption (less than 82.8% of all entangled pairs were taken into account). The locality-loophole was closed by an experiment with entangled photon pairs, at which the photons were analyzed $400\,\mathrm{m}$ apart from each other [9], and the detection-loophole was closed by measurement on entangled ions [10]. But until now no experiment closed both loopholes at the same time. Therefore, the question about the existence of LHV-theories is still an open one.

Entanglement of separated particles can also be used for applications in quantum information science, quantum cryptography and quantum metrology as the quantum state of each particle can be interpreted as qubit [11, 12, 13, 14, 15, 16]. A qubit is defined as quantum mechanical analog to a classical bit that, in contrast to a classical bit, may also be in a superposition state $a\ket{0} + b\ket{1}$. It can be read out in a projective measurement yielding as result 0 or 1. The entanglement of those

qubits enables the demonstration of basic quantum information protocols, e.g., a quantum repeater link [17] or teleportation of quantum states [18] as well as quantum communication protocols like device independent quantum cryptography [19]. An entire quantum processor consisting of many qubits would also be able to process computational tasks like factorization of large numbers [20] and database search [21] much faster than classical processors. However, these applications are far from any practical realization.

First demonstrations of entanglement were performed with photon pairs using atomic cascade transitions in 1967 [22]. Since then techniques for the generation of entanglement improved drastically. Today entanglement between up to eight photons has been verified by using parametric down conversion [23]. Furthermore, entanglement has not only been verified for photons but also for massive particles. The successful entanglement of 14 ions trapped in a linear Paul-trap has been achieved [24] as well as entanglement of thousands of atoms trapped in an optical lattice [25]. These experiments have demonstrated entanglement between particles of the same species. But many enhanced protocols in quantum information and communication demand so called *"hybrid systems"* which make use of the long coherence times and high detection efficiency of massive particles and the capability of photons to distribute information over long distances. This hybrid entanglement has already been verified for atoms and ions in free space [26, 27], for atoms and ions in optical cavities [28, 29] as well as for ensembles of atoms [30]. Recently it has even been verified for nitrogen-vacancy centers in diamonds, which is a much more complex system than atoms due to influences of its bulk surrounding [31]. There exists also another kind of hybrid entanglement. Here, entanglement is generated between a single atom and a Bose-Einstein condensate of atoms of the same species [32]. The presented systems already are suited for demonstrations of basic quantum computational algorithms [33, 34, 35, 36, 37, 38, 39, 40, 41, 42, 25, 43].

The experiment presented in this thesis is using two ^{87}Rb atoms, which are separated by $20\,\mathrm{m}$, for demonstration of entanglement of massive particles over long distances. Due to the huge distance of the atoms no direct interaction can be established in order to entangle the atoms. Therefore, this experiment utilizes single photons for long distance distribution of entanglement as they can be easily guided trough fibers of almost arbitrary length. In a first step hybrid entanglement between a single atom, trapped in an optical dipole trap inside an high vacuum chamber, and a single photon is generated in two almost independent setups. The single photons emitted by each atom are guided to a detection setup at which they arrive at the very same time. Inside the detection setup the two photons interfere, and are projected according to the respective detection results onto Bell-states. A two-photon coincidence detection projects the photons and the atoms each on the very same Bell-state, and thus serves as a heralding signal for every atom-atom entanglement event. This so called *"entanglement swapping protocol"* entangles the two atoms, although they never directly interacted with each other.

However, this experimental setup is not suited for a loophole-free test of Bell's inequality as the detection of the atomic states won't be space-like separated. But the demonstration of heralded entanglement is a very important step towards this goal, and the setup is already capable to close the detection loophole as well as to demonstrate basic quantum information protocols like teleportation. Moreover, the required experimental improvements for a loophole-free Bell test are already developed making it a realistic short term goal.

This thesis starts by discussing the experimental setup and the generation of atom-photon entanglement. Thereafter, the experimental requirements for a high entanglement swapping quality are examined (single-photon emission, two-photon interference), and the actual experimental performance is evaluated. In the end measurements are presented which verify the generation of entanglement between two widely separated atoms.

2. Experimental Setup and Atom-Photon Entanglement

Hybrid entanglement between a massive particle and a photon has already been achieved for atoms and ions in free space [26, 27], for atoms and ions in optical cavities [28, 29] as well as for ensembles of atoms [30] and for nitrogen-vacancy centers [31].

Atom-photon entanglement (APE) is the basis for the more complex atom-atom entanglement protocol which is also presented in this thesis. Therefore, high-quality APE is an inalienable demand on the experimental setup.

This chapter describes the generation and verification of entanglement between a single trapped atom and a photon in two different experiments (the experiments are denoted as trap1 and trap2). The atomic system is introduced first, followed by basic theory of APE. Thereafter, the experimental realization of such an experiment is illustrated using the example of trap1. A comparison of the setups of trap1 and trap2 is presented in appendix E. Finally, measurements are presented verifying the entanglement in both experiments. A more detailed description of the generation of atom-photon entanglement in this experiment is given in the theses [44, 45, 46].

2.1. The Atomic System

In this experiment Rubidium 87 (^{87}Rb) serves as massive particle for experimental realization of hybrid entanglement. ^{87}Rb is an alkaline metal, and thus has a single electron in the outer shell. The ground state is $5^2S_{1/2}$, and its first excited state 5^2P is split into two levels $5^2P_{1/2}$ ($D1$) and $5^2P_{3/2}$ ($D2$) due to fine splitting. It has a nuclear spin of $3/2$, which splits the ground state into two levels $F = 1$ and $F = 2$, due to hyperfine interactions, and the first excited state into several levels which will be denoted as $F' = N$. Each level of the ground state and the excited states further splits into Zeeman sub-states. The sub-states of the atomic ground and the excited states will be denoted with $|F, m_F\rangle$ and $|F', m_F\rangle$, respectively. A scheme of all relevant states of ^{87}Rb is presented in appendix B.

^{87}Rb is well suited for the experimental purpose of atom-photon entanglement because it fulfills all main requirements: It has a stable ground state, in which a qubit can be encoded, and its cooling and entanglement transitions are at a wavelength of $780\,nm$ which is easily accessible by state of the art laser systems. Furthermore, photons of this wavelength are distributable over long distances via optical fibers. In this experiment the qubit is encoded in the ground states $5^2S_{1/2}$, $|F = 1, m_F = \pm 1\rangle$. This long-lived Zeeman sub-states are degenerated, if there is no external magnetic field. Together with the excited state $5^2P_{3/2}$, $|F' = 1, m_F = 0\rangle$ they form a Λ-type system ideal for the generation of atom-photon entanglement.
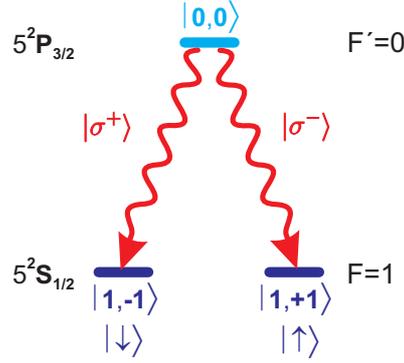
Figure 2.1.: λ-scheme for entanglement generation: If the atom decays to the state $|F = 1,\, m_F = -1\rangle$, it emits a σ^+ (left-circular polarized)-photon and if it decays to the state $|F = 1,\, m_F = +1\rangle$, it emits a σ^- (right-circular polarized)-photon. This way a maximally entangled state is formed $|\Psi^+\rangle = \frac{1}{\sqrt{2}}(|F = 1,\, m_F = -1\rangle\,|\sigma^+\rangle + |F = 1,\, m_F = +1\rangle\,|\sigma^-\rangle)$.

2.2. Basic Entanglement Generation

In order to generate entanglement between a single ^{87}Rb atom and a single photon, the atom is excited to the state $5^2P_{3/2}$, $|F' = 1,\, m_F = 0\rangle$ by a laser pulse. Subsequently, it decays spontaneously to the ground state $5^2S_{1/2}$, $|F = 1\rangle$, thereby emitting a single photon. In detail, if it decays to the state $|F = 1,\, m_F = -1\rangle$, it emits a σ^+ (left-circularly polarized)-photon and if it decays to the state $|F = 1,\, m_F = +1\rangle$, it emits a σ^- (right-circularly polarized)-photon (see figure 2.1). For a decay into $|F = 1,\, m_F = 0\rangle$ the atom emits a π-polarized photon which has a polarization linear along the quantization axis (z-axis). All three decay channels occur with the same probability.

In the experiment the single photons are collected with an objective, which experimentally defines the quantization axis, and coupled into a single mode fiber. It is important for the generation of entanglement that π-polarized photons can not couple into the single mode fiber (for detailed discussion see [45]). Thus, only $\sigma^\pm$ photons can be detected by this arrangement. Without any further interactions with the environment both detectable decay channels are in a coherent superposition, and therefore form a maximally entangled state:

$$\left|\Psi^+\right\rangle = \frac{1}{\sqrt{2}}(|F = 1,\, m_F = -1\rangle\left|\sigma^+\right\rangle + |F = 1,\, m_F = +1\rangle\left|\sigma^-\right\rangle). \tag{2.1}$$

In qubit notation the atomic states $|F = 1,\, m_F = -1\rangle$ and $|F = 1,\, m_F = +1\rangle$ are defined as $|\downarrow\rangle_z$ and $|\uparrow\rangle_z$, respectively, and the σ^--photon and σ^+-photon will be denoted by R and L, respectively. In this notation $|\Psi^+\rangle$ is given by

$$\left|\Psi^+\right\rangle = \frac{1}{\sqrt{2}}(|\downarrow\rangle_z\,|L\rangle + |\uparrow\rangle_z\,|R\rangle). \tag{2.2}$$

The entangled state can easily be expressed in any basis state of the Pauli operators $\hat{\sigma}_x$, $\hat{\sigma}_y$ and $\hat{\sigma}_z$ (see appendix D).
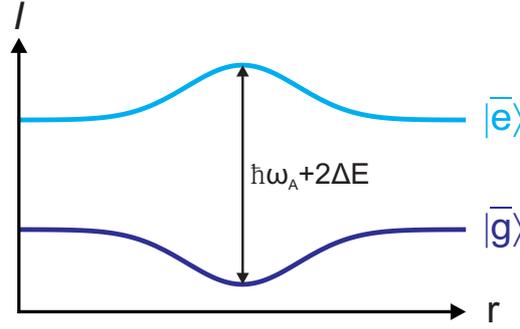
Figure 2.2.: Light shift of a two level atom which passes a red detuned laser light field with Gaussian shape. It forms a conservative potential for an atom.

2.3. A Trap for Single Atoms

In all subsequently described experiments a single ^{87}Rb atom at a well defined location is needed which is also shielded from the environment as good as possible. Therefore, a single atom is trapped in an optical dipole trap inside an ultra-high vacuum (UHV) camber. The loading into the dipole trap is performed by a magneto optical trap (MOT).

In the following subsections the experimental realization of vacuum system, dipole trap, MOT, required laser system and optical setup are illustrated.

2.3.1. Optical Dipole Trap

This experimental realization of an optical dipole trap consists of a single strongly focused Gaussian laser beam [47, 48]. The variation of the beam intensity in x-, y- and z-direction introduces a position dependent shift, called AC-Stark shift, of the atomic states. The direction and magnitude of this shift are determined by the detuning of the laser beam from the atomic transition frequency $\Delta = \omega_A - \omega_L$, where ω_A is the atomic transition frequency and ω_L the frequency of the laser beam, and the local intensity of the laser beam. The shift can be calculated by diagonalizing the interaction Hamiltonian:

$$\mathcal{H} = \frac{\hbar}{2} \begin{bmatrix} -2\Delta & \Omega_0 \\ \Omega_0 & 0 \end{bmatrix}. \tag{2.3}$$

For $\Omega_0 \ll |\Delta|$ the energies are shifted by

$$\Delta E = \mp \frac{\hbar \Omega_0^2}{4\Delta}, \tag{2.4}$$

where $\Omega_0 = \frac{1}{\hbar} d E_0$ is the on-resonance Rabi-frequency with the atomic dipole moment d and the amplitude of the electric field E_0.

For red detuning ($\Delta > 0$) the ground states are shifted down (see figure 2.2) forming a attractive potential for an atom. Note that this is a conservative potential. It can only trap atoms which are additionally cooled during their transit through the dipole trap region.

The experimentally realized dipole trap (trap1) uses laser light at a wavelength of $851\,\mathrm{nm}$. The light is guided trough a single mode fiber to achieve a Gaussian mode profile of the laser beam in front of the focusing optics, which focuses the beam down to a waist of $w_0 = 3.5\,\mu\mathrm{m}$ with a Rayleigh range

$z_R = 45\,\mu$m. The laser power is set to be $\sim 40\,$mW in front of the glass-cell, and causes a trap depth $U_0 =\sim 0.65\,$mK. The different intensity gradients in z- and x-, y-direction result in trap frequencies:

$$\omega_{x,y} = \sqrt{\frac{4U_0}{m \cdot w_0^2}} = 2\pi{\cdot}22.7\,\text{kHz} \tag{2.5}$$

and

$$\omega_z = \sqrt{\frac{2U_0}{m \cdot z_R^2}} = 2\pi{\cdot}1.25\,\text{kHz}, \tag{2.6}$$

where m is the mass of the atom (for detailed discussion seeVolz [45], Rosenfeld [46] and for data of trap2 appendix E).

2.3.2. Vacuum System

The main limitation of the storage time of single atoms in a dipole trap are collisions with the background gas. In order to achieve long storage times, the background gas pressure has to be minimized by an UHV setup. Here, a steel vacuum chamber with an attached spectroscopy glass cell (Hellma GmbH & Co. KG) is used. The glass cell offers good optical access from all spatial directions. The vacuum is maintained by an ion-getter pump (Varian StarCell, $24\,l/\text{s}$) guaranteeing a vacuum pressure of $< 1 \cdot 10^{-10}\,$mbar. A built-in Rubidium dispenser serves as source for thermal Rubidium atoms.

2.3.3. Laser System

Nine different laser frequencies provided by six diode lasers are used to trap and manipulate a single atom. The high power laser diode providing the light for the dipole trap does not require stabilization. All other diodes are stabilized in frequency by a diffraction grating in Littrow configuration and FM-lock technique (or locked by a frequency offset lock technique to a FM-locked laser). Acousto-optical modulators are used to derive fine-tuned laser frequencies and to switch the beams. Figure 2.3 shows a schematic of all applied beams and their relative frequencies.

2.3.4. Magneto Optical Trap

A magneto optical trap (MOT) both cools and traps atoms at the same time thereby creating a relatively dense cloud of atoms, suitable for loading a dipole trap. The MOT consists of three pairs of counter-propagating laser beams and a magnetic quadrupole field. The laser beams consist of laser light of two different laser frequencies. The cooling beams (CL) are red detuned with respect to the closed cycle atomic transition $5^2S_{1/2}, |F = 2\rangle {\to} 5^2P_{3/2}, |F' = 3\rangle$ and the repump beams (RP) are resonant to the transition $5^2S_{1/2}, |F = 1\rangle {\to} 5^2P_{3/2}, |F' = 2\rangle$, pumping atoms to the $5^2S_{1/2}, |F = 2\rangle$ state, if they have decayed to the $5^2S_{1/2}, |F = 1\rangle$ caused by off-resonant excitation.

Due to the Doppler effect [49, 50] the detuning of the cooling beam increases the scattering rate of photons for atoms whose direction of motion is oppositely to the direction of propagation of the respective beam. The directed momentum transfer from the photon onto the atom slows (cools), but does not trap the atom. In order to create a spatial confinement, a magnetic quadrupole field with a field gradient of $5\,mG/\text{cm}$ is used. The magnetic field causes a position dependent shift of the atomic Zeeman states which together with a circular polarization of the laser beams lead to a spatial confinement of the atoms (see figure2.4) [51, 52].

The cloud of trapped atoms in this MOT has a diameter of $\sim 1\,$mm, and contains several 10000 atoms.
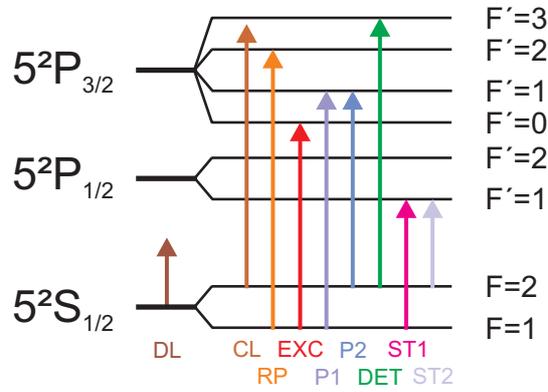
Figure 2.3.: Schematic of the laser beams used and their wavelengths. All laser beams are generated by diode lasers and tuned in frequency by acousto-optical modulators. DL → dipole trap laser; CL→ cooling laser; RP→ repump laser; EXC → excitation laser; P1 → first pump laser; P2 → second pump laser; DET→ hyperfine detection laser; ST1→ STIRAP 1 laser; ST2→ STIRAP 2 laser.
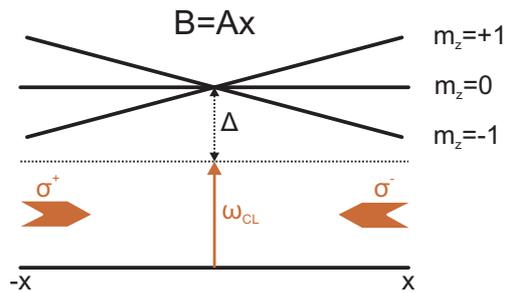
Figure 2.4.: Space depended shift of the Zeeman states: The Zeeman states shift in the magnetic field and thus a spacial confinement is generated together with the red detuned cooling light. The frequency of the cooling light ω_{CL} is red detuned by a frequency Δ.
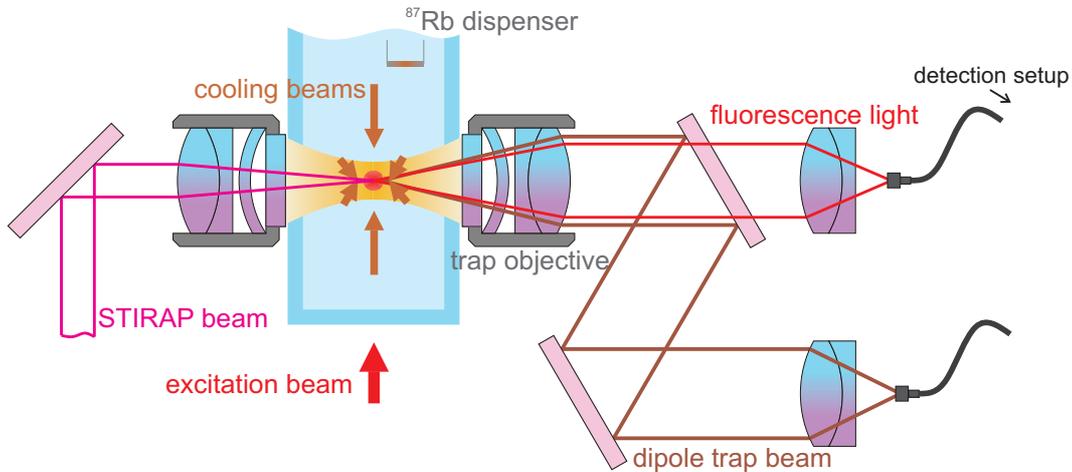
Figure 2.5.: Schematic of the trap setup. It shows the position of both microscope objectives relative to the glass cell which is attached to the UHV-chamber. It also shows the propagation axes of cooling (repump), dipole trap, atomic state readout (STIRAP) and excitation beams.

2.3.5. Optical Setup

The optical setup consists of two parts: The setup to trap and to manipulate the atom and the detection setup. Both setups are connected by a series of optical single mode fibers as discussed below.

Trap Setup

All components of the trap setup are located outside the vacuum chamber, and thus are easily accessible (see figure 2.5). The core of the setup is an objective (Linos HALO) with a numerical aperture of 0.38 and a working distance of $30\,\mathrm{mm}$ (trap objective). It focuses the dipole trap beam, and collects fluorescence light of the trapped atom thereby defining the quantization axis. The fluorescence light is coupled into a single mode fiber which guides the light directly to the detection setup. On the opposite side of the glass cell an identical objective is placed. It is used to focus the beams for the atomic state readout (see 2.4.2). The excitation laser shines through the front of the glass cell - orthogonally to the dipole trap beam. It is focused with a lens which has a focal length of $40\,\mathrm{mm}$. The other laser beams used for pumping and hyperfine detection are orthogonal to the excitation beams as well as to the dipole trap beam. They would shine through the plain of the schematic of figure 2.5, and are therefore not mentioned here.

Detection Setup

The main parts of the detection setup are four avalanche photo diodes (APD) (Laser Components Count-20C) which are able to detect single photons. They have an average dark count frequency of $9.5\,\mathrm{Hz}$ and a quantum efficiency of about 0.5. The total experimental dark count rate as well as the single photon detection probability of the setup is measured in section 2.5.

The detection setup also incorporates a $50:50$ single mode fiber beam splitter which combines the light of both experiments. Its input ports are directly attached to the fibers, which connect the detection setup with the trap setups, and it guides the light into its two output ports (port1 and port2)
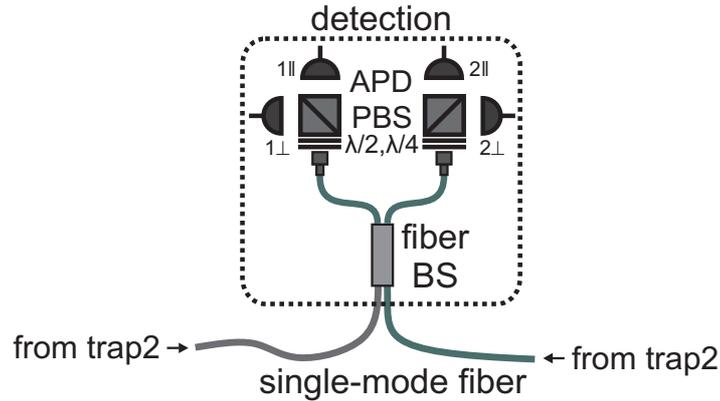
Figure 2.6.: Schematic of the detection setup. It shows the arrangement of the APDs and the polarization analysis as well as the fiber beam-splitter which later combines the light of both experiments.

(for a more detailed discussion see subsection 4.1.1). Behind both output ports of the beam splitter the polarization of the light is analyzed by a setup consisting of a polarizing beam splitter cube (PBS) and two APDs. A combination of a $\lambda/2$- and $\lambda/4$-waveplate placed in front of each PBS allows polarization analysis in arbitrary basis. Figure 2.6 shows a scheme of the detection setup.

2.3.6. Loading of a Single Atom into the Dipole Trap

In order to load a single atom into the dipole trap, the MOT and the dipole trap run simultaneously. The center of the MOT overlaps with the focus of the dipole trap. The MOT cools the atoms, and increases the atom density in the region of the dipole trap. Thus, it is possible to load single atoms from the MOT into the dipole trap. Once an atom enters the dipole trap, scattered light can be collected which leads to a step-like increase of the fluorescence count rate of the detectors (see figure 2.7). This is registered by the main experimental control program which switches off the MOT.

It is important that this realization of an optical dipole trap can trap only one atom at a time due to a collisional blockade effect [53, 48]. There is no need for an extra protocol to assure that only a single atom is trapped. The temperature of the trapped atom is $\sim 105\,\mu\text{K}$ Volz [45].

2.3.7. Polarization Alignment of the Setup

The photonic qubit is encoded in the polarization of the photon as already discussed in section 2.2. Therefore, it is inalienable that the polarization of an emitted photon is maintained until its analysis in the detection setup. Particularly, atom-atom entanglement experiments require minimal polarization errors in order to achieve a high entanglement contrast. Thus, all polarization errors have to be carefully compensated.

Generally, there are two kinds of polarization errors: Firstly, static polarization errors caused by the birefringence of the glass windows of the vacuum chamber or slight misalignments of the detection setup. Secondly, time variable polarization errors caused by the changing birefringence of the optical fibers and the fiber beam splitter combing both traps with the detection setup. The detection setup is aligned individually whereas the birefringence of the glass cell and the fibers are compensated together in both setups.
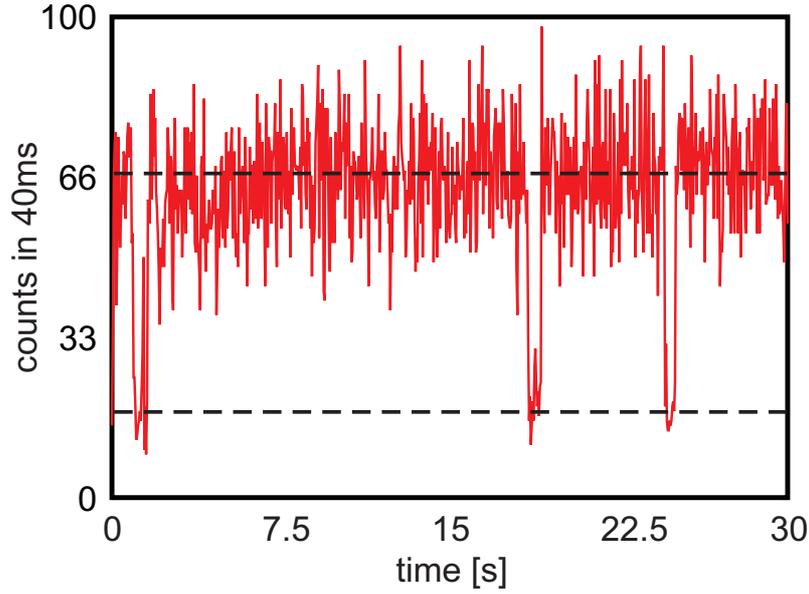
Figure 2.7.: Integrated count rate of single photon detectors. The average detector count rate is $\sim$ 1700 $counts/$s, if an atom is in the trap. There is a background count rate of $\sim$ 400 $counts/$s, if no atom is in the trap. The background count rate is caused mainly by reflections of the cooling beams on the glass cell. The graph demonstrates also the fast reloading, if an atom was lost and a long storage time of the atom inside the trap.

The short detection fiber of trap1 (5 m) and the fibers of the fiber beam splitter are relatively stable, and therefore compensated by hand such that the polarization of light is rotated by less than $1°$ on its way from the front of the glass cell of the vacuum chamber to one of the output ports of the fiber beam splitter. The long fiber connecting trap2 (30 m) to the fiber beam splitter is less stable, and thus its bire-fringence is compensated by a polarization control which runs with an automatic control algorithm. Due to its length the fiber has to be compensated every 5 minutes (a more detailed discussion of the compensation algorithm is presented here [54, 46]). All further polarization errors are compensated with the $\lambda/2$- and $\lambda/4$-waveplates in the detection setup with according to test measurements.

2.4. Entanglement Generation and Verification

This section discusses the experimental realization of APE generation and verification. The sequence required for entanglement generation is presented first, followed by the verification process which differs for both traps. Finally, the evolution of atom-photon correlations are discussed in case the basis, in which both qubits are analyzed, are rotated against each other.

2.4.1. Entanglement Generation

After registration of fluorescence due to an atom inside the dipole trap, the entanglement generation starts by optically pumping the atom into the state $5^2S_{1/2}, |F = 1, m_F = 0\rangle$. This is done by three different laser beams. The cooling- and the pump1-beam pump the atom to the state $|F = 1\rangle$ but without any preference of the Zeeman state $|m_F = 0\rangle$. For that reason an additional laser beam labeled pump2-beam is used. It is resonant to the transition $5^2S_{1/2}, |F = 1\rangle \rightarrow 5^2P_{3/2}, |F' = 1\rangle$ and
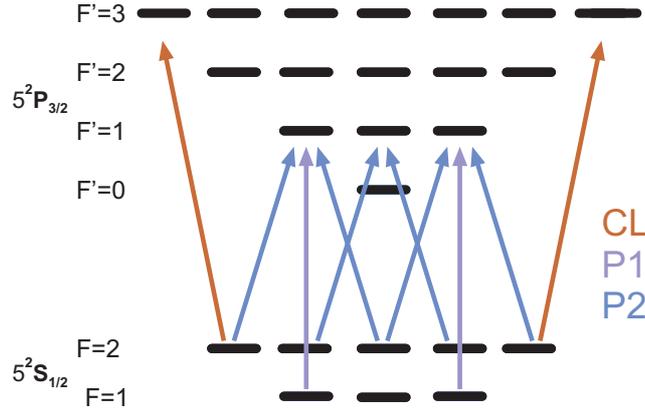
Figure 2.8.: Scheme of the pumping transitions: CL stands for the cooling beam, P1 stands for the pump1 beam and P2 stands for the pump2 beam.

π-polarized. Thus the state $5^2S_{1/2}, |F = 1, m_F = 0\rangle$ is a dark state for that laser beam. This laser combination allows efficient pumping of the atom into the desired state (see figure 2.8). The pumping takes about $6\,\mu\text{s}$ for the first pump process after a cooling period and about $4\,\mu\text{s}$ for all subsequent pump processes.

After the pumping process the atom is excited to the state $5^2P_{3/2}, |F' = 0, m_F = 0\rangle$ by an optical pulse. In the subsequent spontaneous decay the atom emits a single photon whose polarization is entangled with the Zeeman state of the atom (see 2.2). The photon is collected by the trap objective, and guided to the detection optics by a single mode fiber. The overall probability for detecting a single photon in a $120\,\text{ns}$ time-window after excitation is experimentally determined in subsection 2.5.1.

In this experiment the pumping and excitation procedure is repeated 20-times before the atom is cooled for $200\,\mu\text{s}$ in order to counteract heating, which occurs during the pumping process. This leads to a repetition rate of $50\,\text{KHz}$ (note that a normal pumping and excitation process takes $5740\,\text{ns}$). Figure 2.9 a) shows the timing of the pumping and excitation process. This procedure is repeated until the atom is lost, or a single photon is detected within the desired $120\,\text{ns}$ time-window after start of the excitation pulse. In this case the entanglement verification scheme is triggered by the photon signal.

2.4.2. Entanglement Verification

In order to verify entanglement the polarization of the photon as well as the spin of the atom must be analyzed.

Photon State readout

The analysis of the polarization state of the photon is performed by a PBS with subsequent photon detection by APDs. A PBS transmits horizontally polarized light, and reflects vertically polarized light. The APD behind each beam splitter output port detects single photons thereby projecting them onto a certain polarization state. A combination of a $\lambda/2$- and $\lambda/4$-waveplates in front of the PBS allows to select any desired basis for the analysis.
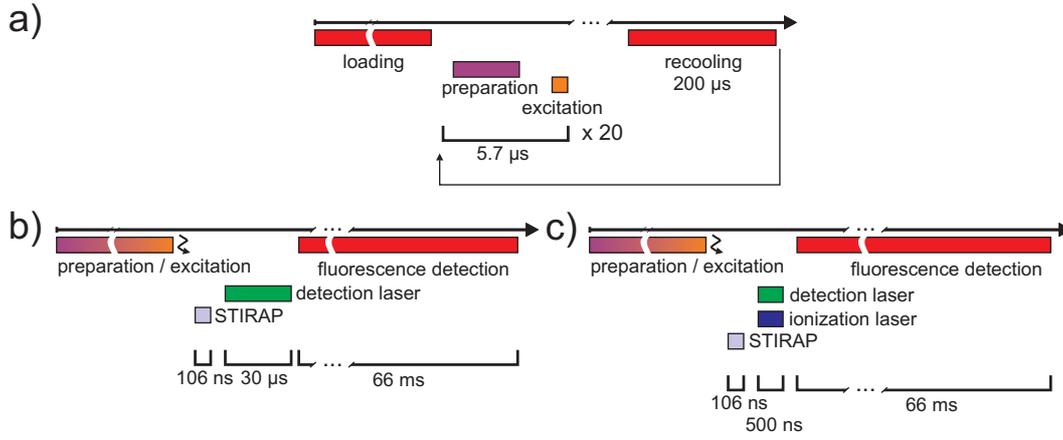
Figure 2.9.: Timing of laser beams: a) shows the timing of the preparation and excitation process as well as the cooling period which takes place after 20 atom excitations. b) shows the laser timing of the atomic state readout scheme of trap1. c) shows the laser timing of the atomic state readout scheme of trap2.

Atom State readout

The detection of the atomic spin state is triggered by the detection of a single photon in the $120\,\mathrm{ns}$ time-window after excitation. It is based on a scheme, in which the atom is pushed out of the dipole trap, if it is in a certain qubit state, and stays in the trap, if it is in the orthogonal state. This method makes use of the weak trapping potential of the dipole traps compared to ion traps, and consists of two steps:

Stimulated Raman Adiabatic Passage

The stimulated Raman adiabatic passage (STIRAP) transfers any chosen superposition of the qubit states $5^2 S_{1/2}, |F = 1, m_F = \pm 1\rangle$ to the $|F = 2\rangle$ hyperfine state [55, 56, 57]. The transfered superposition is hereafter referred to as bright state, and the orthogonal one, which stays in $|F = 1\rangle$, will be called dark state. The STIRAP is realized by two light fields (STIRAP1, STIRAP2). Each light field resonantly couples one hyperfine state to the same excited state $5^2 P_{1/2}, |F' = 1\rangle$ (see figure 2.10 a)) with the respective Rabi-frequencies Ω_1 and Ω_2. The Hamiltonian of this system can be written as

$$\mathcal{H} = \frac{\hbar}{2} \begin{pmatrix} 0 & \Omega_1 & 0 \\ \Omega_1 & 0 & \Omega_2 \\ 0 & \Omega_2 & 0 \end{pmatrix}. \tag{2.7}$$

The most interesting of the three eigenstates of this Hamiltonian is given by the following term:

$$|\Psi_1\rangle = \frac{1}{\sqrt{\Omega_1^2 + \Omega_2^2}} (\Omega_2 |F = 1\rangle - \Omega_1 |F = 2\rangle) \tag{2.8}$$

as it contains no contribution of the excited state $|F' = 1\rangle$. The population of the two states $|F = 1\rangle$ and $|F = 2\rangle$ in $|\Psi_1\rangle$ only depends on the two Rabi-frequencies. Note, the population of the $|F = 1\rangle$ depends of the STIRAP2 light flied coupling $|F = 2\rangle$ to the excited state and vise versa. Thus, by adiabatically switching on the STIRAP2 light flied and then adiabatically changing the ratio $\frac{\Omega_1}{\Omega_2}$ of both light fields from 0 to ∞, it is possible to transfer the population from $|F = 1\rangle$ to $|F = 2\rangle$ without populating the excited state.
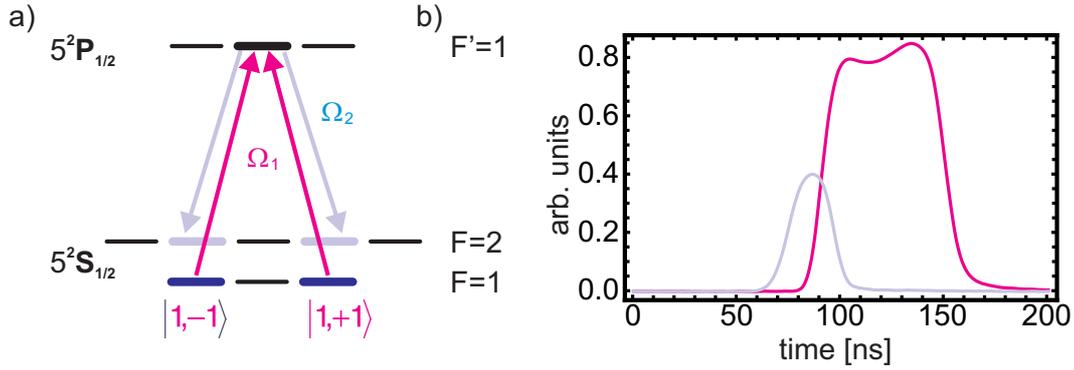
Figure 2.10.: a) Scheme for STIRAP transition: Ω_1 is resonant to the transition $5^2S_{1/2},|F=1\rangle\rightarrow 5^2P_{1/2},|F'=1\rangle$ and Ω_2 is resonant to the transition $5^2S_{1/2},|F=2\rangle\rightarrow 5^2P_{1/2},|F'=1\rangle$, respectively. b) Temporal shape of both STIRAP pulses. The relative peak intensity of both pulses is chosen such that both pulses have almost the same Rabi-frequency.

In this process the polarization of the STIRAP1 light field defines the dark state. The light polarization can be written as a superposition of σ^+ and σ^- polarization:

$$P_{S1} = \cos(\alpha)\sigma^+ + e^{i\phi}\sin(\alpha)\sigma^-, \tag{2.9}$$

This results in the atomic dark state:

$$|\Psi_D\rangle = \cos(\alpha)\,|F=1, m_F=+1\rangle + e^{i\phi}\sin(\alpha)\,|F=1, m_F=-1\rangle \tag{2.10}$$

The STIRAP light shines onto the atom from a direction opposite to the dipole trap, and thus parallel to the axis, in which the photons are collected, defining the quantization axis. The polarization of the light field is adjusted by a $\lambda/2$- and a $\lambda/4$-waveplate placed in front of the microscope objective which focuses the STIRAP light. An additional phaseplate compensates the birefringence of the glass cell. The temporal shapes of both STIRAP laser pulses used in this experiment are plotted in figure 2.10 b). The STIRAP1 pulse has a full width half maximum (FWHM) length of $60\,\mathrm{ns}$ and the STIRAP2 pulse of $25\,\mathrm{ns}$, respectively.

Hyperfine State Detection

Subsequently to the STIRAP follows the detection of the hyperfine state of the atom. Here, a laser pulse (detection laser, see figure2.3), which is resonant to the cycling transition $5^2S_{1/2},|F=2\rangle\rightarrow 5^2P_{3/2},|F'=3\rangle$, pushes the atom out of the dipole trap, if it is in the bright state. The momentum transfer of the photons from the laser beam shining onto the atom for $30\,\mu\mathrm{s}$ is sufficient to push the atom out of the trap. Thereafter, the cooling light is switched on again to check whether the atom has been pushed out or stayed in the trap. The cooling light shines onto the atom for about $60\,\mathrm{ms}$, which is long enough to distinguish by the integrated count rate of the single photon detectors whether the atom is still inside the trap or not (see figure 2.11).

The described scheme is used for all experiments with trap1. In the experiments with trap2 a newly developed , advanced method is used which is based on a state selective ionization of the atom. Here, a laser which is resonant to the transition $5^2S_{1/2},|F=2\rangle\rightarrow 5^2P_{3/2},|F'=3\rangle$ is used to excite the atom,
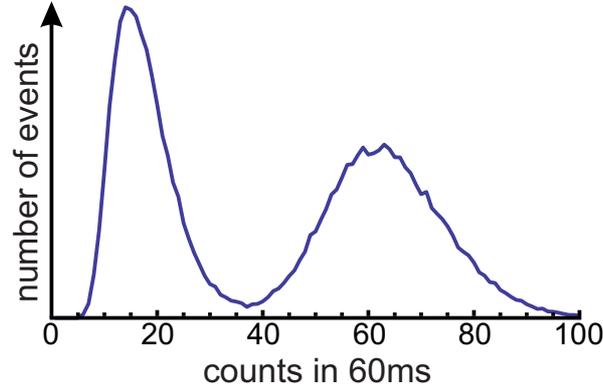
Figure 2.11.: Histogram of the fluorescence count-rate after STIRAP and hyperfine state detection. The peak centered around 15 counts consists of background counts and signals that the atom is not in the trap anymore. The other peak ,centered around 62 count, consists mainly of fluorescence counts and signals that the atom is still in the trap. The threshold discriminating between an atom in the trap or not is chosen to be at 38 counts.

and an additional laser at a wavelength of $445\,\mathrm{nm}$ ionizes it from the excited state. The ion can not be trapped by our laser system, and therefore will get lost. This scheme is much faster and more efficient than the conventional one. The ionization takes only $500\,\mathrm{ns}$, and is limited only by the power of the laser at $445\,\mathrm{nm}$. After ionization the procedure for fluorescence detection is applied like in trap1.

In this work the atom is always analyzed in linear basis. Therefore, it is sufficient to define the combination of STIRAP and hyperfine state as projection of the atom onto the state

$$\cos(\gamma)\left|\uparrow_x\right\rangle + \sin(\gamma)\left|\downarrow_x\right\rangle, \tag{2.11}$$

where γ is the angle of linear polarization of the STIRAP light flied, which defines the measurement basis. Note, the angle of the corresponding orientation of the atomic spin is 2γ. The combination of STIRAP and hyperfine state detection allows a high-fidelity atomic state read out, and in combination with the photon state readout a high-fidelity atom-photon entanglement verification.

2.4.3. Atom-Photon Correlations

In order to verify the entanglement atom-photon correlations are measured by keeping the photon state measurement basis constant and rotating the $\lambda/2$- waveplate which defines the atom state measurement basis. The detection optics behind both output ports of the fiber beam splitter analyzes the photon state in two different bases. Correlations between the orientation of the atomic spin and the photon spin are observed by registering event numbers $N_{SS'}^{(\gamma,\delta)}$, where S, S' are the eigenstates of the atom and photon spin along their individual measurement directions which are defined by $\gamma = 2\beta$ (atom) and δ (photon). Thus, the measured correlation probabilities $cp = \frac{1}{N}(N_{\uparrow\uparrow}^{(\gamma,\delta)} + N_{\downarrow\downarrow}^{(\gamma,\delta)})$ and anti-correlation probabilities $acp = \frac{1}{N}(N_{\uparrow\downarrow}^{(\gamma,\delta)} + N_{\downarrow\uparrow}^{(\gamma,\delta)})$ of the entangled state have following evolution:

$$cp = \frac{1}{2}(1 + V\cos(2(\gamma - \delta))), \tag{2.12}$$

$$acp = \frac{1}{2}(1 + V\cos(2(\gamma - \delta + 90^\circ))), \tag{2.13}$$
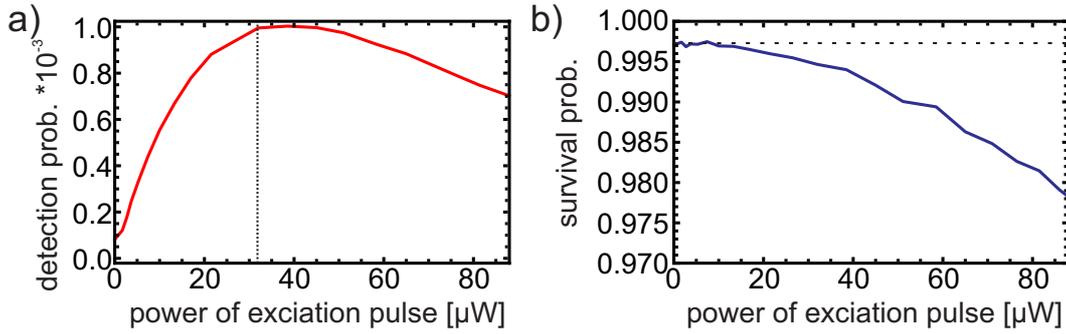
Figure 2.12.: a) shows the probability to detect a photon after an excitation attempt as a function of the power of the excitation laser pulse. The chosen power is $32\,\mu$W (dotted line). b) shows the survival probability for the atom in the trap after illumination with the detection laser, which gives information about the ratio of off-resonant excitations.

where V is the visibility of the entangled state.

2.5. Experimental Results

In this section the ideal power of the pulse exciting the atom and the resulting single photon detection probability after an excitation attempt are experimentally determined as well as the dark count probability of the detectors which derogates all further measurements. Finally data are presented which prove the generation of high fidelity atom-photon entanglement in both experiments.

2.5.1. Single Photon Detection Probability after an Excitation Attempt

In order to determine the single photon detection probability after an excitation attempt, the experiment is run as described above (see subsection 2.4.1), but with the STIRAP beams blocked. The detection laser is used to identify whether the atom decayed to the state $|F = 1\rangle$ or to $|F = 2\rangle$. This allows the estimation of the ratio of off-resonant excitation. During the measurement the maximal power of the excitation pulse is varied from $0.1\,\mu$W to $88\,\mu$W (measured outside the glass cell), and the single photon detection probability is registered for each setting. Graph 2.12 a) shows the measured photon detection probability per excitation trial as a function of the maximal power of the excitation light. The detection probability rises until the excitation pulse has a maximal power of $38, 5\,\mu$W. At this point the probability to detect a single photon after a excitation attempt is $p_{ph}^s = n_{ph}^s/n_{ex}^s = 1 \cdot 10^{-3}$, where the n_{ph}^s is the number of detected photons at measurement setting s and n_{ex}^s is the number of excitation pulses at the same setting. Thereafter, the probability gets smaller again. This is mainly caused by Rabi-oscillations reducing the population of the excited state. The maximal power of the excitation beam is chosen to be $32\,\mu$W in all further experiments as a compromise between excitation probability and unwanted effects like off-resonant excitation which occur at higher powers as shown in the next passage. This excitation power results in a detection probability of $p_{ph}^{32\mu W} = 0.995 \cdot 10^{-3}$.

Off-resonant excitations to higher excited states have to be avoided as it would lead to spurious emission of photons which are not entangled with the atom in the desired way. The direct excitation $5^2S_{1/2}, |F = 1, m_F = 0\rangle \rightarrow 5^2P_{3/2}, |F' = 1, m_F = 0\rangle$ is forbidden by selection rules, but due to imperfect pumping off-resonant excitation via the transition $5^2S_{1/2}, |F = 1, m_F = \pm1\rangle \rightarrow 5^2P_{3/2}, |F' = 1, m_F = \pm1\rangle$ is possible. Excitation to the state $|F' = 2\rangle$ is also possible although with a
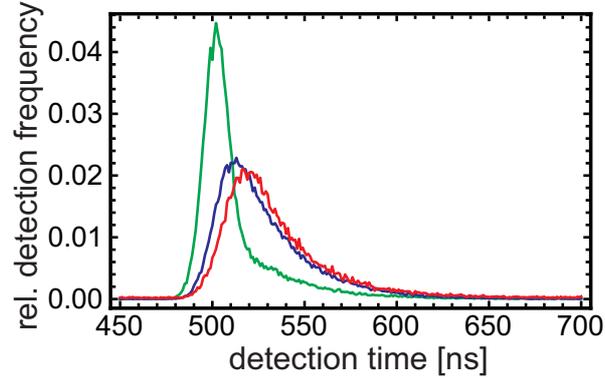
Figure 2.13.: Histogram of the photon detection times for three different power of the excitation laser pulse: $1.7\,\mu\mathrm{W}$ (red), $32\,\mu\mathrm{W}$ (blue) and $88\,\mu\mathrm{W}$ (green). The areas of the histograms are each normalized to 1.

..

smaller probability due to larger detuning. If the atom is excited to the state $5^2P_{3/2}, |F' = 1\rangle$ via the described transition, it may decay to the state $|F = 2\rangle$ instead of $|F = 1\rangle$ with a probability of 0.12. By removing the atom from the trap using the detection laser, the relative probability of this process can be estimated. Graph 2.12 b) shows a measurement of the survival probability of the atom inside the trap after detection of a single photon over the maximal power of the excitation pulse. This allows calculation of the probability of off-resonant excitation for low powers of the excitation pulse. At high excitation powers the off-resonant excitation to higher excited states increases changing also the probability for a decay to the state $|F = 2\rangle$ instead to $|F = 1\rangle$.

In graph 2.12 b) the survival probability is not 1, even for small powers of the excitation laser. This is not caused by off-resonant excitation but by the finite probability to loose the atom during the excitation or detection process due to heating or collision with background gas. Thus, the loss probability $p_l^{0.1\mu\mathrm{W}} = 0.003 \pm 0.0003$, which is measured for a maximal power of the excitation pulse of $0.1\,\mu\mathrm{W}$, can be subtracted. The chosen power of the excitation laser of $32\,\mu\mathrm{W}$ has already a probability for off-resonant excitation of 0.02. At higher powers the probability for off-resonant excitation would rise considerably without significant gain of the single photon detection probability after an excitation attempt.

The maximal power of the excitation laser pulse also influences the relative, time depended probability to detect a photon. In a first approximation this can be interpreted as the shape of the photon wave packed. Histograms of the time dependent detection frequency of single photons are plotted in graph 2.13 for measurements with three different powers of the excitation laser pulse. For a maximal power of $1.7\,\mu\mathrm{W}$ the rising edge is less steep than for higher powers due to the smaller Rabi-frequency. The falling edge is determined by the exponential decay of the excited state. The histogram for a maximal power of the excitation laser pulse of $32\,\mu\mathrm{W}$ has a steeper rising edge, while the falling edge is still determined by the exponential decay of the excited state, which means that the population of the excited state is not reduced by Rabi-oscillations. This occurs for a maximal power of the the excitation pulse of $88\,\mu\mathrm{W}$. Here, the rising edge is the steepest but the excitation pulse also reduces the population of the excited state again due to Rabi-oscillations, and thus reduces the overall excitation probability.

APD	dark count probability $p_{dc}^i \cdot 10^{-6}$,
$APD_{1\perp}$	0.882 ± 0.016
$APD_{1\parallel}$	0.374 ± 0.011
$APD_{2\perp}$	1.551 ± 0.021
$APD_{2\parallel}$	0.886 ± 0.016

Table 2.1.: Probability p_{dc}^i (with $i \in \{1 \perp, 1 \parallel, 2 \perp, 2 \parallel\}$) to detect a dark count in the $120\,\text{ns}$ time window after an excitation trial for all detectors. The overall dark count probability within a single detection window is $p_{dc} = (3.69 \pm 0.03) \cdot 10^{-6}$.

2.5.2. Dark Counts

In order to measure the dark count probability in the $120\,\text{ns}$ time window, in which a single photon is expected, the experimental scheme described above is used, but the atom state readout is skipped and the excitation light is blocked. This way the experimental probability to detect a dark count after an excitation attempt can be estimated which includes all contributions from residual errors like light from the pumping process. The probability to detect a dark count in this time window is listed in table 2.1 for each detector. The overall dark count probability of $p_{dc} = {}^{n_{dc}}/n_{ex} = (3.69 \pm 0.03) \cdot 10^{-6}$, where n_{dc} is the number of detection events in the time window, is more than two orders of magnitude lower than the single photon detection probability per excitation attempt (see 2.5.1). Therefore, it has only minimal effect on atom-photon entanglement fidelity but is still important in the experiments which are described in the following chapters.

2.5.3. Atom-Photon Entanglement

In this section the experimental verification of atom-photon entanglement (APE) in both setups is presented. The data demonstrate that high APE visibilities (peak-to-peak amplitude of a atom-photon correlation measurement) with minimal phase shifts can be generated on demand.

After the entanglement is generated as described in subsection 2.4.1, atom-photon correlations are measured by keeping the photon state measurement basis constant and rotating the $\lambda/2$- waveplate which defines the atom state measurement basis (see subsection 2.4.3). The waveplate is rotated by an angle $\beta = 0°...90°$ in steps of $5.625°$. The detection optics behind both output ports of the fiber beam splitter analyzes the photon state in two different bases: the H/V-basis ($\delta = 0°$) and the P/M-basis ($\delta = 45°$), respectively. In order to minimize polarization errors in the photon analysis, all errors have been carefully compensated as describes in subsection 2.3.7.

The experimental results for entanglement verification are presented in figure 2.14 a) for trap1 and in figure 2.14 b) for trap2, respectively. Here, the photons behind port2 of the fiber beam splitter are analyzed in the H/V-basis and behind port1 in the P/M-basis. Thus, entanglement was analyzed in two bases in one measurement. The correlation measurements of trap1 (trap2) show a visibility of $V_2^{(0°)} = 0.867 \pm 0.008$ ($V_2^{(0°)} = 0.903 \pm 0.005$) in the H/V-basis and of $V_1^{(45°)} = 0.872 \pm 0.007$ ($V_1^{(45°)} = 0.891 \pm 0.006$) in the P/M-basis, respectively. The residual phase shifts caused by polarization errors are $0.26 \pm 0.43°$ ($2.66 \pm 0.26°$) in the H/V-basis and $0.35 \pm 0.33°$ ($1,53 \pm 0.26$) in the P/M-basis. The phase shift of trap2 can be further minimized by rotating the STIRAP waveplate of trap2.

Note, all measurements on both traps are performed with the same photon detection setup. For the verification of entanglement in trap2 the photons are guided to the detection optics via a fiber with a length of $30\,\text{m}$ (for more information see section 4.5). Note that these visibilities are measured
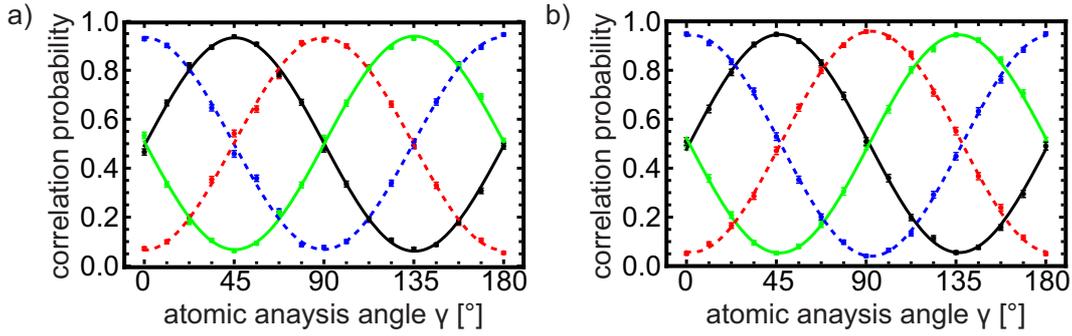
Figure 2.14.: Verification of entanglement in both traps. The graphs show the measured correlation and anti-correlation probabilities in the H/V-basis p_c (black), p_{ac} (yellow), and the P/M-basis p_c (blue, dashed lines), p_{ac} (red, dashed lines) as a function of the respective atomic analysis angle γ. a) Verification of entanglement in trap1. The visibilities are of $V_2^{(0°)} = 0.867 \pm 0.008$ in the H/V-basis and of $V_1^{(45°)} = 0.872 \pm 0.007$ in the PM-basis, respectively. b) Verification of entanglement in trap2. The visibilities are of $V_2^{(0°)} = 0.903 \pm 0.005$ in the H/V-basis and of $V_1^{(45°)} = 0.891 \pm 0.006$ in the PM-basis, respectively

under the same conditions as the later presented atom-atom entanglement visibility. In particular, any reduction of the visibilities because of finite coherence of the entangled states contribiutes in the exact same amount to the atom-photon entanglement visibilities as to the atom-atom entanglement visibility measured in the following. The time between the single photon emission and the atom state readout is the same for all these measurements. Any further information about the coherence of the entangled state is given in [54].

2.6. Summary

In this chapter the generation and verification of atom-photon entanglement in two different setups was characterized. The experimental generation and verification of entanglement was illustrated, and finally experimental results were displayed which show high correlation visibilities. The average visibility of trap1 is $V_a = 0.87$ and of trap2 $V_a = 0.897$, respectively. These results prove that APE can be reliably generated in both operating traps, and is ready for use in the following experiments.

3. An Atom as a Pulsed Single Photon Source

The two-photon interference and atom-atom entanglement experiments to be presented in the oncoming chapters of this thesis ideally require photon sources which emit only a single photon at a time. The single atom, used in this experiment, is in principle a perfect single photon source. It emits a single photon during its spontaneous decay from an excited state to a ground state, and can not emit a second photon before it is re-excited. In a previous work this characteristics was proven for the introduced experimental setting [44]. However, a later demonstration of two-photon quantum interference and atom-atom entanglement imposes additional and more strict specifications for the single photon source (see chapter 4 and 5). The photons have to be emitted via a certain decay path as described in chapter 2, and in addition only one photon must be emitted within a $120\,\mathrm{ns}$ time window after atom excitation.

Until now, single photon emission has been demonstrated for many different sources. It was demonstrated for atoms [58] and ions [59] as well as for bulk sources like N/V-centers in diamond [60], quantum-dots [61] and molecules [62]. Single photon sources are most important for many quantum communication protocols [17, 63] as well as for many quantum cryptography protocols [64].

On the following pages detection-time statistics of photons emitted by a single atom are investigated in order to estimate the quality of this pulsed single photon source. In addition theoretical descriptions of all main causes of two-photon emission are included. All data presented in this chapter is based on measurements with trap1, but the results are also valid for trap 2, due to the fact that both setups are identical in all relevant aspects.

3.1. Pulsed Atom Excitation and Photon Emission

As already mentioned in chapter 2.2, in this experiment entanglement is generated between the spin of an atom and the polarization of a spontaneously emitted photon. Therefore, the atom has to be excited to the state $5^2 P_{3/2}, |F' = 0,\, m_F = 0\rangle$ by a laser pulse, before it decays to the ground state, and entanglement is generated due to coherent superposition of two possible decay channels. This scheme uses a pulsed atom excitation in order to avoid multiple excitations.

A pulsed atom excitation also provides a timing signal which allows the determination of the detection time of the emitted photon relative to the excitation attempt. This is most important for it allows the computation of histograms which show the normalized detection frequency of photons against the detection time (see figure 2.13). These histograms correspond to the temporal distribution of the detection probability of the single photon wave packet, if only a single photon is emitted per excitation attempt. The length of the photon wave packet is defined by the length and power of the excitation pulse and the lifetime of the excited state. The detection probability for the single photon wave packet can also be computed, in case the temporal shape of the excitation pulse is known which is fundamental for many further calculations.

In this experiment the excitation pulse has an almost Gaussian shape, mainly defined by the time response of the employed acousto-optic-modulator (AOM) (see figure 3.1 a) (red)). The bandwidth
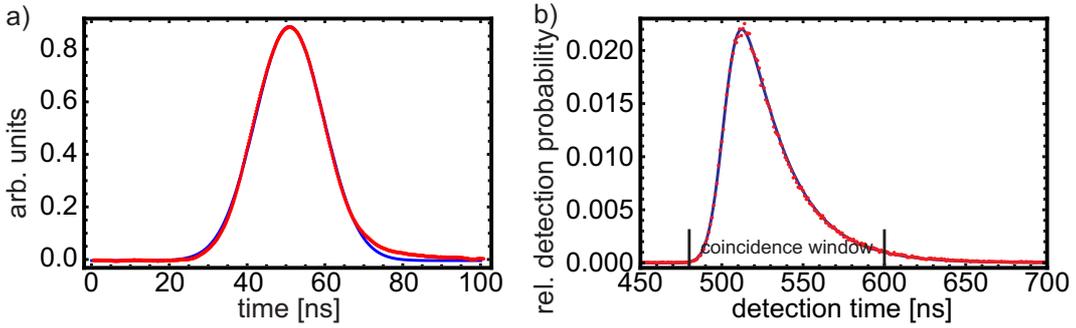
Figure 3.1.: Excitation pulse and detection time histogram: a) temporal shape of the optical excitation pulse measured by a fast photodiode (red) and the fitted Gaussian pulse used in calculations (blue). b) normalized histogram of the photon detection times (red dots) which corresponds to temporal distribution of photon detection probability which is calculated and fitted to the histogram (blue line).

of the driving electric signal is slightly decreased by a $10.7\,\text{MHz}$ low pass filter accentuating the Gaussian-like shape of the optical pulse. The optical excitation pulse has a full width half maximum length (FWHM) of $21.65\,\text{ns}$. The stated length is derived by fitting a Gaussian to the temporal shape of the pulse (see figure 3.1 a) (blue)).

The knowledge of the temporal shape and power of the excitation pulse and of the atomic properties of ^{87}Rb allows calculations of the temporal distribution of the photon detection probability using Liouville equations (see appendix F). By using only the intensity of the excitation pulse at the location of the atom and its delay to the trigger pulse, the calculated photon detection probabilities can be fitted to the normalized histogram of the photon detection times. The result is plotted in figure 3.1 b). It provides a delay of the center of the excitation pulse to the trigger of $t_0 = 501.9 \pm 0.1\,\text{ns}$ and a maximal pulse power of $lp = 14.58 \pm 0.09\,\mu\text{W}$ (these values are regarded as given in all further calculations).

The estimated value of the maximal power of the excitation pulse is smaller than the measured value of $32\,\mu\text{W}$ (see subsection 2.5.1). The difference is caused by reflections at the glass cell and the fact that the waist of the laser beam is not exactly known at the location of the atom.

3.2. Two-Photon Emission

If an excitation pulse is not extremely short compared to the lifetime of the excited state, there is a finite probability that the atom has already decayed to the initial state while the excitation pulse is still present. In that case it might get excited a second time, and thus more than just one photon per excitation pulse is emitted and detected. These *two-photon emission events* can not be distinguished from photon coincidence detections caused by two atoms, each emitting a single photon. Therefore, two photon emission events must be avoided in two-photon interference experiments.

In this experiment the FWHM of the excitation pulse ($21.65\,\text{ns}$) is of the same order of magnitude as the lifetime of the excited state of the atom ($26.23\,\text{ns}$) which causes a non-negligible probability of two-photon emission events. Shorter pulses can not be applied because the Fourier broadening of the spectrum of the excitation pulse would lead to a higher rate of off-resonant excitations. This would reduce the atom-photon entanglement fidelity, because the photons would not originate from the described λ-decay scheme (see subsection 3.2.2). Longer pulses would increase the probability for emis-
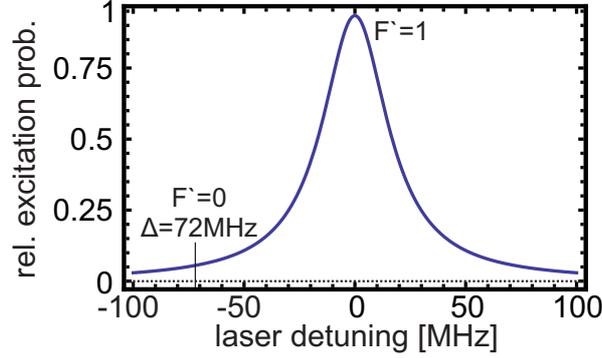
Figure 3.2.: Relative excitation probability of excited state $5^2P_{3/2}, |F' = 1\rangle$ for cw-excitation over the detuning of the excitation laser. It is possible to excite this state by laser light resonant to the transition $5^2S_{1/2}, |F = 1, m_F = \pm1\rangle \rightarrow 5^2P_{3/2}, |F' = 0\, m_F = 0\rangle$ due to a residual overlap of the Lorenz profile of the excited state and the laser wavelength of ~ 0.07.

label	detector combinations	
$D+$	$APD_{1\perp}$ and $APD_{1\|}$	$APD_{2\perp}$ and $APD_{2\|}$
$D-$	$APD_{1\perp}$ and $APD_{2\|}$	$APD_{1\|}$ and $APD_{2\perp}$
$D\varnothing$	$APD_{1\|}$ and $APD_{2\|}$	$APD_{1\perp}$ and $APD_{2\perp}$

Table 3.1.: This table shows certain detector combinations which are summarized under new labels for easy reference in the oncoming chapters.

sion of a second photon via the transition $5^2S_{1/2}, |F = 1, m_F = \pm1\rangle \rightarrow 5^2P_{3/2}, |F' = 1\, m_F = \pm1\rangle$ due to the residual overlap of the excited state with the central wavelength of the excitation pulse (see figure 3.2). Long pulses also increase the probability of excitation via the transition $5^2S_{1/2}$, $|F = 1, m_F = \pm1\rangle \rightarrow 5^2P_{3/2}, |F' = 0\, m_F = 0\rangle$ due to imperfections in the excitation pulse polarization (see subsection 3.2.1). The chosen excitation pulse length is a compromise between both effects, which minimizes direct off-resonant excitations (see figure 2.12 b)), but can not exclude all two-photon emission events.

Two-photon emission events are detected as two-photon coincidences within a $120\,\mathrm{ns}$ time window with a set of four APDs (see figure 2.6). There are six different combinations, in which the two photons can impinge on different detectors, and thereby be both detected. The six combinations can be further summarized into three pairs of detector combinations ($D+$,$D-$ and $D\varnothing$) listed in table 3.1, which become important, if the arrangement is used for Bell-state measurements. The first two of these detector combinations $D+$ and $D-$ correspond each with a projection of two interfering photons onto a Bell-state, whereas the detector combinations $D\varnothing$ don't correspond to any Bell-state projection as will be discussed in chapter 4. The four detectors are not photon number resolving. Events, at which both photons impinge on the same detector, can not be registered.

The following subsections describe the main types of two-photon emission events.
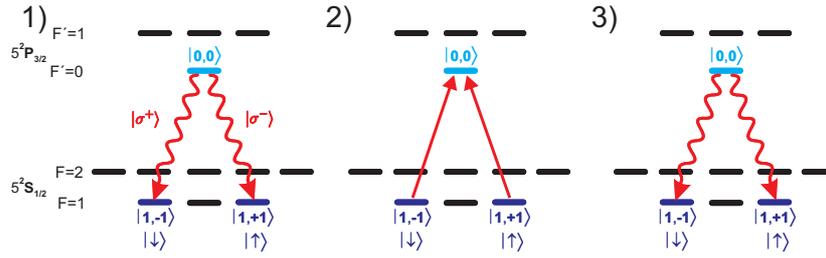
Figure 3.3.: Two-photon emission due to imperfect alignment of the polarization of the excitation light (type I). 1) shows the spontaneous decay of the atom after first excitation and generation of atom-photon entanglement. 2) shows the second excitation due to the residual components of wrong polarization of the excitation light and 3) shows the second spontaneous decay of the atom via the same transition as the first decay. Here, the photon might also be π-polarized. This decay is not considered.

3.2.1. Two-Photon Emission due to Imperfections of the Polarization of the Excitation Light (type I)

One of the two main reasons for two-photon emission events is a imperfect alignment of the polarization of the excitation beam. This is caused by birefringence of the glass-cell and errors in the angle of incidence of the excitation beam. Consequently, it is not perfectly orthogonal to the quantization axis. These polarization errors enable the transitions $5^2S_{1/2}, |F = 1, m_F = \pm 1\rangle \rightarrow 5^2P_{3/2}, |F' = 0\,m_F = 0\rangle$, and thereby the possibility to excite the atom a second time (see figure 3.3). This second excitation excites the atom to the very same state as the first excitation, and the atom decays a second time via the same decay channels. Therefore, entanglement between the second photon and the atom is generated, if the second photon is not π-polarized. The probability for emission of a π-polarized photon after the second excitation is $1/3$ and given by the Glebsch-Gordan coefficients.

At this kind of two-photon emission the probability for a second excitation depends on the polarization of the first photon. Only if the atom decays into a state, which can be excited by the polarization of the excitation light, a second excitation becomes possible. Therefore, the two photons show polarization dependent correlations. In at least one basis of photon analysis there should be an unequal distribution of two-photon coincidences. However, these correlations do not change the statistics of $D-$, $D+$ and $D\varnothing$. A combination of detectors, which shows less coincidences, is always combined with a combination, which shows more of coincidences. This equal distribution is further referred to as *white noise*.

Calculations with a quantum jump model based on optical Liouville equations (see appendix F) can predict the probability of emitting two not π-polarized photons by this type of two-photon emission event with respect to the ratio of polarization errors. As example: If the polarization is linearly rotated by $1°$, the possibility to emit a second photon, if a first one has already been emitted, is $p_{\text{tp}-\text{I}} = 0.0025$.

3.2.2. Two-Photon Emission due to Off-Resonant Excitation (type II)

The second main cause for two-photon emission events is an off-resonant excitation via the transition $5^2S_{1/2}, |F = 1, m_F = \pm 1\rangle \rightarrow 5^2P_{3/2}, |F' = 1\,m_F = \pm 1\rangle$ after the first decay (see figure 3.4 1) and 2)). Due to the small distance of only $72\,\text{MHz}$ between the levels $|F' = 0\rangle$ and $|F' = 1\rangle$ and the Lorentzian shape, there is a non negligible overlap between the level $|F' = 1\rangle$ and the Fourier broad-
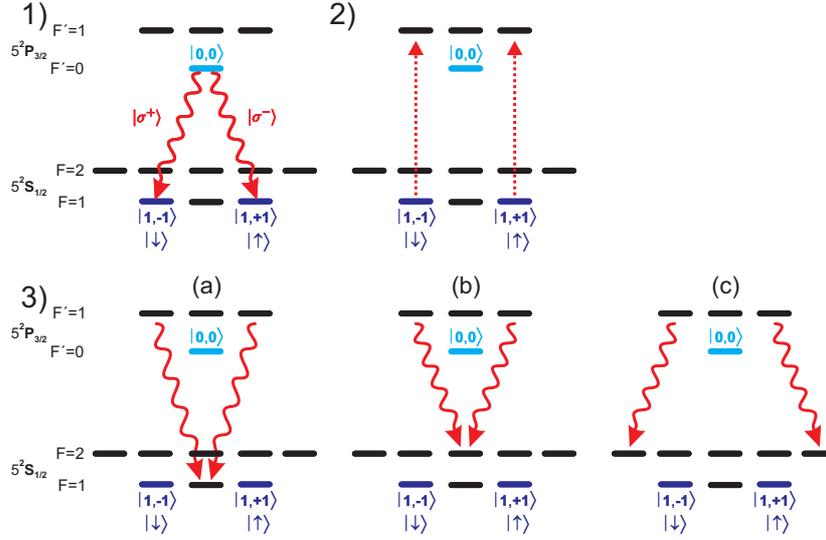
Figure 3.4.: Two-photon emission via off-resonant excitation (type II). 1) shows the spontaneous de-
cay of an atom after first excitation and generation of atom-photon entanglement. 2)
shows the second off-resonant excitation to the state $|F' = 1\rangle$. 3) shows the second
spontaneous decay of the atom. The decays, where a π-polarized photon is emitted,
are not considered. a) shows the decay to the state $|F = 1\rangle$. The two emitted photons
form an entangled state $|\Psi^+\rangle_{tp}$. b) shows the decay to the state $|F = 2, m_F = 0\rangle$. The
two emitted photons form an entangled state $|\Psi^-\rangle_{tp}$. c) shows the decay to the states
$|F = 2, m_F = \pm 2\rangle$. Here the photons form a partially mixed state $\hat{\rho}_{tp}$.

ened excitation pulse, which results in the possibility to excite the atom a second time (see figure
3.2).

After the second excitation the atom decays to the $|F = 1\rangle$ or the $|F = 2\rangle$ ground state, thereby
emitting a not π-polarized photon with a probability of $8/15$ determined by Clebsch-Gordan coeffi-
cients. If the two emitted photons are both not π-polarized, they form different two-photon states
depending on the decay channel of the atom. The relative probabilities of these two-photon states are
also determined by Clebsch-Gordan coefficients. Their full derivation is shown in appendix C. The
three two-photon states are the following:

a)   With a probability of $p_a = 0.781$ the atom decays into the state $5^2S_{1/2}, |F = 1, m_{F'} = 0\rangle$
(see figure 3.4 3 a)). Here, the two photons form a polarization entangled state. Note,
a photon scattered this way has the same center frequency as the photon emitted in the
regular λ-decay - although the transition itself has another center frequency.

$$|\Psi^+\rangle_{tp} = \frac{1}{\sqrt{2}}(|R\rangle_1|L\rangle_2 + |L\rangle_1|R\rangle_2)$$
$$= \frac{1}{\sqrt{2}}(|H\rangle_1|H\rangle_2 + |V\rangle_1|V\rangle_2).$$

b)   With a probability of $p_b = 0.031$ the atom decays into the state $5^2S_{1/2}, |F = 2, m_{F'} = 0\rangle$
(see figure3.4 3 b)). In this case both photons form an entangled state, which is orthogonal
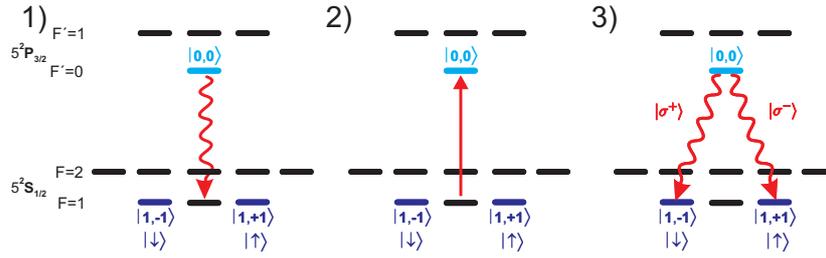
Figure 3.5.: Two photon due to a first decay into the initial state (type III). 1) shows the sponta-
neous decay of the atom into the initial state $5^2P_{3/2}, |F = 1\, m_F = 0\rangle$ and the emission
of a π-polarized photon which can not be detected by our detection setup. 2) shows the
second resonant excitation via the transition as the first excitation. 3) shows the sec-
ond instantaneous decay of the atom to the states $5^2P_{3/2}, |F = 1\, m_F = \pm 1\rangle$, thereby
generating atom-photon entanglement. Here, the atom might also decay to the state
$5^2P_{3/2}, |F = 1\, m_F = 0\rangle$. This decay is not considered in the figure.

to the first one due to opposite sign of the Clebsch-Gordan coefficients.

$$
\begin{aligned}
|\Psi^-\rangle_{tp} &= \frac{1}{\sqrt{2}}(|R\rangle_1|L\rangle_2 - |L\rangle_2|R\rangle_2) \\
&= \frac{1}{\sqrt{2}}(|H\rangle_1|V\rangle_2 - |V\rangle_1|H\rangle_2).
\end{aligned}
$$

c)   Finally, with a probability of $p_c = 0.188$ the atom decays into one of the two states
$5^2S_{1/2}, |F = 2, m_{F'} = \pm 2\rangle$ and a partially mixed state is formed (see figure 3.4 3 c))

$$
\hat{\rho}_{tp} = \frac{1}{2}|L\rangle_1|L\rangle_2\langle L|_1\langle L|_2 + \frac{1}{2}|R\rangle_1|R\rangle_2\langle R|_1\langle R|_2.
$$

These considerations predict that coincidence detections caused by these two-photon emission events
have different probabilities for the detector combinations $D+,D-$ and $D\varnothing$, if analyzed in different
photon measurement basis. This effect is further referred to as *colored noise*. Calculations with the
quantum jump model (appendix F) show that in case a first photon has already been emitted, a second
not π-polarized photon is expected to be emitted due to off-resonant excitation with a probability of
$p_{tp-\mathrm{II}} = 0.0048$. This is on the same order of magnitude than the two-photon emission events caused
by an imperfect adjustment of the polarization of the excitation light.

3.2.3. Two-Photon Emission due to a first Decay into the Initial State (type III)

Events, where the atom decays to the ground state $5^2P_{3/2}, |F = 1\, m_F = 0\rangle$ and thereafter is excited
again via the same transition like the first time, never cause coincidence detections because the first
photon is π-polarized, and can not be detected by the detection optics (see figure 3.5). Still, they
significantly decrease the two-photon interference contrast as shown in detail in chapter 4. However,
they do not decrease the atom-photon entanglement fidelity because the detectable second photon is
perfectly entangled with the atom. This effect is the by far most common two-photon emission event.
Calculations show that the probability for detecting a photon emitted this way instead of a single
photon event is $p_{\mathrm{tp-III}} = 0.052$.

3.2.4. Two-Photon Coincidences Caused by Dark Counts

A detection event, where a single photon and a detector dark count appear in the same time window, is not a two-photon event in the common sense, but can not be distinguished in experiment from any other coincidence detection, and like other two-photon emission events it also decreases the two-photon interference contrast. The probability to detect such an event can be derived from the dark count rate of each detector p_{dc} (see table 2.1) and their individual single photon detection probability after an excitation attempt p_{ph}. It can be calculated by the following expression for any detector combination:

$$p_{dce}^{ij} = p_{dc}^i p_{ph}^j + p_{dc}^j p_{ph}^i, \tag{3.1}$$

where $i \neq j$ and $i, j \in \{1 \perp, 1 \parallel, 2 \perp, 2 \parallel\}$ stand for the different detectors.

The single photon detection probability varies for every measurement caused by a slightly different overlap of detection fiber and dipole trap and by a varying coupling efficiency of the light into the detectors. Therefore, the dark count caused coincidence detection probability is calculated for every measurement separately taking into account the actual single photon detection probability. It is on the same order of magnitude as the two-photon emission probability of events of type I and II, and almost the same for all classes of detector combinations ($D+$, $D-$, $D\varnothing$). Detection events with two dark counts but no photon are negligible.

3.3. Characteristics of a Pulsed Single Photon Source

The quality of a pulsed single photon source is best ascertained by determining the probability to emit more than one photon per excitation attempt. This is done by measuring correlations of photon detection times. In such a measurement the atom is excited in a pulsed way, and photons in a fixed $120\,\mathrm{ns}$ time window after the excitation pulse are registered. The detection time difference of each two-photon coincidence is calculated with respect to that data for each detector combination resulting in histograms, which display the detection time differences of all coincidences. Such histograms show multiple peaks at constant intervals. The middle peak of each histogram (henceforth labeled $peak = 0$) gives the number of two fold coincidences after an excitation pulse. The two neighboring peaks then give the number of events where the event in detector i is registered before ($peak = -1$) or after ($peak = +1$) the one in detector j. The distance between these peaks corresponds to the repetition rate of the excitation pulse.

The number of coincidences in a given detector combination i, j $n_{\pm 1}^{ij}$ (with $i \neq j$ and $i, j \in \{1 \perp, 1 \parallel, 2 \perp, 2 \parallel\}$), where the two photons originate from subsequent excitation attempts, is given by

$$n_{\pm 1}^{ij} = (\eta^i p_{1st} \cdot \eta^j p_{1st} + \eta^j p_{1st} \cdot \eta^i p_{1st}) n_{ex}, \tag{3.2}$$

where n_{ex} is the overall number of atom excitation attempts, η^i and η^j are the detection efficiencies for a detection in detectors i and j, respectively (including all coupling losses and losses at other optical devices) and p_{1st} is the probability to emit a single photon. In this term contributions of two-photon emission events are neglected.

The number of coincidences in a certain detector combination i, j n_0^{ij}, at which both photons originate from the same excitation attempt, is given by the following equation:

$$n_0^{ij} = (\eta^i p_{1st} \cdot \eta^j p_{2nd}^j + \eta^j p_{1st} \cdot \eta^i p_{2nd}^i) n_{ex}, \tag{3.3}$$

where p_{2nd}^i and p_{2nd}^j are the probabilities to emit a second photon within the same time-window as the first photon. These probabilities may be different as the probability to emit a second photon might depend on the polarization of the first photon.

The ratio of quantities 3.3 and 3.2 is independent of the efficiencies η^i and η^j as well as of the number of excitation attempts. It only depends on the probabilities to emit a single photon and a second photon within the same excitation attempt:

$$\frac{n_0^{ij}}{n_{\pm 1}^{ij}} = \frac{(\eta^i p_{1st} \cdot \eta^j p_{2nd}^j + \eta^j p_{1st} \cdot \eta^i p_{2nd}^i) \cdot n_{ex}}{2\eta^i p_{1st} \cdot \eta^j p_{1st} \cdot n_{ex}} = \frac{1}{2}(\frac{p_{2nd}^i + p_{2nd}^j}{p_{1st}}). \tag{3.4}$$

The result of this fraction can be interpreted as the value for the peak 0 ($g^2(0)$) of the second order correlation function for pulsed excitation, if all errors cause only white noise. Furthermore, it can also be corrected for the dark count events described in section 3.2.4 as the number of events of a single photon and a dark count in one time window for a given detector combination $n_{dc,0}^{ij}$ is

$$n_{dc,0}^{ij} = (\eta_i p_{1st} p_{dc}^j + \eta_j p_{1st} p_{dc}^i)n_{ex}, \tag{3.5}$$

and the number of events of a single photon and a dark count in subsequent time windows for a given detector combination $n_{dc,\pm 1}^{i,j}$ is

$$n_{dc,\pm 1}^{ij} = 2(\eta_i p_{1st} p_{dc}^j + \eta_j p_{1st} p_{dc}^i)n_{ex} = 2n_{dc,0}^{ij}. \tag{3.6}$$

Thus, the dark count corrected ratio $n_0^{ij}/n_{\pm 1}^{ij}$ is:

$$p_{tp}^{ij} = \frac{n_0^{ij} - n_{dc,0,}^{ij}}{n_{\pm 1}^{ij} - 2n_{dc,0}^{ij}}. \tag{3.7}$$

This can easily be expanded for coincidences in given classes of detector combinations d ($d \in \{D+, D-, D\varnothing\}$). Therefore, pairs of n_0^{ij} and $n_{\pm 1}^{ij}$ are summarized to numbers of coincidences in given classes of detector combinations:

$$n_o^{D+} = n_0^{1\perp 1\|} + n_0^{2\perp 2\|}, \tag{3.8}$$

$$n_o^{D-} = n_0^{1\perp 2\|} + n_0^{2\perp 1\|}, \tag{3.9}$$

$$n_o^{D\varnothing} = n_0^{1\|2\|} + n_0^{1\perp 2\perp} \tag{3.10}$$

as well as

$$n_{\pm 1}^{D+} = n_{\pm 1}^{1\perp 1\|} + n_{\pm 1}^{2\perp 2\|}, \tag{3.11}$$

$$n_{\pm 1}^{D-} = n_{\pm 1}^{1\perp 2\|} + n_{\pm 1}^{2\perp 1\|}, \tag{3.12}$$

$$n_{\pm 1}^{D\varnothing} = n_{\pm 1}^{1\|2\|} + n_{\pm 1}^{1\perp 2\perp}. \tag{3.13}$$

The number of dark count events in given classes of detector combinations is calculated in the same way:

$$n_{dc}^{D+} = n_{dc,0}^{1\perp 1\|} + n_{dc,0}^{2\perp 2\|}, \tag{3.14}$$

$$n_o^{D-} = n_{dc,0}^{1\perp 2\|} + n_{dc,0}^{2\perp 1\|}, \tag{3.15}$$

$$n_o^{D\varnothing} = n_{dc,0}^{1\|2\|} + n_{dc,0}^{1\perp 2\perp}. \tag{3.16}$$

Thus, the dark count corrected ratio $n_0^d/n_{\pm 1}^d$ is:

$$p_{tp}^d = \frac{n_0^d - n_{dc}^d}{n_{\pm 1}^d - 2n_{dc}^d}, \tag{3.17}$$

which can also be expanded for all coincidences

$$p_{tp}^{all} = \frac{n_0^{D-} - n_{dc}^{D-} + n_0^{D+} - n_{dc}^{D+} + n_0^{D\varnothing} - n_{dc}^{D\varnothing}}{n_{\pm 1}^{D-} - 2n_{dc}^{D-} + n_{\pm 1}^{D+} - 2n_{dc}^{D+} + n_{\pm 1}^{D\varnothing} - 2n_{dc}^{D\varnothing}}. \tag{3.18}$$

In analogy the ratio can be defined for dark count events in given classes of detector combinations:

$$p_{dc}^d = \frac{n_{dc}^d}{n_{\pm 1}^d - 2n_{dc}^d}. \tag{3.19}$$

In case of no correlations between the two emitted photons (no colored noise), the ratios p_{tp}^{ij}, p_{tp}^d and p_{tp}^{all} would have the same value and be equivalent to the probability to emit a second, not π-polarized photon, if a first , not π-polarized photon has been emitted. But because of the colored noise of the two-photon emission events of type II (see subsection 3.2.2) additional calculations are needed to estimate that probability. The experimental setup can be reduced to a standard Hanbury-Brown-Twiss (HBT) setup by analyzing only events in detector combinations $D-$ and $D\varnothing$ [65, 66]. This way the value for the correlation function ($g^2(0)$) can be calculated, which can be interpreted as the probability to emit a second, not π-polarized photon, in case a first, not π-polarized photon has already been emitted in the very same excitation attempt, even in case of colored noise:

$$g^2(0) = \frac{n_0^{D-} - n_{dc}^{D-} + n_0^{D\varnothing} - n_{dc}^{D\varnothing}}{n_{\pm 1}^{D-} - 2n_{dc}^{D-} + n_{\pm 1}^{D\varnothing} - 2n_{dc}^{D\varnothing}}. \tag{3.20}$$

3.4. Quantitative Analysis of the Single Photon Source

The knowledge of all major causes for two-photon emission events allows a quantitative analysis of this pulsed single photon source. The analysis only considers two-photon emission events, at which both emitted photons are not π-polarized as only those events cause two-photon coincidences. Thus, only $2/3$ of all type I, $8/15$ of all type II and no type III events are registered. The analysis further takes into account that not all two photon events entering the detection setup, can be detected. There is a certain number of events at which the two photons impinge on the same detector. The coincidences caused by type I and type II two-photon emission events are already discussed in subsection 3.2.1 and 3.2.2. The white noise of type I events yields an equal probability for all detector coincidences, whereas the colored noise of type II events causes individual coincidence probabilities for every class of detector combinations. Table 3.2 shows these relative probabilities for analysis in the H/V- and the R/L-basis.

The above considerations show that the total relative probability to detect a coincidence in a given class of detector combinations depends on the ratio of type I to type II events. The relative probability for a type I two-photon emission event, at which both photons are not π-polarized, is given by $p_{\mathrm{I}}^{\sigma\pm}$ and for a type II event by $p_{\mathrm{II}}^{\sigma\pm}$, respectively (with $p_{\mathrm{I}}^{\sigma\pm} + p_{\mathrm{II}}^{\sigma\pm} = 1$). In order to experimentally acquire these relative probabilities, it is feasible to measure the ratio of probability $p_{tp}^{D\varnothing}$ to the probability $p_{tp}^{sum} = p_{tp}^{D\varnothing} + p_{tp}^{D-} + p_{tp}^{D+}$ (see equation 3.17) and relate it to a ratio derived with respect to the relative coincidence probabilities given in table 3.2. This can be done for both measurement bases.

photon analysis basis		H/V		R/L	
involved det. \ tp effect		type I ($p_{tI}^{d,HV}$)	type II ($p_{tII}^{d,HV}$)	type I ($p_{tI}^{d,RL}$)	type II ($p_{tII}^{d,RL}$)
$APD_{1\perp}, APD_{2\parallel}$ $APD_{1\parallel}, APD_{2\perp}$	$D-$	$\frac{1}{4}$	$\frac{1}{2}p_b + \frac{1}{4}p_c$	$\frac{1}{4}$	$\frac{1}{2}p_a + \frac{1}{2}p_b$
$APD_{1\perp}, APD_{1\parallel}$ $APD_{2\parallel}, APD_{2\perp}$	$D+$	$\frac{1}{4}$	$\frac{1}{2}p_b + \frac{1}{4}p_c$	$\frac{1}{4}$	$\frac{1}{2}p_a + \frac{1}{2}p_b$
$APD_{1\perp}, APD_{2\perp}$ $APD_{2\parallel}, APD_{1\parallel}$	$D\varnothing$	$\frac{1}{4}$	$\frac{1}{2}p_a + \frac{1}{4}p_c$	$\frac{1}{4}$	$\frac{1}{2}p_c$
$APD_{1\perp}, APD_{1\perp}$ $APD_{2\perp}, APD_{2\perp}$ $APD_{1\parallel}, APD_{1\parallel}$ $APD_{2\parallel}, APD_{2\parallel}$	$n.d.$	$\frac{1}{4}$	$\frac{1}{2}p_a + \frac{1}{4}p_c$	$\frac{1}{4}$	$\frac{1}{2}p_c$

Table 3.2.: Relative probabilities of two-photon coincidences caused by two-photon emission events of type I $p_{tI}^{d,b}$ and type II $p_{tII}^{d,b}$ (with $d \in \{D+, D-, D\varnothing\}$ and $b \in \{HV, RL\}$). The probabilities are derived from considerations in subsections 3.2.1 and 3.2.2. They respect the values $p_a = 0.781$, $p_b = 0.031$ and $p_c = 0.188$ also presented in subsection 3.2.2. (n.d. stands for not detectable - both photons impinge on the same detector). For easy reference the probabilities for a type I or type II event to cause a coincidence detection are given by $p_{tI}^{sum,b} = p_{tI}^{D+,b} + p_{tI}^{D-,b} + p_{tI}^{D\varnothing,b}$ and $p_{tII}^{sum,b} = p_{tII}^{D+,b} + p_{tII}^{D-,b} + p_{tII}^{D\varnothing,b}$, respectively.

The ratios should be different in the two bases due to the colored noise caused by events of type II. Nevertheless, the results for $p_I^{\sigma\pm}$ and $p_{II}^{\sigma\pm}$ should be the same in both measurement bases:

$$\frac{p_{tp}^{D\varnothing,b}}{p_{tp}^{sum,b}} = \frac{p_{tI}^{D\varnothing,b}p_I^{\sigma\pm,b} + p_{tII}^{D\varnothing,b}p_{II}^{\sigma\pm,b}}{p_{tI}^{sum,b}p_I^{\sigma\pm,b} + p_{tII}^{sum,b}p_{II}^{\sigma\pm,b}} \tag{3.21}$$

(with $b \in \{HV, RL\}$). The relative probabilities $p_I^{\sigma\pm,b}$ and $p_{II}^{\sigma\pm,b}$ can not be calculated and must be experimentally determined because the polarization of the excitation pulse at the location of the atom is not known (see subsection 3.2.1). As the values of $p_I^{\sigma\pm,b}$ and $p_{II}^{\sigma\pm,b}$ should be the same in both measurement basis, the weighted averages of them yield the final, more accurate values $p_I^{\sigma\pm}$ and $p_{II}^{\sigma\pm}$:

$$p_I^{\sigma\pm} = \frac{p_I^{\sigma\pm,HV}\big/(ep_I^{\sigma\pm,HV})^2 + p_I^{\sigma\pm,RL}\big/(ep_I^{\sigma\pm,RL})^2}{1\big/(ep_I^{\sigma\pm,HV})^2 + 1\big/(ep_I^{\sigma\pm,RL})^2} \tag{3.22}$$

and

$$p_{II}^{\sigma\pm} = \frac{p_{II}^{\sigma\pm,HV}\big/(ep_{II}^{\sigma\pm,HV})^2 + p_{II}^{\sigma\pm,RL}\big/(ep_{II}^{\sigma\pm,RL})^2}{1\big/(ep_{II}^{\sigma\pm,HV})^2 + 1\big/(ep_{II}^{\sigma\pm,RL})^2}, \tag{3.23}$$

where $ep_I^{\sigma\pm,b}$ and $ep_{II}^{\sigma\pm,b}$ are the statistical errors of $p_I^{\sigma\pm,b}$ and $p_{II}^{\sigma\pm,b}$, respectively.

This kind of evaluation also allows the estimation of the probability $P_{tp}^{\sigma\pm}$ to emit a second, not π-polarized photon, in case a first not π-polarized photon has already been emitted in the very same excitation attempt. It should give the same result as equation 3.20 presented in the previous section, but also considers events in detector combinations $D+$, and therefore has a smaller statistical error. This method uses the known ratio of two photon coincidences in the same as well as in subsequent excitation attempts in $D+$, $D-$ and $D\varnothing$ detector combinations to events, where both photons impinge

in the same detector. Thus, even the not detected events can be taken into account:

$$P_{tp}^{\sigma\pm,b} \quad = \quad \frac{1}{p_{tI}^{sum,b}p_{I}^{\sigma\pm,b}+p_{tII}^{sum,b}p_{II}^{\sigma\pm,b}} \quad \frac{3}{4} \cdot p_{tp}^{all,b} \tag{3.24}$$

with $b \in \{HV, RL\}$. Note, $P_{tp}^{\sigma\pm,b}$ does not suffer from any unknown detection efficiencies or dark count events being based on the efficiency and dark count corrected values p_{tp}^{sum}, $p_{tp}^{D\varnothing}$ and p_{tp}^{all}. Equally to the previous calculations the weighted average $P_{tp}^{\sigma\pm}$ of both probabilities $P_{tp}^{\sigma\pm,HV}$ and $P_{tp}^{\sigma\pm,RL}$ gives the statistically most significant value:

$$P_{tp}^{\sigma\pm} = \frac{P_{tp}^{\sigma\pm,HV}/(eP_{tp}^{\sigma\pm,HV})^2 + P_{tp}^{\sigma\pm,RL}/(eP_{tp}^{\sigma\pm,RL})^2}{1/(eP_{tp}^{\sigma\pm,HV})^2 + 1/(eP_{tp}^{\sigma\pm,RL})^2}, \tag{3.25}$$

where $eP_{tp}^{\sigma\pm b}$ is the statistical error of the respective value.

$P_{tp}^{\sigma\pm}$ is a significant measure for the quality of a single atom as pulsed single photon source as it takes all evens into account, which causes two photon coincidences. Anyhow, it describes only two-photon emission events, where both photons are not π-polarized. The absolute probability P_{tp} for emission of a second photon, if a first one has already been emitted, is considerably higher. It considers also cases, at which one ore both emitted photons are π-polarized. Thus, it respects all type I and type II events and even type III events. The considerations in subsections 3.2.1 and 3.2.2 show that only $2/3$ of type I and $8/15$ of type II events contribute to $P_{tp}^{\sigma\pm}$. Thus, P_{tp} can be derived with respect to that and the calculated probability of a type III event ($3/2p_{\text{tp-III}}$), where even the second photon might be π-polarized:

$$P_{tp} = (\frac{3}{2}p_{I}^{\sigma\pm} + \frac{15}{8}p_{II}^{\sigma\pm})P_{tp}^{\sigma\pm} + \frac{3}{2}p_{\text{tp-III}}. \tag{3.26}$$

In order to give a final statement about the probability of the three types of two-photon emission events to cause a two-photon emission, it is sufficient to calculate their relative provabilities p_I, p_{II} and p_{III} (with $p_I + p_{II} + p_{III} = 1$):

$$\begin{aligned} p_I &= \frac{3 \cdot p_I^{\sigma\pm} \cdot P_{tp}^{\sigma\pm}}{2 \cdot P_{tp}} \\ p_{II} &= \frac{15 \cdot p_{II}^{\sigma\pm} \cdot P_{tp}^{\sigma\pm}}{8 \cdot P_{tp}} \\ p_{III} &= \frac{3 \cdot p_{\text{tp-III}}}{2 \cdot P_{tp}} \end{aligned} \tag{3.27}$$

3.5. Experimental Results

In this section the two-photon emission frequency is experimentally determined, in order to demonstrate that single ^{87}Rb atoms are a viable source for single photons. For this purpose the introduced quantitative analysis of two-photon emission events is used after verification of its validity. Good overlap of experimental data and theoretical predictions would demonstrate that the understanding of all major two-photon emission processes. To measure the two-photon emission frequencies, correlations of the detection times of two photons in all detector combinations are analyzed.

detector	single photon det. prob. $p_{ph}^{i,b} \cdot 10^{-3}$	
	H/V-basis	R/L-basis
$APD_{1\perp}$	0.25±0.000098	0.23±0.000093
$APD_{1\parallel}$	0.26±0.000093	0.27±0.000097
$APD_{2\perp}$	0.23±0.000099	0.25±0.000096
$APD_{2\parallel}$	0.22±0.000092	0.23±0.000091

Table 3.3.: Single photon detection probability after an excitation attempt $p_{ph}^{i,b}$ (with $i \in \{1 \perp, 1 \parallel, 2 \perp, 2 \parallel\}$ and $b \in \{HV, RL\}$) for all detectors i in both relevant two-photon emission measurements.

3.5.1. Experimental Realization

In order to record correlations of the photon detection times, the experiment is operated almost identical as in the atom-photon entanglement experiments described in chapter 2 (see subsection 2.4.1). But here, no atomic state readout scheme is triggered by a single photon detection. The atom excitation process repeats until the atom is lost. All photons in the 120 ns time windows are registered which is illustrated in figure 3.1 b). In the following analysis two-photon coincidences are selected from the registered data, and the relative time difference of each photon pair is recorded for all three classes of detector combinations.

3.5.2. Dark Count Probabilities

In order to extract relevant information on the two-photon emission frequency from the data, it has to be dark count corrected. The probability to detect a single photon and a dark count in the same time window is calculated by equation 3.1 for a each detector combination. This requires knowledge of the single photon detection probability of every detector which varies between measurements as described in 3.2.4. The single photon detection probabilities for the two relevant measurements are shown in table 3.3.

These data allow calculation of the dark count probabilities for every detector combination, and thus determination of the total expected number of dark counts for these measurements by using equation 3.5, where the number of atom excitations is $n_{ex}^{HV} = 26.5 \cdot 10^9$ for measurement in the H/V-basis and $n_{ex}^{RL} = 27.1 \cdot 10^9$ for measurement in the R/L-basis, respectively. The dark count event probabilities and the total number of expected dark count events for both two-photon emission measurements are shown in table 3.4.

3.5.3. Two-Photon Correlations

All registered two-photon events are summarized in histograms of the detection time differences of the two-photons. Figure 3.6 shows exemplarily the histogram for detector combinations $D+$ and photon analysis in the H/V-basis. The histogram plainly shows correlations of the detection time of both photons. Each peak in the histogram corresponds to a certain time difference between two excitation attempts. The differences of the areas of these peaks are caused by combinatorial reasons. For example, in a burst of 20 atom excitations there are 19 possibilities to obtain a time difference of one cycle, but there is only one possibility to obtain a time difference of 19 cycles.

All following discussions consider only events, at which the photons are emitted in the same or in subsequent atom excitations, normalized by their combinatorial weight (the experiments uses bursts

det. comb.	H/V-basis		R/L-basis	
	$p_{dce}^{ij,b} \cdot 10^{-10}$	$n_{dc}^{ij,b}$	$p_{dce}^{ij,b} \cdot 10^{-10}$	$n_{dc}^{ij,b}$
$APD_{1\perp}, APD_{2\parallel}$	2.98 ± 0.045	08 ± 2.8	3.08 ± 0.047	08 ± 2.9
$APD_{1\parallel}, APD_{2\perp}$	6.04 ± 0.067	12 ± 3.5	6.00 ± 0.066	12 ± 3.4
$APD_{1\perp}, APD_{1\parallel}$	4.55 ± 0.059	15 ± 4.0	4.35 ± 0.056	15 ± 3.9
$APD_{2\parallel}, APD_{2\perp}$	4.41 ± 0.055	08 ± 2.8	4.73 ± 0.058	09 ± 2.9
$APD_{1\perp}, APD_{2\perp}$	5.90 ± 0.065	12 ± 3.4	5.63 ± 0.062	13 ± 3.6
$APD_{2\parallel}, APD_{1\parallel}$	3.02 ± 0.046	16 ± 4.0	3.18 ± 0.049	16 ± 4.0

Table 3.4.: Probability $p_{dce}^{ij,b}$ (with $i \neq j$ and $i, j \in \{1 \perp, 1 \parallel, 2 \perp, 2 \parallel\}$ and $b \in \{HV, RL\}$) to detect a dark count together with a single photon in the same time window (dark count event) per atom excitation for every detector combination i, j and both relevant two-photon emission measurements. It also shows the expected number of these events $n_{dc}^{ij,b}$ in the presented measurements.
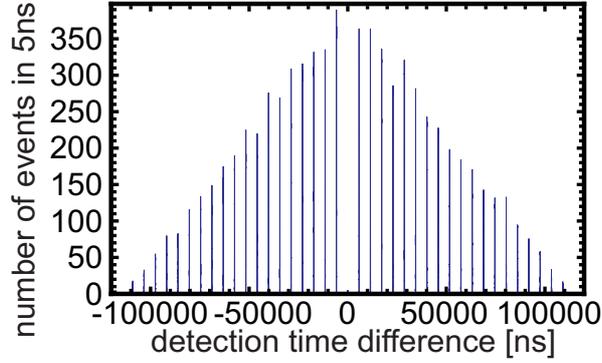
Figure 3.6.: Histogram of two-photon detection time correlations for detector combinations $D+$ in the H/V-basis. The figure shows all possible two-photon coincidences for a sequence of 20 atom excitations. In the following analysis only the inner three peaks are considered.

of 20 excitation trials; see 2.9). The peak ($peak = 0$) at zero photon detection time difference corresponds to events, at which both photons originate from the same atom excitation. For an ideal pulsed single photon source it should vanish.

Figure 3.7 shows two-photon correlations of events from subsequent atom excitations as well as from the same atom excitation in the H/V-basis for all three classes of detector combinations (the correlations for measurements in the R/L-basis offer no deeper insight and therefore are not shown here). These figures give a first impression of the already introduced colored noise caused by two-photon emission events of type II (see $peak = 0$ in all three graphs). Figure 3.7 a) and c), which correspond to detector combinations $D-$ and $D+$, contain less events around a time difference of zero than figure 3.7 b), which corresponds to detector combinations $D\varnothing$. This agrees with the theoretical expectations as shown in table 3.2.

A more detailed analysis allows calculation of the dark count and efficiency corrected probabilities p_{tp}^d (with $d \in \{D+, D-, D\varnothing\}$, see equation 3.17), as well as the probability for dark count events p_{dc}^d itself (see equation 3.19). Therefore, all events, which originate from subsequent atom excitations, are integrated for all detector combinations as well as all events from the same atom excitation. The resulting numbers of events in a certain class of detector combinations $n_{\pm 1}^d$ (events from subsequent
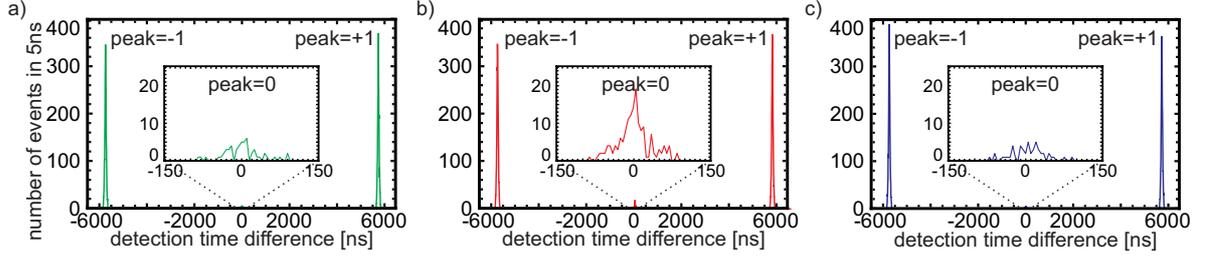
Figure 3.7.: Histograms of two-photon detection time correlations for all three classes of detector combinations in the H/V-basis. The figures show only events which originate from the same ($peak = 0$) and from subsequent ($peak = \pm 1$) atom excitations. a) detector combinations $D-$, b) detector combination $D\varnothing$ and c) detector combinations $D+$. The integrated number of events of $peak = 0$ gives the value n_0^d (with $d \in \{D+, D-, D\varnothing\}$) and the integrated number of events of $peak = \pm 1$ gives the value $n_{\pm 1}^d$.

basis	H/V		R/L	
det. comb.\ prob.	$p_{tp}^{d,b}$	$p_{dc}^{d,b}$	$p_{tp}^{d,b}$	$p_{dc}^{d,b}$
$D-$	0.0033 ± 0.0010	0.0029 ± 0.0006	0.0112 ± 0.0015	0.0030 ± 0.0006
$D+$	0.0019 ± 0.0010	0.0029 ± 0.0006	0.0110 ± 0.0014	0.0029 ± 0.0006
$D\varnothing$	0.0131 ± 0.0015	0.0029 ± 0.0006	0.0050 ± 0.0012	0.0029 ± 0.0006

Table 3.5.: Ratios $p_{tp}^{d,b}$ and $p_{dc}^{d,b}$ (with $d \in \{D+, D-, D\varnothing\}$ and $b \in \{HV, RL\}$) for all relevant detector combinations in the H/V- and the R/L-bases. The total number of contributing events ($n_0^{D-,b} + n_0^{D+,b} + n_0^{D\varnothing,b}$) is 223 in H/V-basis and 298 in R/L-basis, respectively (including dark counts).

atom excitations) and n_o^d (events from the same atom excitation) are inserted in equation 3.17 or in equation 3.19, respectively, yielding the probabilities p_{tp}^d and p_{dc}^d presented in table 3.5.

By substituting the event numbers n_0^d, $n_{\pm 1}^d$ and n_{dc}^d in equation 3.18 the total ratio p_{tp}^{all} of two photons from one atom excitation attempt to two photons from subsequent atom excitation attempts can be calculated. This can be interpreted as the value for the peak $peak = 0$ of the second order correlation function for pulsed excitation. Here, the results are $p_{tp}^{all,HV} = 0.0061 \pm 0.0007$ for analysis in the H/V-basis and $p_{tp}^{all,RL} = 0.0091 \pm 0.0008$ for analysis in the R/L-basis. The numbers differ as the number of two-photon events, which impinge on the same detector (and are not registered), depend on the measurement basis because of the colored noise of two-photon emission events of type II.

3.5.4. Quantitative Analysis of Two-Photon Emission

The characteristics of the two-photon emission events of type II predict different frequencies of coincidences for the different classes of detector combinations. The actual relative probabilities of the coincidences depend on the relative probabilities of two-photon events of type I ($p_I^{\sigma^\pm}$) and type II ($p_{II}^{\sigma^\pm}$) as the considerations of section 3.4 predict. These probabilities can be determined by means of equation 3.21 for the two measurement bases. Therefore, the ratio of coincidences in $D\varnothing$ to all detected coincidences is calculated with respect to the values presented in table 3.5:

$$\frac{p_{tp}^{D\varnothing,HV}}{p_{tp}^{sum,HV}} = \frac{p_{tp}^{D\varnothing,HV}}{p_{tp}^{D-,HV} + p_{tp}^{D+,HV} + p_{tp}^{D\varnothing,HV}} = 0.714 \pm 0.060 \tag{3.28}$$

$$\frac{p_{tp}^{D\varnothing,RL}}{p_{tp}^{sum,RL}} = \frac{p_{tp}^{D\varnothing,RL}}{p_{tp}^{D-,RL} + p_{tp}^{D+,RL} + p_{tp}^{D\varnothing,RL}} = 0.184 \pm 0.037 \tag{3.29}$$

Inserting these values into equation 3.21 yields the relative probabilities $p_{\mathrm{I}}^{\sigma\pm,b}$ and $p_{\mathrm{II}}^{\sigma\pm,b}$ (with $b \in \{HV, RL\}$). The results are $p_{\mathrm{I}}^{\sigma\pm,HV} = 0.111 \pm 0.109$ and $p_{\mathrm{II}}^{\sigma\pm,HV} = 0.888 \pm 0.109$ for H/V-basis and $p_{\mathrm{I}}^{\sigma\pm,RL} = 0.395 \pm 0.170$ and $p_{\mathrm{II}}^{\sigma\pm,RL} = 0.605 \pm 0.170$ for R/L-basis, respectively. The considerable difference between the values of both measurement bases is attributed to the big statistical errors due to the low two-photon event rate. The errors of both values still overlap, and thus it is justified to calculate the weighted average of both measured values as final result for $p_{\mathrm{I}}^{\sigma\pm}$ and $p_{\mathrm{II}}^{\sigma\pm}$ (see equations 3.22 and 3.23). The values are

$$p_{\mathrm{I}}^{\sigma\pm} = 0.19 \pm 0.09$$

and

$$p_{\mathrm{II}}^{\sigma\pm} = 0.81 \pm 0.09,$$

respectively.

The ratio of detected two-photon events to all two-photon events entering the detection setup is larger for photon analysis in the R/L-basis than for the H/V-basis. The colored noise of two-photon emission events of type II causes less two-photons emission events to impinge on the same detector in the R/L measurement basis. The fraction of detectable two-photon emission events is given by $p_{t\mathrm{I}}^{sum,b} p_{\mathrm{I}}^{\sigma\pm,b} + p_{t\mathrm{II}}^{sum,b} p_{\mathrm{II}}^{\sigma\pm,b}$ with $b \in \{HV, RL\}$, which is derived with respect to probabilities shown table 3.2. It yields that 0.599 of all two-photon emission events entering the detection setup should be detectable in the H/V-basis and 0.876 in the R/L-basis, respectively. By dividing these two values following expression is created:

$$\frac{p_{t\mathrm{I}}^{sum,HV} p_{\mathrm{I}}^{\sigma\pm} + p_{t\mathrm{II}}^{sum,HV} p_{\mathrm{II}}^{\sigma\pm}}{p_{t\mathrm{I}}^{sum,RL} p_{\mathrm{I}}^{\sigma\pm} + p_{t\mathrm{II}}^{sum,RL} p_{\mathrm{II}}^{\sigma\pm}} = \frac{0.599}{0.876} = 0.684. \tag{3.30}$$

This ratio should be equal to the measured ratio $p_{tp}^{all,HV}/p_{tp}^{all,RL} = 0.670 \pm 0.095$. Both values overlap very well. It is strong verification of the validity of this quantitative analysis as it shows that the major effects of two-photon emission are respected.

Finally the total probability for the emission of a second, not π-polarized photon, in case a first, not π-polarized photon is already emitted, can be calculated with respect to equation 3.24 for both measurements. It yields

$$P_{tp}^{\sigma\pm,HV} = 0.0076 \pm 0.0008$$

and

$$P_{tp}^{\sigma\pm,RL} = 0.0078 \pm 0.0007,$$

respectively. These values should be comparable to the values of the correlations function $g^2(0)$, which can be calculated with equation 3.20:

$$g^{2,HV}(0) = 0.0074 \pm 0.0009$$

and

$$g^{2,RL}(0) = 0.0081 \pm 0.0009,$$

respectively. The values of the correlation function $g^{2,B}(0)$ are almost identical to the values $P_{tp}^{\sigma\pm,B}$, which are calculated with the presented quantitative analysis. This is another verification of the quantitative analysis. As $P_{tp}^{\sigma\pm,B}$ considers also events in $D+$ detector combinations, the results are statistically more significant and are used for all further calculations.

Both values $P_{tp}^{\sigma\pm,HV}$ and $P_{tp}^{\sigma\pm,RL}$ are almost identical which is an additional confirmation for the accuracy of this analysis. The weighted average of these two probabilities gives the final probability:

$$P_{tp}^{\sigma\pm} = 0.0077 \pm 0.0005.$$

The total probability P_{tp} to emit a second photon, if a first one has already been emitted, is higher than $P_{tp}^{\sigma\pm}$ as one or both emitted photons might be π-polarized. This also includes events, where the second photon of a type I or a type II event is π-polarized, as well as type III events. P_{tp} can be calculated with equation 3.26, which includes the probability $p_{\text{tp}-\text{III}}$ for a type III two-photon event. The value of $p_{\text{tp}-\text{III}}$ is not based on any two-photon coincidence measurement, but is calculated by the quantum jump model.

$$P_{tp} = 0.0919 \pm 0.0009$$

The two-photon emission events are caused by the three types of two-photon emission events the the following relative probabilities (calculated with respect to equation 3.27):

$$
\begin{aligned}
p_{\text{I}} &= 0.024 \pm 0.012 \\
p_{\text{II}} &= 0.127 \pm 0.014 \\
p_{\text{III}} &= 0.849 \pm 0.009
\end{aligned}
$$

This results demonstrate that an atom can serve as an excellent pulsed single photon source as the probability $P_{tp}^{\sigma\pm}$ to emit second $\sigma\pm$-polarized photons within one excitation attempt is sufficiently low and has only a small influence on the two-photon interference experiments presented in the next chapter. The probability to emit a second photon, if a first one has already been emitted P_{tp} (regardless of the photon polarization), is considerably higher. But most of these two-photon emission events can only cause single photon detections or can not be detected at all. Still even a single photon originating from a two-photon emission event reduces the two-photon interference probability. Thus, these events have to be considered in the next chapter.

3.5.5. Verification of the Quantum Jump Model

The introduced quantum jump model (see appendix F) allows calculation of the probability of two-photon emission events. Here, the probabilities presented in section 3.2 are compared to the measurement data in order to test the validity of the models predictions. Therefore, the probability for a two-photon event of type I and of type II are calculated by the following equations (with respect to the measured data):

$$p_{tp-\text{I}} = p_{\text{I}}^{\sigma\pm} P_{tp}^{\sigma\pm} \tag{3.31}$$

$$p_{tp-\text{II}} = p_{\text{II}}^{\sigma\pm} P_{tp}^{\sigma\pm} \tag{3.32}$$

The results are $p_{tp-\text{I}} = 0.0015 \pm 0.0007$ and $p_{tp-\text{II}} = 0.0062 \pm 0.0007$. The values are in good agreement with the values predicted by the quantum jump : $p_{tp-\text{I}} = 0.0025$ (for a linear rotation of the polarization by an angle of $1°$) and $p_{tp-\text{II}} = 0.0048$. The difference between measurement and simulation can be explained as all minor channels for two-photon emission are not considered as well

as polarization errors of the detection optics. In addition the calculated values depend critically on the power of the excitation laser at the position of the atom which slightly varies due to the motion of the atom in the trap. However, the data prove that the two-photon emission probability in function of the excitation pulse can be predicted by the quantum jump model.

3.6. Summary

In this chapter the single atom excitation was explained in detail as well as the major causes for detected two-photon emission events. These are re-excitations of the atom via polarization errors (type I) and via off-resonant excitation (type II) and events where a single photon and a dark count are detected. The frequencies of all effects in this setup are in the same order of magnitude. The probabilities for two-photon emission events were calculated by a quantum jump model and compared to the measured values. Based on knowledge of the causes for two-photon emission events a quantitative analysis, which predicts the relative probabilities for detection of a two-photon emission event in all detector combinations, was introduced. This quantitative analysis of the measurement data allowed to determine the probability to emit a second, $\sigma^\pm$-polarized photon, in case a first, $\sigma^\pm$-polarized photon has already been emitted: $P_{tp}^{\sigma^\pm} = 0.0077 \pm 0.0005$, as well as the total probability to emit a second photon, if a first one has already been emitted $P_{tp} = 0.0919 \pm 0.0009$. Especially the small value of $P_{tp}^{\sigma^\pm}$ shows that this kind of single photon source is suited for use in a two-photon interference experiment as only $\sigma^\pm$-polarized photons cause two-photon detections.

4. Two-Photon Interference

Two-photon quantum interference at a beam splitter is a most nonintuitive phenomena in quantum mechanics. It causes two identical photons, which impinge on a beam-splitter from different input ports, to leave the beam-splitter via the same output port [67, 68, 69, 70]. This phenomenon was studied first by Hong, Ou and Mandel with pairs of photons from a parametric down conversion source [67]. Since then, a variety of sources have been used to observe this effect, e.g. photons emitted consecutively by a single atom in a cavity [71] where the atom serves as the source for indistinguishable photons.

However, it is more difficult to achieve quantum interference of photons from independent sources, as the two sources have to emit indistinguishable photons. Still it could be demonstrated for single atoms and ions [72, 73] as well as for more complex single photon sources such as quantum dots [74], molecules [75] and nitrogen vacancy centers in diamond [76, 77]. Evidently, it is still an experimentally challenging task to guarantee the indistinguishability of photons for molecules and solid state systems due to the influence of the respective environment and fluctuations in the preparation of the samples.

The variety of sources, at which two-photon interference has been demonstrated, reflects its importance for quantum information science. It is an elementally tool enabling linear-optical quantum C-NOT gates [78] and (partial) Bell-state analysis which is an essential part of quantum teleportation. In this experiment the interference is the main part of the entanglement swapping protocol [79] which will be explained in detail in chapter 5. Furthermore, the two-photon quantum interference contrast serves as a measure for the matching of two independent sources.

In this chapter the theoretical principles of two-photon quantum interference are illustrated as well as the influences of the quality of the single photon source and the indistinguishability of photon on the degree of the interference contrast. Based on this knowledge a model is developed predicting the probability of photon coincidences in the three different classes of detector combinations. It allows a more detailed discussion of the interference quality compared to the basic definition of interference contrast. Thereafter, the experimental realization of a two-photon interference experiment is described, and the possible performance of the setup is estimated. Finally, experimental results are presented and analyzed.

4.1. Basic Principles of Two-Photon Interference

This section illustrates the basic principles of two-photon quantum interference at a beam splitter. A quantum mechanical description of a beam splitter is followed by discussion of the evolution of two photons impinging on a beam splitter.

4.1.1. The Beam Splitter

In principle a beam splitter is a partially transparent mirror at which the reflection and the transmission coefficients are assumed to have a fixed ratio. This ratio may vary for different light polarizations which is investigated later. In case of a lossless beam splitter the reflectance ρ and the transmittance
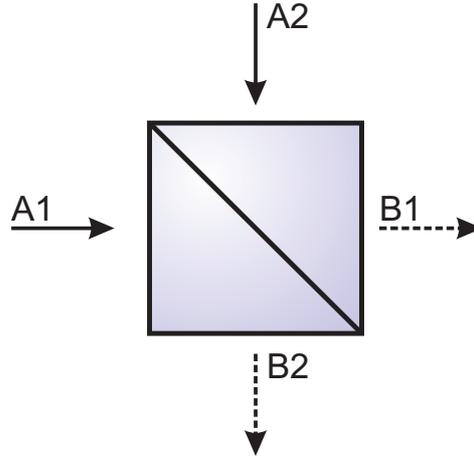
Figure 4.1.: Basic illustration of a beam splitter with two input ports (A1,A2) and two output ports (B1,B2).

σ have to satisfy the following condition:

$$\rho + \sigma = 1 \tag{4.1}$$

Light can enter the beam splitter via two input ports and leafs it via two output ports (see figure 4.1). The light fields at the input and output ports are represented by the bosonic creation / annihilation operators in second quantization which each satisfy the commutation relations $[\hat{a}_i, \hat{a}_j^\dagger] \equiv \hat{a}_i \hat{a}_j^\dagger - \hat{a}_j^\dagger \hat{a}_i = \delta_{i,j}$ or $[\hat{b}_i, \hat{b}_j^\dagger] \equiv \hat{b}_i \hat{b}_j^\dagger - \hat{b}_j^\dagger \hat{b}_i = \delta_{i,j}$, respectively [80, 81]. The interaction of the light fields with the beam splitter is represented by the transformation matrix B with elements $B_{ij} = |B_{ij}|e^{i\phi_{ij}}$, $i, j \in \{1, 2\}$ which are complex to include field phase shifts. Thus, the input and output operators are related by

$$\begin{bmatrix} \hat{b}_1^\dagger \\ \hat{b}_2^\dagger \end{bmatrix} \rightarrow \begin{bmatrix} B_{11} & B_{12} \\ B_{21} & B_{22} \end{bmatrix} \begin{bmatrix} \hat{a}_1^\dagger \\ \hat{a}_2^\dagger \end{bmatrix}$$

The preservation of commutation relations of the operators at the output of the beam splitter lead to the following conditions for the transformation matrix elements $B_{i,j}$:

$$|B_{11}|^2 + |B_{12}|^2 = 1, \tag{4.2}$$

$$|B_{21}|^2 + |B_{22}|^2 = 1, \tag{4.3}$$

$$B_{11}B_{21}^\star + B_{12}B_{22}^\star = 0. \tag{4.4}$$

The terms of equation 4.2 and 4.3 are not independent, but coupled by equation 4.4. By dividing the elements of the transformation matrix into components of phase $e^{i\phi_{ij}}$ and magnitude $|B_{ij}|$ equation 4.4 gives the conditions:

$$|B_{11}||B_{21}| = |B_{12}||B_{22}|, \tag{4.5}$$

$$\phi_{11} - \phi_{21} = \phi_{12} - \phi_{22} \pm \pi. \tag{4.6}$$

The combination of equations 4.2, 4.3 and 4.5 provides the following relations of the elements $B_{i,j}$:

$$|B_{11}|^2 = |B_{22}|^2 = \sigma = \cos^2(\Theta), \tag{4.7}$$

$$|B_{12}|^2 = |B_{21}|^2 = \rho = \sin^2(\Theta), \tag{4.8}$$

where σ and ρ are the transmittance and reflectance. According to this, all magnitudes can be determined by the parameter $\Theta = \arccos(\sqrt{\sigma})$, $0 \leq \Theta \leq \pi/2$. A redefinition of the phases with respect to 4.6 gives a set of new phases:

$$\phi_\sigma \equiv \frac{1}{2}(\phi_{11} - \phi_{22}), \tag{4.9}$$

$$\phi_\rho \equiv \frac{1}{2}(\phi_{12} - \phi_{21} \mp \pi), \tag{4.10}$$

$$\phi_0 \equiv \frac{1}{2}(\phi_{11} + \phi_{22}). \tag{4.11}$$

This allows to redefine the transmission matrix:

$$B = e^{i\phi_0} \begin{bmatrix} \cos(\Theta)e^{\phi_\sigma} & \sin(\Theta)e^{i\phi_\rho} \\ -\sin(\Theta)e^{-i\phi_\rho} & \cos(\Theta)e^{-\phi_\sigma} \end{bmatrix}. \tag{4.12}$$

The minus sign in the matrix caused by reflection at the beam splitter.

The interference effects, which are discussed subsequently, do not depend on the global phase ϕ_0. Therefore, it is assumed to be zero without loss of generality: $\phi_0 = 0$. In addition, it is implied that the beam splitter itself introduces no phase shifts onto the light fields: $\phi_\sigma = \phi_\rho = 0$. These assumptions simplify the transformation matrix to a fundamental rotary matrix:

$$B = \begin{bmatrix} \cos(\Theta) & \sin(\Theta) \\ -\sin(\Theta) & \cos(\Theta) \end{bmatrix}. \tag{4.13}$$

For any further calculations it is necessary to describe also the evolution of the creation operators at the beam splitter. The operators $\hat{a}_i^\dagger$ and $\hat{b}_i^\dagger$ are related by

$$\begin{bmatrix} \hat{b}_1^\dagger & \hat{b}_2^\dagger \end{bmatrix} \rightarrow \begin{bmatrix} \hat{a}_1^\dagger & \hat{a}_2^\dagger \end{bmatrix} B^\star = \begin{bmatrix} \hat{a}_1^\dagger & \hat{a}_2^\dagger \end{bmatrix} \begin{bmatrix} \cos(\Theta) & -\sin(\Theta) \\ \sin(\Theta) & \cos(\Theta) \end{bmatrix}$$

$$\Leftrightarrow \begin{bmatrix} \hat{b}_1^\dagger & \hat{b}_2^\dagger \end{bmatrix} \rightarrow \begin{bmatrix} \cos(\Theta)\hat{a}_1^\dagger + \sin(\Theta)\hat{a}_2^\dagger & -\sin(\Theta)\hat{a}_1^\dagger + \cos(\Theta)\hat{a}_2^\dagger \end{bmatrix}.$$

It allows to express the output creation operators by means of the input creation operators:

$$\hat{b}_1^\dagger \rightarrow \cos(\Theta)\hat{a}_1^\dagger + \sin(\Theta)\hat{a}_2^\dagger, \tag{4.14}$$

$$\hat{b}_2^\dagger \rightarrow -\sin(\Theta)\hat{a}_1^\dagger + \cos(\Theta)\hat{a}_2^\dagger. \tag{4.15}$$

A transformation of equations 4.14 and 4.15 gives the input creation operators in terms of the output creation operators:

$$\hat{a}_1^\dagger \rightarrow \cos(\Theta)\hat{b}_1^\dagger - \sin(\Theta)\hat{b}_2^\dagger, \tag{4.16}$$

$$\hat{a}_2^\dagger \rightarrow \sin(\Theta)\hat{b}_1^\dagger + \cos(\Theta)\hat{b}_2^\dagger. \tag{4.17}$$

This expression is general, and allows the description of the evolution of photons at a beam splitter.
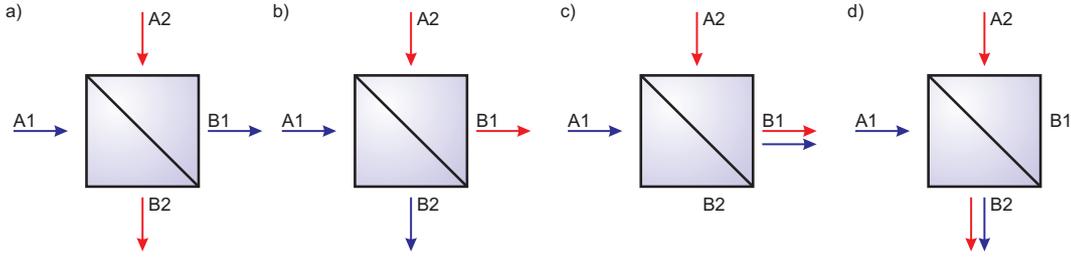
Figure 4.2.: Evolution of two photons at a beam splitter: Two photons impinging at a beam splitter can leave it in four different ways. They can both be transmitted a), they can both be reflected b) or one of them is reflected and one of them is transmitted c), d).

4.1.2. Interference of Single Photons

Generally, two photons entering a beam splitter have four possibilities of leaving its output ports (see figure 4.2).

However, if the two photons are indistinguishable in all degrees of freedom, interference of amplitudes of those processes will occur. This leads to so called bunching and the photons always leave the beam splitter via the same output port as the following calculation shows. Here, equations 4.16 and 4.17 are used to calculate the evolution of those photons at the beam splitter:

$$
\begin{aligned}
\hat{a}_1^\dagger \hat{a}_2^\dagger \left|0\right\rangle_{in} &\rightarrow (\cos(\Theta)\hat{b}_1^\dagger - \sin(\Theta)\hat{b}_2^\dagger)(\sin(\Theta)\hat{b}_1^\dagger + \cos(\Theta)\hat{b}_2^\dagger)\left|0\right\rangle_{out} \\
&= \sin(\Theta)\cos(\Theta)(\hat{b}_1^\dagger\hat{b}_1^\dagger - \hat{b}_2^\dagger\hat{b}_2^\dagger) + \cos(2\Theta)\hat{b}_1^\dagger\hat{b}_2^\dagger \left|0\right\rangle_{out}.
\end{aligned}
\tag{4.18}
$$

Both photons can be described in terms of the same output creation operators since they are indistinguishable.

In the ideal case of a $^{50}/_{50}$ beam splitter, the angle Θ, which describes the ratio of reflectance and transmittance of the beam splitter, has a value of $\Theta = {}^\pi/_4$. This simplifies equation 4.18 to the following expression:

$$
\hat{a}_1^\dagger \hat{a}_2^\dagger \left|0\right\rangle_{in} = \left|1,1\right\rangle_{in} \rightarrow \frac{1}{2}(\hat{b}_1^\dagger\hat{b}_1^\dagger - \hat{b}_2^\dagger\hat{b}_2^\dagger)\left|0\right\rangle_{out} = \frac{1}{2}(\left|2,0\right\rangle_{out} - \left|0,2\right\rangle_{out}),
$$

reproducing the effect of bunching as both photons always leave the beam splitter via the same output port.

In this experiment the single photons originate from two different atoms in two almost independent experiments where each photon is entangled with the respective atom. Their qubit information is encoded in their polarization which means that the photons can be considered as completely unpolarized. Thus, if two photons impinge on the beam splitter at the very same time, they are assumed to be identical in all degrees of freedom except in their polarization. Therefore, it is necessary to distinguish between four different two-photon states and their individual evolution at the beam splitter. These states are the four Bell-states $\left|\Phi^\pm\right\rangle = \frac{1}{\sqrt{2}}(\left|1_H, 1_H\right\rangle_{in} \pm \left|1_V, 1_V\right\rangle_{in})$ and $\left|\Psi^\pm\right\rangle = \frac{1}{\sqrt{2}}(\left|1_H, 1_V\right\rangle_{in} \pm \left|1_V, 1_H\right\rangle_{in})$ (here written in the H/V-basis). The photon pairs impinging on the beam splitter are in an equal mixture of the four Bell-states. In order to calculate the evolution of these two-photon states at the beam splitter, two sets of orthogonal creation operators $\hat{a}_{iH}^\dagger$, $\hat{a}_{iV}^\dagger$ and $\hat{b}_{iH}^\dagger$, $\hat{b}_{iV}^\dagger$ (with $i \in \{1,2\}$ defines the input port of the beam splitter) are introduced ($[\hat{a}_{in}, \hat{a}_{jm}^\dagger] = [\hat{b}_{in}, \hat{b}_{jm}^\dagger] = \delta_{i,j}\delta_{nm}$, with $n, m \in \{H, V\}$ and $i, j \in \{1,2\}$). With respect of these operators the evolution of the Bell-states at the beam splitter are as following:

$$
\begin{aligned}
|\Phi^+\rangle &= \tfrac{1}{\sqrt{2}}(\hat{a}^\dagger_{1H}\hat{a}^\dagger_{2H} + \hat{a}^\dagger_{1V}\hat{a}^\dagger_{2V})\,|0\rangle_{in} = \tfrac{1}{\sqrt{2}}(|1_H,1_H\rangle_{in} + |1_V,1_V\rangle_{in}) \\
&\rightarrow \tfrac{1}{\sqrt{2}}((\cos(\Theta)\hat{b}^\dagger_{1H} - \sin(\Theta)\hat{b}^\dagger_{2H})(\sin(\Theta)\hat{b}^\dagger_{1H} + \cos(\Theta)\hat{b}^\dagger_{2H}) \\
&\qquad + (\cos(\Theta)\hat{b}^\dagger_{1V} - \sin(\Theta)\hat{b}^\dagger_{2V})(\sin(\Theta)\hat{b}^\dagger_{1V} + \cos(\Theta)\hat{b}^\dagger_{2V}))\,|0\rangle_{out} \\
&= \tfrac{1}{\sqrt{2}}(\sin(\Theta)\cos(\Theta)(\hat{b}^\dagger_{1H}\hat{b}^\dagger_{1H} - \hat{b}^\dagger_{2H}\hat{b}^\dagger_{2H} + \hat{b}^\dagger_{1V}\hat{b}^\dagger_{1V} - \hat{b}^\dagger_{2V}\hat{b}^\dagger_{2V}) \\
&\qquad + \cos(2\Theta)(\hat{b}^\dagger_{1H}\hat{b}^\dagger_{2H} + \hat{b}^\dagger_{1V}\hat{b}^\dagger_{2V}))\,|0\rangle_{out}\,,
\end{aligned}
\tag{4.19}
$$

$$
\begin{aligned}
|\Phi^-\rangle &= \tfrac{1}{\sqrt{2}}(\hat{a}^\dagger_{1H}\hat{a}^\dagger_{2H} - \hat{a}^\dagger_{1V}\hat{a}^\dagger_{2V})\,|0\rangle_{in} = \tfrac{1}{\sqrt{2}}(|1_H,1_H\rangle_{in} - |1_V,1_V\rangle_{in}) \\
&\rightarrow \tfrac{1}{\sqrt{2}}((\cos(\Theta)\hat{b}^\dagger_{1H} - \sin(\Theta)\hat{b}^\dagger_{2H})(\sin(\Theta)\hat{b}^\dagger_{1H} + \cos(\Theta)\hat{b}^\dagger_{2H}) \\
&\qquad - (\cos(\Theta)\hat{b}^\dagger_{1V} - \sin(\Theta)\hat{b}^\dagger_{2V})(\sin(\Theta)\hat{b}^\dagger_{1V} + \cos(\Theta)\hat{b}^\dagger_{2V}))\,|0\rangle_{out} \\
&= \tfrac{1}{\sqrt{2}}(\sin(\Theta)\cos(\Theta)(\hat{b}^\dagger_{1H}\hat{b}^\dagger_{1H} - \hat{b}^\dagger_{2H}\hat{b}^\dagger_{2H} - \hat{b}^\dagger_{1V}\hat{b}^\dagger_{1V} + \hat{b}^\dagger_{2V}\hat{b}^\dagger_{2V}) \\
&\qquad + \cos(2\Theta)(\hat{b}^\dagger_{1H}\hat{b}^\dagger_{2H} - \hat{b}^\dagger_{1V}\hat{b}^\dagger_{2V}))\,|0\rangle_{out}\,,
\end{aligned}
\tag{4.20}
$$

$$
\begin{aligned}
|\Psi^+\rangle &= \tfrac{1}{\sqrt{2}}(\hat{a}^\dagger_{1H}\hat{a}^\dagger_{2V} + \hat{a}^\dagger_{1V}\hat{a}^\dagger_{2H})\,|0\rangle_{in} = \tfrac{1}{\sqrt{2}}(|1_H,1_V\rangle_{in} + |1_V,1_H\rangle_{in}) \\
&\rightarrow \tfrac{1}{\sqrt{2}}((\cos(\Theta)\hat{b}^\dagger_{1H} - \sin(\Theta)\hat{b}^\dagger_{2H})(\sin(\Theta)\hat{b}^\dagger_{1V} + \cos(\Theta)\hat{b}^\dagger_{2V}) \\
&\qquad + (\cos(\Theta)\hat{b}^\dagger_{1V} - \sin(\Theta)\hat{b}^\dagger_{2V})(\sin(\Theta)\hat{b}^\dagger_{1H} + \cos(\Theta)\hat{b}^\dagger_{2H}))\,|0\rangle_{out} \\
&= \tfrac{1}{\sqrt{2}}(2\sin(\Theta)\cos(\Theta)(\hat{b}^\dagger_{1H}\hat{b}^\dagger_{1V} - \hat{b}^\dagger_{2H}\hat{b}^\dagger_{2V}) \\
&\qquad + \cos(2\Theta)(\hat{b}^\dagger_{1H}\hat{b}^\dagger_{2V} + \hat{b}^\dagger_{2H}\hat{b}^\dagger_{1V}))\,|0\rangle_{out}
\end{aligned}
\tag{4.21}
$$

and

$$
\begin{aligned}
|\Psi^-\rangle &= \tfrac{1}{\sqrt{2}}(\hat{a}^\dagger_{1H}\hat{a}^\dagger_{2V} - \hat{a}^\dagger_{1V}\hat{a}^\dagger_{2H})\,|0\rangle_{in} = \tfrac{1}{\sqrt{2}}(|1_H,1_V\rangle_{in} - |1_V,1_H\rangle_{in}) \\
&\rightarrow \tfrac{1}{\sqrt{2}}((\cos(\Theta)\hat{b}^\dagger_{1H} - \sin(\Theta)\hat{b}^\dagger_{2H})(\sin(\Theta)\hat{b}^\dagger_{1V} + \cos(\Theta)\hat{b}^\dagger_{2V}) \\
&\qquad - (\cos(\Theta)\hat{b}^\dagger_{1V} - \sin(\Theta)\hat{b}^\dagger_{2V})(\sin(\Theta)\hat{b}^\dagger_{1H} + \cos(\Theta)\hat{b}^\dagger_{2H}))\,|0\rangle_{out} \\
&= \tfrac{1}{\sqrt{2}}(\hat{b}^\dagger_{1H}\hat{b}^\dagger_{2V} - \hat{b}^\dagger_{1V}\hat{b}^\dagger_{2H})\,|0\rangle_{out}\,.
\end{aligned}
\tag{4.22}
$$

This shows that all two-photon states except the $|\Psi^-\rangle$-state are transformed by the beam splitter depending on its splitting ratio. In a first approach the beam splitter is assumed to be a perfect $^{50}/_{50}$ beam splitter. This simplifies equations 4.19-4.22 to the following expressions:

$$
\begin{aligned}
|\Phi^+\rangle &\rightarrow \tfrac{1}{2\sqrt{2}}(\hat{b}^\dagger_{1H}\hat{b}^\dagger_{1H} - \hat{b}^\dagger_{2H}\hat{b}^\dagger_{2H} + \hat{b}^\dagger_{1V}\hat{b}^\dagger_{1V} - \hat{b}^\dagger_{2V}\hat{b}^\dagger_{2V})\,|0\rangle_{out} \\
&= \tfrac{1}{2\sqrt{2}}(|2_H,0\rangle_{out} - |0,2_H\rangle_{out} + |2_V,0\rangle_{out} - |0,2_V\rangle_{out}),
\end{aligned}
\tag{4.23}
$$

$$
\begin{aligned}
|\Phi^-\rangle &\rightarrow \tfrac{1}{2\sqrt{2}}(\hat{b}^\dagger_{1H}\hat{b}^\dagger_{1H} - \hat{b}^\dagger_{2H}\hat{b}^\dagger_{2H} - \hat{b}^\dagger_{1V}\hat{b}^\dagger_{1V} + \hat{b}^\dagger_{2V}\hat{b}^\dagger_{2V})\,|0\rangle_{out} \\
&= \tfrac{1}{2\sqrt{2}}(|2_H,0\rangle_{out} - |0,2_H\rangle_{out} - |2_V,0\rangle_{out} + |0,2_V\rangle_{out}),
\end{aligned}
\tag{4.24}
$$

$$
\begin{aligned}
|\Psi^+\rangle &\rightarrow \tfrac{1}{\sqrt{2}}(\hat{b}^\dagger_{1H}\hat{b}^\dagger_{1V} - \hat{b}^\dagger_{2H}\hat{b}^\dagger_{2V})\,|0\rangle_{out} \\
&= \tfrac{1}{\sqrt{2}}(|1_H 1_V,0\rangle_{out} - |0,1_H 1_V\rangle_{out})
\end{aligned}
\tag{4.25}
$$

and

$$
\begin{aligned}
|\Psi^-\rangle &\rightarrow \tfrac{1}{\sqrt{2}}(\hat{b}^\dagger_{1H}\hat{b}^\dagger_{2V} - \hat{b}^\dagger_{1V}\hat{b}^\dagger_{2H})\,|0\rangle_{out} \\
&= \tfrac{1}{\sqrt{2}}(|1_H,1_V\rangle_{out} - |1_V,1_H\rangle_{out}).
\end{aligned}
\tag{4.26}
$$

The calculations give evidence that the photons only leave the beam splitter via different output ports in case they are in the $|\Psi^-\rangle$-state.

Considering the experimental detection setup introduced in subsection 2.3.5, one observes that it is possible to distinguish two of the four Bell-states due to their different evolution. The $|\Phi^\pm\rangle$-states

can not be detected because here both photons always impinge on the same detector and the detectors are not photon number resolving. Even if they would be, it would not be possible to distinguish between the $|\Phi^+\rangle$- and $|\Phi^-\rangle$-state as the detectors do not resolve the phase of this state. The $|\Psi^+\rangle$-state generates coincidences in the detector combinations $D+$ (see Table 3.1) and the $|\Psi^-\rangle$-state in the detector combinations $D-$. These cases can be distinguished. Note, the detector combinations $D\varnothing$ do not correspond to any Bell-state. Such detector combinations should never occur in a perfect two-photon interference measurement.

As already mentioned, the photons arriving at the beam splitter are completely unpolarized, and therefore the two photons impinging on the beam splitter are in a mixture of all four Bell-states. The detection of the two photons in a certain detector combination projects them onto a certain Bell-state. The whole procedure thus comprises an interferometric Bell-state measurement.

4.1.3. Two-Photon Interference Contrast

In order to quantify the quality of the two-photon interference, a measure has to be employed. In this thesis the interference contrast is used which shall be defined in the following.

The contrast relates the fraction of events in the "forbidden" detector combinations $D\varnothing$ to the events in "allowed" combinations $D+$ or $D-$:

$$C_{D+} = 1 - \frac{n_{D\varnothing}}{n_{D+}} \tag{4.27}$$

$$C_{D-} = 1 - \frac{n_{D\varnothing}}{n_{D-}}. \tag{4.28}$$

C_{D+} defines the interference contrast of photons which are projected in the $|\Psi^+\rangle$-state and C_{D-} defines the contrast of photons projected in the $|\Psi^-\rangle$-state, respectively. This definition is based on two assumptions:

1. The two photons impinging on the beam splitter are in a equal mixture of all four Bell-states.

2. All errors lowering the interference quality affect every photon pair in the same way independent of the Bell-state of the photons because only photons in the $|\Phi^\pm\rangle$-states generate coincidences in detector combinations $D\varnothing$ and only photons in the $|\Psi^\pm\rangle$-states generate coincidences in detector combinations $D+$ and $D-$ as discussed in subsection 4.2.2. Thus, it is assumed that error cause as many $D\varnothing$ coincidences of photons in the $|\Phi^\pm\rangle$-states as $D+$coincidences of photons in the $|\Psi^-\rangle$-state and wise versa.

Additionally, if the requirement of a good beam splitter is fulfilled, the contrasts C_{D+} and C_{D-} should be the same. Therefore, it is sufficient to define a joint interference contrast:

$$C = 1 - \frac{2n_{D\varnothing}}{n_{D+} + n_{D-}}, \tag{4.29}$$

which is just the average of both other contrasts.

4.2. Two-Photon Interference Under Realistic Conditions

In section 4.1 the principles of two-photon interference on a beam splitter by assuming a perfect setup were discussed. In reality the beam splitter is not a perfect $^{50}/_{50}$ beam splitter and the photons are not

completely indistinguishable. Due to technical and other reasons, the photons may have not a perfect temporal, spatial or spectral mode overlap. The influences of these errors on the interference contrast are discussed in this section.

4.2.1. Influence of a Non-Perfect Beam Splitter on the Interference Quality

In the previous section two-photon interference was introduced by the example of a perfect beam splitter. Here derivations resulting from beam splitter imperfections are investigated.

Equations 4.19 and 4.20 already show that two photons in $|\Phi^{\pm}\rangle$-states impinging on a beam splitter, which has no transmittance and reflectance of equal value ($\Theta \neq \pi/4$), may result in a $D\varnothing$ coincidence event. Furthermore, equation 4.21 shows that two photons in a $|\Psi^{+}\rangle$-state impinging on the beam splitter might be detected behind different output ports of the beam splitter, and thus are mistaken for photons in a $|\Psi^{-}\rangle$-state lowering the two-photon interference quality.

These examples illustrate the problems which arise by a non-perfect beam splitter, but it does not allow a full description of all errors caused by a beam splitter, because the transmittance and the reflectance might also depend on the polarization of the impinging photon. In order to provide a complete description of the beam splitter, the definitions of the input creation operators in terms of the output creation operators in equations 4.16 and 4.17 have to be expanded for polarization dependent transmittance and reflectance coefficients:

$$\hat{a}_{1j}^{\dagger} \rightarrow \cos(\Theta_j)\hat{b}_{1j}^{\dagger} - \sin(\Theta_j)\hat{b}_{2j}^{\dagger}, \tag{4.30}$$

$$\hat{a}_{2j}^{\dagger} \rightarrow \sin(\Theta_j)\hat{b}_{1j}^{\dagger} + \cos(\Theta_j)\hat{b}_{2j}^{\dagger}, \tag{4.31}$$

where $j \in \{H, V\}$ denotes the polarization of the impinging photon. Using this new set of creation operators the evolutions of the Bell-states at the beam splitter are the following:

$$
\begin{aligned}
|\Phi^{+}\rangle &= \tfrac{1}{\sqrt{2}}(\hat{a}_{1H}^{\dagger}\hat{a}_{2H}^{\dagger} + \hat{a}_{1V}^{\dagger}\hat{a}_{2V}^{\dagger})\,|0\rangle_{in} \\
&\rightarrow \tfrac{1}{\sqrt{2}}(\cos(\Theta_H)\sin(\Theta_H)(\hat{b}_{1H}^{\dagger}\hat{b}_{1H}^{\dagger} - \hat{b}_{2H}^{\dagger}\hat{b}_{2H}^{\dagger}) + \cos(\Theta_V)\sin(\Theta_V)(\hat{b}_{1V}^{\dagger}\hat{b}_{1V}^{\dagger} - \hat{b}_{2V}^{\dagger}\hat{b}_{2V}^{\dagger}) \\
&\quad + \cos(2\Theta_H)\hat{b}_{1H}^{\dagger}\hat{b}_{2H}^{\dagger} + \cos(2\Theta_V)\hat{b}_{1V}^{\dagger}\hat{b}_{2V}^{\dagger})\,|0\rangle_{out}\,,
\end{aligned}
\tag{4.32}
$$

$$
\begin{aligned}
|\Phi^{-}\rangle &= \tfrac{1}{\sqrt{2}}(\hat{a}_{1H}^{\dagger}\hat{a}_{2H}^{\dagger} - \hat{a}_{1V}^{\dagger}\hat{a}_{2V}^{\dagger})\,|0\rangle_{in} \\
&\rightarrow \tfrac{1}{\sqrt{2}}(\cos(\Theta_H)\sin(\Theta_H)(\hat{b}_{1H}^{\dagger}\hat{b}_{1H}^{\dagger} - \hat{b}_{2H}^{\dagger}\hat{b}_{2H}^{\dagger}) - \cos(\Theta_V)\sin(\Theta_V)(\hat{b}_{1V}^{\dagger}\hat{b}_{1V}^{\dagger} - \hat{b}_{2V}^{\dagger}\hat{b}_{2V}^{\dagger}) \\
&\quad + \cos(2\Theta_H)\hat{b}_{1H}^{\dagger}\hat{b}_{2H}^{\dagger} - \cos(2\Theta_V)\hat{b}_{1V}^{\dagger}\hat{b}_{2V}^{\dagger})\,|0\rangle_{out}\,,
\end{aligned}
\tag{4.33}
$$

$$
\begin{aligned}
|\Psi^{+}\rangle &= \tfrac{1}{\sqrt{2}}(\hat{a}_{1H}^{\dagger}\hat{a}_{2V}^{\dagger} + \hat{a}_{1V}^{\dagger}\hat{a}_{2H}^{\dagger})\,|0\rangle_{in} \\
&\rightarrow \tfrac{1}{\sqrt{2}}((\cos(\Theta_H)\sin(\Theta_V) + \sin(\Theta_H)\cos(\Theta_V))\hat{b}_{1H}^{\dagger}\hat{b}_{1V}^{\dagger} \\
&\quad -(\cos(\Theta_H)\sin(\Theta_V) + \sin(\Theta_H)\cos(\Theta_V))\hat{b}_{2H}^{\dagger}\hat{b}_{2V}^{\dagger} \\
&\quad +(\cos(\Theta_H)\cos(\Theta_V) - \sin(\Theta_H)\sin(\Theta_V))\hat{b}_{1H}^{\dagger}\hat{b}_{2V}^{\dagger} \\
&\quad +(\cos(\Theta_H)\cos(\Theta_V) - \sin(\Theta_H)\sin(\Theta_V))\hat{b}_{2H}^{\dagger}\hat{b}_{1V}^{\dagger})\,|0\rangle_{out}
\end{aligned}
\tag{4.34}
$$

and

$$
\begin{aligned}
|\Psi^-\rangle \;=\;& \tfrac{1}{\sqrt{2}}(\hat{a}^\dagger_{1H}\hat{a}^\dagger_{2V} - \hat{a}^\dagger_{1V}\hat{a}^\dagger_{2H})\,|0\rangle_{in} \\
\to\;& \tfrac{1}{\sqrt{2}}((\cos(\Theta_H)\sin(\Theta_V) - \sin(\Theta_H)\cos(\Theta_V))\hat{b}^\dagger_{1H}\hat{b}^\dagger_{1V} \\
& +(\cos(\Theta_H)\sin(\Theta_V) - \sin(\Theta_H)\cos(\Theta_V))\hat{b}^\dagger_{2H}\hat{b}^\dagger_{2V} \\
& +(\cos(\Theta_H)\cos(\Theta_V) + \sin(\Theta_H)\sin(\Theta_V))\hat{b}^\dagger_{1H}\hat{b}^\dagger_{2V} \\
& -(\cos(\Theta_H)\cos(\Theta_V) + \sin(\Theta_H)\sin(\Theta_V))\hat{b}^\dagger_{2H}\hat{b}^\dagger_{1V})\,|0\rangle_{out}\,.
\end{aligned}
\tag{4.35}
$$

In the experiments only the $|\Psi^\pm\rangle$-states are of importance because only they can be detected. Thus, in order to define a measure for the beam splitter quality, two-photon detection events in the $D-$ detector combinations are examined. These can only be caused by two photons in the $|\Psi^\pm\rangle$-states imping on the beam splitter.

Two photons being in a $|\Psi^-\rangle$-state are detected in a $D-$ detector combination with the following probability (with respect equation 4.35):

$$
\begin{aligned}
P^{D-}_{\Psi^-} \;=\;& |\tfrac{1}{\sqrt{2}}(\cos(\Theta_H)\cos(\Theta_V) + \sin(\Theta_H)\sin(\Theta_V))|^2 \\
& +|-\tfrac{1}{\sqrt{2}}(\cos(\Theta_H)\cos(\Theta_V) + \sin(\Theta_H)\sin(\Theta_V))|^2 \\
=\;& |\cos(\Theta_H - \Theta_V)|^2
\end{aligned}
\tag{4.36}
$$

By detection of the two photons in a $D-$ detector combination, they are correctly identified as photons in the $|\Psi^-\rangle$-state. If two photons, which are prepared in a $|\Psi^+\rangle$-state, impinge on the beam splitter, the probability for a detection in a $D-$ detector combination is (derived from equation 4.34):

$$
\begin{aligned}
P^{D-}_{\Psi^+} \;=\;& 2\,|\tfrac{1}{\sqrt{2}}(\cos(\Theta_H)\cos(\Theta_V) - \sin(\Theta_H)\sin(\Theta_V))|^2 \\
=\;& |\cos(\Theta_H + \Theta_V)|^2
\end{aligned}
\tag{4.37}
$$

Here, the coincidence in a detector combination $D-$ leads to a false identification. The photons are identified as photons in th $|\Psi^-\rangle$-state which is orthogonal to the one they were prepared in.

The total probability to correctly identify the two-photon state with the given beam splitter is defined as beam splitter quality factor $BSQ \in [0...1]$ [82]:

$$
BSQ = \frac{P^{D-}_{\Psi^-}}{P^{D-}_{\Psi^-} + P^{D-}_{\Psi^+}} = \frac{|\cos(\Theta_H - \Theta_V)|^2}{|\cos(\Theta_H - \Theta_V)|^2 + |\cos(\Theta_H + \Theta_V)|^2}.
\tag{4.38}
$$

By substituting Θ_j for the transmittance σ_j ($\Theta_j = \arccos(\sqrt{\sigma_j})$, $j \in \{H,V\}$) the expression is written in terms of a directly measurable parameter:

$$
BSQ = \frac{\sigma_H\sigma_V + (1-\sigma_H)(1-\sigma_V) + 2\sqrt{\sigma_H(1-\sigma_H)\sigma_V(1-\sigma_V)}}{2(\sigma_H\sigma_V + (1-\sigma_H)(1-\sigma_V))}.
\tag{4.39}
$$

This can be further simplified by introducing also the reflectance to the equation as given by equation 4.1:

$$
BSQ = \frac{\sigma_H\sigma_V + \rho_H\rho_V + 2\sqrt{\sigma_H\rho_H\sigma_V\rho_V}}{2(\sigma_H\sigma_V + \rho_H\rho_V)} = \frac{1}{2}\left(1 + \frac{2\sqrt{\sigma_H\rho_H\sigma_V\rho_V}}{\sigma_H\sigma_V + \rho_H\rho_V}\right).
\tag{4.40}
$$

The BSQ yields a value of 1, if the constraint $\sigma_H = \rho_V$ is fulfilled. It shows that even a symmetric, partially polarizing beam splitter does not affect the interference quality. However, it reduces the frequency of events in $D-$ detector combinations. Therefore, a perfect 50/50 beam splitter is still favorable.

4.2.2. Influence of the Temporal Mode Overlap on the Interference Contrast

All previous calculations assumed that the two interfering photons have identical temporal, spectral and spatial properties and arrive at the beam splitter at the same time. But this is not a realistic assumption for a real experiment due to technical limitations. In this subsection the influence of a non perfect temporal mode overlap on the interference contrast is examined. The following subsections discuss the influences of the spectral and spatial mode overlaps.

In order to account for the temporal shape of the photons, a set of time dependent creation and annihilation operators is needed [83]:

$$\hat{A}_{ij}(\alpha) = \int\limits_{0}^{\infty} dt\, \alpha_i^{\star}(t)\hat{a}_{ij}(t), \tag{4.41}$$

$$\hat{A}_{ij}^{\dagger}(\alpha) = \int\limits_{0}^{\infty} dt\, \alpha_i(t)\hat{a}_{ij}^{\dagger}(t), \tag{4.42}$$

where $i \in \{1,2\}$ denotes the input port of the beam splitter and $j \in \{H,V\}$ the polarization of the photon. $\alpha_i(t) \in \mathbb{C}$ describes the temporal amplitude of the single photon wave packet. It is normalized according to

$$\int dt\, |\alpha_i(t)|^2 = 1. \tag{4.43}$$

This allows the following description of the input creation operations in terms of the output creation operators for a non-polarizing beam splitter:

$$\hat{A}_{1j}^{\dagger}(\alpha_1) \to \int\limits_{0}^{\infty} dt\, \alpha_1(t)(\cos(\Theta)\hat{b}_{1j}^{\dagger}(t) - \sin(\Theta)\hat{b}_{2j}^{\dagger}(t)), \tag{4.44}$$

$$\hat{A}_{2j}^{\dagger}(\alpha_2) \to \int\limits_{0}^{\infty} dt\, \alpha_2(t)(\sin(\Theta)\hat{b}_{1j}^{\dagger}(t) + \cos(\Theta)\hat{b}_{2j}^{\dagger}(t)). \tag{4.45}$$

The input and output operators have the same commutation properties:

$$[\hat{a}_{ij}(t), \hat{a}_{i'j'}^{\dagger}(t')] = [\hat{b}_{ij}(t), \hat{b}_{i'j'}^{\dagger}(t')] = \delta_{ii'}\delta_{jj'}\delta(t - t'). \tag{4.46}$$

Unlike the approach of the previous sections, it is more reasonable to calculate the expected two-photon probability for certain detector combinations rather than to calculate the output state for a certain two-photon input state, in order to understand the influence of the temporal mode overlap on the two-photon interference. The expected single photon probability in a time interval $[0, T]$ is:

$$\langle m_{ij}(T)\rangle = \int\limits_{0}^{T} d\tau\, \langle \hat{b}_{ij}^{\dagger}(\tau)\hat{b}_{ij}(\tau)\rangle. \tag{4.47}$$

Here, the detection efficiency is assumed to be equal to one. The expected two-photon probability is calculated the same as way for two photons impinging on the same detector:

$$\langle m_{ij}(T)m_{ij}(T)\rangle = \frac{1}{2}\int\limits_{0}^{T} d\tau \int\limits_{0}^{T} d\tau'\, \langle \hat{b}_{ij}^{\dagger}(\tau')\hat{b}_{ij}^{\dagger}(\tau)\hat{b}_{ij}(\tau)\hat{b}_{ij}(\tau')\rangle \tag{4.48}$$

as well as for two photons impinging on different detectors:

$$\langle m_{ij}(T) m_{i'j'}(T) \rangle = \int_0^T d\tau \int_0^T d\tau' \, \langle \hat{b}_{i'j'}^\dagger(\tau') \hat{b}_{ij}^\dagger(\tau) \hat{b}_{ij}(\tau) \hat{b}_{i'j'}(\tau') \rangle. \tag{4.49}$$

This allows calculation of the evolution of two photons, which do not have a perfect temporal mode overlap, at a beam splitter. Next the evolution is exemplarily presented for the $|\Phi^+\rangle$-state:

$$\begin{aligned}
|\Phi^+\rangle &= \tfrac{1}{\sqrt{2}} (\hat{A}_{1H}^\dagger(\alpha_1) \hat{A}_{2H}^\dagger(\alpha_2) + \hat{A}_{1V}^\dagger(\alpha_1) \hat{A}_{2V}^\dagger(\alpha_2)) \, |0\rangle_{in} \\
&\rightarrow \tfrac{1}{\sqrt{2}} \int_0^\infty dt \int_0^\infty dt' \, \alpha_1(t) \alpha_2(t') \\
&\quad ((\cos(\Theta) \hat{b}_{1H}^\dagger(t) - \sin(\Theta) \hat{b}_{2H}^\dagger(t))(\sin(\Theta) \hat{b}_{1H}^\dagger(t') + \cos(\Theta) \hat{b}_{2H}^\dagger(t')) \\
&\quad + (\cos(\Theta) \hat{b}_{1V}^\dagger(t) - \sin(\Theta) \hat{b}_{2V}^\dagger(t))(\sin(\Theta) \hat{b}_{1V}^\dagger(t') + \cos(\Theta) \hat{b}_{2V}^\dagger(t'))) \, |0\rangle_{out}.
\end{aligned} \tag{4.50}$$

The probability for two photons impinging on the same detector is calculated exemplarily for the detector $APD_{1\parallel}$ which corresponds to the creation operator $\hat{b}_{1H}^\dagger(t)$. By requiring that the amplitudes $\alpha_i(t)$ of the single photon wave packets are negligible outside the detection time interval $[0, T]$, the following result is obtained with respect to equation 4.48:

$$\begin{aligned}
\langle m_{1H}(T) m_{1H}(T) \rangle_{|\Phi^+\rangle} &= \tfrac{1}{2} \int_0^T d\tau \int_0^T d\tau' \, \langle \Phi^+ | \hat{b}_{1H}^\dagger(\tau) \hat{b}_{1H}^\dagger(\tau') \hat{b}_{1H}(\tau) \hat{b}_{1H}(\tau') | \Phi^+ \rangle \\
&= \tfrac{1}{2} \sin^2(\Theta) \cos^2(\Theta)(1 + \int_0^T dt \int_0^T dt' \, \alpha_2^\star(t) \alpha_1^\star(t') \alpha_1(t) \alpha_2(t') \\
&= \tfrac{1}{2} \sin^2(\Theta) \cos^2(\Theta)(1 + |\int_0^T dt \, \alpha_1^\star(t) \alpha_2(t)|^2).
\end{aligned} \tag{4.51}$$

Analogously, the probability for two-photon impinging on different detectors can be obtained with respect to equation 4.49. Here, it is exemplarily calculated for the detector combination $APD_{1\parallel}$, $APD_{2\parallel}$ which corresponds to the creation operators $\hat{b}_{1H}^\dagger(t)$ and $\hat{b}_{2H}^\dagger(t)$:

$$\begin{aligned}
\langle m_{1H}(T) m_{2H}(T) \rangle_{|\Phi^+\rangle} &= \int_0^T d\tau \int_0^T d\tau' \, \langle \Phi^+ | \hat{b}_{1H}^\dagger(\tau) \hat{b}_{2H}^\dagger(\tau') \hat{b}_{1H}(\tau) \hat{b}_{2H}(\tau') | \Phi^+ \rangle \\
&= \tfrac{1}{2} \sin^4(\Theta) + \cos^4(\Theta) - \sin^2(\Theta) \cos^2(\Theta) | \int_0^T dt \, \alpha_1^\star(t) \alpha_2(t)|^2.
\end{aligned} \tag{4.52}$$

The evolution of the other three Bell-states at the beam splitter can be calculated the very same way. Table 4.1 shows the coincidences generated by photons in one of the four Bell-states with their respective probability. All non zero results depend on the term $|\int_0^T dt \, \alpha_1^\star(t) \alpha_2(t)|^2$ which describes the temporal mode overlap of the two single photon wave packets. For perfect overlap the photons would generate the coincidences introduced in section 4.1.2. Otherwise there is a final probability to detect two photons which are in a $|\Psi^+\rangle$-state in detector combinations $D-$, which is assigned to the $|\Psi^-\rangle$-state, and vise versa. In the same way two photons in a $|\Phi^\pm\rangle$-state can be detected in detector combinations $D\varnothing$. For 0 mode overlap the term $|\int_0^T dt \, \alpha_1^\star(t) \alpha_2(t)|^2$ is zero, and the $|\Psi^\pm\rangle$-stats distribute each equally over the detector combinations $D-$ and $D+$ and the $|\Phi^\pm\rangle$-state over the detector combinations $D\varnothing$ and the not detectable detector combinations (white noise). In this case there is no interference. Thus, the mode overlap of the two single photon wave packets has a major influence on the two-photon interference contrast.

According to equation 4.29 the joined interference contrast is defined by the number of two-photon events in the detector combinations $D-$,$D+$ and $D\varnothing$. It can be written down in terms of the coincidence probabilities presented in table 4.1:

$$C = 1 - \frac{2n_{D\varnothing}}{n_{D+} + n_{D-}} = \frac{4 \sin^4(\Theta) + 4 \cos^4(\Theta) - 8 \sin^2(\Theta) \cos^2(\Theta) | \int_0^T dt \, \alpha_1^\star(t) \alpha_2(t)|^2}{2 \sin^4(\Theta) + 2 \cos^4(\Theta) + 4 \sin^2(\Theta) \cos^2(\Theta)} \tag{4.53}$$

Bell-state	det. comb.	mean two-photon count in detection time window $[0, T]$
$\lvert\Phi^+\rangle$	$D-$	0
	$D+$	0
	$D\varnothing$	$\sin^4(\Theta) + \cos^4(\Theta) - 2\sin^2(\Theta)\cos^2(\Theta)\lvert\int_0^T dt\,\alpha_1^\star(t)\alpha_2(t)\rvert^2$
	$n.d.$	$2\sin^2(\Theta)\cos^2(\Theta)(1 + \lvert\int_0^T dt\,\alpha_1^\star(t)\alpha_2(t)\rvert^2)$
$\lvert\Phi^-\rangle$	$D-$	0
	$D+$	0
	$D\varnothing$	$\sin^4(\Theta) + \cos^4(\Theta) - 2\sin^2(\Theta)\cos^2(\Theta)\lvert\int_0^T dt\,\alpha_1^\star(t)\alpha_2(t)\rvert^2$
	$n.d.$	$2\sin^2(\Theta)\cos^2(\Theta)(1 + \lvert\int_0^T dt\,\alpha_1^\star(t)\alpha_2(t)\rvert^2)$
$\lvert\Psi^+\rangle$	$D-$	$\sin^4(\Theta) + \cos^4(\Theta) - 2\sin^2(\Theta)\cos^2(\Theta)\lvert\int_0^T dt\,\alpha_1^\star(t)\alpha_2(t)\rvert^2$
	$D+$	$2\sin^2(\Theta)\cos^2(\Theta)(1 + \lvert\int_0^T dt\,\alpha_1^\star(t)\alpha_2(t)\rvert^2)$
	$D\varnothing$	0
	$n.d.$	0
$\lvert\Psi^-\rangle$	$D-$	$\sin^4(\Theta) + \cos^4(\Theta) + 2\sin^2(\Theta)\cos^2(\Theta)\lvert\int_0^T dt\,\alpha_1^\star(t)\alpha_2(t)\rvert^2$
	$D+$	$2\sin^2(\Theta)\cos^2(\Theta)(1 - \lvert\int_0^T dt\,\alpha_1^\star(t)\alpha_2(t)\rvert^2)$
	$D\varnothing$	0
	$n.d.$	0

Table 4.1.: This table shows the evolution of two photons in a certain Bell-state at a non-polarizing beam splitter. The coincidence probability for each Bell state is listed for every class of detector combinations with respect to the reflectance and transmittance of the beam splitter and the temporal mode overlap of the two photon wave packets. n.d. is for the not detectable detector combinations (both photons impinge on the same detector)

This expression simplifies in case a perfect beam splitter is assumed, which is realistic with respect to subsection 4.5.4:

$$C = \lvert \int_0^T dt\,\alpha_1^\star(t)\alpha_2(t)\rvert^2. \tag{4.54}$$

In this case the contrast is equal to the expectation value of the overlap of the two single photon wave packets.

The expected probability to correctly identify the two-photon state (P^{tmo}) can be calculated the same way as in the previous subsection. The probabilities $P_{\Psi\pm}^{D-}$ to detect two photons in the detector combinations $D-$, which are in the $\lvert\Psi^-\rangle$- or in the $\lvert\Psi^+\rangle$-state, are defined by the mean two photon counts in table 4.1. Thus, the probability is given by

$$P^{tmo} = \frac{P_{\Psi-}^{D-}}{P_{\Psi-}^{D-} + P_{\Psi+}^{D-}} = \frac{\sin^4(\Theta) + \cos^4(\Theta) + 2\sin^2(\Theta)\cos^2(\Theta)\lvert\int_0^T dt\,\alpha_1^\star(t)\alpha_2(t)\rvert^2}{2\sin^4(\Theta) + 2\cos^4(\Theta)}. \tag{4.55}$$

In case of a perfect beam splitter, this term can be simplified to the following expression:

$$P^{tmo} = 0.5 \cdot (1 + \lvert \int_0^T dt\,\alpha_1^\star(t)\alpha_2(t)\rvert^2) \tag{4.56}$$

It shows that also this expression is directly related to the expectation value of the overlap of the two single photon wave packets. Therefore, it is inalienable to secure a high temporal mode overlap in the experiment.

4.2.3. Influence of the Spectral Mode Overlap on the Interference Contrast

The two single photon wave packets which impinge on the beam splitter may have different spectra caused by three main reasons [84]:

1. Doppler broadening due to thermal motions of the atoms.

2. The Zeeman states of the ground state shift because of external magnetic fields.

3. One photon is excited via an off-resonant transition and decays into a different ground state.

In this subsection these three reasons for a non perfect spectral mode overlap of the two single photon wave packets are described in detail followed by discussion of their influence on the two-photon inference contrast.

The finite temperature of the two trapped atoms causes a residual motion of each atom in its dipole trap. The motion along the axis, in which the single photons are collected, leads to a first-order Doppler shift, whereas the motion orthogonal to this axis leads to relativistic higher-order shifts which are negligible. Thus, only the distribution of the motion of the atom along the collection axis contributes to the considered Doppler broadening. The trapping potential can be assumed to be harmonic because the thermal energy of the atom is much lower than the depth of the dipole trap. Therefore, the distribution of the kinetic energy is equal to the one of a one dimensional harmonic oscillator in thermal equilibrium:

$$p(E_{kin}) = \frac{1}{\sqrt{\pi}} \frac{1}{\sqrt{k_B T}} \frac{1}{\sqrt{E_{kin}}} e^{-E_{kin}/k_B T}. \tag{4.57}$$

This leads to the following velocity distribution:

$$p(v) = \sqrt{\frac{m}{2\pi k_B T}} e^{-mv^2/2k_B T}, \tag{4.58}$$

with a standard deviation of $\sigma_v = \sqrt{k_B T/m}$, where m is the mass of a ^{87}Rb atom. The first-order Doppler shift is given by

$$\delta\omega = \omega \frac{v}{c}, \tag{4.59}$$

and therefore the standard deviation of the frequency distribution is given by

$$\sigma_\omega = \omega \frac{\sigma_v}{c}. \tag{4.60}$$

The relative frequency spread between the two singe photon wave packets is calculated by

$$\sigma_{\omega,rel} = \sqrt{\sigma_\omega^2 + \sigma_{\omega'}^2}. \tag{4.61}$$

External magnetic fields are the second reason for a spectral mismatch of the two single photon wave packets. They cause a first-order Zeeman shift of the two atomic ground states $5^2 S_{1/2}$, $|F = 1, m_F = \pm 1\rangle$ by $\pm 2\pi \cdot 0.7\,\mathrm{MHz}/G$, while the excited state $5^2 P_{3/2}$, $|F' = 0, m_F = 0\rangle$ is not affected by a first-order Zeeman shift (see figure 2.1). Thus, the two ground states would be no longer degenerated and the frequencies of both transitions would be different.

The third reason for a spectral mismatch of the two wave packets is an off-resonant excitation of one atom and the subsequent decay into the other ground state of this atom ($5^2S_{1/2}, |F = 2\rangle$). The frequency mismatch of the wave packets is in this case very huge. It will be further discussed in the next section.

After discussing the reasons for a frequency mismatch of the single photon wave packets, the influence of the mismatches on the spectral mode overlap of the two single photon wave packets is illustrated. In principle, the spectral mode overlap of the two wave packets is already discussed in calculations of the previous subsection as the complex function $\alpha_i(t)$ also includes the frequency range of the single photon wave packet. It can be defined as the Fourier transformed frequency dependent function $\alpha_i(\omega)$ [83]:

$$\alpha_i(t) = \sqrt{2\pi} \int d\omega\, \alpha_i(\omega) e^{-i\omega t}. \tag{4.62}$$

Thus, a mismatch of the spectral modes of the single photon wave packets directly influences the two-photon interference contrast as shown in equation 4.54 and 4.56.

In order to evaluate the influence of the above introduced reasons for a frequency mismatch separated from any temporal mode overlaps a photon wave packet is exemplarily assumed where the decay rate 2γ of the atom is much smaller than the Rabi-frequency. Thus, the wave packet can be described by an unit step function St as an approximation for the wave packet observed in the experiment offering a good impression of the influences of wave packets with different frequencies on two photon interference. Here, the temporal amplitude $\alpha_i(t)$ of the wave packet is described by the following equation:

$$\alpha_i(t) = -i\sqrt{2\gamma} e^{-\gamma(t-t_0)} e^{-i\omega_i(t-t_0)} St(t - t_0), \tag{4.63}$$

where t_0 is the time when both atoms are put into the exited state. This allows the calculation of the expectation value of the overlap:

$$| \int_{t_0}^{T} dt\, \alpha_1^\star(t)\alpha_2(t)|^2 = \frac{1}{1 + \Delta\omega^2/4\gamma^2}, \tag{4.64}$$

where the amplitudes of the wave packets outside the detection window $[t_0, T]$ are negligible, and $\Delta\omega = \omega_1 - \omega_2$ is the frequency difference of both wave packets. This serves well for the estimation of the frequency mismatch caused by a constant magnetic field and off-resonant excitation. But for estimation of the frequency mismatch caused by the Doppler shift a distribution of frequency differences $\Delta\omega$ has to be considered. With assumption of a Gaussian distribution the expectation value of spectral overlap is:

$$\frac{1}{\sqrt{2\pi}\sigma_{\omega,rel}} \int_{-\infty}^{\infty} d\Delta\omega\, \frac{1}{1 + \Delta\omega^2/4\gamma^2} e^{-\frac{\Delta\omega^2}{2\sigma_{\omega,rel}^2}}. \tag{4.65}$$

In order to calculate the maximal interference contrast possible with the already introduced reasons for a mismatch of the spectral mode overlap, the expectation value of the overlap in equations 4.54 and 4.56 has to be replaced by equation 4.64 or 4.65, respectively. This leads to the following expressions for interference contrast and the probability to correctly identify the two-photon state (P^{smo}):

$$C = \frac{1}{\sqrt{2\pi}\sigma_{\omega,rel}} \int_{-\infty}^{\infty} d\Delta\omega\, \frac{1}{1 + \Delta\omega^2/4\gamma^2} e^{-\frac{\Delta\omega^2}{2\sigma_{\omega,rel}^2}} \tag{4.66}$$

$$P^{smo} = 0.5 \cdot (1 + \frac{1}{\sqrt{2\pi}\sigma_{\omega,rel}} \int\limits_{-\infty}^{\infty} d\Delta\omega \, \frac{1}{1 + \Delta\omega^2/4\gamma^2} e^{-\frac{\Delta\omega^2}{2\sigma_{\omega,rel}^2}}). \tag{4.67}$$

A frequency mismatch of the two photon wave packets also causes a time dependence of the bunching probability. This leads to an expected two-photon probability for certain detector combination, which depends on the detection time difference of the two photons. In order to calculate this dependence, equations 4.48 and 4.49 have to be rewritten:

$$\langle m_{ij}(T)m_{ij}(T+\Delta t)\rangle = \frac{1}{2} \int\limits_{0}^{T} d\tau \, \langle \hat{b}_{ij}^{\dagger}(\tau+\Delta t)\hat{b}_{ij}^{\dagger}(\tau)\hat{b}_{ij}(\tau)\hat{b}_{ij}(\tau+\Delta t)\rangle, \tag{4.68}$$

$$\langle m_{ij}(T)m_{i'j'}(T+\Delta t)\rangle = \int\limits_{0}^{T} d\tau \, \langle \hat{b}_{i'j'}^{\dagger}(\tau+\Delta t)\hat{b}_{ij}^{\dagger}(\tau)\hat{b}_{ij}(\tau)\hat{b}_{i'j'}(\tau+\Delta t)\rangle. \tag{4.69}$$

Thus, the overlap integral $\int_{0}^{T} dt \, \alpha_1^{\star}(t)\alpha_2(t)$ presented in the results in table 4.1 is replaced by:

$$\int\limits_{0}^{T} dt \, \alpha_2^{\star}(t)\alpha_1^{\star}(t+\Delta t)\alpha_1(t)\alpha_2(t+\Delta t). \tag{4.70}$$

If $\alpha_1(t) = \alpha_2(t)$, this expression represents the convolution of the detection time probabilities of two identical photons. But if the two single photon wave packets have different frequencies, the expression is more complicated. If the temporal shape, which is defined by equation 4.63, is applied to equation 4.70, this expression reduces to the following term:

$$\int\limits_{t_0}^{T} dt \, 4\gamma^2 e^{4\gamma(t_0-t)-2\gamma\Delta t} e^{i\Delta\omega\Delta t} = \gamma e^{-2\gamma\Delta t} e^{i\Delta\omega\Delta t}. \tag{4.71}$$

Equation 4.71 indicates that the two-photon coincidence probability for photons with a frequency difference of $\Delta\omega$, oscillate with the detection time difference of both photons. Table 4.2 shows this probabilities for photons with a detection time difference of Δt and a frequency difference of $\Delta\omega$ for every detector combination and each two-photon input state.

The two-photon count coincidence probability as function of the detection time difference of the two photons presented in table 4.2 is directly measurable. Therefore, it is a good alternative in order to check for frequency differences of the two single photon wave packets. Note, only the detector combinations $D\varnothing$ show observable oscillations. The other two detectable detector combinations just exchange two-photon events as indicated by table 4.2.

4.2.4. Influence of the Spatial Mode Overlap on the Interference Contrast

A non perfect spatial mode overlap of the two single photon wave packets reduces the maximal achievable interference contrast analogously to the discussions in the previous subsections.

However, this experiment uses a single mode fiber beam splitter as introduced in subsection 2.3.5. This kind of fiber beam splitter guaranties a perfect spatial mode overlap of the two single photon wave packets, and therefore the interference contrast is not reduced by any spatial mode mismatches.

Bell-state	det. comb.	mean two-photon count
$|\Phi^+\rangle$	$D-$	0
	$D+$	0
	$D\varnothing$	$\sin^4(\Theta) + \cos^4(\Theta) - 2\sin^2(\Theta)\cos^2(\Theta)\gamma e^{-2\gamma\Delta t}\cos(\Delta\omega\Delta t)$
	$n.d.$	$2\sin^2(\Theta)\cos^2(\Theta)(1 + \gamma e^{-2\gamma\Delta t}\cos(\Delta\omega\Delta t))$
$|\Phi^-\rangle$	$D-$	0
	$D+$	0
	$D\varnothing$	$\sin^4(\Theta) + \cos^4(\Theta) - 2\sin^2(\Theta)\cos^2(\Theta)\gamma e^{-2\gamma\Delta t}\cos(\Delta\omega\Delta t)$
	$n.d.$	$2\sin^2(\Theta)\cos^2(\Theta)(1 + \gamma e^{-2\gamma\Delta t}\cos(\Delta\omega\Delta t))$
$|\Psi^+\rangle$	$D-$	$\sin^4(\Theta) + \cos^4(\Theta) - 2\sin^2(\Theta)\cos^2(\Theta)\gamma e^{-2\gamma\Delta t}\cos(\Delta\omega\Delta t)$
	$D+$	$2\sin^2(\Theta)\cos^2(\Theta)(1 + \gamma e^{-2\gamma\Delta t}\cos(\Delta\omega\Delta t))$
	$D\varnothing$	0
	$n.d.$	0
$|\Psi^-\rangle$	$D-$	$\sin^4(\Theta) + \cos^4(\Theta) + 2\sin^2(\Theta)\cos^2(\Theta)\gamma e^{-2\gamma\Delta t}\cos(\Delta\omega\Delta t)$
	$D+$	$2\sin^2(\Theta)\cos^2(\Theta)(1 - \gamma e^{-2\gamma\Delta t}\cos(\Delta\omega\Delta t))$
	$D\varnothing$	0
	$n.d.$	0

Table 4.2.: This table shows the time-dependent evolution of two photons in a certain Bell-state at a non polarizing beam splitter. The coincidence probability for every detection time difference of the two photons is listed for every class of detector combinations with respect to the reflectance and transmittance of the beam splitter and the frequency difference of the two photon wave packets. n.d. stands for the not detectable detector combinations (both photons impinge on the same detector)

4.3. Model for Analysis of Two-Photon Interference Measurements

A two-photon interference experiment is influenced by two-photon emission events as discussed in the previous section. These events cause specific detector coincidences (colored noise) in every basis of photon analysis (see chapter 3). Therefore, the measured interference contrast C, defined in section 4.1, would be different for different bases of photon analysis emphasizing its limited validity. The fraction of photon pairs P_{int} impinging on the beam splitter, which show interference, provides a more significant number. It does not only involve coincidence detections but all photon pairs impinging on the beam splitter and entering the detection setup. Thus, even photon pairs which impinge on one detector are taken into account. This is imported because the probability to detected a two-photon emission event is different in the two measurement bases as especially the relative amount of those events, which impinge on the same detector, differs (see 3.5.4). Only by taking into account all photon pairs, a statement about the interference quality, which is independent of the measurement basis, can be made.

The considerations in section 4.2 show that two photons at a beam splitter, which originate from two different atoms, have an interference probability according to their mode overlap. Thus, in case of a perfect mode overlap, the photons interfere perfectly, and only cause detection events, which correspond to a Bell-state, as shown in table 4.1. But in case of a non perfect mode overlap, the

photons have a reduced interference probability. Then, photons in a $|\Phi^{\pm}\rangle$-state may impinge on $D\varnothing$ detector combinations , photons in a $|\Psi^+\rangle$-state may cause detection events in $D-$ detector combinations and photons in a $|\Psi^-\rangle$-state may be detected in $D+$ detector combinations. In case of zero mode overlap, coincidences in all detector combinations have the same probability (white noise) as the photons are in an equal mixture of all four Bell-states. In summary, a reduced mode overlap causes background events like white noise.

The discussion above shows, that the photons impinging on the beam splitter can be divided into three categories. In the following a photon arriving at the beam splitter is labeled by a full dot ($\bullet$) as well as a photon not arriving at the beam splitter by an empty dot ($\circ$), respectively as graphical short notation:

1. Photons, which perfectly interfere, and only cause coincidences in detector combinations which correspond to an Bell-state (P_{int}).

2. Photons, which do not interfere because of a reduced mode overlap, and cause the same coincidences as white noise (P_{ni}).

3. Photons, which originate from a two photon emission event, and cause colored noise ($P_{\bullet\bullet|\circ}$).

All the categories have a specific probability ($p_{\bullet\bullet|\circ}^{d,b}$, p_{int}^d and p_{ni}^d with $d \in \{D+, D-, D\varnothing\}$ and $b \in \{HV, RL\}$) to cause a given two-photon coincidence. These probabilities are shown in table 4.3.

involved det. \ tp effect		$p_{\bullet\bullet|\circ}^{d,HV}$	$p_{\bullet\bullet|\circ}^{d,RL}$	p_{int}^d	p_{ni}^d
$APD_{1\perp}, APD_{2\parallel}$ $APD_{1\parallel}, APD_{2\perp}$	$D-$	$\frac{1}{4}p_{\mathrm{I}}^{\sigma^{\pm}} + (\frac{1}{2}p_b + \frac{1}{4}p_c)p_{\mathrm{II}}^{\sigma^{\pm}}$	$\frac{1}{4}p_{\mathrm{I}}^{\sigma^{\pm}} + (\frac{1}{2}p_a + \frac{1}{2}p_b)p_{\mathrm{II}}^{\sigma^{\pm}}$	$\frac{1}{4}$	$\frac{1}{4}$
$APD_{1\perp}, APD_{1\parallel}$ $APD_{2\parallel}, APD_{2\perp}$	$D+$	$\frac{1}{4}p_{\mathrm{I}}^{\sigma^{\pm}} + (\frac{1}{2}p_b + \frac{1}{4}p_c)p_{\mathrm{II}}^{\sigma^{\pm}}$	$\frac{1}{4}p_{\mathrm{I}}^{\sigma^{\pm}} + (\frac{1}{2}p_a + \frac{1}{2}p_b)p_{\mathrm{II}}^{\sigma^{\pm}}$	$\frac{1}{4}$	$\frac{1}{4}$
$APD_{1\perp}, APD_{2\perp}$ $APD_{2\parallel}, APD_{1\parallel}$	$D\varnothing$	$\frac{1}{4}p_{\mathrm{I}}^{\sigma^{\pm}} + (\frac{1}{2}p_a + \frac{1}{4}p_c)p_{\mathrm{II}}^{\sigma^{\pm}}$	$\frac{1}{4}p_{\mathrm{I}}^{\sigma^{\pm}} + \frac{1}{2}p_c p_{\mathrm{II}}^{\sigma^{\pm}}$	0	$\frac{1}{4}$
$APD_{1\perp}, APD_{1\perp}$ $APD_{2\perp}, APD_{2\perp}$ $APD_{1\parallel}, APD_{1\parallel}$ $APD_{2\parallel}, APD_{2\parallel}$	$n.d.$	$\frac{1}{4}p_{\mathrm{I}}^{\sigma^{\pm}} + (\frac{1}{2}p_a + \frac{1}{4}p_c)p_{\mathrm{II}}^{\sigma^{\pm}}$	$\frac{1}{4}p_{\mathrm{I}}^{\sigma^{\pm}} + \frac{1}{2}p_c p_{\mathrm{II}}^{\sigma^{\pm}}$	$\frac{1}{2}$	$\frac{1}{4}$

Table 4.3.: This table shows probabilities $p_{\bullet\bullet|\circ}^{d,b}$, p_{int}^d and p_{ni}^d (with $d \in \{D+, D-, D\varnothing\}$ and $b \in \{HV, RL\}$) to generate a specific detector coincidence for all three categories $P_{\bullet\bullet|\circ}$, P_{int} and P_{ni}. The probabilities are derived from considerations about coincidence detections caused by two-photon emission events in the H/V- and R/L-basis presented in section 3.2.1 and 3.2.2 as well as from considerations about the influence of a reduced mode overlap of the two-photon interference probability presented in section 4.2. The values of probabilities shown in this table are each introduced in previous sections and are only summarized here: $p_a = 0.781$, $p_b = 0.031$ and $p_c = 0.188$ (see subsection 3.2.2) - $p_{\mathrm{I}}^{\sigma^{\pm}} = 0.19 \pm 0.10$ and $p_{\mathrm{II}}^{\sigma^{\pm}} = 0.81 \pm 0.10$ (see subsection 3.5.4). "n.d." stands for not detectable. The detectable fraction of these relative probabilities can be summarized as follows: $p_{\bullet\bullet|\circ}^{sum,b} = p_{\bullet\bullet|\circ}^{D+,b} + p_{\bullet\bullet|\circ}^{D-,b} + p_{\bullet\bullet|\circ}^{D\varnothing,b}$, $p_{int}^{sum} = p_{int}^{D+} + p_{int}^{D-} + p_{int}^{D\varnothing}$ and $p_{ni}^{sum} = p_{ni}^{D+} + p_{ni}^{D-} + p_{ni}^{D\varnothing}$.

In analogy to the quantitative analysis of the single photon source presented in section 3.4 the colored noise of two-photon emission events can be used to analyze two-photon interference measurements and to determine the values of the fractions P_{int}, P_{ni} and $P_{\bullet\bullet|\circ}$. The ratio of events in detector combinations $D\varnothing$ to events in all detector combinations ($D+$, $D-$ and $D\varnothing$) can be calculated from the dark count and efficiency corrected values $p_{tp}^{d,b}$ for both measurement bases. These are introduced in section 3.3 for coincidences in a two-photon emission measurement but can also be used for a two-photon interference measurement, if the probability to detect a single photon after an excitation attempt is the same for both traps. This yields a ratio based on measured coincidences.

$$\frac{p_{tp}^{D\varnothing,b}}{p_{tp}^{D+,b} + p_{tp}^{D-,b} + p_{tp}^{D\varnothing,b}} = R^b \tag{4.72}$$

with $b \in \{HV, RL\}$. It can be related to a ratio, which is based on the relative coincidence probabilities of the fractions P_{int}, P_{ni} and $P_{\bullet\bullet|\circ}$ in different detector combinations shown in table 4.3:

$$R^b \overset{!}{=} \frac{p_{\bullet\bullet|\circ}^{D\varnothing,b} P_{\bullet\bullet|\circ} + p_{int}^{D\varnothing} P_{int} + p_{ni}^{D\varnothing} P_{ni}}{p_{\bullet\bullet|\circ}^{sum,b} P_{\bullet\bullet|\circ} + p_{int}^{sum} P_{int} + p_{ni}^{sum} P_{ni}}. \tag{4.73}$$

By considering measurements in two bases and the normalization $P_{int} + P_{ni} + P_{\bullet\bullet|\circ} = 1$ this forms a solvable set of equations yielding P_{int}, P_{ni} and $P_{\bullet\bullet|\circ}$.

In case of no two-photon emission events, only a measurement in one basis of photon analysis is nessesary to solve the set of equations, and to determine P_{int} and P_{ni}. It yields

$$P_{int}^b = 1 - \frac{2 \cdot p_{tp}^{D\varnothing,b}}{p_{tp}^{D+,b} + p_{tp}^{D-,b}}, \tag{4.74}$$

which is equivalent to the interference contrast, if one uses dark count and efficiency corrected values instead of the pure count rates n_d for its calculation.

4.4. Interference Probability of Photons Originating from Two-Photon Emission Events

Two-photon emission events have a considerable influence on the effective interference results as already discussed in the previous section. But not only the detection of a two-photon emission event reduces the interference contrast, but also the detection of a single photon from one atom and the first or second photon from a two-photon emission event from the other atom influences the contrast. It is sufficient to distinguish between three cases of two-photon events:

1. events at which both photons originate from the same atom: ($\bullet \bullet | \circ$)

2. events at which a single photon from one atom and the first photon out of a two-photon emission event from the other atom impinge on the beam splitter: ($\bullet \circ | \bullet$)

3. events at which a single photon from one atom and the second photon out of a two-photon emission event from the other atom impinge on the beam splitter: ($\circ \bullet | \bullet$)

The first case shows no interference as the two involved photons have zero mode overlap (see chapter 3). The latter two cases are fundamentally different from the first case. These are still events at which two-photons impinge on the beam splitter, but here three photons are emitted altogether as also a single photon is emitted from the other atom. Contrary to the events of the first case, which show no interference at all, these events might show a reduced interference contrast. The second case contains two-photon emission events of the types I and II ($\bullet \circ_i |\bullet$) with $i \in \{$I, II$\}$ (see subsections 3.2.1 and 3.2.2), equally to the first case, whereas the third case also contains events of the type III ($\circ \bullet_i |\bullet$) with $i \in \{$I, II, III$\}$, i.e. the first emitted photon was π-polarized (see subsection 3.2.3).

Higher order multi-photon events, at which all three photons of the second or third case impinge on the beam splitter, or four photon events, at which both atoms emit two photons, are neglected as their probabilities are low compared to the probabilities of the above introduced events.

In the following subsections the relative probabilities of the three cases of two-photon events are discussed as well as the influence of the latter two cases on a two-photon interference measurement. Finally, the model presented in section 4.3 is extended in order to give an analysis of two-photon interference measurements which respects ($\bullet \circ |\bullet$)- and ($\circ \bullet |\bullet$)-events.

4.4.1. Probabilities of the Three Cases of Two-Photon Events

The three cases of two-photon events have fixed probabilities. As the probability for a ($\bullet \bullet |\circ$)-event is given by $P_{\bullet\bullet|\circ}$ calculated using the model introduced in section 4.3, the probabilities $P_{\bullet\circ|\bullet}$ and $P_{\circ\bullet|\bullet}$ of the other two cases can also be determined. In these two cases the second atom has to emit a single, $\sigma^\pm$-polarized photon in addition to the two-photon emission event of the first atom. The probability for the emission of a single, $\sigma^\pm$-polarized photon is $n_{1st} = 0.65$ (see equation F.29). Subsequently, the considerations nessesarry to calculate $P_{\bullet\circ|\bullet}$ and $P_{\circ\bullet|\bullet}$ are presented:

In case of a ($\bullet \circ |\bullet$) two-photon event, the second photon of the two-photon emission event does not impinge on the beam splitter. It need not couple into the detection fiber, and thus may also be π-polarized. Considerations in section 3.4 show that in $1/3$ of all type I and in $7/15$ of all type II two-photon emission events the second emitted photon is π-polarized. This yields the following probability of a ($\bullet \circ |\bullet$)-event:

$$P_{\bullet\circ|\bullet} = 0.65 \cdot (3/2 \cdot p_{\mathrm{I}}^{\sigma^\pm} + 15/8 \cdot p_{\mathrm{II}}^{\sigma^\pm}) \cdot P_{\bullet\bullet|\circ}. \tag{4.75}$$

Type I and type II two-photon emission events have the following relative probabilities in a two-photon event of the second case:

$$p_{\mathrm{I},\bullet\circ|\bullet} = 0.65 \cdot \frac{3 \cdot p_{\mathrm{I}}^{\sigma^\pm} \cdot P_{\bullet\bullet|\circ}}{2 \cdot P_{\bullet\circ|\bullet}} \tag{4.76}$$

and

$$p_{\mathrm{II},\bullet\circ|\bullet} = 0.65 \cdot \frac{15 \cdot p_{\mathrm{II}}^{\sigma^\pm} \cdot P_{\bullet\bullet|\circ}}{8 \cdot P_{\bullet\circ|\bullet}}, \tag{4.77}$$

where $p_{\mathrm{I}}^{\sigma^\pm}$ and $p_{\mathrm{II}}^{\sigma^\pm}$ are given in subsection 3.5.4.

In case of a ($\circ \bullet |\bullet$) two-photon event, the first photon of the two-photon emission event does not impinge on the beam splitter, and may be π-polarized. This allows type III two-photon emission events. Thus, the probability for such an event is:

$$P_{\circ\bullet|\bullet} = 0.65 \cdot (P_{\bullet\bullet|\circ} + (1 - (1 - p_{\mathrm{tp-III}})^2)), \tag{4.78}$$

where $p_{tp-\text{III}} = 0.052$ is calculated by the quantum jump model presented in appendix F (see also subsection 3.2.3). Here, type I, type II and type III two-photon emission events have the following relative probabilities:

$$p_{\text{I},\circ\bullet|\bullet} = 0.65 \cdot \frac{p_{\text{I}}^{\sigma^{\pm}} \cdot P_{\bullet\bullet|\circ}}{P_{\circ\bullet|\bullet}}, \tag{4.79}$$

$$p_{\text{II},\circ\bullet|\bullet} = 0.65 \cdot \frac{p_{\text{II}}^{\sigma^{\pm}} \cdot P_{\bullet\bullet|\circ}}{P_{\circ\bullet|\bullet}} \tag{4.80}$$

and

$$p_{\text{III},\circ\bullet|\bullet} = 0.65 \cdot \frac{1 - (1 - p_{\text{tp}-\text{III}})^2}{P_{\circ\bullet|\bullet}}. \tag{4.81}$$

In summary, the relative probabilities for the three cases of two-photon events are given by the following equation:

$$P_{\bullet\bullet|\circ} = (0.65 \cdot (^3/_2 \cdot p_{\text{I}}^{\sigma^{\pm}} + {}^{15}/_8 \cdot p_{\text{II}}^{\sigma^{\pm}}))^{-1} \cdot P_{\bullet\circ|\bullet} = 0.65^{-1} \cdot P_{\circ\bullet|\bullet} - (1 - (1 - p_{\text{tp}-\text{III}})^2) \tag{4.82}$$

4.4.2. Interference Probability of Events of the Second Case ($\bullet \circ |\bullet$)

In case of a ($\bullet\circ$)-event (only the first photon of a two-photon emission event impinges on the beam splitter) the emission of the second photon influences the temporal shape of the first emitted photon although the second photon is not even detected. Therefore, the expectation value of the temporal overlap of a photon from a ($\bullet\circ$)-event and a single photon from the other atom impinging on a beam splitter is reduced. The two photons emitted by one atom form a two-photon state $\int dt_1 dt_2 \, \alpha_i(t_1, t_2)|t_1\rangle|t_2\rangle$ (with $i \in \{$I, II$\}$ - depending on the two-photon emission type), where the first photon is emitted at time t_1, the second one at time t_2 and $\alpha_i(t_1, t_2)$ is the temporal amplitude of this state. The projection of this state on a certain emission time t_2 of the second photon yields the (pure) state $\int dt_1 \beta_i(t_1|t_2)|t_1\rangle$ for the first photon, where:

$$\beta_i(t_1|t_2) = \sqrt{\frac{|\alpha_i(t_1, t_2)|^2}{\int dt_1 \, |\alpha_i(t_1, t_2)|^2}}. \tag{4.83}$$

The temporal amplitude $\beta_i(t_1|t_2)$ describes the temporal shape of the wave packet of the first emitted photon, if the second one is emitted at a given time t_2. It differs for both involved types of two-photon emission events (I and II; see subsections 3.2.1 and 3.2.2, respectively) and it's expectation value can be calculated for both types as the full description in appendix F shows.

In detail, the quantum jump model, introduced in appendix F, allows calculation of the probability $p_{tpe,i}(t_1, t_2)$ to emit a first photon at time t_1 and the second one at time t_2 for every type of two-photon emission event (see equation F.33). This probability is plotted for two-photon emission events of types I and II in figure 4.3 and 4.4, respectively. After normalization by $n_{2nd,i}$ (see equation F.34), $p_{tpe,i}(t_1, t_2)$ corresponds to the probability distribution of $\alpha(t_1, t_2)$:

$$|\alpha(t_1, t_2)|^2 = \frac{p_{tpe,i}(t_1, t_2)}{n_{2nd,i}}. \tag{4.84}$$

This expression allows also the calculation of $\beta_i(t_1; t_2)$ with expression 4.83, and thus the calculation the overlap $O_{\bullet\circ_i|\bullet}^2(t_2)$ (see equation F.39) of the wave function of a single photon and a photon originating from a ($\bullet\circ$)-event for every emission time t_2 of the second photon. These overlaps are plotted for both types of two-photon emission events (I and II) in figure 4.5.
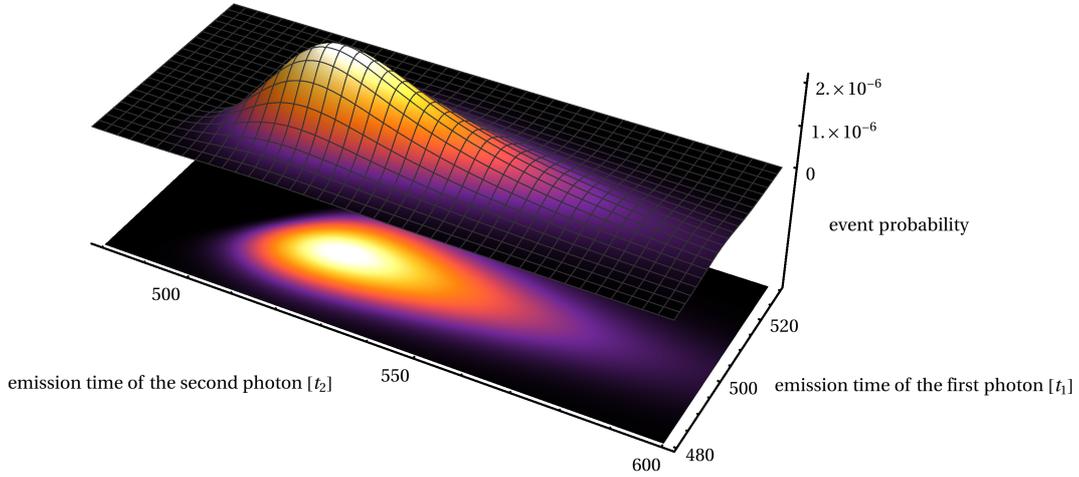
Figure 4.3.: Probability to emit a first photon at time t_1 and a second photon at time t_2 ($|\alpha_\mathrm{I}(t_1, t_2)|^2$) if the atom was excited a second time caused by imperfections of the polarization of the excitation light per excitation attempt (two-photon emission event type I). The upper plot is a 3D-Plot and the lower plot is a density plot of the same probability.
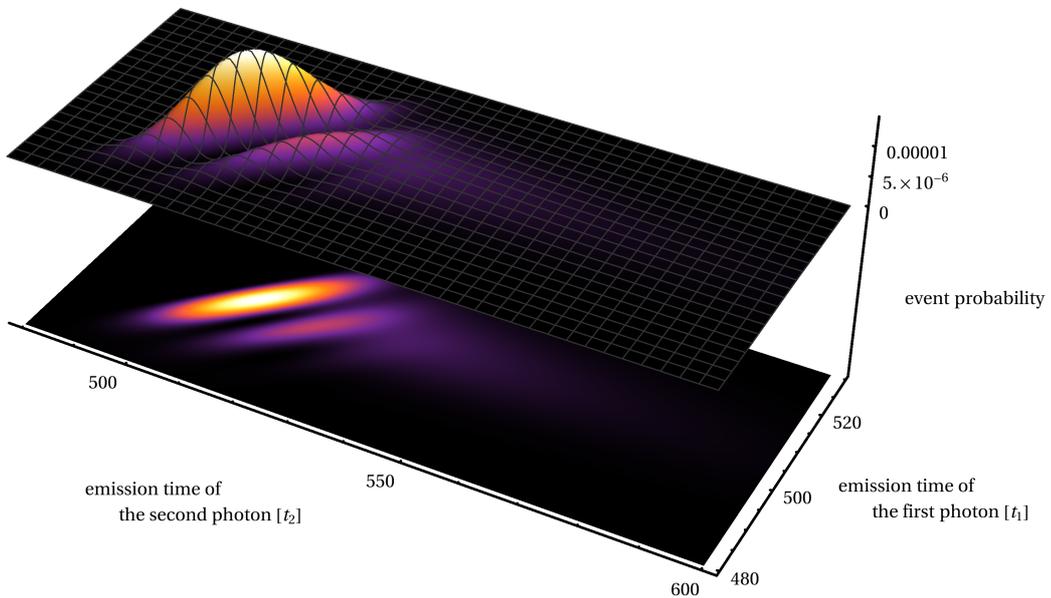
Figure 4.4.: Probability to emit a first photon at time t_1 and a second photon at time t_2 ($|\alpha_\mathrm{II}(t_1, t_2)|^2$)) if the atom was excited a second time caused by off-resonant excitation per excitation attempt (two-photon emission event type II). The upper plot is a 3D-Plot and the lower plot is a density plot of the same probability.
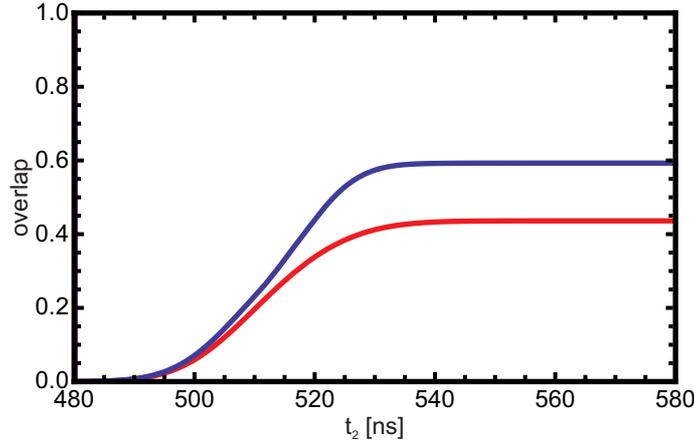
Figure 4.5.: Calculated overlap of a photon originating from ($\bullet\circ$)-event with a single photon $O^2_{\bullet\circ_I|\bullet}(t_2)$ (red) and $O^2_{\bullet\circ_{II}|\bullet}(t_2)$ (blue) against the emission time of the second photon t_2.

In order to determine the expectation value of the total mode overlap $O^2_{\bullet\circ_i|\bullet}$, the coherent overlaps ($O^2_{\bullet\circ_i|\bullet}(t_2)$) weighted with their respective probability ($p_{t_1,i}(t_2) = \int dt_1 |\alpha_i(t_1,t_2)|^2$) are summed incoherently (see equation F.40). In this experiment the results are $O^2_{\bullet\circ_I|\bullet} = 0.382$ and $O^2_{\bullet\circ_{II}|\bullet} = 0.385$.

4.4.3. Interference Probability of Events of the Third Case ($\circ \bullet |\bullet$)

For events of the third case the atom can only be excited a second time after emission of a first photon. Therefore, the temporal shape of the wave packet of a second photon originating from a ($\circ\bullet$)-event must differ from that of a single photon. Analogously to the previous subsection, the resulting two-photon state is described by $\int dt_1 dt_2 \, \alpha_i(t_1,t_2)|t_1\rangle|t_2\rangle$ (with $i \in \{\text{I, II, III}\}$), where the first photon is emitted at time t_1, the second one at time t_2 and $\alpha_i(t_1,t_2)$ is the probability amplitude of this state for every two-photon emission type i (see equation F.35). The projection on a given emission time t_1 of the first photon yields the (pure) state $\int dt_2 \beta_i(t_2|t_1)|t_2\rangle$ for the second photon, where:

$$\beta(t_2|t_1) = \sqrt{\frac{|\alpha_i(t_1,t_2)|^2}{\int dt_2 \, |\alpha_i(t_1,t_2)|^2}}. \tag{4.85}$$

In contrast to the second case, the third case of two-photon events also includes two-photon emission events of type III (see subsection 3.2.3). The probability to emit a first photon at time t_1 and a second photon at time t_2 caused by a two photon emission event of type III is given by expression $p_{tpe,\text{III}}(t_1,t_2)$ (see equation F.33). After normalization this corresponds to the expectation value the temporal amplitude $|\alpha_{\text{III}}(\tau,t)|^2$, which is shown in figure 4.6.

Furthermore, in contrast to ($\bullet \circ |\bullet$)-events the two photons impinging on the beam splitter might have different central frequencies. In a type II two-photon emission event the atom decays to the ground state $5^2S_{1/2},|F = 2\rangle$ with a probability of 0.219 thereby emitting a photon whose frequency is different by $6.8\,\text{GHz}$. According to subsection 4.2.3 this causes fast oscillations of the probability to detect coincidences of two photons, being in a $|\Psi^\pm\rangle$-state ($|\Phi^\pm\rangle$-state), in detector combinations $D+$ or $D-$ ($D\varnothing$ and n.d. - both photons impinge on the same detector) with respect to their detection time difference (see table 4.2). These oscillations are much faster than the temporal resolution of the
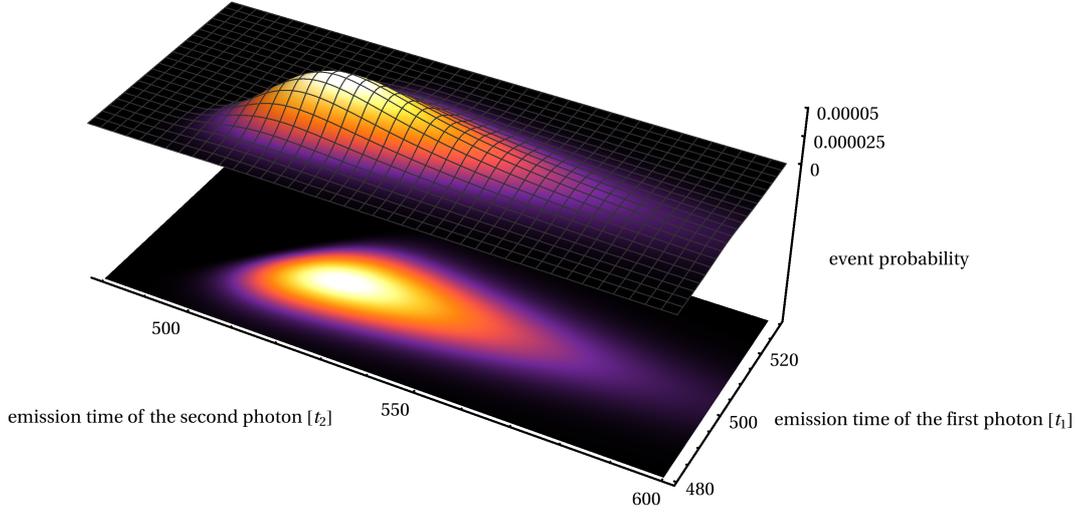
Figure 4.6.: Probability to emit a first photon at time t_1 and a second photon at time t_2 ($|\alpha_{\mathrm{III}}(t_1, t_2)|^2$)) if the atom was excited a second time caused by a decay into the initial state after first excitation per excitation trial (two-photon emission event type III). The upper plot is a 3D-Plot and the lower plot is a density plot of the same probability.

installed detectors. Therefore, these events are treated as non-interfering, generating all coincidences with equal probability.

In case the atom decays to the ground state $5^2 S_{1/2}, |F = 1\rangle$ after the second excitation, $\beta_i(t_2; t_1)$ describes the temporal amplitude of the (pure) state $\int dt_2 \beta_i(t_2; t_1)|t_2\rangle$ for the second photon in analogy to the previous subsection, and the mode overlap of a single photon with a photon of a $(\circ\bullet)$-event $O^2_{\circ\bullet_i|\bullet}(t_1)$ is calculated by equation F.42 for the three types of two-photon emission. The results are presented in figure 4.7.

The expectation value of the total mode overlap $O^2_{\circ\bullet_i|\bullet}$ is determined by incoherently summing all individual coherent overlaps ($O^2_{\circ\bullet_i|\bullet}(t_1)$) weighted with their respective probability ($p_{t_2,i}(t_1) = \int dt_2 \, |\alpha_i(t_1, t_2)|^2$) as shown in equation F.43. This gives $O^2_{\circ\bullet_{\mathrm{I}}|\bullet} = 0.80$, $O^2_{\circ\bullet_{\mathrm{II}}|\bullet} = 0.69$ and $O^2_{\circ\bullet_{\mathrm{III}}|\bullet} = 0.79$.

4.4.4. Expanded Analysis of a Two-Photon Interference Measurement

Section 4.3 discusses a model which allows the calculation of the three fractions P_{int}, P_{ni} and $P_{\bullet\bullet|\circ}$. The fractions P_{int} and P_{ni} consider all photons impinging on the beam splitter, which originate from different atoms. This includes $(\bullet \circ |\bullet)$- and $(\circ \bullet |\bullet)$-events as well as events where both atoms emit a single atom $(\bullet|\bullet)$. The distribution of those events over P_{int} and P_{ni} is defined by their respective interference probability.The interference probabilities of $(\bullet \circ |\bullet)$- and $(\circ \bullet |\bullet)$-events depend on the mode overlaps determined in the previous subsections.

The average mode overlap of photons of a $(\bullet \circ |\bullet)$-event is

$$O^2_{\bullet\circ|\bullet} = O^2_{\bullet\circ_{\mathrm{I}}|\bullet} \cdot p_{\mathrm{I},\bullet\circ|\bullet} + O^2_{\bullet\circ_{\mathrm{II}}|\bullet} \cdot p_{\mathrm{II},\bullet\circ|\bullet}, \tag{4.86}$$

where $O^2_{\bullet\circ_i|\bullet}$ (with $i \in \{\mathrm{I}, \mathrm{II}\}$) is defined in subsection 4.4.2 and $p_{i,\bullet\circ|\bullet}$ in subsection 4.4.1.
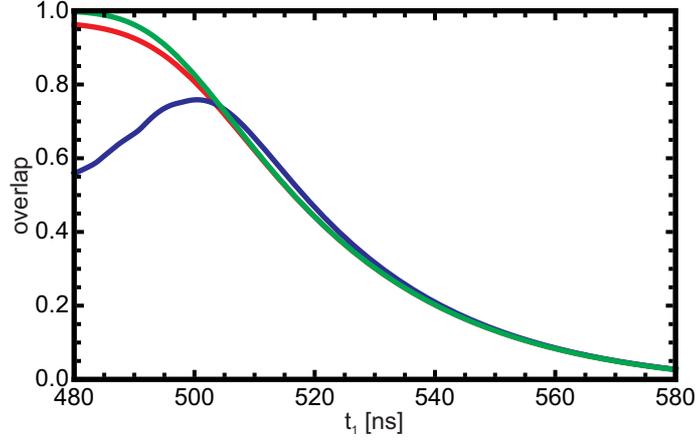
Figure 4.7.: Calculated overlap of a photon originating from ($\circ\bullet$)-event with a single photon $O^2_{\circ\bullet_{\mathrm{I}}|\bullet}(t_1)$ (red), $O^2_{\circ\bullet_{\mathrm{II}}|\bullet}(t_1)$ (blue) and $O^2_{\circ\bullet_{\mathrm{III}}|\bullet}(t_1)$ (green) against the emission time of the first photon t_1.

Analogously, the average mode overlap of photons of a ($\circ\bullet\,|\bullet$)-event is

$$O^2_{\circ\bullet|\bullet} = O^2_{\circ\bullet_{\mathrm{I}}|\bullet} \cdot p_{\mathrm{I},\circ\bullet|\bullet} + O^2_{\circ\bullet_{\mathrm{II}}|\bullet} \cdot p_a \cdot p_{\mathrm{II},\circ\bullet|\bullet} + O^2_{\circ\bullet_{\mathrm{III}}|\bullet} \cdot p_{\mathrm{III},\circ\bullet|\bullet}, \tag{4.87}$$

where $O^2_{\circ\bullet_i|\bullet}$ (with $i \in \{\mathrm{I}, \mathrm{II}, \mathrm{III}\}$) is defined in subsection 4.4.3, p_a in subsection 3.2.2 and $p_{i,\circ\bullet|\bullet}$ in subsection 4.4.1. The fact that a ($\circ\bullet_{\mathrm{II}}\,|\bullet$)-event shows only a reduced interference contrast, if the atom decays to the state $5^2S_{1/2}, |F = 1\rangle$ after the second excitation, is respected by p_a.

Now P_{int}, P_{ni} and $P_{\bullet\bullet|\circ}$ can be converted into a new set of fractions $P_{\bullet\bullet|\circ}$, $P_{\bullet\circ|\bullet}$, $P_{\circ\bullet|\bullet}$, $P_{\bullet|\bullet}$ and P_{error}, where $P_{\bullet|\bullet}$ is the fraction of events, where two single photons impinge on the beam splitter and P_{error} is the fraction of events, which do not interfere because of other errors than a reduced mode overlap (a further discussion of P_{error} is given in subsection 4.6.5):

$$
\begin{aligned}
P_{int} &= O^2_{\bullet\circ|\bullet} \cdot P_{\bullet\circ|\bullet} + O^2_{\circ\bullet|\bullet} \cdot P_{\circ\bullet|\bullet} + O^2_{\bullet|\bullet} \cdot P_{\bullet|\bullet} \\
P_{ni} &= (1 - O^2_{\bullet\circ|\bullet}) \cdot P_{\bullet\circ|\bullet} + (1 - O^2_{\circ\bullet|\bullet}) \cdot P_{\circ\bullet|\bullet} + (1 - O^2_{\bullet|\bullet}) \cdot P_{\bullet|\bullet} + P_{error} \\
P_{\bullet\bullet|\circ} &= P_{\bullet\bullet|\circ}
\end{aligned}
\tag{4.88}
$$

The fractions $P_{\bullet\bullet|\circ}$, $P_{\bullet\circ|\bullet}$ and $P_{\circ\bullet|\bullet}$ can be calculated due to their fixed ratio (see subsection 4.4.1). The respective overlaps are also known. The overlap of ($\bullet\bullet$)-events is approximately $O^2_{\circ\bullet|\bullet} = 1$ as test measurements will show (see subsection 4.5.4). $P_{\bullet|\bullet}$ and P_{error} can be calculated with the following equations:

$$P_{\bullet|\bullet} = P_{int} - O^2_{\bullet\circ|\bullet} \cdot P_{\bullet\circ|\bullet} + O^2_{\circ\bullet|\bullet} \cdot P_{\circ\bullet|\bullet} \tag{4.89}$$

and

$$P_{error} = P_{ni} - (1 - O^2_{\bullet\circ|\bullet}) \cdot P_{\bullet\circ|\bullet} - (1 - O^2_{\circ\bullet|\bullet}) \cdot P_{\circ\bullet|\bullet} \tag{4.90}$$

This newly defined set of fractions is important for a estimation of the quality of the entanglement swapping protocol, which is presented in the next chapter.

4.5. Experimental Realization

In order to study two-photon interference, the two atomic traps introduced in chapter 2 need to be combined. Here, a perfect synchronization of both experiments is necessary to guarantee high temporal mode overlap of photons emitted by the atoms. This is inalienable for a high two-photon interference quality (see subsection 4.2.2). Also the possible frequency mismatch of single photons from both traps and the quality of the fiber beam splitter have to be considered.

In this section the coupling of both experiments and their synchronization as well as the experimental procedure are described. Thereafter, the experimental limitations on the achievable interference contrast are calculated according to the theoretical considerations of section 4.2.

4.5.1. Experimental Setup

The experimental setup basically consists of the two single atom traps (trap1 and trap2) which are described in chapter 2. Photons collected in both experiments are guided to the same fiber beam splitter (see figure 2.6). The Bell-state projection of the two-photon states is performed by the same detection setup, which is also used for the experiments described in the previous chapters, and a FPGA signals a two-photon coincidence detected in the correct time window.

Note, the two setups are independent with exception of the synchronization, and both atoms are excited by pulses from independent laser setups.

4.5.2. Synchronization of both Experiments

As already emphasized in this chapter, it is most important that the wave packets of the single photons, which are generated in both experiments, overlap perfectly. Therefore, it is necessary to synchronize the independently operating experiments.

In order to synchronize both experiments, the computer controlling trap1 is used as master control, and the computer, which controls trap2, as slave control. The master control sends commands to the slave control, which allows to switch the status of trap2 between different modes, e.g., the mode, where an atom is loaded into the trap, and the experimental mode. Furthermore, the so called "pattern generators" of trap1 and trap2, which control the switching of all lasers, and generate the experimental sequences shown subsection 2.4.1, share the same clock signal. This allows them to control the switching of the laser beams in each experiment with a relative jitter of $31\,\text{ps}$. It implies the switching of the excitation laser, which are operated in a way that single photons emitted by both atoms impinge on the beam splitter simultaneously as the relative jitter is far below the lifetime of the excited state of the atom ($26.23\,\text{ns}$).

The synchronization is continuously monitored by controlling patters from both patten generators. Any disturbance of the synchronization, e.g., caused by electrostatic discharges disturbing the clock signal, are therefore observed by a reduced temporal overlap of the controlling patterns within $60\,\text{ms}$. In such a case they resynchronized during the next $60\,\text{ms}$.

The switching of the pattern generators from "loading the atom" to the "experimental" pattern is performed with respect to a common start signal control which is operated by the slave computer of trap2. The start signal control is synchronized to the common clock, and allows switching of both pattern generator status with a fixed relative time difference. A scheme of the synchronized setup is presented in figure 4.8.
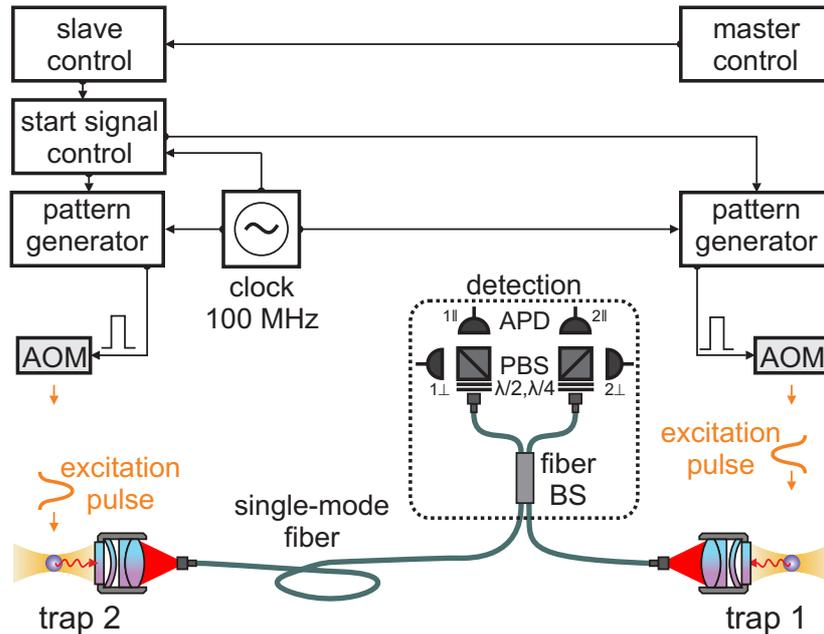
Figure 4.8.: Synchronized experimental setup: The scheme shows the master control which processes the counts from the detectors and controls the slave control. The start signal control switches both pattern generators synchronously into the "experimental pattern", thus the two single photons impinge on the beam splitter at the same time.

4.5.3. Experimental Scheme

Each experimental run starts by loading a single atom in each experiment's dipole trap (see subsection 2.3.6). The successful trapping of an atom in one of the traps leads to a rise of the single photon count rate in the detection setup above a first threshold. In oder to discriminate, which experiment has trapped an atom, the cooling light of one experiment is switched off and the remaining photon count rate is observed. In case the light of the trap, which trapped the atom, is switched off, the single photon count rate falls to the background level. Otherwise, it stays stable. With that information the cooling light of the trap, which already trapped an atom, is switched off as this extends the trapping time. The other trap remains in the loading mode until it also traps an atom. Then, the cooling light of both traps is switched on again, and if the photon count rate exceeds a second threshold, which is roughly twice as high as the first threshold, it is considered that two atoms are trapped, and the main experiment begins. If the trap, which first trapped an atom, has lost its atom during waiting for the other trap, the loading procedure starts from the beginning.

   In case both traps contain an atom, the master computer sends the "start-experiment"-command to the slave computer which controls the common start signal control. The start signal controller switches both pattern generators to the experimental mode, where both atoms are subsequently prepared in a particular ground state $5^2S_{1/2}, |F = 1, m_F = 0\rangle$, before they are excited with a π-pulse to the state $5^2P_{3/2}, |F' = 0, m_F = 0\rangle$ (see subsection 2.4.1). The synchronization is set such that the emitted single photon wave packets impinge on the fiber beam splitter at the same time. This atom excitation procedure is repeated 20-times before the two atoms have to be cooled to counteract heating, and thereafter starts from the beginning (the exact timing of the procure is shown in figure 2.9 a), b)). The atom excitation continuous until the detection of two photons in different detectors within a $120\,\text{ns}$

coefficient	value
σ_H	0.527
ρ_H	0.473
σ_V	0.505
ρ_V	0.495

Table 4.4.: This table shows the transmittance and reflectance for a horizontally or vertically polarized light impinging on the beam splitter installed in the experiment.

time window after the excitation of the atoms signals a two-photon coincidence (the coincidence window is shown in figure 3.1 b)) or one of the atoms is lost. The coincidence window is defined locally by the pattern generator of trap1, and the coincidences are processed by a FPGA-based logic device.

4.5.4. Reduction of the Interference Contrast Caused by Imperfections of the Setup

The two-photon interference contrast depends critically on the temporal, spectral and spatial mode overlap of the two single photon wave packets as well as on the quality of the beam splitter in use. Section 4.2 already discussed the influences of possible imperfections of the setup on the interference contrast. In this subsection the magnitude of every source of error is calculated based on several test measurements.

Beam Splitter Quality

The quality of the beam splitter depends on its transmittance and reflectance for different polarizations as shown in equation 4.40. This equation allows the calculation of the probability to correctly identify the two-photon, which can be maximally achieved, with a specific beam splitter. The transmittance and reflectance of the beam splitter, which is installed in the experiment, are presented in table 4.4. The beam splitter quality factor calculates to $BSP = 0.998$ with respect to these values. It shows that the influence of the beam splitter on the two-photon interference quality is practically negligible.

Temporal Mode Overlap of the Single Photon Wave Packets

The temporal mode overlap depends on two main characteristics. The first one is the difference of the temporal shapes of the single photon wave packets and the second one is the relative detection time difference of both wave packets.

The temporal shape of the wave packets is determined by the time dependence of the power of the excitation lasers, the excitation frequency and the lifetime of the excited state of the atom. While the spontaneous decay is equal for both atoms, the shape and frequency of the excitation pulses need to be carefully matched. Figure 4.9 shows the well-matching temporal shapes of both excitation pulses. The frequencies of both pulses are tuned exactly to the excitation transition by calibration measurements.

The fixed delay between both excitation pulses is guaranteed by the synchronization of the pattern generators which are responsible for the timing of the pulses. The delay is adjusted by delaying the electrical signal for one excitation pulse by a tune-able delay in a way that the wave packets impinge simultaneously on the beam splitter.
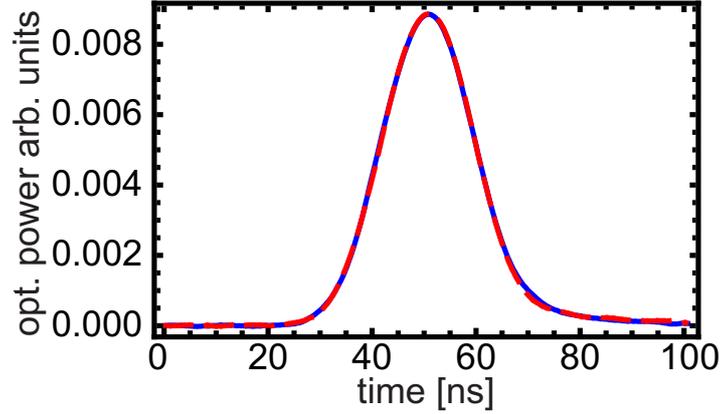
Figure 4.9.: Temporal shape of optical excitation pulses measured by a fast photodiode: The blue curve describes the temporal shape of the excitation pulse which excites the atom in trap1 and the dashed red curve the temporal shape of the excitation pulse which excites the atom in trap2, respectively.

The temporal mode overlap of the photon wave packets can be determined by a measurement of the detection time of single photons relative to a fixed trigger for photons from both atoms. A normalized histogram of the detection time of photons emitted by trap1 is already shown in figure 3.1 b). The normalization fulfills the following condition:

$$\sum_{i=480\,\text{ns}}^{600\,\text{ns}} \frac{n_i}{A} = 1, \tag{4.91}$$

where n_i is the number of detected events in a $1\,\text{ns}$ bin of the $120\,\text{ns}$ detection time window and A is the normalization constant. Figure 4.10 b) shows also a histogram of the detection times of photons emitted by trap2 which are normalized in the same way. The square root of the resulting curves can be interpreted as the temporal shape of the single photon wave packets. Therefore, they correspond to $\alpha_{single}(t)$ (see equation F.30), and the overlap integral $\int_0^T dt\, \alpha^{\star}_{single1}(t)\alpha_{single2}(t)$ can be calculated. The data of the presented histograms yields the following overlap of the single photon wave packets of photons from both traps:

$$O_{histo} = \sum_{i=480\,\text{ns}}^{600\,\text{ns}} \sqrt{\frac{n_{1i}}{A_1}}\sqrt{\frac{n_{2i}}{A_2}} = 0.9997. \tag{4.92}$$

It shows that a reduction of the interference contrast caused by a non-perfect temporal mode overlap of the single photon wave packets is negligible, although there is still noise on the data. The actual mode overlap can be considered even higher.

It is also possible to determine the temporal mode overlap of the two photon wave packets using a curves fitted to each histogram presented in figure 4.10 b) (see F). These curves correspond the temporal distributions of detection probability for the single photon wave packet $|\alpha(t)|^2$ and are shown in figure 4.10 a). They are normalized to fulfill the following condition:

$$\int_{480\,\text{ns}}^{600\,\text{ns}} dt\, |\alpha(t)|^2 = 1 \tag{4.93}$$

71
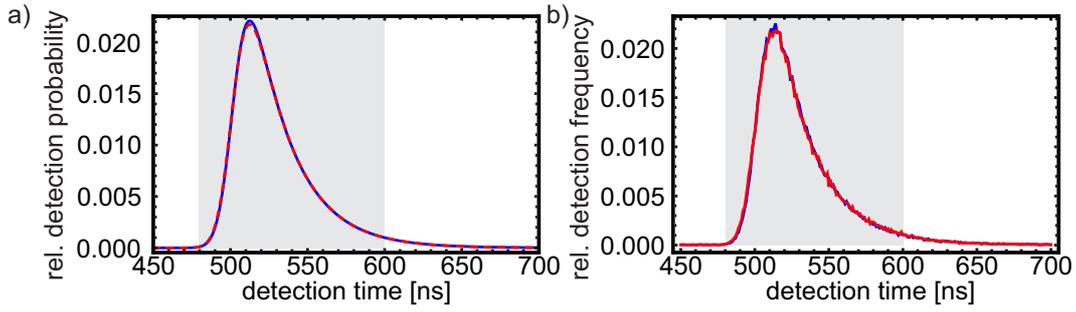
Figure 4.10.: This figure shows the relative single photon detection probability depending on the detection time. a) shows the calculated relative detection probability of photons emitted by trap1 (blue) and trap2 (red, dashed), respectively based on experimental parameters (see appendix F.3.1). b) shows the histogram of the relative detection frequency of single photons emitted by trap 1 (blue) and trap2 (red). The gray shading marks the defined coincidence time window.

The temporal mode overlap of the two wave packets is calculated numerically and gives the following value:

$$O_{\beta(t)} = \int\limits_{480\,\mathrm{ns}}^{600\,\mathrm{ns}} dt \, \sqrt{|\alpha_1(t)|^2}\sqrt{|\alpha_2(t)|^2} = 0.9999,$$

Here, an even higher temporal mode overlap is achieved because the overlap calculation is not affected by any noise. Nevertheless, both calculations show that the temporal mode overlap is almost perfect. Equations 4.54 and 4.56 allow the calculation of the contrast and the probability to correctly identify the two-photon state which is achievable with that temporal mode overlap:

$$C_{histo} = 0.9994$$

$$C_{\alpha(t)} = 0.9998$$

$$P_{histo}^{tmo} = 0.9997$$

$$P_{\alpha(t)}^{tmo} = 0.9999$$

The results show that the decrease of the interference contrast, which is caused by imperfections of the temporal mode overlap, is negligible. All these calculations are restricted to the approximation that the atom only emits one photon per excitation attempt. By including two-photon emission events the interpretation of the histograms as temporal distributions of detection probability for the single photon wave packet is not justified.

Spectral Mode Overlap of the Single Photon Wave Packets

The spectral mode overlap suffers from Doppler broadening of the photons caused by the residual motion of the atoms and from shifts of the Zeeman levels of the ground state caused be magnetic fields. Note, the dipole traps in both experiments are switched off during the excitation of the atoms

and the subsequent single photon emission. Thus, the spectral mode of the photons is not influenced by any AC-Stark shift.

The relative frequency spread of the two photon frequencies caused by Doppler shifts can be calculated with respect to equation 4.61 and the temperatures of both trapped atoms. An atom in trap1 has a temperature of $105\,\mu K$ Volz [45] and an atom in trap2 has a temperature of $57\,\mu K$ [84]. This results in a relative frequency spread of photons emitted by atoms in both traps of:

$$\sigma_{\omega,rel} = 2\pi \cdot 159.6\,\text{kHz}.$$

Equation 4.65 allows the calculation of the expectation value of the mode overlap of the two wave packets with respect to their relative frequency spread. Since the frequency of the photons is much higher than $\sigma_{\omega,rel}$, the expectation value of the mode overlap is also nearly perfect:

$$O^2_{Doppler} = 0.9993.$$

The result allows an estimation of the maximal achievable interference contrast and the probability to correctly identify the two-photon state:

$$C_{Doppler} = 0.9993$$

$$P^{smo}_{Doppler} = 0.9997$$

The effect of external magnetic fields on the atoms is small because the magnetic fields in the trap regions are actively stabilized to a value are smaller than $10\,\text{mG}$ [54]. For a worst case estimation the magnetic fields are assumed to be $B = 10\,\text{mG}$ with opposite orientation for the two traps. This way the emitted photons would have a maximal frequency difference of $2\pi \cdot 14\,\text{kHz}$, which is yet an order of magnitude smaller than $\sigma_{\omega,rel}$ and results in an overlap

$$O^2_{magn} > 1 - 10^{-5},$$

It shows that both Doppler broadening and residual magnetic fields have only a negligible effect on the two photon interference contrast.

All effects discussed in this subsection combined have still a negligible influence on the interference contrast, with the latter expected to be better than 0.997, in case the experiment suffers only from these errors. The two-photon emission will have a far bigger impact as discussed in section 4.4. Polarization errors in the detection setup do not have a notable influence on the measured two-photon interference contrast as the detection setup is very carefully adjusted.

4.6. Experimental Results

In this section the results of a two-photon interference measurement are presented. The experiments were performed as described in the previous section. To apply the model introduced in section 4.3, the Bell-state measurement analysis was performed in the H/V-basis and in the R/L-basis, respectively.
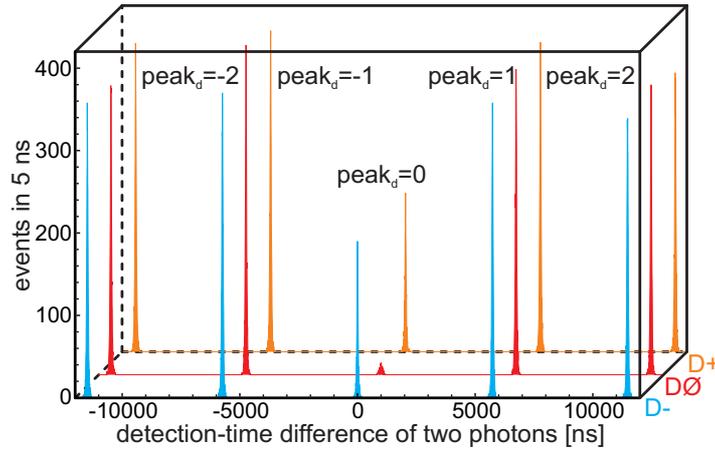
Figure 4.11.: Two-photon detection time correlations: The graphic shows histograms of the detection time difference of two single photons. The blue curve corresponds to events in a $D-$ detector combination, the red curve to events in a $D\varnothing$ detector combination and the orange curve to events in a $D+$ detector combination, respectively. The area of the peak $peak_{D\varnothing} = 0$ is considerably smaller than the area of the peaks $peak_{D+} = 0$ and $peak_{D-} = 0$ due to two-photon interference. The number of events in peaks $peak_d = 0$ and $peak_d = \pm 1$ with $d \in \{D+, D-, D\varnothing\}$ are summarized in table 4.5.

4.6.1. Two-Photon Correlations

The registered two-photon detection time correlations are summarized into three histograms for detector combinations $D+$, $D-$ and $D\varnothing$. These three histograms are presented in figure 4.11 for the measurement in the H/V-basis. They show all detected two-photon events with a maximal detection time difference of $12\,\mu$s which fulfill the additional restriction that the photons are registered within the already described $120\,$ns time window after an excitation trial (see subsection 4.5.3). In analogy to the correlation measurements with photons originating from one atom, the area of the peaks increases by $^1/_{19}$ when going to lower detection time differences. This is caused by combinatorial reasons as described in subsection 3.5.3. The peaks around zero photon detection time difference ($peak_d = 0$ with $d \in \{D+, D-, D\varnothing\}$) show the two-photon interference effect. The other peaks ($peak_d = \pm n$, where the peaks at lowest detection time difference are labeled $n = 1$) contain two-photon events where the wave packets of the single photons did not overlap in time. These photons did not interfere. But these events can be used for normalization of the peaks $p_d = 0$ in upcoming data analysis. The area of the peaks $peak_d = \pm 1$ is roughly twice as large as the area of the peaks at $peak_{D+} = 0$ and $peak_{D-} = 0$. This is also caused by combinatorial reasons. The peaks $peak_d = \pm 1$ include events, where the photons originate from one atom as well as from different atoms, whereas the peak $peak_d = 0$ ideally includes only events where both photons originate from different atoms.

The two-photon interference effect is observable by comparing the area of the two peaks $peak_{D+} = 0$ and $peak_{D-} = 0$ with the peak $peak_{D\varnothing} = 0$. The area of the peak for detector combinations $D\varnothing$ is much smaller than the other two areas due to photon bunching. The total two-photon event numbers in the peaks $peak_d = 0$ and $peak_d = \pm 1$ are given in table 4.5 for all detector combinations.

number of coincidences $n_{tp}^{d,b}$				
basis	peak	detector combinations		
		$D-$	$D+$	$D\varnothing$
H/V	$peak_d = -1$	4327	4402	4384
	$peak_d = 0$	1965	1968	186
	$peak_d = +1$	4243	4293	4313
R/L	$peak_d = -1$	3919	3944	3939
	$peak_d = 0$	1693	1824	135
	$peak_d = +1$	3798	3811	3839

Table 4.5.: This table shows two-photon correlation event numbers $n_{tp}^{d,b}$ (with $d \in \{D+, D-, D\varnothing\}$ and $b \in \{HV, RL\}$) taken in two different measurements. All events, where the photons originate from the same or subsequent excitations, are registered.
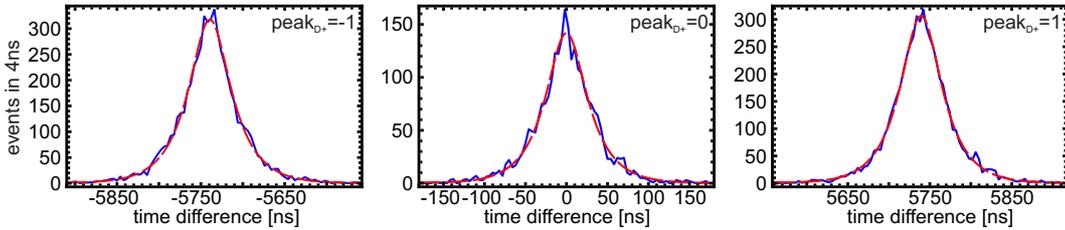
Figure 4.12.: Two-photon detection time correlations for the $D+$ detector combinations in the H/V-basis: These graphs show histograms of the two-photon detection time correlations for the peaks $p_{D+} = 0$ and $p_{D+} = \pm1$ (blue) as well as the calculated temporal shape of those peaks (red, dashed). The good agreement of the calculation and measurement indicates a high degree of control over the relevant experimental parameters.

4.6.2. Temporal Shape of the Two-Photon Correlation Peaks

The temporal shape of the correlation peaks for non-interfering photons in figure 4.11 is determined by the convolution of the temporal shapes of the two single photon wave packets. Figure 4.12 shows the expected and the measured temporal shape of the two-photon correlations for a selection of the discussed peaks. There is a high agreement of both curves which shows that these measurements are not subject to errors affecting the temporal shape of the two photon correlations.

The peak $peak_{D\varnothing} = 0$ might have a more complex temporal shape as discussed in subsection 4.2.3. Here, possible mismatches of the frequencies of photons from both atoms lead to oscillations of the two-photon correlations depending on the time difference of the detected photons. Figure 4.13 shows the expected and the measured temporal shape of the two-photon correlations for these detector combinations. Although the measured curve suffers considerably from dark count events and two-photon emission events, it is observable that both curves fit well. This proves that photons from both atoms have no frequency mismatch bigger than $10\,\mathrm{MHz}$. Any smaller mismatches are not observable because of the described errors.
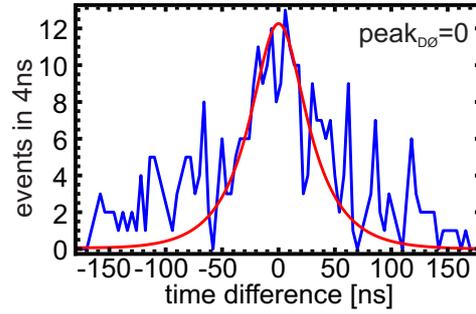
Figure 4.13.: Two-photon detection time correlations for the $D\varnothing$ detector combinations in the H/V-basis: This graph shows a histogram of the two-photon detection time correlations for the peak around zero delay (blue) as well as the calculated temporal shape of those peaks (red). Although the histogram suffers strongly from dark count and two-photon events it is observable that the peak is not disturbed by high frequency modulations. It shows that the photons which originate from both traps have the same spectral modes.

basis of photon analysis	contrast C
H/V	$C_{D-} = 0.905 \pm 0.007$
	$C_{D+} = 0.905 \pm 0.007$
	$C = 0.905 \pm 0.007$
R/L	$C_{D-} = 0.920 \pm 0.007$
	$C_{D+} = 0.926 \pm 0.007$
	$C = 0.923 \pm 0.007$

Table 4.6.: Contrast of two-photon interference for the two detectable Bell-States with photon analysis in the H/V- and R/L-basis. C_{D-} represents detector combinations which correspond to projection onto the Ψ^--state and C_{D+} onto the Ψ^+-state. The value C is the combined contrast for both Bell states.

4.6.3. Estimation of Two-Photon Interference Contrast

The data presented in table 4.5 allow an estimation of the two-photon interference contrast. For this purpose, the data are corrected for different detector efficiencies as shown in section 3.3, but are not corrected for dark counts. The new values are put into equations 4.27 - 4.29 in order to calculate the two-photon interference contrast. The results are given in table 4.6. They show that the interference contrast is better than 0.91 in both bases.

The results show a statistical significant deviation of the contrast for the two bases. While they still provide an estimate of the interference quality, application of the detailed model allows a better understanding of the underlying effects.

4.6.4. Dark Count Probabilities

A more detailed analysis of the two-photon interference probability requires knowledge of the amount of dark count events in the measurement data first. According to the previous chapter a dark count event is defined as a detection of a dark count and a single photon in the same time window or in subsequent time windows (see subsection 3.2.4).

	single photon det. prob. $p_{ph}^{i,b} \cdot 10^{-3}$	
detector \ basis	H/V	R/L
$APD_{1\perp}$	0.48±0.00024	0.55±0.00031
$APD_{1\parallel}$	0.51±0.00024	0.59±0.00032
$APD_{2\perp}$	0.46±0.00023	0.56±0.00031
$APD_{2\parallel}$	0.48±0.00024	0.59±0.00031

Table 4.7.: Single photon detection probability $p_{ph}^{i,b}$ (with $i \in \{1 \perp, 1 \parallel, 2 \perp, 2 \parallel\}$ and $b \in \{HV, RL\}$) after an excitation attempt for all detectors in both basis.

basis	H/V		R/L	
det. comb. \ parameter	$p_{dce}^{ij,b} \cdot 10^{-10}$	$n_{dc}^{ij,b}$	$p_{dce}^{ij,b} \cdot 10^{-10}$	$n_{dc}^{ij,b}$
$APD_{1\perp}, APD_{2\parallel}$	06.05 ± 0.093	05 ± 2.3	07.29 ± 0.112	04 ± 2.0
$APD_{1\parallel}, APD_{2\perp}$	11.89 ± 0.131	10 ± 3.2	14.10 ± 0.156	08 ± 2.8
$APD_{1\perp}, APD_{1\parallel}$	08.71 ± 0.113	08 ± 2.7	10.10 ± 0.131	06 ± 2.4
$APD_{2\parallel}, APD_{2\perp}$	09.19 ± 0.114	08 ± 2.8	11.28 ± 0.140	06 ± 2.5
$APD_{1\perp}, APD_{2\perp}$	11.47 ± 0.127	10 ± 3.2	13.45 ± 0.149	08 ± 2.7
$APD_{2\parallel}, APD_{1\parallel}$	06.16 ± 0.095	05 ± 2.3	07.47 ± 0.115	04 ± 2.0

Table 4.8.: Probability $p_{dce}^{ij,b}$ (with $i \neq j$ and $i, j \in \{1 \perp, 1 \parallel, 2 \perp, 2 \parallel\}$ and $b \in \{HV, RL\}$) to detect a dark count together with a single photon in the same time window (dark count event) per atom excitation for every detector combination i, j and both relevant two-photon interference measurements. It also shows the expected number of these events $n_{dc}^{ij,b}$ in the presented measurements. The total number of atom excitations was $n_{ex}^{HV} = 86.7 \cdot 10^8$ and $n_{ex}^{RL} = 56.1 \cdot 10^8$, respectively.

Analogous to subsection 3.5.2, equation 3.1 allows the calculation of the probability of specific dark counts events as a function of the dark count probability of each detector (see table 3.2.4) and the single photon detection probability per excitation attempt of the current measurements (see table 4.7). The dark count event probabilities and the total numbers of dark count events are given in table 4.8.

The results show that the single photon detection probability slightly varied between the two measurements. This is probably caused by a different adjustment of the optical setup. A comparison of the event numbers in table 4.5 with the expected dark count event numbers also show that these events have a significant influence in these measurements.

4.6.5. Analysis of Interference Quality

This subsection presents a more detailed discussion of the two-photon interference quality. It is based on the model for the analysis of two-photon interference measurements introduced in section 4.3. For a most precise analysis the measured event numbers of table 4.5 must be corrected for the photon detection efficiencies of the different detector combinations and for dark count events (see subsection 3.3).

The corrected data allow the calculation of the values $R^{HV} = 0.042 \pm 0.003$ and $R^{RL} = 0.034 \pm 0.003$ with respect to equation 4.73. They depend on the ratio of events in detector combinations

$D\varnothing$ to all measured events. By solving the set of equations given by 4.73 and the normalization $P_{int} + P_{ni} + P_{\bullet\bullet|\circ} = 1$, the three probabilities P_{int}, P_{ni} and $P_{\bullet\bullet|\circ}$ can be extracted. The calculation gives the following values:

$$
\begin{aligned}
P_{int} &= 0.922 \pm 0.008 \\
P_{ni} &= 0.064 \pm 0.010 \\
P_{\bullet\bullet|\circ} &= 0.014 \pm 0.009
\end{aligned}
$$

These results show that two photons impinging on the beam splitter interfere with a probability $P_{int} = 0.922$ in the executed experiments. It is a more precise statement than the one provided by the interference contrast, which depends on the measurement basis. This analysis also shows that with a probability of 0.014 ± 0.009 the two photons impinging on the beam splitter both originate from a two-photon emission process. The value is in good agreement with the expected value based on the two-photon emission measurements: $1 - (1 - P_{tp}^{\sigma\pm})^2 = 0.015 \pm 0.001$ (see chapter 3). The difference might be caused by a slightly different power of the excitation laser in these measurements.

In oder to achieve a deeper understanding of the interference experiment, case two and three two-photon events (($\bullet\circ|\bullet$) and ($\circ\bullet|\bullet$)) have to be considered, too. These events show a reduced interference contrast. Therefore, P_{int} and P_{ni} are converted into a new set of fractions $P_{\bullet|\bullet}$, $P_{\bullet\circ|\bullet}$, $P_{\circ\bullet|\bullet}$ and P_{error}. According to the discussions in subsections 4.4.1 and 4.4.4 $P_{\bullet\circ|\bullet}$ and $P_{\circ\bullet|\bullet}$ show the fraction of case two and case three two photon events impinging on the beam splitter, respectively. $P_{\bullet|\bullet}$ shows the fraction of photon originating from single photon emission from different atoms, and P_{error} represents the events, where the photons do not interfere because of further errors:

$$
\begin{aligned}
P_{\bullet|\bullet} &= 0.859 \pm 0.009 \\
P_{\bullet\bullet|\circ} &= 0.014 \pm 0.009 \\
P_{\bullet\circ|\bullet} &= 0.016 \pm 0.010 \\
P_{\circ\bullet|\bullet} &= 0.075 \pm 0.006 \\
P_{error} &= 0.036 \pm 0.018
\end{aligned}
$$

P_{error} is caused by other erroneous events: For instance, the probability for two-photon emission events of type I is only determined for trap1, and may have a slightly larger value for trap2 due to different errors in the adjustment of the setup. This would cause additional two-photon emission events, which generate detection events similar to that caused by white noise. These events would be summarized in P_{rest}, although they are two-photon emission events. Furthermore, P_{error} includes any polarization adjustment errors in the detection setup reducing the interference quality.

The representation of the result of the interference measurement by the five fraction $P_{\bullet|\bullet}$, $P_{\bullet\bullet|\circ}$, $P_{\bullet\circ|\bullet}$, $P_{\circ\bullet|\bullet}$ and P_{error} is further needed for a detailed analysis of the entanglement swapping protocol in the next chapter.

4.7. Summary

This chapter discussed the basic principles of two-photon interference at a beam splitter and errors which may reduce the interference contrast. The experimental setup for two-photon interference was introduced and characterized. Contrary to most earlier experiments, the two single photon sources are operated independently. The data recorded in two two-photon interference measurements with photon analysis in different bases allowed the calculation of the interference contrast. The measured contrast is better than $90.5\,\%$ in both analysis bases. Thereafter, a detailed analysis of the two photon interference measurement was given, which also accounts for various two-photon emission events from one atom. The dark count and single photon detection probability corrected fraction of photon pairs

impinging on the beam splitter which show interference could be estimated: $P_{int} = 0.922 \pm 0.008$. It is a more significant value than the interference contrast as it considers the special characteristics of the atomic emission events and is also independent of the basis of photon analysis.

The high interference probability proves that this experimental setup is well suited for implementation of an entanglement swapping protocol in order to generate atom-atom entanglement.

5. Atom-Atom-Entanglement and a Test of Bell's Inequality

Heralded long distance entanglement of massive particles is the key which opens up new possibilities in quantum communication as it enables new applications like quantum repeaters [17] and quantum networks [12]. Additionally, it allows insights into the foundation of physics because it is a further important step towards a loophole-free test of Bell's inequality [6, 85, 86].

Until now, the heralded generation of entangled massive particles has been observed in several different setups like trapped ions [87, 88], cold atomic ensembles [89, 90] and diamond crystals [91]. In all these experiments the two particles were in a single setup at close distance. Long distance entanglement of massive particles has only been achieved using not-heralding protocols. Here two atoms located up to $21\,\mathrm{m}$ apart from each other could be entangled [92, 26, 93].

In this experiment heralded entanglement is generated between two single neutral atoms which are trapped $20\,\mathrm{m}$ apart from each other in two independent setups. The entanglement between both particles is generated via entanglement swapping, which implies that entanglement is achieved, although the two atoms never interacted directly with each other.

In this chapter the entanglement swapping protocol, which generates the atom-atom entanglement (AAE), is introduced as well as the basic principles of a test of Bell's inequality. Thereafter, the atom-atom entanglement experiment is described and its results are presented.

5.1. The EPR-Paradox and Bell's Inequality

In 1935 Einstein, Podolsky and Rosen published a paper in which they raised the question whether the quantum mechanical description can be considered complete [1]. They formulated three requirements which that a physical theory should fulfill to be satisfactory in their opinion:

1. completeness: *"Every element of the physical reality must have a counterpart in the physical theory."*

2. realism: *"If, without in any way disturbing a system, we can predict with certainty (i.e., with probability equal to unity) the value of a physical quantity, then there exits an element of physical reality corresponding to this physical quantity."*

3. locality: Measurements, which are outside each others light combs should not influence each other.

Quantum mechanics can't fulfill the latter two conditions at once. Therefore, they introduced the possibility of local hidden variables, which determine the outcome of any possible measurement, but can't be measured themselves. This extended theory would fulfill their constrains on realism and locality.

The question, whether those local hidden variables exist, remained a purely philosophical one, until Bell introduced a way to experimentally test their possible existence in 1964 [2, 3]. The test
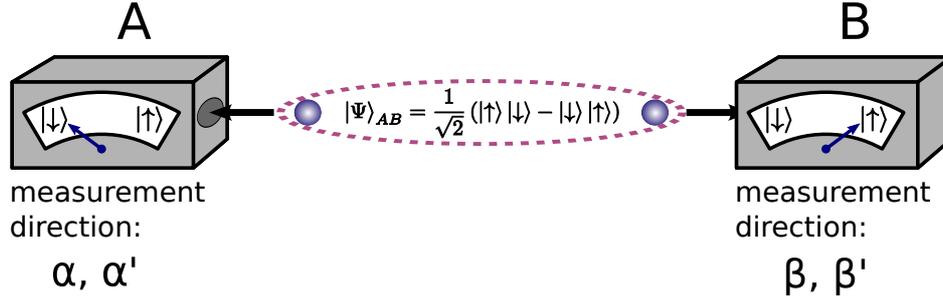
Figure 5.1.: A basic EPR-experiment: A source provides pairs of entangled particles. These are distributed to Bell state analyzers (A, B) and their spins are measured each in one of two distinct measurement directions. The observed correlations for every combination of the measurement directions yield the parameter S.

is based on correlation measurements on two entangled spin $1/2$ particles. However, the test required perfect correlations between the particles which is experimentally not feasible. Five years later in 1969 Clauser, Horne, Shimony and Holt presented an inequality which did not require perfect correlations [4]. They showed that a specific expression is bound by 2, in case any local hidden variable theory is assumed, but takes values up to $2\sqrt{2}$ according to quantum mechanics. The expression depends on the results of correlation measurements between two entangled particles, where each particle can be analyzed in two different bases (see figure 5.1):

$$S := \left| \langle \sigma^\alpha, \sigma^\beta \rangle - \langle \sigma^\alpha, \sigma^{\beta'} \rangle \right| + \left| \langle \sigma^{\alpha'}, \sigma^\beta \rangle + \langle \sigma^{\alpha'}, \sigma^{\beta'} \rangle \right| \leq 2, \tag{5.1}$$

where $\langle \sigma^\alpha, \sigma^\beta \rangle$ is the expectation value of the joint measurement of the spins of both particles and $\{\alpha, \alpha'\}$, $\{\beta, \beta'\}$ are two sets of measurement bases of the first and second particle, respectively.

In the following, many experiments were performed violating this inequality [5, 6, 7, 8]. They were based on correlation measurements between photons as well as massive particles and hybrid systems. But until now all these experiments suffered from at least one loophole, and thus did not allow a final statement about the existence of local hidden variables. The two main loopholes, which are not closed simultaneously yet, are:

1. the detection loophole: at least 82.8% of particles have to be detected on each side

2. the locality loophole: the analysis of both particles (including the choice of the measurement basis) must be space-like separated

The first loophole was closed by measurements with massive particles [10] and only recently for measurements with photons [94, 95], whereas the second loophole was closed by measurements with photons [9] but not by measurements with massive particles. It is still an experimentally challenging task to entangle massive particles at large distances as well as to detect photons with a sufficiently high efficiency.

A modification of the experiment presented in this thesis will be able to close both loopholes at once, and thus give a final statement about the existence of local hidden variables [85, 86]. It combines the advantages of both the high detection efficiency of massive particles and the possibility to distribute the entanglement over large distances using photons. In order to achieve this, a new, faster atomic state detection is required as well as an even larger distance between the two atoms relaxing the conditions

on the speed of the atomic state detection. In a final stage both atoms will be about $400\,\mathrm{m}$ apart from each other and the total atomic state detection will take less than $1\,\mu\mathrm{s}$ enabling the closing of the locality loophole.

In this thesis only the detection loophole will be closed. The so called event-ready scheme, implemented in this experiment allows to take every entanglement event into account, because the atoms are not entangled until the projection of the two photons onto a Bell-state reduces the four particle Hilbert-space. Thus, two-photon coincidence detections, which are already described in chapter 4, herald every atom-atom entanglement event, and a detection efficiency of 1 is guaranteed. Any errors of the atomic state detection only decrease the possible violation of the Bell inequality but not the detection efficiency as discussed in subsequent sections.

5.2. Entanglement Swapping and Atom-Atom Entanglement Generation

This section describes the entanglement swapping protocol, which entangles the single atoms in the two experiments, although the two atoms never interacted directly with each other. The protocol was described first in 1993 [79] and demonstrated in 1998 [96] with two pairs of entangled photons, but can also be applied on two entangled atom-photon pairs.

In subsequent subsections the entanglement swapping protocol is discussed in detail, and the model introduced in the previous chapter is extended to describe the expected quality of the entanglement swapping protocol in this experiment. In the end the experimentally observable atom-atom correlations are discussed.

5.2.1. Basic Principles

The entanglement swapping protocol is based on Bell-state projection. In this experiment, it is implemented by two-photon coincidence detections in an optical Bell-state analyzer. In case each of the two detected photons is again entangled with another particle, the entanglement will swap onto those other particles. It is a way to achieve entanglement between very distant particles. The actual entangled state of the two final particles depends on the the state on which the two photons are projected. Here, the entangled state of the two particles in dependence on the two-photon Bell-state projection is calculated for this experiment.

As described by equation 2.2, the following entangled atom-photon state is generated in each setup:

$$
\begin{aligned}
\left|\Psi^+\right\rangle & = \tfrac{1}{\sqrt{2}}(\left|\uparrow\right\rangle_z \left|R\right\rangle + \left|\downarrow\right\rangle_z \left|L\right\rangle) \\
& = \tfrac{1}{\sqrt{2}}(\left|\uparrow\right\rangle_x \left|H\right\rangle + \left|\downarrow\right\rangle_x \left|V\right\rangle).
\end{aligned}
\tag{5.2}
$$

Thus, the total four particle state can described by

$$
\left|\Psi\right\rangle_{12} = \left|\Psi^+\right\rangle_1 \otimes \left|\Psi^+\right\rangle_2,
\tag{5.3}
$$

where the indexes 1 and 2 denote the entangled atom-photon pair in trap1 and trap2, respectively.

To calculate the entangled atom-atom state depending on the state the two photons are projected on, the photons are expressed in terms of creation operators acting on a vacuum mode in analogy to the calculations in chapter 4. The entangled state is shown in the H/V-basis as it is the basis in which the photons are analyzed in the detection setup:

$$
\left|\Psi^+\right\rangle_i = \frac{1}{\sqrt{2}}(\left|\uparrow\right\rangle_{xi}\, \hat{a}_{iH}^\dagger + \left|\downarrow\right\rangle_{xi}\, \hat{a}_{iV}^\dagger)\left|0\right\rangle_{in},
\tag{5.4}
$$

with $i \in \{1, 2\}$. The tensor product in equation 5.3 yields to the following expression:

$$
\begin{aligned}
|\Psi\rangle_{12} \;=\; \tfrac{1}{2}(\;\; & \hat{a}_{1H}^{\dagger}\hat{a}_{2H}^{\dagger}\,|\!\uparrow\rangle_{x1}\,|\!\uparrow\rangle_{x2} &+\;\; & \hat{a}_{1H}^{\dagger}\hat{a}_{2V}^{\dagger}\,|\!\uparrow\rangle_{x1}\,|\!\downarrow\rangle_{x2} \\
+\;\; & \hat{a}_{1V}^{\dagger}\hat{a}_{2H}^{\dagger}\,|\!\downarrow\rangle_{x1}\,|\!\uparrow\rangle_{x2} &+\;\; & \hat{a}_{1V}^{\dagger}\hat{a}_{2V}^{\dagger}\,|\!\downarrow\rangle_{x1}\,|\!\downarrow\rangle_{x2} \;\;)|0\rangle_{in}.
\end{aligned}
\tag{5.5}
$$

This expression can be expanded by adding and subtracting the terms $\frac{1}{2} \cdot \hat{a}_{1V}^{\dagger}\hat{a}_{2V}^{\dagger}\,|\!\uparrow\rangle_{x1}\,|\!\uparrow\rangle_{x2}$ and $\frac{1}{2} \cdot \hat{a}_{1H}^{\dagger}\hat{a}_{2H}^{\dagger}\,|\!\downarrow\rangle_{x1}\,|\!\downarrow\rangle_{x2}$, respectively:

$$
\begin{aligned}
|\Psi\rangle_{12} \;=\; \tfrac{1}{2}(\;\; & \hat{a}_{1H}^{\dagger}\hat{a}_{2H}^{\dagger}\,|\!\uparrow\rangle_{x1}\,|\!\uparrow\rangle_{x2} &+\;\; & \hat{a}_{1H}^{\dagger}\hat{a}_{2V}^{\dagger}\,|\!\uparrow\rangle_{x1}\,|\!\downarrow\rangle_{x2} \\
+\;\; & \hat{a}_{1V}^{\dagger}\hat{a}_{2H}^{\dagger}\,|\!\downarrow\rangle_{x1}\,|\!\uparrow\rangle_{x2} &+\;\; & \hat{a}_{1V}^{\dagger}\hat{a}_{2V}^{\dagger}\,|\!\downarrow\rangle_{x1}\,|\!\downarrow\rangle_{x2} \\
+\;\; & \tfrac{1}{2}\hat{a}_{1V}^{\dagger}\hat{a}_{2V}^{\dagger}\,|\!\uparrow\rangle_{x1}\,|\!\uparrow\rangle_{x2} &-\;\; & \tfrac{1}{2}\hat{a}_{1V}^{\dagger}\hat{a}_{2V}^{\dagger}\,|\!\uparrow\rangle_{x1}\,|\!\uparrow\rangle_{x2} \\
+\;\; & \tfrac{1}{2}\hat{a}_{1H}^{\dagger}\hat{a}_{2H}^{\dagger}\,|\!\downarrow\rangle_{x1}\,|\!\downarrow\rangle_{x2} &-\;\; & \tfrac{1}{2}\hat{a}_{1H}^{\dagger}\hat{a}_{2H}^{\dagger}\,|\!\downarrow\rangle_{x1}\,|\!\downarrow\rangle_{x2} \;\;)|0\rangle_{in}.
\end{aligned}
\tag{5.6}
$$

The input creation operator $\hat{a}_{ij}^{\dagger}$ are expressed by the output creation operators $\hat{b}_{ij}^{\dagger}$, thereby assuming a perfect beam splitter:

$$
\begin{aligned}
|\Psi\rangle_{12} \;\rightarrow\; \tfrac{1}{4}(\;\; & (\hat{b}_{1H}^{\dagger}-\hat{b}_{2H}^{\dagger})(\hat{b}_{1H}^{\dagger}+\hat{b}_{2H}^{\dagger})\,|\!\uparrow\rangle_{x1}\,|\!\uparrow\rangle_{x2} \\
+\;\; & (\hat{b}_{1H}^{\dagger}-\hat{b}_{2H}^{\dagger})(\hat{b}_{1V}^{\dagger}+\hat{b}_{2V}^{\dagger})\,|\!\uparrow\rangle_{x1}\,|\!\downarrow\rangle_{x2} \\
+\;\; & (\hat{b}_{1V}^{\dagger}-\hat{b}_{2V}^{\dagger})(\hat{b}_{1H}^{\dagger}+\hat{b}_{2H}^{\dagger})\,|\!\downarrow\rangle_{x1}\,|\!\uparrow\rangle_{x2} \\
+\;\; & (\hat{b}_{1V}^{\dagger}-\hat{b}_{2V}^{\dagger})(\hat{b}_{1V}^{\dagger}+\hat{b}_{2V}^{\dagger})\,|\!\downarrow\rangle_{x1}\,|\!\downarrow\rangle_{x2} \\
+\;\; & \tfrac{1}{2}(\hat{b}_{1V}^{\dagger}-\hat{b}_{2V}^{\dagger})(\hat{b}_{1V}^{\dagger}+\hat{b}_{2V}^{\dagger})\,|\!\uparrow\rangle_{x1}\,|\!\uparrow\rangle_{x2} \\
-\;\; & \tfrac{1}{2}(\hat{b}_{1V}^{\dagger}-\hat{b}_{2V}^{\dagger})(\hat{b}_{1V}^{\dagger}+\hat{b}_{2V}^{\dagger})\,|\!\uparrow\rangle_{x1}\,|\!\uparrow\rangle_{x2} \\
+\;\; & \tfrac{1}{2}(\hat{b}_{1H}^{\dagger}-\hat{b}_{2H}^{\dagger})(\hat{b}_{1H}^{\dagger}+\hat{b}_{2H}^{\dagger})\,|\!\downarrow\rangle_{x1}\,|\!\downarrow\rangle_{x2} \\
-\;\; & \tfrac{1}{2}(\hat{b}_{1H}^{\dagger}-\hat{b}_{2H}^{\dagger})(\hat{b}_{1H}^{\dagger}+\hat{b}_{2H}^{\dagger})\,|\!\downarrow\rangle_{x1}\,|\!\downarrow\rangle_{x2} \;\;)|0\rangle_{out}.
\end{aligned}
\tag{5.7}
$$

A new arrangement of the various terms gives:

$$
\begin{aligned}
|\Psi\rangle_{12} \;=\; (\;\; & \tfrac{1}{4}((|\!\uparrow\rangle_{x1}\,|\!\uparrow\rangle_{x2}+|\!\downarrow\rangle_{x1}\,|\!\downarrow\rangle_{x2}) &\otimes\;\; & \tfrac{1}{2}(\hat{b}_{1H}^{\dagger}\hat{b}_{1H}^{\dagger}-\hat{b}_{2H}^{\dagger}\hat{b}_{2H}^{\dagger}+\hat{b}_{1V}^{\dagger}\hat{b}_{1V}^{\dagger}-\hat{b}_{2V}^{\dagger}\hat{b}_{2V}^{\dagger})) \\
+\;\; & \tfrac{1}{4}((|\!\uparrow\rangle_{x1}\,|\!\uparrow\rangle_{x2}-|\!\downarrow\rangle_{x1}\,|\!\downarrow\rangle_{x2}) &\otimes\;\; & \tfrac{1}{2}(\hat{b}_{1H}^{\dagger}\hat{b}_{1H}^{\dagger}-\hat{b}_{2H}^{\dagger}\hat{b}_{2H}^{\dagger}-\hat{b}_{1V}^{\dagger}\hat{b}_{1V}^{\dagger}+\hat{b}_{2V}^{\dagger}\hat{b}_{2V}^{\dagger})) \\
+\;\; & \tfrac{1}{4}((|\!\uparrow\rangle_{x1}\,|\!\downarrow\rangle_{x2}+|\!\downarrow\rangle_{x1}\,|\!\uparrow\rangle_{x2}) &\otimes\;\; & (\hat{b}_{1H}^{\dagger}\hat{b}_{1V}^{\dagger}-\hat{b}_{2H}^{\dagger}\hat{b}_{2V}^{\dagger})) \\
+\;\; & \tfrac{1}{4}((|\!\uparrow\rangle_{x1}\,|\!\downarrow\rangle_{x2}-|\!\downarrow\rangle_{x1}\,|\!\uparrow\rangle_{x2}) &\otimes\;\; & (\hat{b}_{1H}^{\dagger}\hat{b}_{2V}^{\dagger}-\hat{b}_{1V}^{\dagger}\hat{b}_{2H}^{\dagger})))|0\rangle_{out},
\end{aligned}
\tag{5.8}
$$

where the left hand component of the tensor product describes the state of the two atoms and the right hand side the two-photon state. The four two-atom states each are a Bell-state and so are the two-photon states (see equation 4.23-4.26). Thus, the state can be further summarized as:

$$
\begin{aligned}
|\Psi\rangle_{12} \;=\; & \tfrac{1}{4}(|\phi^{+}\rangle_{aa} &\otimes\;\; & |\phi^{+}\rangle_{ph}) \\
+\;\; & \tfrac{1}{4}(|\phi^{-}\rangle_{aa} &\otimes\;\; & |\phi^{-}\rangle_{ph}) \\
+\;\; & \tfrac{1}{4}(|\Psi^{+}\rangle_{aa} &\otimes\;\; & |\Psi^{+}\rangle_{ph}) \\
+\;\; & \tfrac{1}{4}(|\Psi^{-}\rangle_{aa} &\otimes\;\; & |\Psi^{-}\rangle_{ph}),
\end{aligned}
\tag{5.9}
$$

where aa labels the atomic and ph the photonic Bell-states. It shows that the projection of the two photons onto a Bell-state swaps the entanglement onto the atoms, yielding the very same entangled state on which the photons have been projected. Note, the entanglement only swaps onto the atoms by the photon projection. Thus, the photon projection also serves as heralding signal for a successful atom-atom entanglement generation. The detection setup of this experiment can only detect two-photon coincidences, if the two photons are in a $|\Psi^{+}\rangle_{ph}$- or $|\Psi^{-}\rangle_{ph}$ -state by detection of coincidences in a $D+$- or $D-$-detector combinations, respectively.

5.2.2. Model for Estimating the Entanglement Swapping Quality

All errors, which reduce the interference quality, also negatively influence the entanglement swapping quality. Thus, the quality of the entanglement swapping protocol critically depends on the two-photon quantum interference quality (see section 4.2). Photon coincidences, which herald the wrong Bell-state, cause a direct reduction of the AAE visibility. In addition two-photon emission events as well as dark count events further reduce the quality of the entanglement swapping protocol.

Here, the probability that the two atoms are in the same Bell-state, which the two-photon coincidence detection heralded, is calculated. It will be called Bell-state projection (BSP) quality. This calculation is based on the five probabilities $P_{\bullet\bullet|\circ}$, $P_{\bullet\circ|\bullet}$, $P_{\circ\bullet|\bullet}$, P_{error} and $P_{\bullet|\bullet}$ presented in subsection 4.6.5. They show the relative probabilities for the introduced categories of photons pairs to impinge on the beam splitter. But only photon coincidences in $D-$ or $D+$ detector combinations are used for photonic BSP. Thus, in a first step the relative probabilities of these categories of photon pairs in $D-$ and $D+$ detector combinations are calculated with respect to the considerations in section 4.2 and table 4.3. The fraction of ($\bullet \bullet |\circ$)-events in detector combinations $D-$ and $D+$ is given by $p_{\bullet\bullet|\circ}^{D+,b} + p_{\bullet\bullet|\circ}^{D-,b}$ (with $b \in \{HV, RL\}$) for both bases of photon analysis. ($\bullet \circ |\bullet$)- and ($\circ \bullet |\bullet$)-events show a reduced interference contrast. Thus, photon pairs in a $|\Psi^+\rangle_{ph}$-state can also impinge on $D-$ detector combinations and photons in a $|\Psi^-\rangle_{ph}$-state can impinge on $D+$ detector combinations. Photon pairs in $|\Phi^\pm\rangle_{ph}$-states never impinge on $D-$ or $D+$ detector combinations as both photons have the same polarization, and therefore can only impinge on the same detector or on $D\varnothing$ detector combinations. The overall fraction of ($\bullet \circ |\bullet$)- and ($\circ \bullet |\bullet$)-events, which impinge on $D-$ or $D+$ detector combinations is $1/2$. $P_{\bullet|\bullet}$ summarizes all ($\bullet|\bullet$)-events. All events in a $|\Psi^+\rangle_{ph}$-state impinge on $D+$ detector combinations and photons in a $|\Psi^-\rangle_{ph}$-state can impinge on $D-$ detector combinations. Thus the overall fraction of those events in a $D-$ or $D+$ detector combinations is also $1/2$ as photons in $|\Phi^\pm\rangle_{ph}$-states always impinge on the same detector. P_{error} summarizes events which do not interfere because of residual errors. These events are expected to show white noise. For combinatorial reasons $1/2$ of these events impinge on $D-$ or $D+$ detector combinations. The considerations yield the basis depended probabilities $P_{\bullet\bullet|\circ}^{D\pm,b}$, $P_{\bullet\circ|\bullet}^{D\pm,b}$, $P_{\circ\bullet|\bullet}^{D\pm,b}$, $P_{error}^{D\pm,b}$ and $P_{\bullet|\bullet}^{D\pm,b}$. They describe the relative probabilities for the five categories of photon pairs to cause a two-photon coincidence in a $D-$ or $D+$ detector combination:

$$
\begin{aligned}
P_{\bullet\bullet|\circ}^{D\pm,b} &= 1/n^b \cdot (p_{\bullet\bullet|\circ}^{D+,b} + p_{\bullet\bullet|\circ}^{D-,b}) \cdot P_{\bullet\bullet|\circ} \\
P_{\bullet\circ|\bullet}^{D\pm,b} &= 1/n^b \cdot \tfrac{1}{2} P_{\bullet\circ|\bullet} \\
P_{\circ\bullet|\bullet}^{D\pm,b} &= 1/n^b \cdot \tfrac{1}{2} P_{\circ\bullet|\bullet} \\
P_{\bullet|\bullet}^{D\pm,b} &= 1/n^b \cdot \tfrac{1}{2} P_{\bullet|\bullet} \\
P_{error}^{D\pm,b} &= 1/n^b \cdot \tfrac{1}{2} P_{error},
\end{aligned}
\tag{5.10}
$$

where $n^b = ((p_{\bullet\bullet|\circ}^{D+,b} + p_{\bullet\bullet|\circ}^{D-,b}) \cdot P_{\bullet\bullet|\circ} + \tfrac{1}{2} P_{\bullet\circ|\bullet} + \tfrac{1}{2} P_{\circ\bullet|\bullet} + \tfrac{1}{2} P_{\bullet|\bullet} + \tfrac{1}{2} P_{error})$ with $b \in \{HV, RL\}$ normalizes the sum of this new probabilities to 1.

This set of relative probabilities still does not consider any dark count events as the calculations are based on the dark count corrected event probabilities $p_{tp}^{d,b}$ (see section 3.3). The total number of events in $D-$ and $D+$ detector combinations $n_{tp}^{D\pm,b} = n_{tp}^{D-,b} + n_{tp}^{D+,b}$ is given in table 4.5 and the number of expected dark count events in every detector combination $n_{dc}^{ij,b}$ (with $i, j \in \{1 \perp, 1 \parallel, 2 \perp, 2 \parallel\}$) is given in table 4.8. Thus, in a second step, the relative probability of a dark count event in a $D-$ and $D+$ detector combination can be calculated with respect to the data given in the two tables by

probability \ basis of photon analysis	$b = HV$	$b = RL$
$\overline{P}_{dc}^{D\pm,b}$	0.008 ± 0.001	0.007 ± 0.001
$\overline{P}_{\bullet\bullet\mid\circ}^{D\pm,b}$	0.006 ± 0.004	0.021 ± 0.013
$\overline{P}_{\bullet\circ\mid\bullet}^{D\pm,b}$	0.016 ± 0.010	0.016 ± 0.010
$\overline{P}_{\circ\bullet\mid\bullet}^{D\pm,b}$	0.075 ± 0.006	0.074 ± 0.005
$\overline{P}_{\bullet\mid\bullet}^{D\pm,b}$	0.859 ± 0.006	0.847 ± 0.012
$\overline{P}_{error}^{D\pm,b}$	0.036 ± 0.018	0.036 ± 0.018

Table 5.1.: Relative probabilities that a coincidence detection in a $D+$ or $D-$ detector combination is caused by one of the listed categories of photon pairs for the two measurement bases (with $b \in \{HV, RL\}$).

following equation:

$$\overline{P}_{dc}^{D\pm,b} = \frac{n_{dc}^{1\perp1\parallel,b} + n_{dc}^{2\perp2\parallel,b} + n_{dc}^{1\perp2\parallel,b} + n_{dc}^{1\parallel2\perp,b}}{n_{tp}^{D\pm,b}}. \tag{5.11}$$

In addition, the set of probabilities $P_{\bullet\bullet\mid\circ}^{D\pm,b}$, $P_{\bullet\circ\mid\bullet}^{D\pm,b}$, $P_{\circ\bullet\mid\bullet}^{D\pm,b}$, $P_{error}^{D\pm,b}$ and $P_{\bullet\mid\bullet}^{D\pm,b}$ can be expanded by the probability for a dark count event forming a new set of six probabilities:

$$
\begin{aligned}
\overline{P}_{\bullet\bullet\mid\circ}^{D\pm,b} &= P_{\bullet\bullet\mid\circ}^{D\pm,b} \cdot (1 - \overline{P}_{dc}^{D\pm,b}) \\
\overline{P}_{\bullet\circ\mid\bullet}^{D\pm,b} &= P_{\bullet\circ\mid\bullet}^{D\pm,b} \cdot (1 - \overline{P}_{dc}^{D\pm,b}) \\
\overline{P}_{\circ\bullet\mid\bullet}^{D\pm,b} &= P_{\circ\bullet\mid\bullet}^{D\pm,b} \cdot (1 - \overline{P}_{dc}^{D\pm,b}) \\
\overline{P}_{\bullet\mid\bullet}^{D\pm,b} &= P_{\bullet\mid\bullet}^{D\pm,b} \cdot (1 - \overline{P}_{dc}^{D\pm,b}) \\
\overline{P}_{error}^{D\pm,b} &= P_{error}^{D\pm,b} \cdot (1 - \overline{P}_{dc}^{D\pm,b})
\end{aligned}
\tag{5.12}
$$

This new set of relative probabilities $\overline{P}_{\bullet\bullet\mid\circ}^{D\pm,b}$, $\overline{P}_{\bullet\circ\mid\bullet}^{D\pm,b}$, $\overline{P}_{\circ\bullet\mid\bullet}^{D\pm,b}$, $\overline{P}_{\bullet\mid\bullet}^{D\pm,b}$, $\overline{P}_{error}^{D\pm,b}$ and $\overline{P}_{dc}^{D\pm,b}$ finally yields the relative probabilities of all six categories of photon coincidences occurring in $D+$ and $D-$ detector combination. The values of the probabilities are given in table 5.1 for both measurement basis.

In order to calculate the Bell-state projection quality by using this latest set of probabilities, the influence of every category of photon coincidence on the Bell-state projection quality has to be examined. The influence depends on the probability that the atomic spins are in the qubit-space (a superposition of the states $5^2S_{1/2}, |F = 1, m_{F'} = \pm1\rangle$) after emission of the last photon as well as on interference probability of two photons impinging on the beam splitter. All categories of photon coincidences have a certain probability for heralding the correct atomic Bell-state :

- The probability $\overline{P}_{\bullet\mid\bullet}^{D\pm,b}$ represents ($\bullet\mid\bullet$)-events, which according to the mode overlap perfectly interfere. They have per definition a probability to herald the correct Bell-state of one:

$$\overline{p}_{\bullet\mid\bullet}^{D\pm} = 1. \tag{5.13}$$

- The probability $\overline{P}_{\bullet\bullet\mid\circ}^{D\pm,b}$ represents two-photon events of the first case ($\bullet \bullet \mid\circ$). Here, no interference takes place. Still, there is a residual probability that the correct Bell-state is heralded.

The atom, which emitted the two photons, can be in the state $5^2S_{1/2}, |F = 1\rangle$ as well as in the state $5^2S_{1/2}, |F = 2\rangle$. It depends on the different types of two-photon emission, which relative provabilities in $D+$ and $D-$ detector combinations are given by

$$p_{I,D\pm}^{\sigma\pm,HV} = \frac{\frac{1}{2}p_I^{\sigma\pm}}{\frac{1}{2}p_I^{\sigma\pm} + (p_b + \frac{1}{2}p_c)p_{II}^{\sigma\pm}}, \tag{5.14}$$

$$p_{II,D\pm}^{\sigma\pm,HV} = \frac{(p_b + \frac{1}{2}p_c)p_{II}^{\sigma\pm}}{\frac{1}{2}p_I^{\sigma\pm} + (p_b + \frac{1}{2}p_c)p_{II}^{\sigma\pm}} \tag{5.15}$$

as well as

$$p_{I,D\pm}^{\sigma\pm,RL} = \frac{\frac{1}{2}p_I^{\sigma\pm}}{\frac{1}{2}p_I^{\sigma\pm} + (p_a + p_b)p_{II}^{\sigma\pm}}, \tag{5.16}$$

$$p_{II,D\pm}^{\sigma\pm,RL} = \frac{(p_a + p_b)p_{II}^{\sigma\pm}}{\frac{1}{2}p_I^{\sigma\pm} + (p_a + p_b)p_{II}^{\sigma\pm}} \tag{5.17}$$

(see also section 3.4 and table 4.3). The spin of this atom is only in the qubit-space at a type I two-photon emission processes. The spin of the other atom is in the state $5^2S_{1/2}$, $|F = 1, m_{F'} = +1\rangle$, $5^2S_{1/2}, |F = 1, m_{F'} = -1\rangle$ or $5^2S_{1/2}, |F = 1, m_{F'} = 0\rangle$ with equal probability as it is expected that is also emitted a photon, although it does not impinged on the beam splitter. If the first atom emitted two-photons via a type I two-photon emission process and the second atom emitted a $\sigma\pm$-polarized photon (probability for that is $2/3$), the chance for heralding the correct Bell-state is the same as for white noise:

$$\overline{p}_{\bullet\bullet|\circ}^{D\pm,b} = \frac{1}{4}\frac{2}{3}p_{I,D\pm}^{\sigma\pm,b}. \tag{5.18}$$

- The probability $\overline{P}_{\bullet\circ|\bullet}^{D\pm,b}$ represents ($\bullet\circ|\bullet$)-events, which have a reduced interference probability. But in this case, the interference probability is irrelevant as the emission of a second photon changes the maybe correctly heralded atom-atom state. Still, there is a change for the heralding of the correct Bell-state, which is equal to white noise, if both atom spins are in the qubit-space. The spin of the atom, which emits only a single photon, is always in the qubit-space. The spin of the other atom is in the qubit-space with following probability: $2/3p_{I,\bullet\circ|\bullet} + 5/12p_{II,\bullet\circ|\bullet}$ (calculated be Clebsch-Gordan Coefficients - see 4.4.1 and C). Thus, the overall probability to herald the correct Bell-state is:

$$\overline{p}_{\bullet\circ|\bullet}^{D\pm} = \frac{1}{4}\left(\frac{2}{3}p_{I,\bullet\circ|\bullet} + \frac{5}{12}p_{II,\bullet\circ|\bullet}\right). \tag{5.19}$$

- The probability $\overline{P}_{\circ\bullet|\bullet}^{D\pm,b}$ represents ($\circ\bullet|\bullet$)-events. These events have a reduced interference probability. The interfering fraction of these events, where additionally the atom spin is in the qubit-space, is given by $O_{\circ\bullet I|\bullet}^2 \cdot p_{I,\circ\bullet|\bullet} + O_{\circ\bullet III|\bullet}^2 \cdot p_{III,\circ\bullet|\bullet}$ (see subsection 4.4.4), and has per definition a probability to herald the correct Bell-state of one. But also the non interfering fraction might herald the correct Bell-state with a probability of $1/2$, if both atom spins are in the qubit-space. The two photons impinging on a $D+$ or $D-$ detector combination have different polarizations, thus the atoms can only be in one of the states $|\Psi^\pm\rangle_{aa}$. Analogously to the previous category, the spin of the atom, which emits the single photon, is always in the qubit-space. The spin of the other atom is in the qubit-space with following probability (including

the reduced interference probability): $(1 - O^2_{\circ\bullet\text{I}|\bullet}) \cdot p_{\text{I},\circ\bullet|\bullet} + (1 - O^2_{\circ\bullet\text{III}|\bullet}) \cdot p_{\text{III},\circ\bullet|\bullet}$. The total probability to herald the correct Bell-state is:

$$\overline{p}^{D\pm}_{\circ\bullet|\bullet} = (O^2_{\circ\bullet\text{I}|\bullet} + \frac{1}{2}(1 - O^2_{\circ\bullet\text{I}|\bullet})) \cdot p_{\text{I},\circ\bullet|\bullet} + (O^2_{\circ\bullet\text{III}|\bullet} + \frac{1}{2}(1 - O^2_{\circ\bullet\text{III}|\bullet})) \cdot p_{\text{III},\circ\bullet|\bullet}. \quad (5.20)$$

- The probability $\overline{P}^{D\pm,b}_{dc}$ represents the dark count events. Here, only one photon is detected and the change for heralding the correct Bell-state is the same as white noise, if both atomic spins are in the qubit-space. The spin of the atom, which emitted the detected photon, is always in the qubit-space. The spin of the other atom is in the qubit-space with a probability of $2/3$. The overall probability to herald the correct Bell-state is:

$$\overline{p}^{D\pm}_{dc} = \frac{1}{4}\frac{2}{3}. \quad (5.21)$$

- The probability $\overline{P}^{D\pm,b}_{error}$ represents photon pairs, which do not interfere because of residual errors. Here, the two atomic spins are always expected in the qubit-space, and as the two photons have different polarizations, the change for heralding the correct Bell-state is $1/2$. Thus, the overall probability to herald the correct Bell-state is also:

$$\overline{p}^{D\pm}_{error} = \frac{1}{2} \quad (5.22)$$

.

The BSP quality can be calculated by weighing the relative probabilities $\overline{P}^{D\pm,b}_{\bullet\bullet|\circ}, \overline{P}^{D\pm,b}_{\bullet\circ|\bullet}, \overline{P}^{D\pm,b}_{\circ\bullet|\bullet}, \overline{P}^{D\pm,b}_{\bullet|\bullet}$, $\overline{P}^{D\pm,b}_{error}$ and $\overline{P}^{D\pm,b}_{dc}$ with their individual probability to herald the correct Bell-state:

$$
\begin{aligned}
Q^b_{BSP} = \quad & \overline{p}^{D\pm,b}_{\bullet\bullet|\circ} \cdot \overline{P}^{D\pm,b}_{\bullet\bullet|\circ} + \overline{p}^{D\pm}_{\bullet\circ|\bullet} \cdot \overline{P}^{D\pm,b}_{\bullet\circ|\bullet} + \overline{p}^{D\pm}_{\circ\bullet|\bullet} \cdot \overline{P}^{D\pm,b}_{\circ\bullet|\bullet} \\
& + \overline{p}^{D\pm}_{\bullet|\bullet} \cdot \overline{P}^{D\pm,b}_{\bullet|\bullet} + \overline{p}^{D\pm}_{error} \cdot \overline{P}^{D\pm,b}_{error} + \overline{p}^{D\pm}_{dc} \cdot \overline{P}^{D\pm,b}_{dc},
\end{aligned} \quad (5.23)
$$

where $b \in \{HV, RL\}$. This yields a BSP quality of $Q^{HV}_{BSP} = 0.941 \pm 0.009$ in the H/V-basis and of $Q^{RL}_{BSP} = 0.928 \pm 0.017$ in the R/L-basis, respectively. It shows that a BSP in the H/V-basis is favorable. The higher quality is caused by the lower probability of $(\bullet \bullet |\circ)$-events in $D+$ and $D-$ detector combinations, in case of photon analysis in the H/V-basis.

5.2.3. Atom-Atom Entanglement Correlations

In order to verify atom-atom entanglement by correlation-measurements, the two atomic spins are analyzed after entanglement generation, analogously to the atom-photon entanglement verification discussed in subsection 2.4.3. For this purpose, the measurement basis for one atomic spin state is kept constant, while the one for other atomic spin state is rotated for each measurement setting. The measured relative orientation of both atomic spins in each entanglement swapping event is added up to the event numbers $N^{(\alpha,\beta)}_{SS'}$, where $S, S' \in \{\uparrow\uparrow, \downarrow\downarrow, \uparrow\downarrow, \downarrow\uparrow\}$ are the observed eigenstates of the two atomic spins along their individual linear measurement directions which are defined by α (trap1) and β (trap2). Thus, the measured correlation probability is $cp = \frac{1}{N}(N^{(\alpha,\beta)}_{\uparrow\uparrow} + N^{(\alpha,\beta)}_{\downarrow\downarrow})$ and the anti-correlations probability is $acp = \frac{1}{N}(N^{(\alpha,\beta)}_{\uparrow\downarrow} + N^{(\alpha,\beta)}_{\downarrow\uparrow})$, where N is the total number of events at this measurement setting.

Before discussing the evolution of the correlation and anti-correlation probabilities, in case the measurement basis of one atomic spin is rotated, the expected kind of correlations has to be determined. The Bell-state projection of the two photons is performed in the H/V-basis, and therefore the atoms are projected onto one of the following two Bell-states ($\hat{\sigma}^x$-basis):

$$
\begin{aligned}
|\Psi^+\rangle_{aa} &= \tfrac{1}{\sqrt{2}}(|\uparrow\rangle_x |\downarrow\rangle_x + |\downarrow\rangle_x |\uparrow\rangle_x) \\
|\Psi^-\rangle_{aa} &= \tfrac{1}{\sqrt{2}}(|\uparrow\rangle_x |\downarrow\rangle_x - |\downarrow\rangle_x |\uparrow\rangle_x).
\end{aligned}
$$

The two atomic spins show anti-correlations in the $\hat{\sigma}^x$-basis independent of the Bell-state they are projected on. This has considerable consequences as it shows that these correlations are independent of the two-photon interference quality. In this case events summarized in P_r as well as ($\circ \bullet_{\mathrm{I}} |\bullet$)- and ($\circ \bullet_{\mathrm{III}} |\bullet$)-events do not reduce the expected AAE visibility. If the atomic spins are analyzed in a basis orthogonal to the one, in which the photonic BSP took place, the atoms in a $|\Psi^+\rangle$-state or in a $|\Psi^-\rangle$-state show different correlations. While for the $|\Psi^-\rangle$-singlet-state still shows anti-correlations between both atomic spins , the $|\Psi^+\rangle$-state shows varying correlations (see appendix D):

$$
\begin{aligned}
|\Psi^+\rangle_{ph} &\rightarrow \tfrac{1}{\sqrt{2}}(|\uparrow\rangle_x |\downarrow\rangle_x + |\downarrow\rangle_x |\uparrow\rangle_x) \\
&= -\tfrac{1}{\sqrt{2}}(|\uparrow\rangle_y |\uparrow\rangle_y - |\downarrow\rangle_y |\downarrow\rangle_y) \\
&= -\tfrac{1}{\sqrt{2}}i(|\uparrow\rangle_z |\uparrow\rangle_z - |\downarrow\rangle_z |\downarrow\rangle_z)
\end{aligned}
$$

$$
\begin{aligned}
|\Psi^-\rangle_{ph} &\rightarrow \tfrac{1}{\sqrt{2}}(|\uparrow\rangle_x |\downarrow\rangle_x - |\downarrow\rangle_x |\uparrow\rangle_x) \\
&\quad -\tfrac{1}{\sqrt{2}}(|\uparrow\rangle_y |\downarrow\rangle_y - |\downarrow\rangle_y |\uparrow\rangle_y) \\
&= -\tfrac{1}{\sqrt{2}}i(|\uparrow\rangle_z |\downarrow\rangle_z - |\downarrow\rangle_z |\uparrow\rangle_z)
\end{aligned}
$$

Evidently, it is most important that the two-photon coincidence detection heralds the correct Bell-state because the AAE visibility directly depends on the two-photon interference quality.

Finally, the correlation and anti-correlation probabilities depend on the state at which the two atomic spins are projected on. In case the two atomic spins are in the $|\Psi^-\rangle$-state, they have the following evolution:

$$
cp^{\Psi^-} = \frac{1}{2}V_{\Psi^-}(1 + \cos(2(\alpha - \beta + 90°))) \tag{5.24}
$$

$$
acp^{\Psi^-} = \frac{1}{2}V_{\Psi^-}(1 + \cos(2(\alpha - \beta))), \tag{5.25}
$$

where V_{Ψ^-} is the visibility of the two entangled atoms (peak-to-peak amplitude of a atom-atom correlation measurement) . In case the two atomic spins are in the $|\Psi^+\rangle$ state, a different evolution is obtained:

$$
cp^{\Psi^+} = \frac{1}{2}V_{\Psi^+}(1 + \cos(2(\alpha + \beta + 90°))) \tag{5.26}
$$

$$
acp^{\Psi^+} = \frac{1}{2}V_{\Psi^+}(1 + \cos(2(\alpha + \beta))), \tag{5.27}
$$

where V_{Ψ^+} describes the visibility.

5.2.4. Estimation of Atom-Atom Entanglement Visibilities

The visibilities to be observed in an atom-atom entanglement experiment can be estimated by consideration of the results of the atom-photon entanglement measurements and the two-photon interference measurements. This estimation also respects the events where the spin of one of the atoms or of both atoms is not in the qubit-space.

In general, after the heralding signal both atomic states are analyzed, and only two measurement results are possible for each atom: either the atom is lost or survived in the trap (see subsection 2.4.2). In case the atom is lost, it was in the state $|\downarrow\rangle_x$ and in case it survived, it was in the state $|\uparrow\rangle_x$ (for measurements in the H/V-basis). Also events, where the atomic spin is not in the qubit-space, generate one of these two results, yielding a false projection of the atomic spin, and thereby reducing the entanglement visibilities.

The probability for erasing the atom from the trap $p_{e,i}$ (where $i \in \{1, 2\}$ represents trap1 or trap2, respectively), in case it is in the state $|\downarrow\rangle_x$, is given by atom-photon entanglement measurements. These measurements also give the survival probability of the atom $p_{s,i}$, in case it is in the state $|\uparrow\rangle_x$. Furthermore, in case the atom is in the state $5^2 S_{1/2}, |F = 1, m_{F'} = 0\rangle$, it is treated as it is in the bright state $|\downarrow\rangle_x$, and in case it is in the state $5^2 S_{1/2}, |F = 2\rangle$, it is assumed to be erased from the trap with a probability of 0.99. These considerations allow to calculate the correlation probability (cp) and anti-correlation probability (acp) for every combination of the two atomic spins with respect to the following equations:

$$cp = p_{in,1} p_{in,2} + p_{out,1} p_{out,2} \tag{5.28}$$

and

$$acp = p_{in,1} p_{out,2} + p_{out,1} p_{in,2}, \tag{5.29}$$

where p_{in} and p_{out} are the probabilities that the atom of the respective trap is erased from the trap or survived in it. According to the previous discussion, four different states of the atomic spin have to be distinguished:

1. In case the atom is in the state $|\downarrow\rangle_x$, they are defined as follows:

$$p_{in,i} = 1 - p_{e,i} \tag{5.30}$$

   and

$$p_{out,i} = p_{e,i}. \tag{5.31}$$

2. In case the atom is in the state $|\uparrow\rangle_x$, $p_{in,i}$ and $p_{out,i}$ are defined by the survival probability:

$$p_{in,i} = p_{s,i} \tag{5.32}$$

   and

$$p_{out,i} = 1 - p_{s,i}. \tag{5.33}$$

3. In case the atom is in the state $5^2 S_{1/2}, |F = 1, m_{F'} = 0\rangle$, $p_{in,i}$ and $p_{out,i}$ are also defined by probability to erase the atom from the trap:

$$p_{in} = 1 - p_{e,i} \tag{5.34}$$

   and

$$p_{out} = p_{e,i}. \tag{5.35}$$

4. In case the atom is in the state $5^2 S_{1/2}, |F = 2\rangle$, $p_{in,i}$ and $p_{out,i}$ are defined by the push out or ionization probability itself. It has a defined value of 0.99:

$$p_{in} = 1 - 0.99 \tag{5.36}$$

and

$$p_{out} = 0.99. \tag{5.37}$$

cp and acp are given for every combination of the atomic spins in table 5.2.

combination of atomic spins (SS')	$cp^{SS'}$	$acp^{SS'}$
$\uparrow\uparrow$	0.922	0.078
$\downarrow\downarrow$	0.858	0.142
$\uparrow\downarrow$	0.089	0.911
$\downarrow\uparrow$	0.132	0.868
$\uparrow\, m_F 0$	0.089	0.911
$\downarrow\, m_F 0$	0.858	0.142
$m_F 0\, \uparrow$	0.132	0.868
$m_F 0\, \downarrow$	0.858	0.142
$\uparrow\, F2$	0.045	0.955
$\downarrow\, F2$	0.896	0.104
$F2\, \uparrow$	0.054	0.946
$F2\, \downarrow$	0.934	0.066
$mF0mF0$	0.858	0.142
$F2mF0$	0.934	0.066
$mF0F2$	0.896	0.104

Table 5.2.: Correlation probability (cp) and anti-correlation probability (acp) for every combination of the two atomic spins occurring in the experiment. The spin-states are represented by S and S', where S is the spin-state of the atom in trap1 and S' the one of the atom in trap2, respectively (with $S, S' \in \{\uparrow, \downarrow, m_F 0, F2\}$). The symbols $\downarrow$ and $\uparrow$ represent the bright-sate $|\downarrow\rangle_x$ and dark-sate $|\uparrow\rangle_x$, respectively. $m_F 0$ indicates that the atom is in the state $5^2 S_{1/2}, |F = 1, m_{F'} = 0\rangle$ and $F2$ indicates that it is in the state $5^2 S_{1/2}, |F = 2\rangle$. The values are calculated with respect to equations 5.28-5.37 and with $p_{e,1} = 0.904$, $p_{s,1} = 0.964$, $p_{e,2} = 0.943$ and $p_{s,2} = 0.955$, which are derived from atom-photon entanglement measurements.

The spins of the two atoms have one of the combinations shown in table 5.2 at every heralded atom-atom-entanglement event. The exact probabilities for every combination depend on the relative probabilities of the six categories of photon pairs impinging on $D+$ and $D-$ detector combinations, which are given in table 5.1. Every category has an individual probability for every spin combination. These provabilities determine the total correlation and anti-correlation probability for every category, and thus the expected visibilities. Note that the two spins show correlations or anti-correlations according to the heralded entangled state and the basis, in which the atoms are analyzed (see subsection 5.2.3):

1. Events represented by the probability $\overline{P}_{\bullet|\bullet}^{D\pm,HV}$ have the following visibilities:

$$V_{\Psi^+,\bullet|\bullet}^{HV} = \frac{1}{2}(acp^{\downarrow\uparrow} + acp^{\uparrow\downarrow}) - \frac{1}{2}(cp^{\downarrow\uparrow} + cp^{\uparrow\downarrow}), \tag{5.38}$$

$$V^{HV}_{\Psi^-,\bullet|\bullet} = \frac{1}{2}(acp^{\downarrow\uparrow} + acp^{\uparrow\downarrow}) - \frac{1}{2}(cp^{\downarrow\uparrow} + cp^{\uparrow\downarrow}), \tag{5.39}$$

$$V^{PM}_{\Psi^+,\bullet|\bullet} = \frac{1}{2}(acp^{\uparrow\uparrow} + acp^{\downarrow\downarrow}) - \frac{1}{2}(cp^{\uparrow\uparrow} + cp^{\downarrow\downarrow}) \tag{5.40}$$

and

$$V^{PM}_{\Psi^-,\bullet|\bullet} = \frac{1}{2}(acp^{\downarrow\uparrow} + acp^{\uparrow\downarrow}) - \frac{1}{2}(cp^{\downarrow\uparrow} + cp^{\uparrow\downarrow}). \tag{5.41}$$

2. Events represented by the probability $\overline{P}^{D\pm,HV}_{error}$ have the following visibilities:

$$V^{HV}_{\Psi^+,error} = \frac{1}{2}(acp^{\downarrow\uparrow} + acp^{\uparrow\downarrow}) - \frac{1}{2}(cp^{\downarrow\uparrow} + cp^{\uparrow\downarrow}), \tag{5.42}$$

$$V^{HV}_{\Psi^-,error} = \frac{1}{2}(acp^{\downarrow\uparrow} + acp^{\uparrow\downarrow}) - \frac{1}{2}(cp^{\downarrow\uparrow} + cp^{\uparrow\downarrow}), \tag{5.43}$$

$$V^{PM}_{\Psi^+,error} = \frac{1}{4}(cp^{\uparrow\uparrow} + cp^{\downarrow\downarrow} + cp^{\downarrow\uparrow} + cp^{\uparrow\downarrow}) - \frac{1}{4}(acp^{\uparrow\uparrow} + acp^{\downarrow\downarrow} + acp^{\downarrow\uparrow} + acp^{\uparrow\downarrow}) \tag{5.44}$$

and

$$V^{PM}_{\Psi^-,error} = \frac{1}{4}(acp^{\uparrow\uparrow} + acp^{\downarrow\downarrow} + acp^{\downarrow\uparrow} + acp^{\uparrow\downarrow}) - \frac{1}{4}(cp^{\uparrow\uparrow} + cp^{\downarrow\downarrow} + cp^{\downarrow\uparrow} + cp^{\uparrow\downarrow}). \tag{5.45}$$

3. Events represented by the probability $\overline{P}^{D\pm,HV}_{dc}$ have the following visibilities:

$$
\begin{aligned}
V^{HV}_{\Psi^+,dc} = \;& (\tfrac{2}{3}\tfrac{1}{4}(acp^{\uparrow\uparrow} + acp^{\downarrow\downarrow} + acp^{\downarrow\uparrow} + acp^{\uparrow\downarrow}) \\
& + \tfrac{1}{3}\tfrac{1}{4}(acp^{m_F0\uparrow} + acp^{m_F0\downarrow} + acp^{\downarrow m_F0} + acp^{\uparrow m_F0})) \\
& - (\tfrac{2}{3}\tfrac{1}{4}(cp^{\uparrow\uparrow} + cp^{\downarrow\downarrow} + cp^{\downarrow\uparrow} + cp^{\uparrow\downarrow}) \\
& + \tfrac{1}{3}\tfrac{1}{4}(cp^{m_F0\uparrow} + cp^{m_F0\downarrow} + cp^{\downarrow m_F0} + cp^{\uparrow m_F0})),
\end{aligned}
\tag{5.46}
$$

$$
\begin{aligned}
V^{HV}_{\Psi^-,dc} = \;& (\tfrac{2}{3}\tfrac{1}{4}(acp^{\uparrow\uparrow} + acp^{\downarrow\downarrow} + acp^{\downarrow\uparrow} + acp^{\uparrow\downarrow}) \\
& + \tfrac{1}{3}\tfrac{1}{4}(acp^{m_F0\uparrow} + acp^{m_F0\downarrow} + acp^{\downarrow m_F0} + acp^{\uparrow m_F0})) \\
& - (\tfrac{2}{3}\tfrac{1}{4}(cp^{\uparrow\uparrow} + cp^{\downarrow\downarrow} + cp^{\downarrow\uparrow} + cp^{\uparrow\downarrow}) \\
& + \tfrac{1}{3}\tfrac{1}{4}(cp^{m_F0\uparrow} + cp^{m_F0\downarrow} + cp^{\downarrow m_F0} + cp^{\uparrow m_F0})),
\end{aligned}
\tag{5.47}
$$

$$
\begin{aligned}
V^{PM}_{\Psi^+,dc} = \;& (\tfrac{2}{3}\tfrac{1}{4}(cp^{\uparrow\uparrow} + cp^{\downarrow\downarrow} + cp^{\downarrow\uparrow} + cp^{\uparrow\downarrow}) \\
& + \tfrac{1}{3}\tfrac{1}{4}(cp^{m_F0\uparrow} + cp^{m_F0\downarrow} + cp^{\downarrow m_F0} + cp^{\uparrow m_F0})) \\
& - (\tfrac{2}{3}\tfrac{1}{4}(acp^{\uparrow\uparrow} + acp^{\downarrow\downarrow} + acp^{\downarrow\uparrow} + acp^{\uparrow\downarrow}) \\
& + \tfrac{1}{3}\tfrac{1}{4}(acp^{m_F0\uparrow} + acp^{m_F0\downarrow} + acp^{\downarrow m_F0} + acp^{\uparrow m_F0}))
\end{aligned}
\tag{5.48}
$$

and

$$
\begin{aligned}
V^{PM}_{\Psi^-,dc} = \;& (\tfrac{2}{3}\tfrac{1}{4}(acp^{\uparrow\uparrow} + acp^{\downarrow\downarrow} + acp^{\downarrow\uparrow} + acp^{\uparrow\downarrow}) \\
& + \tfrac{1}{3}\tfrac{1}{4}(acp^{m_F0\uparrow} + acp^{m_F0\downarrow} + acp^{\downarrow m_F0} + acp^{\uparrow m_F0})) \\
& - (\tfrac{2}{3}\tfrac{1}{4}(cp^{\uparrow\uparrow} + cp^{\downarrow\downarrow} + cp^{\downarrow\uparrow} + cp^{\uparrow\downarrow}) \\
& + \tfrac{1}{3}\tfrac{1}{4}(cp^{m_F0\uparrow} + cp^{m_F0\downarrow} + cp^{\downarrow m_F0} + cp^{\uparrow m_F0})).
\end{aligned}
\tag{5.49}
$$

4. Events represented by the probability $\overline{P}_{\bullet\bullet|\circ}^{D\pm,HV}$ have the following visibilities:

$$
\begin{aligned}
V_{\Psi+,\bullet\bullet|\circ}^{HV} = \ & (p_{\mathrm{I},D\pm}^{\sigma\pm,HV}\,(\tfrac{2}{3}\tfrac{1}{4}(acp^{\uparrow\uparrow}+acp^{\downarrow\downarrow}+acp^{\downarrow\uparrow}+acp^{\uparrow\downarrow}) \\
& +\tfrac{1}{3}\tfrac{1}{4}(acp^{m_F0\uparrow}+acp^{m_F0\downarrow}+acp^{\downarrow m_F0}+acp^{\uparrow m_F0})) \\
& +p_{\mathrm{II},D\pm}^{\sigma\pm,HV}\,(\tfrac{p_b}{p_{b+1/2}p_c}(\tfrac{2}{3}\tfrac{1}{4}(acp^{\uparrow F2}+acp^{\downarrow F2}+acp^{F2\uparrow}+acp^{F2\downarrow}) \\
& +\tfrac{1}{3}\tfrac{1}{2}(acp^{m_F0F2}+acp^{F2m_F0})) \\
& +\tfrac{p_c}{p_{b+1/2}p_c}(\tfrac{2}{3}\tfrac{1}{4}(acp^{\uparrow F2}+acp^{\downarrow F2}+acp^{F2\uparrow}+acp^{F2\downarrow}) \\
& +\tfrac{1}{3}\tfrac{1}{2}(acp^{m_F0F2}+acp^{F2m_F0})))) \\
& -(p_{\mathrm{I},D\pm}^{\sigma\pm,HV}\,(\tfrac{2}{3}\tfrac{1}{4}(cp^{\uparrow\uparrow}+cp^{\downarrow\downarrow}+cp^{\downarrow\uparrow}+cp^{\uparrow\downarrow}) \\
& +\tfrac{1}{3}\tfrac{1}{4}(cp^{m_F0\uparrow}+cp^{m_F0\downarrow}+cp^{\downarrow m_F0}+cp^{\uparrow m_F0})) \\
& +p_{\mathrm{II},D\pm}^{\sigma\pm,HV}\,(\tfrac{p_b}{p_{b+1/2}p_c}(\tfrac{2}{3}\tfrac{1}{4}(cp^{\uparrow F2}+cp^{\downarrow F2}+cp^{F2\uparrow}+cp^{F2\downarrow}) \\
& +\tfrac{1}{3}\tfrac{1}{2}(cp^{m_F0F2}+cp^{F2m_F0})) \\
& +\tfrac{p_c}{p_{b+1/2}p_c}(\tfrac{2}{3}\tfrac{1}{4}(cp^{\uparrow F2}+cp^{\downarrow F2}+cp^{F2\uparrow}+cp^{F2\downarrow}) \\
& +\tfrac{1}{3}\tfrac{1}{2}(cp^{m_F0F2}+cp^{F2m_F0})))),
\end{aligned}
\tag{5.50}
$$

$$
\begin{aligned}
V_{\Psi-,\bullet\bullet|\circ}^{HV} = \ & (p_{\mathrm{I},D\pm}^{\sigma\pm,HV}\,(\tfrac{2}{3}\tfrac{1}{4}(acp^{\uparrow\uparrow}+acp^{\downarrow\downarrow}+acp^{\downarrow\uparrow}+acp^{\uparrow\downarrow}) \\
& +\tfrac{1}{3}\tfrac{1}{4}(acp^{m_F0\uparrow}+acp^{m_F0\downarrow}+acp^{\downarrow m_F0}+acp^{\uparrow m_F0})) \\
& +p_{\mathrm{II},D\pm}^{\sigma\pm,HV}\,(\tfrac{p_b}{p_{b+1/2}p_c}(\tfrac{2}{3}\tfrac{1}{4}(acp^{\uparrow F2}+acp^{\downarrow F2}+acp^{F2\uparrow}+acp^{F2\downarrow}) \\
& +\tfrac{1}{3}\tfrac{1}{2}(acp^{m_F0F2}+acp^{F2m_F0})) \\
& +\tfrac{p_c}{p_{b+1/2}p_c}(\tfrac{2}{3}\tfrac{1}{4}(acp^{\uparrow F2}+acp^{\downarrow F2}+acp^{F2\uparrow}+acp^{F2\downarrow}) \\
& +\tfrac{1}{3}\tfrac{1}{2}(acp^{m_F0F2}+acp^{F2m_F0})))) \\
& -(p_{\mathrm{I},D\pm}^{\sigma\pm,HV}\,(\tfrac{2}{3}\tfrac{1}{4}(cp^{\uparrow\uparrow}+cp^{\downarrow\downarrow}+cp^{\downarrow\uparrow}+cp^{\uparrow\downarrow}) \\
& +\tfrac{1}{3}\tfrac{1}{4}(cp^{m_F0\uparrow}+cp^{m_F0\downarrow}+cp^{\downarrow m_F0}+cp^{\uparrow m_F0})) \\
& +p_{\mathrm{II},D\pm}^{\sigma\pm,HV}\,(\tfrac{p_b}{p_{b+1/2}p_c}(\tfrac{2}{3}\tfrac{1}{4}(cp^{\uparrow F2}+cp^{\downarrow F2}+cp^{F2\uparrow}+cp^{F2\downarrow}) \\
& +\tfrac{1}{3}\tfrac{1}{2}(cp^{m_F0F2}+cp^{F2m_F0})) \\
& +\tfrac{p_c}{p_{b+1/2}p_c}(\tfrac{2}{3}\tfrac{1}{4}(cp^{\uparrow F2}+cp^{\downarrow F2}+cp^{F2\uparrow}+cp^{F2\downarrow}) \\
& +\tfrac{1}{3}\tfrac{1}{2}(cp^{m_F0F2}+cp^{F2m_F0})))),
\end{aligned}
\tag{5.51}
$$

$$
\begin{aligned}
V_{\Psi+,\bullet\bullet|\circ}^{PM} = \ & (p_{\mathrm{I},D\pm}^{\sigma\pm,HV}\,(\tfrac{2}{3}\tfrac{1}{4}(cp^{\uparrow\uparrow}+cp^{\downarrow\downarrow}+cp^{\downarrow\uparrow}+cp^{\uparrow\downarrow}) \\
& +\tfrac{1}{3}\tfrac{1}{4}(cp^{m_F0\uparrow}+cp^{m_F0\downarrow}+cp^{\downarrow m_F0}+cp^{\uparrow m_F0})) \\
& +p_{\mathrm{II},D\pm}^{\sigma\pm,HV}\,(\tfrac{p_b}{p_{b+1/2}p_c}(\tfrac{2}{3}\tfrac{1}{4}(cp^{\uparrow F2}+cp^{\downarrow F2}+cp^{F2\uparrow}+cp^{F2\downarrow}) \\
& +\tfrac{1}{3}\tfrac{1}{2}(cp^{m_F0F2}+cp^{F2m_F0})) \\
& +\tfrac{p_c}{p_{b+1/2}p_c}(\tfrac{2}{3}\tfrac{1}{4}(cp^{\uparrow F2}+cp^{\downarrow F2}+cp^{F2\uparrow}+cp^{F2\downarrow}) \\
& +\tfrac{1}{3}\tfrac{1}{2}(cp^{m_F0F2}+cp^{F2m_F0})))) \\
& -(p_{\mathrm{I},D\pm}^{\sigma\pm,HV}\,(\tfrac{2}{3}\tfrac{1}{4}(acp^{\uparrow\uparrow}+acp^{\downarrow\downarrow}+acp^{\downarrow\uparrow}+acp^{\uparrow\downarrow}) \\
& +\tfrac{1}{3}\tfrac{1}{4}(acp^{m_F0\uparrow}+acp^{m_F0\downarrow}+acp^{\downarrow m_F0}+acp^{\uparrow m_F0})) \\
& +p_{\mathrm{II},D\pm}^{\sigma\pm,HV}\,(\tfrac{p_b}{p_{b+1/2}p_c}(\tfrac{2}{3}\tfrac{1}{4}(acp^{\uparrow F2}+acp^{\downarrow F2}+acp^{F2\uparrow}+acp^{F2\downarrow}) \\
& +\tfrac{1}{3}\tfrac{1}{2}(acp^{m_F0F2}+acp^{F2m_F0})) \\
& +\tfrac{p_c}{p_{b+1/2}p_c}(\tfrac{2}{3}\tfrac{1}{4}(acp^{\uparrow F2}+acp^{\downarrow F2}+acp^{F2\uparrow}+acp^{F2\downarrow}) \\
& +\tfrac{1}{3}\tfrac{1}{2}(acp^{m_F0F2}+acp^{F2m_F0}))))
\end{aligned}
\tag{5.52}
$$

and

$$
\begin{aligned}
V^{PM}_{\Psi^-,\bullet\bullet|\circ} = \ & (p^{\sigma^{\pm,HV}}_{\mathrm{I},D\pm}(\tfrac{2}{3}\tfrac{1}{4}(acp^{\uparrow\uparrow}+acp^{\downarrow\downarrow}+acp^{\downarrow\uparrow}+acp^{\uparrow\downarrow}) \\
& +\tfrac{1}{3}\tfrac{1}{4}(acp^{m_F 0\uparrow}+acp^{m_F 0\downarrow}+acp^{\downarrow m_F 0}+acp^{\uparrow m_F 0})) \\
& +p^{\sigma^{\pm,HV}}_{\mathrm{II},D\pm}(\tfrac{p_b}{p_{b+1/2}p_c}(\tfrac{2}{3}\tfrac{1}{4}(acp^{\uparrow F2}+acp^{\downarrow F2}+acp^{F2\uparrow}+acp^{F2\downarrow}) \\
& +\tfrac{1}{3}\tfrac{1}{2}(acp^{m_F 0F2}+acp^{F2m_F 0})) \\
& +\tfrac{p_c}{p_{b+1/2}p_c}(\tfrac{2}{3}\tfrac{1}{4}(acp^{\uparrow F2}+acp^{\downarrow F2}+acp^{F2\uparrow}+acp^{F2\downarrow}) \\
& +\tfrac{1}{3}\tfrac{1}{2}(acp^{m_F 0F2}+acp^{F2m_F 0})))) \\
& -(p^{\sigma^{\pm,HV}}_{\mathrm{I},D\pm}(\tfrac{2}{3}\tfrac{1}{4}(cp^{\uparrow\uparrow}+cp^{\downarrow\downarrow}+cp^{\downarrow\uparrow}+cp^{\uparrow\downarrow}) \\
& +\tfrac{1}{3}\tfrac{1}{4}(cp^{m_F 0\uparrow}+cp^{m_F 0\downarrow}+cp^{\downarrow m_F 0}+cp^{\uparrow m_F 0})) \\
& +p^{\sigma^{\pm,HV}}_{\mathrm{II},D\pm}(\tfrac{p_b}{p_{b+1/2}p_c}(\tfrac{2}{3}\tfrac{1}{4}(cp^{\uparrow F2}+cp^{\downarrow F2}+cp^{F2\uparrow}+cp^{F2\downarrow}) \\
& +\tfrac{1}{3}\tfrac{1}{2}(cp^{m_F 0F2}+cp^{F2m_F 0})) \\
& +\tfrac{p_c}{p_{b+1/2}p_c}(\tfrac{2}{3}\tfrac{1}{4}(cp^{\uparrow F2}+cp^{\downarrow F2}+cp^{F2\uparrow}+cp^{F2\downarrow}) \\
& +\tfrac{1}{3}\tfrac{1}{2}(cp^{m_F 0F2}+cp^{F2m_F 0})))).
\end{aligned}
\tag{5.53}
$$

5. Events represented by the probability $\overline{P}^{D\pm,HV}_{\bullet\circ|\bullet}$ have the following visibilities:

$$
\begin{aligned}
V^{HV}_{\Psi^+,\bullet\circ|\bullet} = \ & (p_{\mathrm{I},\bullet\circ|\bullet}(\tfrac{2}{3}\tfrac{1}{4}(acp^{\uparrow\uparrow}+acp^{\downarrow\downarrow}+acp^{\downarrow\uparrow}+acp^{\uparrow\downarrow}) \\
& +\tfrac{1}{3}\tfrac{1}{4}(acp^{m_F 0\uparrow}+acp^{m_F 0\downarrow}+acp^{\downarrow m_F 0}+acp^{\uparrow m_F 0})) \\
& +p_{\mathrm{II},\bullet\circ|\bullet}(\tfrac{5}{12}\tfrac{1}{4}(acp^{\uparrow\uparrow}+acp^{\downarrow\downarrow}+acp^{\downarrow\uparrow}+acp^{\uparrow\downarrow}) \\
& +\tfrac{5}{12}\tfrac{1}{4}(acp^{m_F 0\uparrow}+acp^{m_F 0\downarrow}+acp^{\downarrow m_F 0}+acp^{\uparrow m_F 0}) \\
& +\tfrac{2}{12}\tfrac{1}{4}(acp^{\uparrow F2}+acp^{\downarrow F2}+acp^{F2\uparrow}+acp^{F2\downarrow}))) \\
& -(p_{\mathrm{I},\bullet\circ|\bullet}(\tfrac{2}{3}\tfrac{1}{4}(cp^{\uparrow\uparrow}+cp^{\downarrow\downarrow}+cp^{\downarrow\uparrow}+cp^{\uparrow\downarrow}) \\
& +\tfrac{1}{3}\tfrac{1}{4}(cp^{m_F 0\uparrow}+cp^{m_F 0\downarrow}+cp^{\downarrow m_F 0}+cp^{\uparrow m_F 0})) \\
& +p_{\mathrm{II},\bullet\circ|\bullet}(\tfrac{5}{12}\tfrac{1}{4}(cp^{\uparrow\uparrow}+cp^{\downarrow\downarrow}+cp^{\downarrow\uparrow}+cp^{\uparrow\downarrow}) \\
& +\tfrac{5}{12}\tfrac{1}{4}(cp^{m_F 0\uparrow}+cp^{m_F 0\downarrow}+cp^{\downarrow m_F 0}+cp^{\uparrow m_F 0}) \\
& +\tfrac{2}{12}\tfrac{1}{4}(cp^{\uparrow F2}+cp^{\downarrow F2}+cp^{F2\uparrow}+cp^{F2\downarrow}))),
\end{aligned}
\tag{5.54}
$$

$$
\begin{aligned}
V^{HV}_{\Psi^-,\bullet\circ|\bullet} = \ & (p_{\mathrm{I},\bullet\circ|\bullet}(\tfrac{2}{3}\tfrac{1}{4}(acp^{\uparrow\uparrow}+acp^{\downarrow\downarrow}+acp^{\downarrow\uparrow}+acp^{\uparrow\downarrow}) \\
& +\tfrac{1}{3}\tfrac{1}{4}(acp^{m_F 0\uparrow}+acp^{m_F 0\downarrow}+acp^{\downarrow m_F 0}+acp^{\uparrow m_F 0})) \\
& +p_{\mathrm{II},\bullet\circ|\bullet}(\tfrac{5}{12}\tfrac{1}{4}(acp^{\uparrow\uparrow}+acp^{\downarrow\downarrow}+acp^{\downarrow\uparrow}+acp^{\uparrow\downarrow}) \\
& +\tfrac{5}{12}\tfrac{1}{4}(acp^{m_F 0\uparrow}+acp^{m_F 0\downarrow}+acp^{\downarrow m_F 0}+acp^{\uparrow m_F 0}) \\
& +\tfrac{2}{12}\tfrac{1}{4}(acp^{\uparrow F2}+acp^{\downarrow F2}+acp^{F2\uparrow}+acp^{F2\downarrow}))) \\
& -(p_{\mathrm{I},\bullet\circ|\bullet}(\tfrac{2}{3}\tfrac{1}{4}(cp^{\uparrow\uparrow}+cp^{\downarrow\downarrow}+cp^{\downarrow\uparrow}+cp^{\uparrow\downarrow}) \\
& +\tfrac{1}{3}\tfrac{1}{4}(cp^{m_F 0\uparrow}+cp^{m_F 0\downarrow}+cp^{\downarrow m_F 0}+cp^{\uparrow m_F 0})) \\
& +p_{\mathrm{II},\bullet\circ|\bullet}(\tfrac{5}{12}\tfrac{1}{4}(cp^{\uparrow\uparrow}+cp^{\downarrow\downarrow}+cp^{\downarrow\uparrow}+cp^{\uparrow\downarrow}) \\
& +\tfrac{5}{12}\tfrac{1}{4}(cp^{m_F 0\uparrow}+cp^{m_F 0\downarrow}+cp^{\downarrow m_F 0}+cp^{\uparrow m_F 0}) \\
& +\tfrac{2}{12}\tfrac{1}{4}(cp^{\uparrow F2}+cp^{\downarrow F2}+cp^{F2\uparrow}+cp^{F2\downarrow}))),
\end{aligned}
\tag{5.55}
$$

$$
\begin{aligned}
V^{PM}_{\Psi+,\bullet\circ|\bullet} =\ & (p_{\mathrm{I},\bullet\circ|\bullet}(\tfrac{2}{3}\tfrac{1}{4}(cp^{\uparrow\uparrow} + cp^{\downarrow\downarrow} + cp^{\downarrow\uparrow} + cp^{\uparrow\downarrow}) \\
& + \tfrac{1}{3}\tfrac{1}{4}(cp^{m_F0\uparrow} + cp^{m_F0\downarrow} + cp^{\downarrow m_F0} + cp^{\uparrow m_F0})) \\
& + p_{\mathrm{II},\bullet\circ|\bullet}(\tfrac{5}{12}\tfrac{1}{4}(cp^{\uparrow\uparrow} + cp^{\downarrow\downarrow} + cp^{\downarrow\uparrow} + cp^{\uparrow\downarrow}) \\
& + \tfrac{5}{12}\tfrac{1}{4}(cp^{m_F0\uparrow} + cp^{m_F0\downarrow} + cp^{\downarrow m_F0} + cp^{\uparrow m_F0}) \\
& + \tfrac{2}{12}\tfrac{1}{4}(cp^{\uparrow F2} + cp^{\downarrow F2} + cp^{F2\uparrow} + cp^{F2\downarrow}))) \\
& - (p_{\mathrm{I},\bullet\circ|\bullet}(\tfrac{2}{3}\tfrac{1}{4}(acp^{\uparrow\uparrow} + acp^{\downarrow\downarrow} + acp^{\downarrow\uparrow} + acp^{\uparrow\downarrow}) \\
& + \tfrac{1}{3}\tfrac{1}{4}(acp^{m_F0\uparrow} + acp^{m_F0\downarrow} + acp^{\downarrow m_F0} + acp^{\uparrow m_F0})) \\
& + p_{\mathrm{II},\bullet\circ|\bullet}(\tfrac{5}{12}\tfrac{1}{4}(acp^{\uparrow\uparrow} + acp^{\downarrow\downarrow} + acp^{\downarrow\uparrow} + acp^{\uparrow\downarrow}) \\
& + \tfrac{5}{12}\tfrac{1}{4}(acp^{m_F0\uparrow} + acp^{m_F0\downarrow} + acp^{\downarrow m_F0} + acp^{\uparrow m_F0}) \\
& + \tfrac{2}{12}\tfrac{1}{4}(acp^{\uparrow F2} + acp^{\downarrow F2} + acp^{F2\uparrow} + acp^{F2\downarrow})))
\end{aligned} \tag{5.56}
$$

and

$$
\begin{aligned}
V^{PM}_{\Psi-,\bullet\circ|\bullet} =\ & (p_{\mathrm{I},\bullet\circ|\bullet}(\tfrac{2}{3}\tfrac{1}{4}(acp^{\uparrow\uparrow} + acp^{\downarrow\downarrow} + acp^{\downarrow\uparrow} + acp^{\uparrow\downarrow}) \\
& + \tfrac{1}{3}\tfrac{1}{4}(acp^{m_F0\uparrow} + acp^{m_F0\downarrow} + acp^{\downarrow m_F0} + acp^{\uparrow m_F0})) \\
& + p_{\mathrm{II},\bullet\circ|\bullet}(\tfrac{5}{12}\tfrac{1}{4}(acp^{\uparrow\uparrow} + acp^{\downarrow\downarrow} + acp^{\downarrow\uparrow} + acp^{\uparrow\downarrow}) \\
& + \tfrac{5}{12}\tfrac{1}{4}(acp^{m_F0\uparrow} + acp^{m_F0\downarrow} + acp^{\downarrow m_F0} + acp^{\uparrow m_F0}) \\
& + \tfrac{2}{12}\tfrac{1}{4}(acp^{\uparrow F2} + acp^{\downarrow F2} + acp^{F2\uparrow} + acp^{F2\downarrow}))) \\
& - (p_{\mathrm{I},\bullet\circ|\bullet}(\tfrac{2}{3}\tfrac{1}{4}(cp^{\uparrow\uparrow} + cp^{\downarrow\downarrow} + cp^{\downarrow\uparrow} + cp^{\uparrow\downarrow}) \\
& + \tfrac{1}{3}\tfrac{1}{4}(cp^{m_F0\uparrow} + cp^{m_F0\downarrow} + cp^{\downarrow m_F0} + cp^{\uparrow m_F0})) \\
& + p_{\mathrm{II},\bullet\circ|\bullet}(\tfrac{5}{12}\tfrac{1}{4}(cp^{\uparrow\uparrow} + cp^{\downarrow\downarrow} + cp^{\downarrow\uparrow} + cp^{\uparrow\downarrow}) \\
& + \tfrac{5}{12}\tfrac{1}{4}(cp^{m_F0\uparrow} + cp^{m_F0\downarrow} + cp^{\downarrow m_F0} + cp^{\uparrow m_F0}) \\
& + \tfrac{2}{12}\tfrac{1}{4}(cp^{\uparrow F2} + cp^{\downarrow F2} + cp^{F2\uparrow} + cp^{F2\downarrow}))).
\end{aligned} \tag{5.57}
$$

Events represented by the probability $\overline{P}^{D\pm,HV}_{\circ\bullet|\bullet}$ have the following visibilities:

$$
\begin{aligned}
V^{HV}_{\Psi+,\circ\bullet|\bullet} =\ & (p_{\mathrm{I},\circ\bullet|\bullet}(O^2_{\circ\bullet\mathrm{I}|\bullet}\tfrac{1}{2}(acp^{\downarrow\uparrow} + acp^{\uparrow\downarrow}) + (1 - O^2_{\circ\bullet\mathrm{I}|\bullet})\tfrac{1}{2}(acp^{\downarrow\uparrow} + acp^{\uparrow\downarrow})) \\
& + p_{\mathrm{II},\circ\bullet|\bullet}(p_a\tfrac{1}{4}(acp^{m_F0\uparrow} + acp^{m_F0\downarrow} + acp^{\downarrow m_F0} + acp^{\uparrow m_F0}) \\
& + p_b\tfrac{1}{4}(acp^{\uparrow F2} + acp^{\downarrow F2} + acp^{F2\uparrow} + acp^{F2\downarrow}) \\
& + p_c\tfrac{1}{4}(acp^{\uparrow F2} + acp^{\downarrow F2} + acp^{F2\uparrow} + acp^{F2\downarrow})) \\
& + p_{\mathrm{III},\circ\bullet|\bullet}(O^2_{\circ\bullet\mathrm{III}|\bullet}\tfrac{1}{2}(acp^{\downarrow\uparrow} + acp^{\uparrow\downarrow}) + (1 - O^2_{\circ\bullet\mathrm{III}|\bullet})\tfrac{1}{2}(acp^{\downarrow\uparrow} + acp^{\uparrow\downarrow}))) \\
& - (p_{\mathrm{I},\circ\bullet|\bullet}(O^2_{\circ\bullet\mathrm{I}|\bullet}\tfrac{1}{2}(cp^{\downarrow\uparrow} + cp^{\uparrow\downarrow}) + (1 - O^2_{\circ\bullet\mathrm{I}|\bullet})\tfrac{1}{2}(cp^{\downarrow\uparrow} + cp^{\uparrow\downarrow})) \\
& + p_{\mathrm{II},\circ\bullet|\bullet}(p_a\tfrac{1}{4}(cp^{m_F0\uparrow} + cp^{m_F0\downarrow} + acp^{\downarrow m_F0} + acp^{\uparrow m_F0}) \\
& + p_b\tfrac{1}{4}(cp^{\uparrow F2} + acp^{\downarrow F2} + cp^{F2\uparrow} + cp^{F2\downarrow}) \\
& + p_c\tfrac{1}{4}(cp^{\uparrow F2} + cp^{\downarrow F2} + cp^{F2\uparrow} + cp^{F2\downarrow})) \\
& + p_{\mathrm{III},\circ\bullet|\bullet}(O^2_{\circ\bullet\mathrm{III}|\bullet}\tfrac{1}{2}(cp^{\downarrow\uparrow} + cp^{\uparrow\downarrow}) + (1 - O^2_{\circ\bullet\mathrm{III}|\bullet})\tfrac{1}{2}(cp^{\downarrow\uparrow} + cp^{\uparrow\downarrow}))),
\end{aligned} \tag{5.58}
$$

$$
\begin{aligned}
V^{HV}_{\Psi-,\circ\bullet|\bullet} =\ & (p_{\mathrm{I},\circ\bullet|\bullet}(O^2_{\circ\bullet\mathrm{I}|\bullet}\tfrac{1}{2}(acp^{\downarrow\uparrow} + acp^{\uparrow\downarrow}) + (1 - O^2_{\circ\bullet\mathrm{I}|\bullet})\tfrac{1}{2}(acp^{\downarrow\uparrow} + acp^{\uparrow\downarrow})) \\
& + p_{\mathrm{II},\circ\bullet|\bullet}(p_a\tfrac{1}{4}(acp^{m_F0\uparrow} + acp^{m_F0\downarrow} + acp^{\downarrow m_F0} + acp^{\uparrow m_F0}) \\
& + p_b\tfrac{1}{4}(acp^{\uparrow F2} + acp^{\downarrow F2} + acp^{F2\uparrow} + acp^{F2\downarrow}) \\
& + p_c\tfrac{1}{4}(acp^{\uparrow F2} + acp^{\downarrow F2} + acp^{F2\uparrow} + acp^{F2\downarrow})) \\
& + p_{\mathrm{III},\circ\bullet|\bullet}(O^2_{\circ\bullet\mathrm{III}|\bullet}\tfrac{1}{2}(acp^{\downarrow\uparrow} + acp^{\uparrow\downarrow}) + (1 - O^2_{\circ\bullet\mathrm{III}|\bullet})\tfrac{1}{2}(acp^{\downarrow\uparrow} + acp^{\uparrow\downarrow}))) \\
& - (p_{\mathrm{I},\circ\bullet|\bullet}(O^2_{\circ\bullet\mathrm{I}|\bullet}\tfrac{1}{2}(cp^{\downarrow\uparrow} + cp^{\uparrow\downarrow}) + (1 - O^2_{\circ\bullet\mathrm{I}|\bullet})\tfrac{1}{2}(cp^{\downarrow\uparrow} + cp^{\uparrow\downarrow})) \\
& + p_{\mathrm{II},\circ\bullet|\bullet}(p_a\tfrac{1}{4}(cp^{m_F0\uparrow} + cp^{m_F0\downarrow} + acp^{\downarrow m_F0} + acp^{\uparrow m_F0}) \\
& + p_b\tfrac{1}{4}(cp^{\uparrow F2} + acp^{\downarrow F2} + cp^{F2\uparrow} + cp^{F2\downarrow}) \\
& + p_c\tfrac{1}{4}(cp^{\uparrow F2} + cp^{\downarrow F2} + cp^{F2\uparrow} + cp^{F2\downarrow})) \\
& + p_{\mathrm{III},\circ\bullet|\bullet}(O^2_{\circ\bullet\mathrm{III}|\bullet}\tfrac{1}{2}(cp^{\downarrow\uparrow} + cp^{\uparrow\downarrow}) + (1 - O^2_{\circ\bullet\mathrm{III}|\bullet})\tfrac{1}{2}(cp^{\downarrow\uparrow} + cp^{\uparrow\downarrow}))),
\end{aligned} \tag{5.59}
$$

$$
\begin{aligned}
V_{\Psi^+,\circ\bullet|\bullet}^{PM} = \ & (p_{\mathrm{I},\circ\bullet|\bullet}(O_{\circ\bullet_{\mathrm{I}}|\bullet}^2 \tfrac{1}{2}(acp^{\downarrow\uparrow} + acp^{\uparrow\downarrow}) \\
& + (1 - O_{\circ\bullet_{\mathrm{I}}|\bullet}^2)\tfrac{1}{4}(acp^{\downarrow\uparrow} + acp^{\uparrow\downarrow} + acp^{\uparrow\uparrow} + acp^{\downarrow\downarrow})) \\
& + p_{\mathrm{II},\circ\bullet|\bullet}(p_a \tfrac{1}{4}(acp^{m_F 0\uparrow} + acp^{m_F 0\downarrow} + acp^{\downarrow m_F 0} + acp^{\uparrow m_F 0}) \\
& + p_b \tfrac{1}{4}(acp^{\uparrow F2} + acp^{\downarrow F2} + acp^{F2\uparrow} + acp^{F2\downarrow}) \\
& + p_c \tfrac{1}{4}(acp^{\uparrow F2} + acp^{\downarrow F2} + acp^{F2\uparrow} + acp^{F2\downarrow})) \\
& + p_{\mathrm{III},\circ\bullet|\bullet}(O_{\circ\bullet_{\mathrm{III}}|\bullet}^2 \tfrac{1}{2}(acp^{\downarrow\uparrow} + acp^{\uparrow\downarrow})) \\
& + (1 - O_{\circ\bullet_{\mathrm{III}}|\bullet}^2)\tfrac{1}{4}(acp^{\downarrow\uparrow} + acp^{\uparrow\downarrow} + acp^{\uparrow\uparrow} + acp^{\downarrow\downarrow})) \\
& - (p_{\mathrm{I},\circ\bullet|\bullet}(O_{\circ\bullet_{\mathrm{I}}|\bullet}^2 \tfrac{1}{2}(cp^{\downarrow\uparrow} + cp^{\uparrow\downarrow}) \\
& + (1 - O_{\circ\bullet_{\mathrm{I}}|\bullet}^2)\tfrac{1}{4}(cp^{\downarrow\uparrow} + cp^{\uparrow\downarrow} + cp^{\uparrow\uparrow} + cp^{\downarrow\downarrow})) \\
& + p_{\mathrm{II},\circ\bullet|\bullet}(p_a \tfrac{1}{4}(cp^{m_F 0\uparrow} + cp^{m_F 0\downarrow} + acp^{\downarrow m_F 0} + acp^{\uparrow m_F 0}) \\
& + p_b \tfrac{1}{4}(cp^{\uparrow F2} + acp^{\downarrow F2} + cp^{F2\uparrow} + cp^{F2\downarrow}) \\
& + p_c \tfrac{1}{4}(cp^{\uparrow F2} + cp^{\downarrow F2} + cp^{F2\uparrow} + cp^{F2\downarrow})) \\
& + p_{\mathrm{III},\circ\bullet|\bullet}(O_{\circ\bullet_{\mathrm{III}}|\bullet}^2 \tfrac{1}{2}(cp^{\downarrow\uparrow} + cp^{\uparrow\downarrow}) \\
& + (1 - O_{\circ\bullet_{\mathrm{III}}|\bullet}^2)\tfrac{1}{4}(cp^{\downarrow\uparrow} + cp^{\uparrow\downarrow} + cp^{\uparrow\uparrow} + cp^{\downarrow\downarrow})))
\end{aligned}
\tag{5.60}
$$

and

$$
\begin{aligned}
V_{\Psi^-,\circ\bullet|\bullet}^{PM} = \ & (p_{\mathrm{I},\circ\bullet|\bullet}(O_{\circ\bullet_{\mathrm{I}}|\bullet}^2 \tfrac{1}{2}(acp^{\downarrow\uparrow} + acp^{\uparrow\downarrow}) \\
& + (1 - O_{\circ\bullet_{\mathrm{I}}|\bullet}^2)\tfrac{1}{4}(acp^{\downarrow\uparrow} + acp^{\uparrow\downarrow} + acp^{\uparrow\uparrow} + acp^{\downarrow\downarrow})) \\
& + p_{\mathrm{II},\circ\bullet|\bullet}(p_a \tfrac{1}{4}(acp^{m_F 0\uparrow} + acp^{m_F 0\downarrow} + acp^{\downarrow m_F 0} + acp^{\uparrow m_F 0}) \\
& + p_b \tfrac{1}{4}(acp^{\uparrow F2} + acp^{\downarrow F2} + acp^{F2\uparrow} + acp^{F2\downarrow}) \\
& + p_c \tfrac{1}{4}(acp^{\uparrow F2} + acp^{\downarrow F2} + acp^{F2\uparrow} + acp^{F2\downarrow})) \\
& + p_{\mathrm{III},\circ\bullet|\bullet}(O_{\circ\bullet_{\mathrm{III}}|\bullet}^2 \tfrac{1}{2}(acp^{\downarrow\uparrow} + acp^{\uparrow\downarrow})) \\
& + (1 - O_{\circ\bullet_{\mathrm{III}}|\bullet}^2)\tfrac{1}{4}(acp^{\downarrow\uparrow} + acp^{\uparrow\downarrow} + acp^{\uparrow\uparrow} + acp^{\downarrow\downarrow})) \\
& - (p_{\mathrm{I},\circ\bullet|\bullet}(O_{\circ\bullet_{\mathrm{I}}|\bullet}^2 \tfrac{1}{2}(cp^{\downarrow\uparrow} + cp^{\uparrow\downarrow}) \\
& + (1 - O_{\circ\bullet_{\mathrm{I}}|\bullet}^2)\tfrac{1}{4}(cp^{\downarrow\uparrow} + cp^{\uparrow\downarrow} + cp^{\uparrow\uparrow} + cp^{\downarrow\downarrow})) \\
& + p_{\mathrm{II},\circ\bullet|\bullet}(p_a \tfrac{1}{4}(cp^{m_F 0\uparrow} + cp^{m_F 0\downarrow} + acp^{\downarrow m_F 0} + acp^{\uparrow m_F 0}) \\
& + p_b \tfrac{1}{4}(cp^{\uparrow F2} + acp^{\downarrow F2} + cp^{F2\uparrow} + cp^{F2\downarrow}) \\
& + p_c \tfrac{1}{4}(cp^{\uparrow F2} + cp^{\downarrow F2} + cp^{F2\uparrow} + cp^{F2\downarrow})) \\
& + p_{\mathrm{III},\circ\bullet|\bullet}(O_{\circ\bullet_{\mathrm{III}}|\bullet}^2 \tfrac{1}{2}(cp^{\downarrow\uparrow} + cp^{\uparrow\downarrow}) \\
& + (1 - O_{\circ\bullet_{\mathrm{III}}|\bullet}^2)\tfrac{1}{4}(cp^{\downarrow\uparrow} + cp^{\uparrow\downarrow} + cp^{\uparrow\uparrow} + cp^{\downarrow\downarrow}))).
\end{aligned}
\tag{5.61}
$$

The values for these visibilities are given in table 5.3.

The visibility of an atom-atom entanglement experiment can be calculated by weighting the visibilities, shown in table 5.3, with the relative probability that the respective photon pairs cause a heralding coincidence. These probabilities are given by $\overline{P}_{\bullet\bullet|\circ}^{D\pm,HV}$, $\overline{P}_{\bullet\circ|\bullet}^{D\pm,HV}$, $\overline{P}_{\circ\bullet|\bullet}^{D\pm,HV}$, $\overline{P}_{\bullet|\bullet}^{D\pm,HV}$, $\overline{P}_{error}^{D\pm,HV}$ and $\overline{P}_{dc}^{D\pm,HV}$ (see subsection 5.2.2), yielding the following equation:

$$
V_{bs}^b = \sum_c \overline{P}_c^{D\pm,HV} \cdot V_{bs,c}^b,
\tag{5.62}
$$

where $c \in \{\bullet|\bullet, error, dc, \bullet\bullet|\circ, \bullet\circ|\bullet, \circ\bullet|\bullet\}$, $b \in \{HV, RL\}$ and $bs \in \{\Psi^+, \Psi^-\}$. The results are:

$$
V_{\Psi^+}^{HV} = 0.750 \pm 0.015,
$$

$$
V_{\Psi^-}^{HV} = 0.750 \pm 0.015,
$$

$$
V_{\Psi^+}^{PM} = 0.712 \pm 0.006
$$

photon pair category	$V_{\Psi^+,c}^{HV}$	$V_{\Psi^-,c}^{HV}$	$V_{\Psi^+,c}^{PM}$	$V_{\Psi^-,c}^{PM}$
$\bullet\|\bullet$	0.779	0.779	0.780	0.779
$error$	0.779	0.779	0.001	0.001
dc	0.010	0.010	-0.010	0.010
$\bullet\bullet\|\circ$	-0.124	-0.124	0.124	-0.124
$\bullet\circ\|\bullet$	0.017	0.017	-0.017	0.017
$\circ\bullet\|\bullet$	0.706	0.706	0.553	0.553

Table 5.3.: Expected atom-atom entanglement visibilities after a heralding signal caused by one of the six categories of photon pairs (with $c \in \{\bullet|\bullet, error, dc, \bullet\bullet\,|\circ, \bullet\circ\,|\bullet, \circ\bullet\,|\bullet\}$). The visibilities are given for atom analysis in the H/V- ($\hat{\sigma}^x$) and P/M- ($\hat{\sigma}^y$) basis, respectively, and for both Bell-states which are detectable by the setup. The values are calculated with respect to equations 5.38-5.61 and the values given in table 5.2. A minus sign in front of the value for the visibility shows that a measurement would show correlations although anti-correlations are expected and vise versa.

and

$$V_{\Psi^-}^{PM} = 0.711 \pm 0.005.$$

The indicated errors respect only the statistical errors of the atom-photon entanglement and the two-photon interference measurements. They do not respect any systematic errors. There are two main sources for errors which are not considered in these calculations as their exact influence can not be estimated.

The first error is caused by the birefringence of the glass cells, in which the atoms are captured. The birefringence hardly influences H or V polarized light but strongly influences P or M polarized light. As the birefringence of each window of the glass cells can not be compensated individually, the STIRAP laser system and the detection setup are compensated in a way that the phase shift in an atom-photon entanglement measurement is minimized (see subsection 2.3.7). In an atom-atom entanglement experiment the photon is always analyzed in the H/V-basis and only the atom might be analyzed in the P/M-basis. In this case, only the birefringence of one window disturbs the experiment - a situation which does not correspond to the situation the setup is compensated for. Therefore, the visibilities for measurement in the P/M-basis should be lower than the ones given by these calculation.

The second error influences both measurement bases. The probability for erasing the atom from the trap and the survival of the atom in the trap are given be atom-photon entanglement measurements. But the measured probabilities do not only depend on these probabilities but also on the quality of the detection setup, the compensation of it and all other errors reducing the entanglement visibilities. These other errors also reduce the two-photon interference probability, and therefore are already taken into account by the results of the two-photon measurements. The bottom line is that these errors are taken into account twice. Thus, the calculated visibilities are only a lower bound. The actual atom-atom entanglement visibilities should be higher.

In summary the visibilities in the actual experiment should be higher than the calculated ones for analysis in the H/V-basis. For analysis in the P/M basis no final statement can be made as one error reduces the visibilities and the other increases it. The relative influence of both errors can not be estimated beforehand.

5.3. Experimental Results

Here, the experimental realization of an AAE experiment is presented and the experimental data are analyzed in order to verify AAE and a violation of the CHSH-inequality while closing the detection loophole.

5.3.1. Experimental Realization

The experimental realization of an AAE experiment combines a two-photon quantum interference experiment with a subsequent analysis of the atomic spin states. Analogously to the description in section 4.5, a single atom is loaded in each trap before the main experiments starts. Thereafter, the single atoms in both traps are excited synchronously (see figure 2.9), until a two-photon coincidence detection in a $D+$ or $D-$ detector combination heralds a BSP (the photons are analyzed in the H/V-basis). This instantly triggers the analysis of the atomic spin states (see section 2.4.2). The fluorescence detection at the end of the spin state analysis is performed alternately for both atoms. First, the single photon detectors analyze light of trap2 for $30\,\mathrm{ms}$ before light of trap1 is detected for the same amount of time.

5.3.2. Verification of Atom-Atom Entanglement

The correlations between both atomic spins were observed by keeping the measurement basis of trap1 fixed to $\alpha = 90°$ (for analysis in the σ^x-basis) or to $\alpha = 135°$ (for analysis in the σ^y-basis), respectively, while rotating the measurement basis of trap2 from $\beta = 90°$ to $\beta = 180°$ (when analyzing in the σ^x-basis) or from $\beta = 45°$ to $\beta = 135°$ (for measurements in the σ^y-basis), respectively in steps of $22.5°$. This measurements were performed for both Bell-state projection results. The correlation- and anti-correlation probabilities (cp and acp) are calculated for each setting.

The results are shown for projection onto the photonic $|\Psi^-\rangle_{ph}$-state in figure 5.2 a) and b), and onto the $|\Psi^+\rangle_{ph}$-state in figure 5.2 c) and d), respectively. The AAE visibilities $V_s^{(\alpha)}$ (with $s \in \{\Psi^-, \Psi^+\}$) are obtained by fitting a sinusoidal function to each set of data points:

$$
\begin{aligned}
V_{\Psi^-}^{(90°)} &= 0.788 \pm 0.031 \\
V_{\Psi^-}^{(135°)} &= 0.728 \pm 0.032 \\
V_{\Psi^+}^{(90°)} &= 0.813 \pm 0.030 \\
V_{\Psi^+}^{(135°)} &= 0.723 \pm 0.034
\end{aligned}
$$

The visibilities for the σ^x-basis are considerably higher as the ones for the σ^y-basis as mentioned before (see subsections 5.2.3 and 5.2.4). Here, atoms in a $|\Psi^-\rangle_{aa}$ state and a $|\Psi^+\rangle_{aa}$ state have the same correlations. Therefore, a false projection onto the wrong Bell-sate doesn't reduce the visibility.

The measured visibilities are higher than predicted in subsection 5.2.4 as expected because of the systematic errors in the visibility calculations. The visibilities analyzed in the σ^x-basis are considerably higher than predicted because the calculations are only perturbed by one of the errors. The visibilities for analysis in the σ^y-basis are hardly higher than predicted. It shows that the two systematic errors described in subsection 5.2.4, which perturb the calculations for the σ^y-basis, compensate each other almost exactly.

In order to calculate the AAE fidelity, measurements in all three bases ($\hat\sigma^x$, $\hat\sigma^y$ and $\hat\sigma^z$) are required, but only measurements in both linear bases were executed. Therefore, the unmeasured third basis ($\hat\sigma^z$) is estimated to have a visibility equal the lower visibility measured in the $\hat\sigma^y$-basis. This yields a total fidelity of $F_{\Psi^-} = 0.811 \pm 0.028$ and $F_{\Psi^+} = 0.815 \pm 0.028$, respectively.
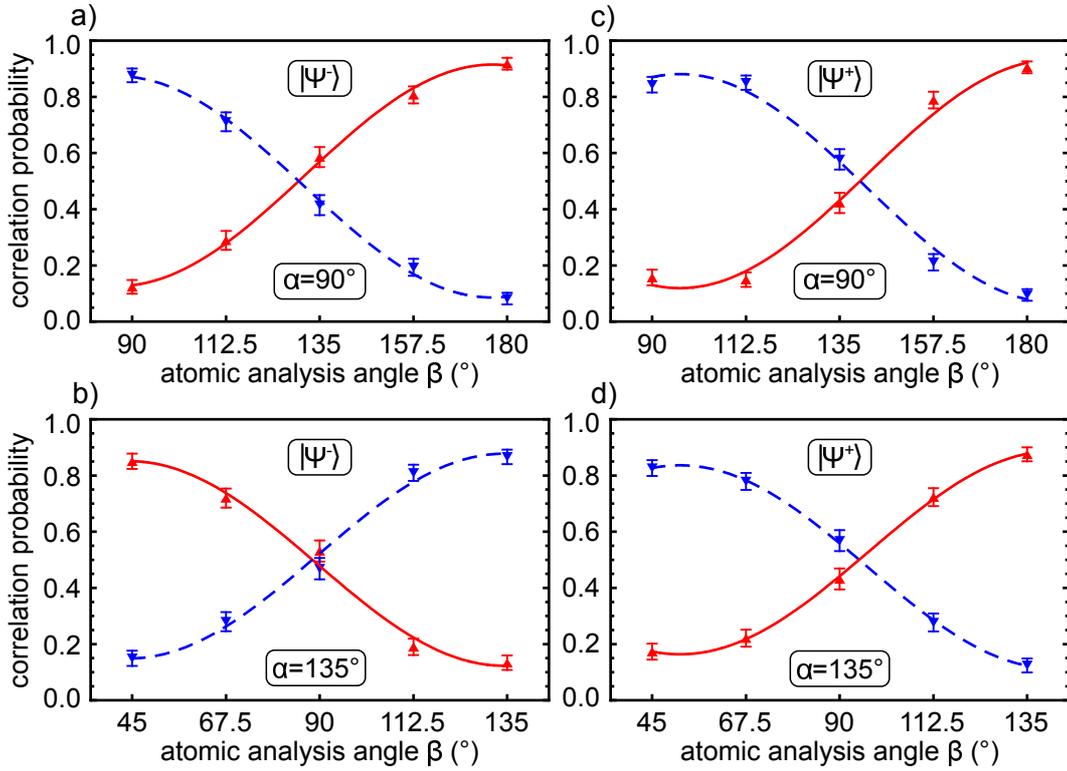
Figure 5.2.: Atom-atom correlations: a) and b) show correlations in the two linear measurement bases after projection of the photons onto the $|\Psi^-\rangle_{ph}$ state and c) and d) show the correlations in the same measurement bases after after projection of the photons onto the $|\Psi^+\rangle_{ph}$ state. cp is plotted as red, solid line and acp is plotted as blue, dashed line in all four graphics [97].

These results clearly prove that heralded entanglement between the two atoms has been generated.

5.3.3. A Test of Bell's Inequality

The data presented in figure 5.2 can also be used for a test of Bell's inequality. The expectation values $\langle \sigma^\alpha, \sigma^\beta \rangle = \frac{1}{N}(N_{\uparrow\uparrow}^{(\alpha,\beta)} + N_{\downarrow\downarrow}^{(\alpha,\beta)} - N_{\uparrow\downarrow}^{(\alpha,\beta)} - N_{\downarrow\uparrow}^{(\alpha,\beta)})$ are calculated, and the parameter S is evaluated (see equation 5.1). In order to violate the inequality, the following four settings are chosen:

$$\begin{aligned} \alpha &= 135°, & \beta &= 67.5° \\ \alpha &= 135°, & \beta' &= 112.5° \\ \alpha' &= 90°, & \beta' &= 112.5° \\ \alpha' &= 90°, & \beta'' &= 157.5° \end{aligned}$$

The last setting $\beta'' = 157.5°$ replaces the standard Bell stetting of $\beta = 67.5°$ which has not been measured for the corresponding angle of $\alpha' = 90°$. The expectation values of these settings have the same value but a different algebraic sign ($\langle \sigma^{90°}, \sigma^{67.5°} \rangle = -\langle \sigma^{90°}, \sigma^{157.5°} \rangle$). Thus, the inequality has to be adapted to:

$$S' := \left| \langle \sigma^{135°}, \sigma^{67.5°} \rangle - \langle \sigma^{135°}, \sigma^{112.5°} \rangle \right| + \left| -\langle \sigma^{90°}, \sigma^{157.5°} \rangle + \langle \sigma^{90°}, \sigma^{112.5°} \rangle \right| \leq 2. \qquad (5.63)$$

The experimental data yield a value of $S' = 2.19 \pm 0.09$, thereby clearly violating the classical limit of 2. It is the first violation of a Bell inequality without relying on the fair sampling assumption for particles at macroscopic distances. Furthermore, it is another strong proof for AAE generation.

5.4. Summary

In this chapter entanglement swapping was applied to observe entanglement between atoms separated by $20\,\text{m}$. It was pointed out that the installed setup takes advantage from both the possibility to distribute entanglement over long distances via photons and the high detection efficiency of massive particles. In combination with the heralding signal provided by the entanglement swapping protocol, this allows to close the detection loophole in an experiment at which both entangled atoms are separated by macroscopic distance for the first time. The actual realization of this AAE experiment is equal to the one described in chapter 4 extended by the atomic state readout described in subsection 2.4.2.

Finally, the experimental results clearly proved the generation of AAE. The entanglement was estimated to be $F_{\Psi^-} = 0.811 \pm 0.028$ for atoms projected onto the $|\Psi^-\rangle_{aa}$-state and $F_{\Psi^+} = 0.815 \pm 0.028$ for atoms projected onto the $|\Psi^+\rangle_{aa}$-state, respectively. Evaluation of a CHSH-inequality yielded a value $S' = 2.19 \pm 0.09$ which clearly violates the classical limit of $S' = 2$.

6. Conclusion and Outlook

This work presented the successful generation and verification of heralded entanglement between two widely separated atoms.

The experiments were performed with single ^{87}Rb atoms stored in strongly focused optical dipole traps. Entanglement between the atomic spin and the polarization of a single photon was generated via pulsed excitation of the trapped atoms and their subsequent optical decay in a λ-scheme. This atom-photon entanglement was verified in two independent setups installed at two locations separated by $20\,\mathrm{m}$, achieving visibilities up to $V_{ap} = 0.897$.

In a next step both setups have been combined by overlapping the photons emitted by each atom at a beam splitter. Synchronized pulsed excitation of both atoms guaranteed that the emitted single photons impinged at the beam splitter simultaneously. The observed quantum interference of the two photons was analyzed in detail. This included analysis of the probability to emit two photons from one atom within a single excitation. These spurious two-photon events show distinct polarization correlations, which reduce the two-photon interference quality. Experimental tests show that the total probability to emit a second, $\sigma^{\pm}$-polarized photon, in case a first, $\sigma^{\pm}$-polarized photon has already been emitted in the same excitation attempt, is $P_{tp}^{\sigma^{\pm}} = 0.0077 \pm 0.0005$ (only $\sigma^{\pm}$-polarized photons can be detected by the detection optics). This value is determined within a model including the dominating processes of two-photon emission. Further reasons for a reduced interference quality, e.g., a non-perfect mode overlap of the two impinging photons or a non-perfect beam splitter were analyzed yielding their exact influence on the interference quality. The overall interference quality is given by the fraction of interfering photon pairs impinging on the beam splitter P_{int}. Contrary to a standard interference quality measure, this measure is independent of the basis of photon analysis. The performed measurements show a value of $P_{int} = 0.922 \pm 0.008$.

The achievement of both a high atom-photon entanglement visibility as well as a high two-photon interference quality enabled the demonstration of atom-atom entanglement with this setup. The projection of the two photons, each entangled with one atom, onto a Bell-state is used to swap the entanglement onto the atoms. Furthermore, the atoms are not projected onto an entangled state until the two-photon coincidence detection reduces the four particle Hilbert-space. The coincidence detection serves as an entanglement heralding signal, which allows to take every single atom-atom entanglement event into account. The atom-atom entanglement experiment performed shows a fidelity of $F_{\Psi^-} = 0.811 \pm 0.028$ for photons projected into the $|\Psi^-\rangle_{ph}$-state and $F_{\Psi^+} = 0.815 \pm 0.028$ for photons projected into the $|\Psi^+\rangle_{ph}$-state, respectively. These results prove the successful generation of atom-atom entanglement.

The recorded atom-atom entanglement data can also be used to perform a test of Bell's inequality without relying on a fair sampling assumption due to the heralded generation of entanglement and the fact that a result for the atomic state analysis is given for every heralded event. It is the first time that the detection loophole was closed for massive particles at macroscopic distances. The measurement yields a value of $S' = 2.19 \pm 0.09$ which clearly violates the classical limit of $S' = 2$ by more than two standard deviations.

Future improvements on the setup will additionally allow to close also the locality loophole in a Bell test. The loophole-free test of Bell's inequality will answer the almost 80 year old question,
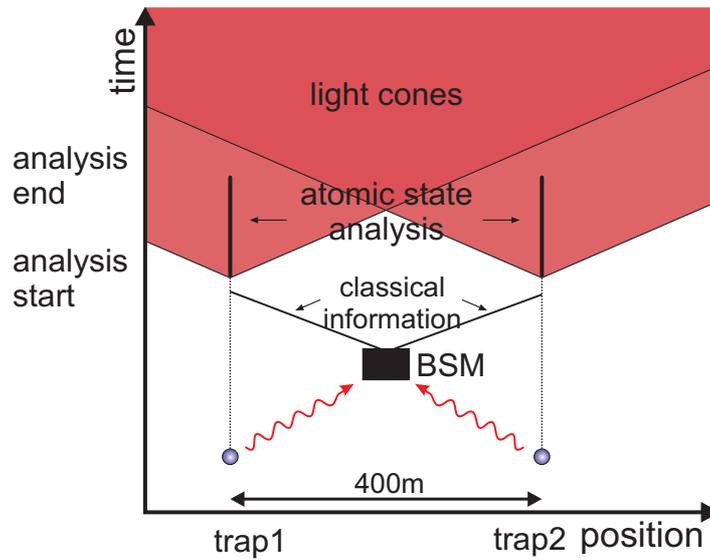
Figure 6.1.: Time-space diagram for a loophole-free Bell-test: The diagram shows the position of both atoms and the Bell-state detector. After the projection of the two photons onto a Bell-state the classical heralding signal is distributed to both experiments and the atomic state analysis is triggered. The total analysis of one experiment (including the choice of the measurement basis) must be outside the light cone of the other system.

whether quantum mechanics can be considered complete. The improvements must enable a space-like separated readout of the atomic states (see figure 6.1). This includes also the random choice of the measurement basis. The current readout takes about $60\,\mathrm{ms}$, which would require a distance between both atoms of $1800\,\mathrm{km}$, in order to execute both atomic state readouts outside each others light cone. Therefore, a realistic experiment requires a readout scheme which is orders of magnitudes faster. Oncoming experiments will use the ionization scheme described in subsection 2.4.2 combined with a detection of the ionization fragments by channel electron multipliers. This scheme, together with a fast quantum random number generator for choice of the measurement basis, allows analysis of the atomic states in less than $1\,\mu\mathrm{s}$ which reduces the required distance between the atoms to $300\,\mathrm{m}$ [98, 86]. A new laboratory situated at a distance of $400\,\mathrm{m}$ from the first one is already prepared, and a fiber link between both laboratories is installed.

The experimental setup can also be used for a demonstration of device-independent security of quantum cryptography [19] over a distance of $400\,\mathrm{m}$. The protocol works with pairs of entangled particles, and it is secure against all possible collective attacks for entanglement visibilities $V_{aa} > 0.858$ in a loophole-free Bell measurement setup - independent of the nature of the entangled particles and the protocol used for entanglement generation. For that purpose the atom-atom entanglement visibility has to be increased considerably. First promising steps in that direction have already been made. New data show atom-photon entanglement visibilities up to $V_{ap} = 0.93$ which is a lot higher than the visibilities presented in this thesis. By forcing the quality of all experimental steps to their limits the required atom-atom entanglement visibility can be achieved.

A. Physical Constants and Properties of ^{87}Rb

constant	description	value
$\hbar = \frac{h}{2\pi}$	reduced Plank constant	$1.054571726 \cdot 10^{-34}\,\text{J} \cdot \text{s}$
c	speed of light in vacuum	$2.99792458 \cdot 10^8\,\text{m/s}$
μ_0	permeability of free space	$1.25663770614 \cdot 10^{-6}\,\text{N/A}^2$
$\epsilon_0 = \frac{1}{c^2 \mu_0}$	permittivity of free space	$8.8541878176 \cdot 10^{-12}\,\text{F/m}$
e	elementary charge	$1.602176565 \cdot 10^{-19}\,\text{C}$
u	atomic mass unit	$1.660538921 \cdot 10^{-27}\,\text{Kg}$
$m_{^{87}Rb}$	mass of ^{87}Rb	$86.90918020 \cdot u$
Γ_{D1}	decay rate of ^{87}Rb D1 transition	$2\pi \cdot 5.7500\,\text{MHz}$
Γ_{D2}	decay rate of ^{87}Rb D2 transition	$2\pi \cdot 6.0666\,\text{MHz}$
d_{D1}	dipole matrix element of ^{87}Rb D1 transition	$2.53766 \cdot 10^{-29}\,\text{C} \cdot \text{m}$
d_{D2}	dipole matrix element of ^{87}Rb D2 transition	$3.58424 \cdot 10^{-29}\,\text{C} \cdot \text{m}$

Table A.1.: Physical constants and properties of ^{87}Rb [99]

B. Level Scheme of ^{87}Rb $D1$ and $D2$ Line

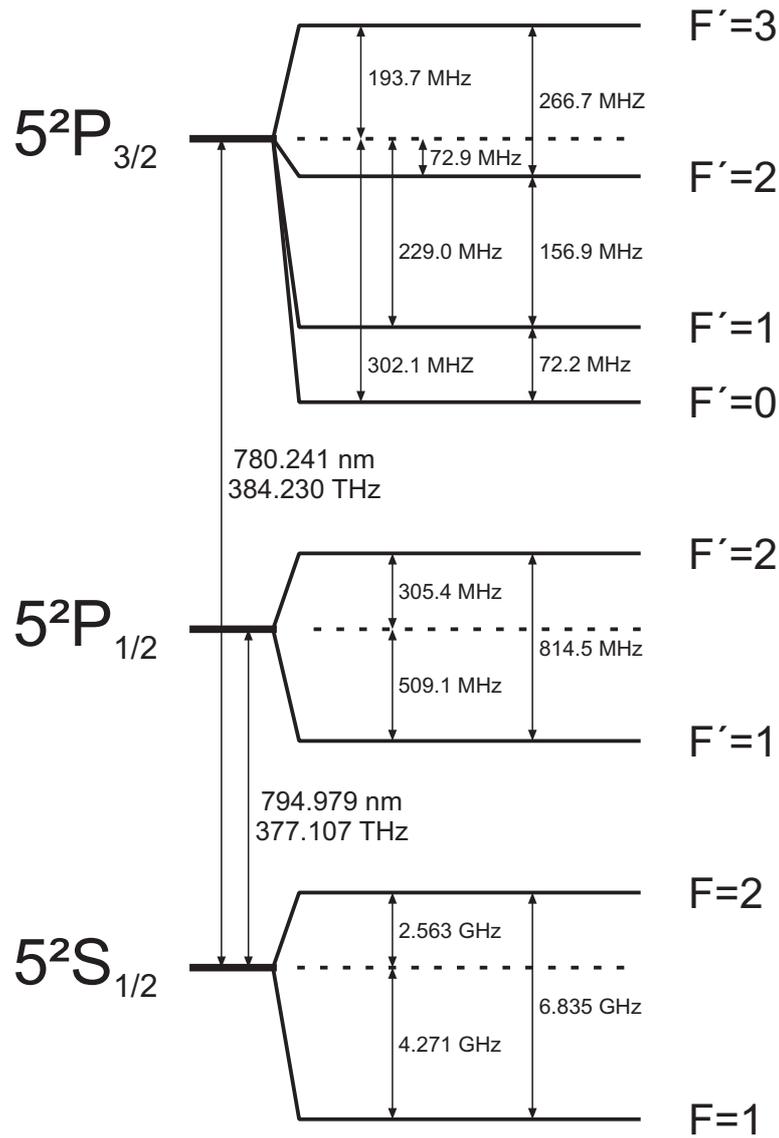Figure B.1.: ^{87}Rb $D1$ and $D2$ transition hyperfine structure with all frequencies splittings. The relative hyperfine shifts are shown as schematic and are not exact within every fine state. [99]

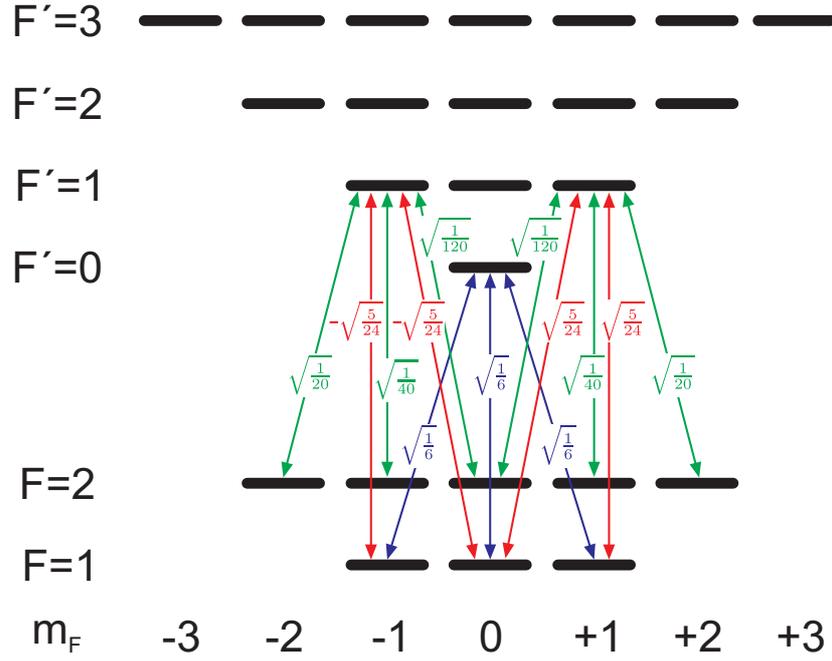# C. Clebsch-Gordan Coefficients of Important ^{87}Rb $D2$ Transitions

Figure C.1.: The figure shows all transitions, which are involved in single photon as well as in two-photon emission events, with their respective Clebsch-Gordan coefficients. [99]

States of Two-Photons Originating from a Two-Photon Emission Event Caused by Off-Resonant Excitation

Two-photon events caused by off-resonant excitation are discussed in subsection 3.4. After decay of the atom into the states $5^2S_{1/2}$, $|F = 1, m_F = \pm 1\rangle$ the atom is excited a second time to the states $5^2P_{3/2}$, $|F' = 1\, m_F = \pm 1\rangle$. Thus, the total system is in the state:

$$\frac{1}{\sqrt{2}}(|1', 1\rangle|R\rangle_1 - |1', -1\rangle|L\rangle_1),$$

where $|R\rangle_1$ and $|L\rangle_1$ describe the polarization state of the first emitted photon and e.g. $|1', 1\rangle$ the atomic state $5^2P_{3/2}$, $|F' = 1\, m_F = +1\rangle$. From there it may decay into a series of ground states as shown in figure C.1 The decays at which a not detectable π-polarized photon is emitted are not considered. Therefore, the normalized state after the second photon emission is given by

$$\sqrt{\tfrac{25}{32}}|1,0\rangle\tfrac{1}{\sqrt{2}}(|R\rangle_1|L\rangle_2 + |L\rangle_1|R\rangle_2) + \sqrt{\tfrac{1}{32}}|2,0\rangle\tfrac{1}{\sqrt{2}}(|R\rangle_1|L\rangle_2 - |L\rangle_1|R\rangle_2)$$
$$-\sqrt{\tfrac{3}{32}}|2,-2\rangle|L\rangle_1|L\rangle_2 + \sqrt{\tfrac{3}{32}}|2,2\rangle|R\rangle_1|R\rangle_2.$$

The two-photon density matrix is deduced by tracing over the atomic states:

$$\rho = \frac{25}{32}|\Psi^+\rangle\langle\Psi^+| + \frac{1}{32}|\Psi^-\rangle\langle\Psi^-| + \frac{3}{32}|L\rangle_1|L\rangle_2\langle L|_1\langle L|_2 + \frac{3}{32}|R\rangle_1|R\rangle_2\langle R|_1\langle R|_2$$

with

$$|\Psi^+\rangle = \frac{1}{\sqrt{2}}|R\rangle_1|L\rangle_2 + |L\rangle_1|R\rangle_2) = \frac{1}{\sqrt{2}}|H\rangle_1|H\rangle_2 + |V\rangle_1|V\rangle_2)$$

and

$$|\Psi^-\rangle = \frac{1}{\sqrt{2}}|R\rangle_1|L\rangle_2 - |L\rangle_1|R\rangle_2) = \frac{1}{\sqrt{2}}|H\rangle_1|V\rangle_2 - |V\rangle_1|H\rangle_2).$$

$|\Psi^+\rangle$ and $|\Psi^-\rangle$ are both entangled states which are obtained with the relative probabilities $p_a = {}^{25}\!/_{32} = 0.78125$ (Ψ^+) and $p_b = {}^1\!/_{32} = 0.03125$ (Ψ^-), respectively. The partial mixed state

$$\frac{3}{32}|L\rangle_1|L\rangle_2\langle L|_1\langle L|_2 + \frac{3}{32}|R\rangle_1|R\rangle_2\langle R|_1\langle R|_2$$

is observed with a relative probability of $p_c = {}^6\!/_{32} = 0.1875$.

Ratio of Emission of Detectable and not Detectable Photons

The detection optics installed in the experiment can't detect π-polarized photons as they don't couple into the detection fiber. However, knowledge of the exact ratio of emitted detectable to emitted not detectable photons is required to calculate the single photon and two-photon emission event frequencies.

If the atom is excited only once by the excitation pulse it is in the state $5^2P_{3/2}, |F' = 0\, m_F = 0\rangle$. It is also in this state if it is excited a second time caused by errors of the polarization of the excitation pulse (see subsection 3.2.1) or by a previous decay into the initial state (see subsection 3.2.3). From this state the atom can decay in all three Zeeman sub-states of the $5^2S_{1/2}, |F = 1\rangle$ ground state with equal probability (see figure C.1) whereby it only emits a detectable photon if it decays to the states $5^2S_{1/2}, |F = 1,\, m_F = \pm 1\rangle$. The ratio of not detectable to detectable photon is $1/2$ in this case.

If the atom is excited to the states $5^2P_{3/2}, |F' = 1\, m_F = \pm 1\rangle$ by off-resonant excitation (see subsection 3.2.2), it can decay into all Zeeman sub-states of the two ground states $5^2S_{1/2}, |F = 1\rangle$ and $5^2S_{1/2}, |F = 2\rangle$. The relative probabilities of the different decay channels are defined by the Clebsch-Gordan coefficients. In this case the ratio of not detectable to detectable photons is $7/8$.

D. Notation of Atomic States and Light Polarization

The entangled atom-photon state is introduced in equations 2.1 and 2.2 for analysis in the $\hat{\sigma}^z$-basis. It can also be expressed in the two orthogonal basis of the Pauli operators $\hat{\sigma}^x$ and $\hat{\sigma}^y$. Table D.1 shows the light polarization and the atomic states in the three bases.

symbol (pol.)	composition	qubit state	atomic dark state
R	σ^-	$\vert\downarrow\rangle_z$	$\vert F=1,\, m_F=-1\rangle$
L	σ^+	$\vert\uparrow\rangle_z$	$\vert F=1,\, m_F=+1\rangle$
H	$\frac{1}{\sqrt{2}}(\sigma^+ + \sigma^-)$	$\vert\uparrow\rangle_x$	$\frac{1}{\sqrt{2}}(\vert F=1,\, m_F=+1\rangle + \vert F=1,\, m_F=-1\rangle)$
V	$\frac{i}{\sqrt{2}}(\sigma^+ - \sigma^-)$	$\vert\downarrow\rangle_x$	$\frac{i}{\sqrt{2}}(\vert F=1,\, m_F=+1\rangle - \vert F=1,\, m_F=-1\rangle)$
P	$\frac{1}{\sqrt{2}}e^{i\pi/4}(\sigma^+ - i\sigma^-)$	$\vert\downarrow\rangle_y$	$\frac{1}{\sqrt{2}}e^{i\pi/4}(\vert F=1,\, m_F=+1\rangle - i\,\vert F=1,\, m_F=-1\rangle)$
M	$-\frac{1}{\sqrt{2}}e^{-i\pi/4}(\sigma^+ + \sigma^-)$	$\vert\uparrow\rangle_y$	$-\frac{1}{\sqrt{2}}e^{-i\pi/4}(\vert F=1,\, m_F=+1\rangle + i\,\vert F=1,\, m_F=-1\rangle)$

Table D.1.: Definition of light polarizations and the corresponding atomic states. The atomic dark states are the superposition of atomic states which are not excited by the corresponding light field polarization.

The atomic qubit states have the following relations (according to the eigenstates of $\hat{\sigma}^x$, $\hat{\sigma}^y$ and $\hat{\sigma}^z$):

$$
\begin{aligned}
\vert\uparrow\rangle_x &= \tfrac{1}{\sqrt{2}}(\vert\uparrow\rangle_z + \vert\downarrow\rangle_z) = -\tfrac{1}{\sqrt{2}}(\vert\uparrow\rangle_y - \vert\downarrow\rangle_y) \\
\vert\downarrow\rangle_x &= \tfrac{i}{\sqrt{2}}(\vert\uparrow\rangle_z - \vert\downarrow\rangle_z) = \tfrac{1}{\sqrt{2}}(\vert\uparrow\rangle_y + \vert\downarrow\rangle_y)
\end{aligned}
$$

$$
\begin{aligned}
\vert\uparrow\rangle_y &= -\tfrac{1}{\sqrt{2}}(\vert\uparrow\rangle_x - \vert\downarrow\rangle_x) = -\tfrac{1}{\sqrt{2}}e^{-i\pi/4}(\vert\uparrow\rangle_z + i\,\vert\downarrow\rangle_z) \\
\vert\downarrow\rangle_y &= \tfrac{1}{\sqrt{2}}(\vert\uparrow\rangle_x + \vert\downarrow\rangle_x) = \tfrac{1}{\sqrt{2}}e^{i\pi/4}(\vert\uparrow\rangle_z - i\,\vert\downarrow\rangle_z)
\end{aligned}
$$

$$
\begin{aligned}
\vert\uparrow\rangle_z &= \tfrac{1}{\sqrt{2}}(\vert\uparrow\rangle_x + \tfrac{1}{i}\,\vert\downarrow\rangle_x) = -\tfrac{1}{\sqrt{2}}e^{i\pi/4}(\vert\uparrow\rangle_y + i\,\vert\downarrow\rangle_y) \\
\vert\downarrow\rangle_z &= \tfrac{i}{\sqrt{2}}(\vert\uparrow\rangle_x - \tfrac{1}{i}\,\vert\downarrow\rangle_x) = -\tfrac{1}{\sqrt{2}}e^{-i\pi/4}(\vert\uparrow\rangle_y - i\,\vert\downarrow\rangle_y)
\end{aligned}
$$

With that information the entangled atom-photon states can be written in all three basis with respect of table D.1:

$$
\begin{aligned}
\vert\Psi^+\rangle &= \tfrac{1}{\sqrt{2}}(\vert\uparrow\rangle_z \vert R\rangle + \vert\downarrow\rangle_z \vert L\rangle) \\
&= \tfrac{1}{\sqrt{2}}(\vert\uparrow\rangle_y \vert M\rangle + \vert\downarrow\rangle_y \vert P\rangle) \\
&= \tfrac{1}{\sqrt{2}}(\vert\uparrow\rangle_x \vert H\rangle + \vert\downarrow\rangle_x \vert V\rangle)
\end{aligned}
$$

E. Comparison of Setups of Trap1 and Trap2

Due to installed enhancements in the setup of trap2, some characteristics of both setups differ. Particularly the objective, which focuses the dipole trap and collects spontaneously emitted photons has a higher N/A, and the atomic readout out scheme has changed to an ionization based scheme. The main differences of both setups are shown in table E.1.

	trap1	trap2
control type	master	slave
distance to detection setup	$0.5\,\text{m}$	$20\,\text{m}$
fiber stabilization	passive	active
dipole trap waist (ω_0)	$3.5\,\mu\text{m}$	$1.9\,\mu\text{m}$
trap depth	$k_B \cdot 0,65\,\text{mK}$	$k_B \cdot 1.5\,\text{mK}$
trap frequencies	$\omega_{x,y} = 2\pi{\cdot}22.7\,\text{kHz}$ $\omega_z = 2\pi{\cdot}1.25\,\text{kHz}$	$\omega_{x,y} = 2\pi{\cdot}63.5\,\text{kHz}$ $\omega_z = 2\pi{\cdot}6.37\,\text{kHz}$ [100]
atom temperature	$105\,\mu\text{K}$	$57\,\mu\text{K}$
atomic state readout scheme	STIRAP + push out beam	STIRAP + ionizaion
STIRAP beams focused by	microscope objective	aspheric lens
atom photon entanglement visibility	~ 0.87	~ 0.90

Table E.1.: Key features of both traps which differ.

F. Quantum jump model / optical Liouville Equations

The experiment described in this thesis is based on atom-light interactions. A single ^{87}Rb atom is excited by several laser fields shining onto it. In order to give any predictions on the atom-light interactions a model is needed which describes these interactions. It is based on optical Liouville equations and is expanded to describe the two-photon emission events discussed in chapter 3. In addition, it allows calculation of the temporal mode overlap of photon wave packets with different temporal amplitudes.

F.1. Louiville Equation

In this first section the Louiville equation of motion is derived from basic descriptions of a light field, an atom and their interaction.

F.1.1. Quantum Mechanical Description of a Light Field

In a first approximation an electric field with a spatial dependence is considered which is appropriate for a cavity resonator. This electromagnetic field can be quantized by identifying the canonical momentum p_j and the normal mode amplitude q_j of the classical electromagnetic field as operators which follows the commutation relations [101]:

$$[\hat{q}_j, \hat{p}_{j'}] = i\hbar\delta_{jj'}, \tag{F.1}$$

$$[\hat{q}_j, \hat{q}_{j'}] = [\hat{p}_j, \hat{p}_{j'}] = 0 \tag{F.2}$$

This enables a canonical transformation to a new set of operators $\hat{a}$ and $\hat{a}^\dagger$:

$$\begin{aligned}
\hat{a}e^{-i\omega_j t} &= \frac{1}{\sqrt{2m_j\hbar\omega_j}}(m_j\omega_j\hat{q}_j + i\hat{p}_j) \\
\hat{a}^\dagger e^{i\omega_j t} &= \frac{1}{\sqrt{2m_j\hbar\omega_j}}(m_j\omega_j\hat{q}_j - i\hat{p}_j),
\end{aligned} \tag{F.3}$$

where ω_j are the eigenfrequencies of the cavity and m_j are constants. The commutation relations of $\hat{a}_j$ and $\hat{a}_j^\dagger$ are identical to those between $\hat{q}_j$ and $\hat{p}_j$. The new operators are referred to as annihilation operator $\hat{a}_j$ and creation operator $\hat{a}_j^\dagger$ and define the electric field operator:

$$\hat{E}_X(z,t) = \sum_j \sqrt{\frac{\hbar\omega_j}{\epsilon_0 V}}(\hat{a}_j e^{-i\omega_j t} + \hat{a}_j^\dagger e^{i\omega_j t})\sin(k_j z) \tag{F.4}$$

It describes an electric field which is linear polarized in x-direction and expands in the normal modes of the cavity. ϵ_0 is the free space permittivity, V the volume of the cavity and $k = j\pi/L$, whereby L is the length of the cavity and $j = 1, 2, 3...$.

So far, these considerations describe only the electric field inside a finite one-dimensional cavity. In order to expand these for description of a field in a unbounded free space, a large but finite cubic cavity is considered. It finally leads to the following three-dimensional definition of the electric field operator:

$$\hat{\mathbf{E}}(\mathbf{r}, t) = \hat{\mathbf{E}}^+(\mathbf{r}, t) + \hat{\mathbf{E}}^-(\mathbf{r}, t), \tag{F.5}$$

where

$$
\begin{aligned}
\hat{\mathbf{E}}^+(\mathbf{r}, t) &= \sum_{\lambda,\mathbf{k}} \sqrt{\tfrac{\hbar\omega_k}{2\epsilon_0 V}} \boldsymbol{\epsilon}_{\lambda\mathbf{k}} \hat{a}_{\lambda\mathbf{k}} e^{-i(\omega_k t - \mathbf{kr})} \\
\hat{\mathbf{E}}^-(\mathbf{r}, t) &= \sum_{\lambda,\mathbf{k}} \sqrt{\tfrac{\hbar\omega_k}{2\epsilon_0 V}} \boldsymbol{\epsilon}_{\lambda\mathbf{k}} \hat{a}^\dagger_{\lambda\mathbf{k}} e^{+i(\omega_k t - \mathbf{kr})}.
\end{aligned} \tag{F.6}
$$

Here, $\mathbf{k}$ is the wave vector, ϵ is a unit polarization vector and λ describes the two orthogonal polarization modes of the light. The constant V describes the quantization volume.

F.1.2. Basic Atom-Light Interactions

The atom as well as the light field can be described individually by an Hamiltonian [101, 102]:

$$\mathcal{H}_A = \sum_i \hbar\omega_i |i\rangle\langle i| \tag{F.7}$$

$$\mathcal{H}_L = \sum_{\lambda,\mathbf{k}} \hbar\omega_k \left(\hat{a}^\dagger_{\lambda,\mathbf{k}} \hat{a}_{\lambda,\mathbf{k}} + \frac{1}{2}\right). \tag{F.8}$$

$\mathcal{H}_L$ describes the light field, and is defined by the annihilation and creation operator $\hat{a}_{\lambda,\mathbf{k}}$ and $\hat{a}^\dagger_{\lambda,\mathbf{k}}$, respectively introduced in the previous section. $\mathcal{H}_A$ describes the the atomic structure. $|i\rangle$ are the levels of the atoms with their respective energies $\hbar\omega_i$. This includes already the near-resonance approximation which allows only to consider a finite number of levels. The Hamiltonian, which describes the atom-light interaction, is given by the following equation:

$$
\begin{aligned}
\mathcal{H}_{AL} &= \hat{\mathbf{d}} \cdot \hat{\mathbf{E}} \\
&= e \sum_{\lambda,\mathbf{k}} \sum_{i,j} \mathbf{g}_{ij\lambda\mathbf{k}} e^{i(\omega_i - \omega_j)t} \left(\hat{a}_{\lambda\mathbf{k}} e^{-i(\omega_k t - \mathbf{kr})} + \hat{a}^\dagger_{\lambda\mathbf{k}} e^{+i(\omega_k t - \mathbf{kr})}\right) |i\rangle\langle j|,
\end{aligned} \tag{F.9}
$$

where the electric field $\hat{\mathbf{E}}$ is defined by equation F.5 and the dipole operator $\hat{\mathbf{d}}$ describes the coupling strength between the light field and an atomic transition:

$$\mathbf{d}_{ij} = \langle i|\hat{\mathbf{d}}|j\rangle. \tag{F.10}$$

This leads to the coupling coefficient

$$\mathbf{g}_{ij\lambda\mathbf{k}} = \sqrt{\frac{\omega_k t}{2\hbar\epsilon_0 V}} \boldsymbol{\epsilon}_{\lambda\mathbf{k}} \mathbf{d}_{ij}. \tag{F.11}$$

Thus, the total Hamiltonian is

$$\mathcal{H} = \mathcal{H}_A + \mathcal{H}_L + \mathcal{H}_{AL}. \tag{F.12}$$

A so called rotating wave approximation (RWA) allows to write the Hamiltonian as follows:

$$\mathcal{H} = \frac{\hbar}{2} \begin{pmatrix} 2\Delta_{1,2} & \Omega_{1,2} & 0 \\ \Omega^*_{1,2} & 0 & \Omega_{2,3} \\ 0 & \Omega^*_{2,3} & 2\Delta_{2,3} \end{pmatrix} \tag{F.13}$$

In this notation $\Omega_{ij} \equiv \frac{E_0}{\hbar} \langle i|\hat{\mathbf{d}}|j \rangle$ describes the on-resonance Rabi frequency where E_0 is the maximum amplitude of the electric field and $\Delta_{ij} \equiv (\omega_i - \omega_j) - \omega_k$ describes the detuning of the light field from the atomic transition. The Rabi frequency is given by $\Omega_{R,ij} = \sqrt{\Omega_{ij}^2 + \Delta_{ij}^2}$.

This Hamiltonian does not consider spontaneous decay of the excited state of the atom but only describes a coherent evolution. Therefore, a relaxation matrix Γ has to be introduced which describes the spontaneous decay. It is defined by the following expression:

$$\gamma_{nm} = \langle n|\Gamma|m \rangle. \tag{F.14}$$

F.1.3. Equation of Motion (Liouville Equation)

This section introduces the equation of motion with respect to the density matrix. The density matrix is defined by

$$\rho = \sum_{\Psi} P_{\Psi} |\Psi\rangle\langle\Psi|, \tag{F.15}$$

where P_{Ψ} is the time independent probability that the system is in the state $|\Psi\rangle$. The basic equation of motion is given by the Schrödinger equation:

$$|\dot{\Psi}\rangle = \frac{i}{\hbar}\mathcal{H}|\Psi\rangle. \tag{F.16}$$

The time derivative of ρ is

$$\dot{\rho} = \sum_{\Psi} P_{\Psi}(|\dot{\Psi}\rangle\langle\Psi| + |\Psi\rangle\langle\dot{\Psi}|) \tag{F.17}$$

with respect to equation F.15. The equation of motion for the density matrix is derived from this equation by using equation F.16 to replace $|\dot{\Psi}\rangle$ and $\langle\dot{\Psi}|$:

$$\dot{\rho} = \frac{i}{\hbar}[\mathcal{H}, \rho]. \tag{F.18}$$

This equation is also called the Liousville equation describing the coherent evolution of the system. The spontaneous decay is considered by addition of a second term which leads to the following equation:

$$\dot{\rho} = \frac{i}{\hbar}[\mathcal{H}, \rho] + \frac{1}{2}\{\Gamma, \rho\}, \tag{F.19}$$

where $\{\Gamma, \rho\} = \Gamma\rho + \rho\Gamma$.

F.2. Definition of Excitation Pulse and Time Dependent Rabi Frequency

Here, the time-depended Rabi frequency is derived from the laser pulse which excites the atom. It is included in the Hamiltonian given by equation F.13, and therefore necessary for any further examinations of the atom light interactions.

F.2.1. The Excitation Pulse

In all experiments discussed in this thesis the single atom is excited by an optical pulse. In order to simulate the interaction of the atom with such a pulse a mathematical description of the pulse is needed. The optical pulse has an almost Gaussian shape due to the time response of the employed acousto-optic-modulator (AOM) which switches the light on and off. Therefore, the following function is fitted to the measured data:

$$f_{ep}(t) = a e^{-\frac{1}{2}(\frac{t-t_l}{T})^2}, \tag{F.20}$$

where a, t_l and T are defined by the fitting routine. A plot of the optical pulse and the model defined by equation F.20 is presented in figure 3.1 a).

The further model of the excitation pulse uses only the constant T determined by the fit. It is related to the full width half maximum (FWHM) by $2\sqrt{2\ln 2}T$. The other two constants a and t_l, describing the amplitude and the timing of the recorded excitation pulse, respectively, are of no further relevance.

The temporal intensity of the light field at the position of the atom is given by

$$ti(t) = int \cdot e^{\frac{1}{2}(\frac{t-t_0}{T})^2}, \tag{F.21}$$

where t_0 defines the delay of the excitation pulse to an experimental trigger and int defines the maximal intensity of the pulse:

$$int = \frac{2 \cdot lp}{\omega_o^2 \pi}, \tag{F.22}$$

where lp is the peak laser power and ω_0 is the waist of the excitation beam.

F.2.2. The On-Resonance Rabi Frequency

The on-resonance Rabi frequency depends on the electric field and the atomic dipole moment of the respective transition as defined in the previous section:

$$\Omega(t) = cs \cdot \sqrt{\frac{2ti(t)}{c \cdot \epsilon_0}}. \tag{F.23}$$

In this thesis only transitions of the D2-line of ^{87}Rb are considered. Thus, cs is defined by

$$cs = \frac{d_{D2} \cdot cgc}{\hbar}, \tag{F.24}$$

where d_{D2} is the respective dipole matrix element and cgc is the Clebsch-Gordan coefficient of the respective transition.

F.3. Simulation of a Standard Atom Excitation Process

The standard atom excitation process can be reduced to a process involving only three atomic states (see figure F.1 a)). At the beginning the atom is in the first ground state $\rho_{11}(0) = 1$ which represents the state $5^2S_{1/2}, |F = 1, m_F = 0\rangle$. The light field resonantly couples the state to the excited state ($\rho_{22}(t)$) which represents the state $5^2P_{3/2}, |F' = 1, m_F = 0\rangle$. The excited state may decay in the already introduced ground state or into a second ground state ($\rho_{33}(t)$) which represents the two states $5^2S_{1/2}, |F = 1, m_F = \pm 1\rangle$. This ground state is not coupled to the excited state by the laser field.
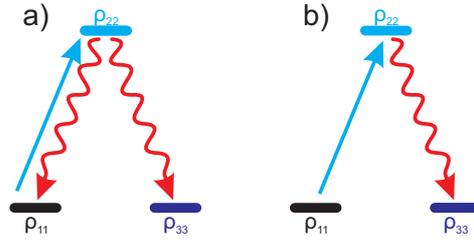
Figure F.1.: Scheme of the coupling between the three levels in the model. a) shows the case at which a decay into the initial state and a possible second excitation are allowed. b) shows the case at which the atom can only decay into a state which does not couple to the excited state. Here, maximal one photon can be emitted.

The evolution of this process is determined with respect of equation F.19 where $\rho_{33}(t)$ describes the present population of the sates $5^2S_{1/2}$, $|F = 1, m_F = \pm 1\rangle$ for any time t. The temporal derivation of $\rho_{33}(t)$ gives the time dependent probability to emit a photon which may couple into the detection fiber (by decay into the state $5^2P_{3/2}, |F' = 1, m_F = 0\rangle$ the atom would emit a π-polarized photon which is not detectable by the detection optics):

$$\rho'_{33}(t) = \frac{d\rho_{33}(t)}{dt}. \tag{F.25}$$

The total number of these photons emitted in a time window $[t_{start}, t_{end}]$ is given by

$$n_{ph} = \int_{t_{start}}^{t_{end}} dt \, \rho'_{33}(t). \tag{F.26}$$

This allows the calculation of the relative probability to emit a photon at a certain time t (with $t_{ent} > t > t_{start}$):

$$p_{rem}(t) = \frac{\rho'_{33}(t)}{n_{ph}}. \tag{F.27}$$

It can be interpreted as the temporal distribution of detection probability for the single photon wave packet under the condition that the amplitude of the wave packed outside the time window is negligible and that the total number of scattered photons is smaller than one. The total number of scattered photons per atom excitation attempt is given by

$$n_{total} = \int_{t_{start}}^{t_{end}} dt \, \rho_{22}(t). \tag{F.28}$$

This also includes events at which π-polarized photons are emitted. All results still depend on the power of the excitation pulse lp.

F.3.1. Determination of Laser Power and Timing of the Excitation Pulse

The relative probability to emit a photon in a certain time window $[t_{start}, t_{end}]$ is given by equation F.27 for every time t inside the time window. A histogram of the photon detection times which is normalized analogously to equation 4.91 also shows the relative probability to emit a photon in

a certain time window for every time t (see figure 4.10 b)). Thus, a normalized histogram is the measured equivalent to $p_{rem}(t)$. The temporal shape of p_{rem} can be fitted to the shape of the histogram just by varying the parameters t_0 and lp as presented in figure 3.1 b) It determines the parameters $t_0 = 501.9 \pm 0.05 \, \text{ns}$ and $lp = 14,58 \pm 0.09 \, \mu\text{W}$ for the certain measurement, which are regarded as a given in all further calculations. The total number of scattered photons per atom excitation attempt (which are not π-polarized) is $n_{ph} = 0.685$ with respect to the determined values of t_0 and lp.

F.3.2. Single-Photon Emission

The precious calculations already include one type of two-photon emission events as decay into the initial state and a subsequent second excitation is allowed (see subsection 3.2.3). Thus, the overall number of scattered photons n_{total} might be larger than one. In the subsequent considerations of two-photon events it is assumed that the atom decayed only once before it is excited a second time via a certain transition. Therefore, it is necessary to model a single-photon emission. This model is almost equivalent to the already introduce one but here, the atom may only decay into $\rho_{33}(t)$ (see figure F.1 b)). Thus, it can't be excited a second time after the first decay. The total number of detectable photons scattered this way is

$$n_{1st} = \frac{2}{3} \int\limits_{t_{start}}^{t_{end}} dt \, p_{1st}(t) \tag{F.29}$$

where $p_{1st}(t)$ is temporal derivation of $\rho_{33}(t)$ in the current solution of equation F.19. The factor $^2/_3$ respects the branching ratio for decay into the states $5^2S_{1/2}$, $|F = 1, m_F = \pm 1\rangle$ and $5^2P_{3/2}$, $|F' = 1, m_F = 0\rangle$. The total number of single detectable photons is $n_{1st} = 0.65$ with respect to the determined values of t_0 and lp. The relative probability to emit a photon at a given time t in a certain time window is given by

$$|\alpha_{single}(t)|^2 = \frac{p_{1st}(t)}{\int_{t_{start}}^{t_{end}} dt \, p_{1st}(t)} \tag{F.30}$$

and can be interpreted as expectation value of the temporal amplitude of the single photon wave function under the assumption that an analytic continuation of $\sqrt{|\alpha_{single}(t)|}$ exists. It's temporal shape slightly differs from the one defined by p_{rem} as shown in figure F.2.

F.4. Two-Photon Emission (Quantum Jump Model)

If the atom spontaneously emits a photon while the excitation pulse is still present, the possibility arises to excite the atom a second time and a the two emitted photons form a two photon state $\int dt_1 dt_2 \alpha_i(t_1, t_2)|t_1\rangle|t_2\rangle$, where $\alpha_i(t_1, t_2)$ temporal amplitude of this state (with $i \in \{\text{I, II, III}\}$). Section 3.2 discusses three different types of two-photon emission events. In order to simulate these different processes, a model is needed which considers that the atom is excited a second time by only the rest of the excitation pulse and only a fraction of the full intensity of the pulse (see subsection 3.2.1). Also the transition strength of the second excitation might be different as the atom may be excited to a different state (see subsection 3.2.2). Therefore, a piecewise function is introduced which is zero until the emission time of the first photon t_1 and is equal to equation F.21 thereafter:

$$ti2nd_i(t_1, t_2) = \begin{cases} 0 & , t_2 < t_1 \\ a_i \cdot ti(t_2) & , t_2 \geq t_1 \end{cases}, \tag{F.31}$$
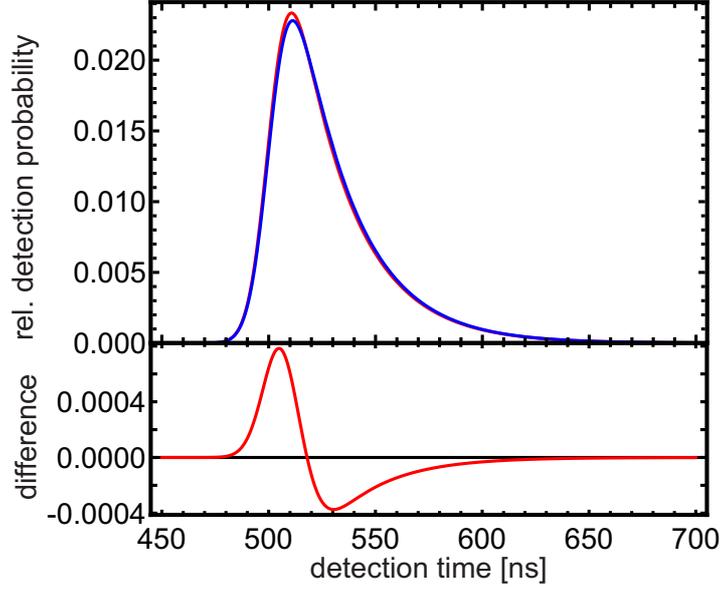
Figure F.2.: upper figure: Temporal distribution of detection probability for the single photon wave packet $|\alpha_{single}(t)|^2$ (red) and the temporal distribution of detection probability $p_{rem}(t)$ which also includes two-photon emission events at which the first photon is π-polarized (blue, see section 3.2.3). The offset of the starting time of $450\,\mathrm{ns}$ is defined by an external trigger and has no further relevance. lower figure: difference of both graphs plotted in the upper figure: $|\alpha_{single}(t)|^2 - p_{rem}(t)$.

where $a_i \in [0..1]$ allows to adjust the optical power of the residual pulse for every type of two-photon emission event.

The solution of the Liousville equation now depends on two parameters (t_1 and t_2), and respects the new Rabi-frequencies $\Omega_i(t_1, t_2)$ which also include different coupling strengths for the three types of two-photon emission. Analogous to previous explanations, the temporal derivation of $\rho2_{33,i}(t_1, t_2)$ gives the time dependent probability to emit a second photon at time t_2, if a first photon has been emitted at time t_1, for every type of two-photon emission, if the atom can only decay once (see figure F.1 b)):

$$\rho2'_{33,i}(t_1, t_2) = \frac{d\rho2_{33,i}(t_1, t_2)}{dt_2}. \tag{F.32}$$

In oder to calculate the total probability to emit a first photon at time t_1 and second one at time t_2, all emission times t_1 have to be weighted by their respective probability:

$$p_{tpe,i}(t_1, t_2) = A_{2nd,i} \cdot A_{1st,i} \cdot p_{1st}(t_1) \cdot \rho2'_{33,i}(t_1, t_2), \tag{F.33}$$

where $A_{2nd,i}$ is the ratio of $\sigma^{\pm}$-polarized to all emitted photons of the second decay of the atom for a given type of two-photon emission, and $A_{1st,i}$ is the ratio first photon emissions, after what a second excitation is possible for a given type of two-photon emission, to all first photon emissions. Thus, the number of emission of a second photons is given by

$$n_{2nd,i} = \int\limits_{t_{start}}^{t_{end}} dt_1 \int\limits_{t_{start}}^{t_{end}} dt_2 \, p_{tpe,i}(t_1, t_2). \tag{F.34}$$

It allows to calculate the expectation value of the probability amplitude of the generated two-photon state $\int dt d\tau \alpha_i(t_1, t_2)|t_1\rangle|t_2\rangle$:

$$|\alpha_i(t_1, t_2)|^2 = \frac{p_{tpe,i}(t_1, t_2)}{n_{2nd,i}} \tag{F.35}$$

F.5. Two-Photon Emission Probabilities

There are three major types of two-photon emission events as discussed in section 3.2. Their individual probabilities depend in the laser power $ti2nd_i(t_1, t_2)$, which is present for the second excitation and the rations $A_{1st,i}$ and $A_{2nd,i}$ with $i \in \{\text{I, II, III}\}$.

A measure for the relative probability of a certain two photon process is given by the ratio of the probabilities for such an event to a single photon emission event:

$$p_{tp-i} = \frac{n_{tpe,i}}{n_{1st}}. \tag{F.36}$$

This can be interpreted as the probability to emit a second, detectable photon, if a first, detectable photon has already been emitted.

F.6. Mode Overlap Calculations

The mode overlap of two photon wave packets significantly influences the interference probability of the two photons as discussed in chapter 4. Its expectation value can be determined by $|\int_{t_{start}}^{t_{end}} dt\, \alpha_1^\star(t) \cdot \alpha_2(t)|^2$, where $\alpha_j(t)$ is a complex function which describes the temporal amplitude of the single photon wave packet. Above calculations can't determine this complex function, but only its expectation value $|\alpha_j(t)|^2$ which corresponds to the relative probability to emit a photon at a certain time t. Nevertheless the expectation value of the mode overlap can be calculated for two single photons by the following equation

$$O^2 = (\int_{t_{start}}^{t_{end}} dt \sqrt{\sqrt{|\alpha_{single,1}(t)|^2} \cdot \sqrt{|\alpha_{single,2}(t)|^2}})^2 \tag{F.37}$$

under the assumption that $|\alpha_{single,j}(t)|^2$ are the expectation values of the temporal amplitudes of two single photon wave functions calculated by equation F.30 and both single photons have the same center wavelength.

The calculation of the expectation value of the mode overlap of a single photon and a photon which originates from a two-photon emission process is more complex as the emission probability of the second photon $p_{tpe,i}(t_1, t_2)$ (with $i \in \{\text{I, II, III}\}$) depends on both the emission time of the first photon t_1 and the emission time of the second photon t_2. The mode overlap calculations for the two cases which may occur are presented in the following subsections.

Overlap of a Single Photon and the First Photon of a Two-photon Emission Process ($\bullet \circ |\bullet$)

The expectation value of the mode overlap of a single photon and the first photon of a two-photon emission process highly depends on the emission time t_2 of the second photon of a two-photon emission process (see section 4.4). The projection of the two-photon state $\int dt_1 dt_2\, \alpha_i(t_1, t_2)|t_1\rangle|t_2\rangle$ (with

$i \in \{\text{I, II}\}$) on a certain emission time t_2 of the second photon yields the (pure) state $\int dt_1 \beta_i(t_1|t_2)|t_1\rangle$ for the first photon with

$$\beta_i(t_1|t_2) = \sqrt{\frac{|\alpha_i(t_1, t_2)|^2}{\int dt_1 \, |\alpha_i(t_1, t_2)|^2}}, \tag{F.38}$$

where $|\alpha_i(t_1, t_2)|^2$ is defined by expression F.35. Thus, for every time t_2 the expectation value of the mode overlap of a single photon and the first photon of a two-photon emission process can be calculated by

$$O^2_{\bullet \circ_i | \bullet}(t_2) = \left| \int_{t_{start}}^{t_{end}} dt_1 \beta_i(t_1|t_2) \cdot \sqrt{|\alpha_{single}(t_1)|^2} \right|^2. \tag{F.39}$$

The overall mode overlap is determined by

$$O^2_{\bullet \circ_i | \bullet} = \int_{t_{start}}^{t_{end}} dt_2 \, p_{t_1}(t_2) \cdot O^2_{\bullet \circ_i | \bullet}(t_2), \tag{F.40}$$

where $p_{t_1,i}(t_2) = \int dt_1 \, |\alpha_i(t_1, t_2)|^2$ serves as a weight for $O^2_{\bullet \circ_i | \bullet}(t_2)$. It describes the relative probability of a second photon emission at time t_2.

Overlap of a Single Photon and the Second Photon of a Two-Photon Emission Process ($\circ \bullet | \bullet$)

In analogy to the previous subsection the expectation value of the mode overlap of a single photon and the second photon of a two-photon emission process highly depends on the emission time t_1 of the first photon of the two-photon emission process as described in subsection 4.4. The emission time t_1 of the first photon determines the residual time of excitation pulse which might excite the atom again. Thus, the normalized solutions of F.35 for a fixed emission time t_1 of the first photon corresponds to the temporal amplitude $\beta_i(t_2|t_1)$ (with $i \in \{\text{I, II, III}\}$) of the (pure) state $\int dt_2 \beta_i(t_2|t_1)|t_2\rangle$ for the second photon with:

$$\beta_i(t_2|t_1) = \sqrt{\frac{|\alpha_i(t_1, t_2)|^2}{\int dt_1 \, |\alpha_i(t_1, t_2)|^2}}, . \tag{F.41}$$

The expectation value of the mode overlap of a single photon and a second photon of a two-photon emission event can be calculated for every emission time t_1 of the first photon for a given type of two-photon emission events:

$$O^2_{\circ \bullet_i | \bullet}(t_1) = \left| \int_{t_{start}}^{t_{end}} dt_2 \beta_i(t_2|t_1) \cdot \sqrt{|\alpha_{single}(t_2)|^2} \right|^2. \tag{F.42}$$

The overall mode overlap is also determined by the same way as in the previous subsection:

$$O^2_{\circ \bullet_i | \bullet} = \int_{t_{start}}^{t_{end}} d\tau t_1 \, p_{t_2}(t_1) \cdot O^2_{\circ \bullet_i | \bullet}(t_1), \tag{F.43}$$

where $p_{t_2,i}(t_1) = \int dt_2 \, |\alpha_i(t_1, t_2)|^2$ serves as a wight for $O^2_{\circ \bullet_i | \bullet}(t_1)$ describing the relative probability of a first photon emission at time t_1

Bibliography

[1] A. Einstein, B. Podolsky, and N. Rosen, Phys. Rev. **47**, 777 (1935).

[2] J. S. Bell *et al.*, Physics **1**, 195 (1964).

[3] J. S. Bell, Reviews of Modern Physics **38**, 447 (1966).

[4] J. F. Clauser, M. A. Horne, A. Shimony, and R. A. Holt, Phys. Rev. Lett. **23**, 880 (1969).

[5] S. J. Freedman and J. F. Clauser, Phys. Rev. Lett. **28**, 938 (1972).

[6] J. F. Clauser and A. Shimony, Reports on Progress in Physics **41**, 1881 (1978).

[7] A. Aspect, P. Grangier, and G. Roger, Phys. Rev. Lett. **49**, 91 (1982).

[8] A. Aspect, J. Dalibard, and G. Roger, Phys. Rev. Lett. **49**, 1804 (1982).

[9] G. Weihs, T. Jennewein, C. Simon, H. Weinfurter, and A. Zeilinger, Phys. Rev. Lett. **81**, 5039 (1998).

[10] M. A. Rowe, D. Kielpinski, V. Meyer, C. A. Sackett, W. M. Itano, C. Monroe, and D. J. Wineland, Nature **409**, 791 (2001).

[11] K. Hammerer, A. S. Sørensen, and E. S. Polzik, Rev. Mod. Phys. **82**, 1041 (2010).

[12] S. J. van Enk, J. I. Cirac, and P. Zoller, Phys. Rev. Lett. **78**, 4293 (1997).

[13] L.-M. Duan and C. Monroe, Rev. Mod. Phys. **82**, 1209 (2010).

[14] N. Sangouard, C. Simon, H. de Riedmatten, and N. Gisin, Rev. Mod. Phys. **83**, 33 (2011).

[15] V. Giovannetti, S. Lloyd, and L. Maccone, Phys. Rev. Lett. **96**, 010401 (2006).

[16] V. Giovannetti, S. Lloyd, and L. Maccone, Nat Photon **5**, 222 (2011).

[17] H.-J. Briegel, W. Dür, J. I. Cirac, and P. Zoller, Phys. Rev. Lett. **81**, 5932 (1998).

[18] C. H. Bennett, G. Brassard, C. Crépeau, R. Jozsa, A. Peres, and W. K. Wootters, Phys. Rev. Lett. **70**, 1895 (1993).

[19] A. Acin, N. Brunner, N. Gisin, S. Massar, S. Pironio, and V. Scarani, Phys. Rev. Lett. **98**, 230501 (2007).

[20] P. Shor, in *Foundations of Computer Science, 1994 Proceedings., 35th Annual Symposium on* (1994) pp. 124–134.

[21] L. K. Grover, in *Proceedings of the twenty-eighth annual ACM symposium on Theory of computing*, STOC '96 (ACM, New York, NY, USA, 1996) pp. 212–219.

[22] C. A. Kocher and E. D. Commins, Phys. Rev. Lett. **18**, 575 (1967).

[23] X.-C. Yao, T.-X. Wang, P. Xu, H. Lu, G.-S. Pan, X.-H. Bao, C.-Z. Peng, C.-Y. Lu, Y.-A. Chen, and J.-W. Pan, Nat Photon **6**, 225 (2012).

[24] T. Monz, P. Schindler, J. T. Barreiro, M. Chwalla, D. Nigg, W. A. Coish, M. Harlander, W. Hänsel, M. Hennrich, and R. Blatt, Phys. Rev. Lett. **106**, 130506 (2011).

[25] O. Mandel, M. Greiner, A. Widera, T. Rom, T. W. Hansch, and I. Bloch, Nature **425**, 937 (2003).

[26] J. Volz, M. Weber, D. Schlenk, W. Rosenfeld, J. Vrana, K. Saucke, C. Kurtsiefer, and H. Weinfurter, Phys. Rev. Lett. **96**, 030404 (2006).

[27] B. B. Blinov, D. L. Moehring, L.-M. Duan, and C. Monroe, Nature **428**, 153 (2004).

[28] T. Wilk, S. C. Webster, A. Kuhn, and G. Rempe, Science **317**, 488 (2007), http://www.sciencemag.org/content/317/5837/488.full.pdf .

[29] A. Stute, B. Casabone, P. Schindler, T. Monz, P. O. Schmidt, B. Brandstatter, T. E. Northup, and R. Blatt, Nature **485**, 482 (2012).

[30] D. N. Matsukevich, T. Chanelière, M. Bhattacharya, S.-Y. Lan, S. D. Jenkins, T. A. B. Kennedy, and A. Kuzmich, Phys. Rev. Lett. **95**, 040405 (2005).

[31] E. Togan, Y. Chu, A. S. Trifonov, L. Jiang, J. Maze, L. Childress, M. V. G. Dutt, A. S. Sorensen, P. R. Hemmer, A. S. Zibrov, and M. D. Lukin, Nature **466**, 730 (2010).

[32] M. Lettner, M. Mücke, S. Riedl, C. Vo, C. Hahn, S. Baur, J. Bochmann, S. Ritter, S. Dürr, and G. Rempe, Phys. Rev. Lett. **106**, 210503 (2011).

[33] I. L. Chuang, N. Gershenfeld, and M. Kubinec, Phys. Rev. Lett. **80**, 3408 (1998).

[34] I. L. Chuang, L. M. K. Vandersypen, X. Zhou, D. W. Leung, and S. Lloyd, Nature **393**, 143 (1998).

[35] M. A. Nielsen, E. Knill, and R. Laflamme, Nature **396**, 52 (1998).

[36] L. M. K. Vandersypen, M. Steffen, G. Breyta, C. S. Yannoni, M. H. Sherwood, and I. L. Chuang, Nature **414**, 883 (2001).

[37] C. Monroe, D. M. Meekhof, B. E. King, W. M. Itano, and D. J. Wineland, Phys. Rev. Lett. **75**, 4714 (1995).

[38] S. Gulde, M. Riebe, G. P. T. Lancaster, C. Becher, J. Eschner, H. Haffner, F. Schmidt-Kaler, I. L. Chuang, and R. Blatt, Nature **421**, 48 (2003).

[39] M. Riebe, H. Haffner, C. F. Roos, W. Hansel, J. Benhelm, G. P. T. Lancaster, T. W. Korber, C. Becher, F. Schmidt-Kaler, D. F. V. James, and R. Blatt, Nature **429**, 734 (2004).

[40] M. D. Barrett, J. Chiaverini, T. Schaetz, J. Britton, W. M. Itano, J. D. Jost, E. Knill, C. Langer, D. Leibfried, R. Ozeri, and D. J. Wineland, Nature **429**, 737 (2004).

[41] J. Chiaverini, D. Leibfried, T. Schaetz, M. D. Barrett, R. B. Blakestad, J. Britton, W. M. Itano, J. D. Jost, E. Knill, C. Langer, R. Ozeri, and D. J. Wineland, Nature **432**, 602 (2004).

[42] R. Reichle, D. Leibfried, E. Knill, J. Britton, R. B. Blakestad, J. D. Jost, C. Langer, R. Ozeri, S. Seidelin, and D. J. Wineland, Nature **443**, 838 (2006).

[43] D. Schrader, I. Dotsenko, M. Khudaverdyan, Y. Miroshnychenko, A. Rauschenbeutel, and D. Meschede, Phys. Rev. Lett. **93**, 150501 (2004).

[44] M. Weber, *Quantum optical experiments towards atom-photon entanglement*, Ph.D. thesis, Ludwig-Maximilians-Universität München (2005).

[45] J. Volz, *Atom-Photon Entanglement*, Ph.D. thesis, Ludwig-Maximilians-Universität München (2006).

[46] W. Rosenfeld, *Experiments with an Entangled System of a Single Atom and a Single Photon*, Ph.D. thesis, Ludwig-Maximilians-Universität München (2008).

[47] J. Dalibard and C. Cohen-Tannoudji, J. Opt. Soc. Am. B **2**, 1707 (1985).

[48] N. Schlosser, G. Reymond, I. Protsenko, and P. Grangier, Nature **411**, 1024 (2001).

[49] T. Haensch and A. Schawlow, Optics Communications **13**, 68 (1975).

[50] S. Chu, L. Hollberg, J. E. Bjorkholm, A. Cable, and A. Ashkin, Phys. Rev. Lett. **55**, 48 (1985).

[51] E. L. Raab, M. Prentiss, A. Cable, S. Chu, and D. E. Pritchard, Phys. Rev. Lett. **59**, 2631 (1987).

[52] H. J. Metcalf and P. van der Straten, J. Opt. Soc. Am. B **20**, 887 (2003).

[53] N. Schlosser, G. Reymond, and P. Grangier, Phys. Rev. Lett. **89**, 023005 (2002).

[54] W. Rosenfeld, F. Hocke, F. Henkel, M. Krug, J. Volz, M. Weber, and H. Weinfurter, Phys. Rev. Lett. **101**, 260403 (2008).

[55] J. R. Kuklinski, U. Gaubatz, F. T. Hioe, and K. Bergmann, Phys. Rev. A **40**, 6741 (1989).

[56] R. Unanyan, M. Fleischhauer, B. Shore, and K. Bergmann, Optics Communications **155**, 144 (1998).

[57] F. Vewinger, M. Heinz, R. Garcia Fernandez, N. V. Vitanov, and K. Bergmann, Phys. Rev. Lett. **91**, 213001 (2003).

[58] H. J. Kimble, M. Dagenais, and L. Mandel, Phys. Rev. Lett. **39**, 691 (1977).

[59] F. Diedrich and H. Walther, Phys. Rev. Lett. **58**, 203 (1987).

[60] C. Kurtsiefer, S. Mayer, P. Zarda, and H. Weinfurter, Phys. Rev. Lett. **85**, 290 (2000).

[61] P. Michler, A. Kiraz, C. Becher, W. V. Schoenfeld, P. M. Petroff, L. Zhang, E. Hu, and A. Imamoglu, Science **290**, 2282 (2000), http://www.sciencemag.org/content/290/5500/2282.full.pdf .

[62] W. E. Moerner and L. Kador, Phys. Rev. Lett. **62**, 2535 (1989).

[63] L. Childress, J. M. Taylor, A. S. Sørensen, and M. D. Lukin, Phys. Rev. Lett. **96**, 070504 (2006).

[64] N. Gisin, G. Ribordy, W. Tittel, and H. Zbinden, Rev. Mod. Phys. **74**, 145 (2002).

[65] R. H. BROWN and R. Q. TWISS, Nature **177**, 27 (1956).

[66] P. GRANGIER, G. ROGER, and A. ASPECT, Annals of the New York Academy of Sciences **480**, 98 (1986).

[67] C. K. Hong, Z. Y. Ou, and L. Mandel, Phys. Rev. Lett. **59**, 2044 (1987).

[68] Z. Y. Ou, Phys. Rev. A **37**, 1607 (1988).

[69] J. G. Rarity and P. R. Tapster, J. Opt. Soc. Am. B **6**, 1221 (1989).

[70] L. Mandel, Rev. Mod. Phys. **71**, S274 (1999).

[71] T. Legero, T. Wilk, M. Hennrich, G. Rempe, and A. Kuhn, Phys. Rev. Lett. **93**, 070503 (2004).

[72] J. Beugnon, M. P. A. Jones, J. Dingjan, B. Darquié, G. Messin, A. Browaeys, and P. Grangier, Nature **440**, 779 (2006).

[73] P. Maunz, D. L. Moehring, S. Olmschenk, K. C. Younge, D. N. Matsukevich, and C. Monroe, Nat Phys **3**, 538 (2007).

[74] E. B. Flagg, A. Muller, S. V. Polyakov, A. Ling, A. Migdall, and G. S. Solomon, Phys. Rev. Lett. **104**, 137401 (2010).

[75] R. Lettow, Y. L. A. Rezus, A. Renn, G. Zumofen, E. Ikonen, S. Götzinger, and V. Sandoghdar, Phys. Rev. Lett. **104**, 123605 (2010).

[76] H. Bernien, L. Childress, L. Robledo, M. Markham, D. Twitchen, and R. Hanson, Phys. Rev. Lett. **108**, 043604 (2012).

[77] A. Sipahigil, M. L. Goldman, E. Togan, Y. Chu, M. Markham, D. J. Twitchen, A. S. Zibrov, A. Kubanek, and M. D. Lukin, Phys. Rev. Lett. **108**, 143601 (2012).

[78] E. Knill, R. Laflamme, and G. J. Milburn, Nature **409**, 46 (2001).

[79] M. Zukowski, A. Zeilinger, M. A. Horne, and A. K. Ekert, Phys. Rev. Lett. **71**, 4287 (1993).

[80] H. Fearn and R. Loudon, Optics Communications **64**, 485 (1987).

[81] R. A. Campos, B. E. A. Saleh, and M. C. Teich, Phys. Rev. A **40**, 1371 (1989).

[82] W. Rosenfeld, "Personal communication," (2012).

[83] H. Fearn and R. Loudon, J. Opt. Soc. Am. B **6**, 917 (1989).

[84] W. Rosenfeld, J. Hofmann, N. Ortegel, M. Krug, F. Henkel, C. Kurtsiefer, M. Weber, and H. Weinfurter, Optics and Spectroscopy **111**, 535 (2011).

[85] C. Simon and W. T. M. Irvine, Phys. Rev. Lett. **91**, 110405 (2003).

[86] W. Rosenfeld, M. Weber, J. Volz, F. Henkel, M. Krug, A. Cabello, M. Zukowski, and H. Weinfurter, Advanced Science Letters **2**, 469 (2009).

[87] D. L. Moehring, P. Maunz, S. Olmschenk, K. C. Younge, D. N. Matsukevich, L.-M. Duan, and C. Monroe, Nature **449**, 68 (2007).

[88] D. N. Matsukevich, P. Maunz, D. L. Moehring, S. Olmschenk, and C. Monroe, Phys. Rev. Lett. **100**, 150404 (2008).

[89] C.-W. Chou, J. Laurat, H. Deng, K. S. Choi, H. de Riedmatten, D. Felinto, and H. J. Kimble, Science **316**, 1316 (2007), http://www.sciencemag.org/content/316/5829/1316.full.pdf .

[90] Z.-S. Yuan, Y.-A. Chen, B. Zhao, S. Chen, J. Schmiedmayer, and J.-W. Pan, Nature **454**, 1098 (2008).

[91] K. C. Lee, M. R. Sprague, B. J. Sussman, J. Nunn, N. K. Langford, X.-M. Jin, T. Champion, P. Michelberger, K. F. Reim, D. England, D. Jaksch, and I. A. Walmsley, Science **334**, 1253 (2011), http://www.sciencemag.org/content/334/6060/1253.full.pdf .

[92] B. Julsgaard, A. Kozhekin, and E. S. Polzik, Nature **413**, 400 (2001).

[93] S. Ritter, C. Nolleke, C. Hahn, A. Reiserer, A. Neuzner, M. Uphoff, M. Mucke, E. Figueroa, J. Bochmann, and G. Rempe, Nature **484**, 195 (2012).

[94] M. Giustina, A. Mech, S. Ramelow, B. Wittmann, J. Kofler, A. Lita, B. Calkins, T. Gerrits, S. Woo Nam, R. Ursin, and Z. A., (Advance Online Publication/AOP). April 14, 2013.

[95] B. G. Christensen, K. T. McCusker, J. Altepeter, B. Calkins, T. Gerrits, A. Lita, A. Miller, L. K. Shalm, Y. Zhang, S. W. Nam, N. Brunner, C. C. W. Lim, N. Gisin, and P. G. Kwiat, arXiv:1306.5772 .

[96] J.-W. Pan, D. Bouwmeester, H. Weinfurter, and A. Zeilinger, Phys. Rev. Lett. **80**, 3891 (1998).

[97] J. Hofmann, M. Krug, N. Ortegel, L. Gérard, M. Weber, W. Rosenfeld, and H. Weinfurter, Science **337**, 72 (2012), http://www.sciencemag.org/content/337/6090/72.full.pdf .

[98] F. Henkel, M. Krug, J. Hofmann, W. Rosenfeld, M. Weber, and H. Weinfurter, Phys. Rev. Lett. **105**, 253001 (2010).

[99] D. A. Steck, "Rubidium 87 d line data," (2001).

[100] N. Ortegel, *Atom-Photon Entanglement*, Master's thesis, Ludwig-Maximilians-Universität München (2009).

[101] M. O. Scully and M. S. Zubairy, *Quantum optics* (University Press, 1997).

[102] G. Lindblad, Communications in Mathematical Physics **48**, 119 (1976).

Danksagung

An dieser Stelle möchte ich die Möglichkeit nutzen, mich bei all jenen Menschen, die diese Arbeit erst möglich gemacht haben, herzlich zu bedanken. Mein besonderer Dank gilt:

- Herrn Prof. Dr. Harald Weinfurter: Für die Möglichkeit an diesem spannenden Projekt mitwirken zu dürfen und die mir gebotenen Freiheiten während meiner Arbeit.

- Den aktuellen und ehemaligen Mitgliedern des Atom-Experiments Wenjamin Rosenfeld, Markus Weber, Florian Henkel, Michael Krug, Norbert Ortegel, Kai Redeker, Daniel Burchardt, Lea Gérard, Christoph Kurz, Chien Ju Lee und Mathias Müller: Für die tolle Arbeitsatmosphäre während der vielen Stunden im Labor und für die vielen guten Diskussionen im und außerhalb des Labors.

- Allen anderen Mitgliedern der Arbeitsgruppe Weinfurter: Juliane Bahe, Stefan Frick, Martin Fürst, Harald Krauss, Nikolai Kiesel, Lukas Knips, Fabian Kössel, Roland Krischek, Lars Liebermeister, Patrick Michelberger, Sebastian Nauert, Alexander Niggebaum, Markus Rau, Daniel Richart, Christian Schwemmer, Toshiyuki Tashima, Johannes Trapp, Almut Tröller, Gwenaelle Vest, Henning Weier, Witlef Wieczorek für die Unterstützung und Hilfsbereitschaft. Ihr alle habt dazu beigetragen, dass die letzten fünf Jahre eine so schöne Zeit waren. Ganz besonders möchte ich Daniel Schlenk für die vielen Kaffepausen und die Ablenkung, wenn sie nötig war, danken.

- Allen QCCC-Mitgliedern: Für spannende Diskussionen bei den Workshops und Seminaren. Besonders möchte ich dem Koordinator Thomas Schulte-Herbrüggen für seine Organisation aller Veranstaltungen danken.

- Frau Gschwendtner und Frau Schmid für Ihre Unterstützung und Hilfsbereitschaft.

- All meinen Freunden und meiner Familie für Ihre Unterstützung und Ihre Motivation, wenn es mal nicht so gut lief.